University of Kentucky Doctoral Dissertations   Graduate School

2006

THERMAL HEAT TRANSPORT AT THE NANO-SCALE LEVEL AND ITS APPLICATION TO NANO-MACHINING

Basil T. Wong
University of Kentucky, btung01@engr.uky.edu

Right click to open a feedback form in a new tab to let us know how this document benefits you.

Recommended Citation

ABSTRACT OF DISSERTATION

Basil T. Wong

The Graduate School

University of Kentucky

2006

THERMAL HEAT TRANSPORT AT THE NANO-SCALE LEVEL
AND ITS APPLICATION TO NANO-MACHINING

———————————————————

ABSTRACT OF DISSERTATION

———————————————————

A dissertation submitted in partial fulfillment of the
requirements for the degree of Doctor of Philosophy in the
College of Engineering
at the University of Kentucky

By

Basil T. Wong

Lexington, Kentucky

Co-Directors: Dr. M. Pınar Mengüç, Professor of Mechanical Engineering Department
and   Dr. R. Ryan Vallance, Professor of Mechanical Engineering Department

Lexington, Kentucky

2006

ABSTRACT OF DISSERTATION

THERMAL HEAT TRANSPORT AT THE NANO-SCALE LEVEL
AND ITS APPLICATION TO NANO-MACHINING

Nano-manufacturing is receiving significant attention in industry due to the ever-growing interest in nanotechnology in research institutions. It is hypothesized that single-step or direct-write nano-scale machining might be achieved by coupling nano-probe field emission with radiation transfer. A laser may be used to heat a workpiece within a microscopic region that encloses an even smaller nanoscopic region subjected to a focused electron beam. The electron-beam supplies marginal heat sufficient to remove a minute volume of material by evaporation or sublimation. Experimentally investigating this hypothesis requires an estimate of the power needed in the electron-beam. To this end, a detailed numerical study is conducted to study the possibility of using the nano-probe field emission for nano-machining. The modeling effort in this case is divided into two parts. The first part deals with the electron-beam propagation inside a target workpiece. The second part considers the temperature increase due to the energy transfer between the electron-beam and the workpiece itself. A Monte Carlo/Ray Tracing technique is used in modeling the electron-beam propagation. This approach is identical to that of a typical Monte Carlo simulation in radiative transfer, except that proper electron scattering properties are employed. The temperature distribution inside a gold film is predicted using the heat conduction equations. Details of the various numerical models employed in the simulation and a series of representative results will be presented in this dissertation.

KEYWORDS: Monte Carlo, Electron-Beam Processing, Radiative Transfer, Nano-Scale Heat
and Energy Transfer, Electron-Phonon

Basil T. Wong

June 16, 2006

THERMAL HEAT TRANSPORT AT THE NANO-SCALE LEVEL
AND ITS APPLICATION TO NANO-MACHINING

By

Basil T. Wong

Dr. M. Pinar Mengüç
_____
Co-Director of Dissertation

Dr. R. Ryan Vallance
_____
Co-Director of Dissertation

Dr. George Huang
_____
Director of Graduate Studies

June 16, 2006
_____

RULES FOR THE USE OF DISSERTATIONS

DISSERTATION

Basil T. Wong

The Graduate School

University of Kentucky

2006

THERMAL HEAT TRANSPORT AT THE NANO-SCALE LEVEL
AND ITS APPLICATION TO NANO-MACHINING

_____

DISSERTATION

_____

A dissertation submitted in partial fulfillment of the
requirements for the degree of Doctor of Philosophy in the
College of Engineering
at the University of Kentucky

By

Basil T. Wong

Lexington, Kentucky

Co-Directors: Dr. M. Pinar Mengüç, Professor of Mechanical Engineering Department
and   Dr. R. Ryan Vallance, Professor of Mechanical Engineering Department

Lexington, Kentucky

2006

This dissertation is dedicated to my beloved parents who greatly supported me and gave me absolute freedom to pursue my undergraduate and graduate studies in the United States.

ACKNOWLEDGEMENTS

TABLE OF CONTENTS

LIST OF TABLES

NOMENCLATURES

A	atomic weight (kg/mol)
C_{xx}	specific heat (J/m^3-K); xx denotes the type of the specific heat
C_{xx}^{xx}	scattering cross-section (m^2); xx changes depending on the definition
c	speed of light (m/s)
d	diameter of scatterer (m)
D	density of states (1/m^3-eV)
e	electric charge (C)
E	electron energy (eV)
E_0	initial kinetic energy of the electron-beam (eV)
$\dot{E}$	input power of the electron-beam (W)
$\vec{E}$	electric field vector (V/m)
f	particle distribution function (-)
$\vec{F}_{ext}$	external force vector (N)
g	average direction cosine in s-direction (-)
h	Planck constant (J-s)
$\hbar$	angular Planck constant (J-s)
H	magnetic field
I	intensity (W/m^2)
J	mean ionization energy (J)
k	wave number (m^{-1})
k_B	Boltzmann's constant (J/K)
k_T	thermal conductivity (J/m-K)
$\vec{k}$	wave vector (m^{-3})
n	energy carrier density (#/m^3)
$\tilde{n}$	complex index of refraction
n_I	imaginary part of the refractive index
N_a	Avogadro number (-)
p	momentum (kg-m/s)
P	volumetric momentum ($=np$) (kg/m^2-s)
q_T	thermal heat flux (W/m^2)
Q	heat (J)
R	cumulative probability distribution function (-)
R_{beam}	1/e^2 Gaussian radius
R_{laser}	radius of laser beam
R_p	penetration depth (m)
$R_{x1 \rightarrow x2}$	reflectivity when light propagates from medium $x1$ to $x2$
Ran	a random number (-)
r	radial location
$\vec{r}$	position vector (m)
s	axis of propagation (-)
S	distance of interaction (m)
S_T	energy source (W/m^3)
t	time (s)

T	temperature (K)
v	velocity (m/s)
V	potential (V)
W	scattering rates (s^{-1})
Z	atomic number (-)

Greek symbols

ℓ	the characteristics length (m)
κ	absorption coefficient (m^{-1})
φ	azimuthal angle measured from an axis normal to *s*-axis (degree)
ρ	density (kg/m^3)
μ	direction cosine (-)
β	extinction coefficient ($=\kappa+\sigma$) (m^{-1})
τ_r	relaxation time (s)
Φ	phase function (sr^{-1})
ν	frequency (s^{-1})
Γ	ratio of ℓ to λ (-)
σ	scattering coefficient (m^{-1})
Θ	scattering polar angle measured from s-axis (rad)
ω	angular frequency (s^{-1})
λ	wavelength (m)
λ_{xx}	mean free path (m)
Ω	solid angle (sr)
θ	polar angle (degree)
ϕ	azimuthal angle (degree)
ε	dielectric function (-)
Ψ	normalized electron-energy deposition profile (m^{-3})

Subscripts

e	for electrons
ph	for phonons
λ	wavelength dependent
ν	for photons
d	drift
T	thermal component
LO	optical phonon
A	acoustic phonon
F	Fermi level

Superscripts

$'$	scattered
el	elastic
inel	inelastic

PREFACE

The content of this dissertation involves thermal transport modeling at various time and length scales ranging from macro-scale to nano-scale levels. Most heat transfer theories and mechanisms that are known thus far are typically applicable for bulk objects. As nanotechnology emerges and becomes one of the most active research topics, the characteristic time and length of the systems of interest are reduced tremendously. However, existing thermal theories including Fourier's law and Ohm's law are developed for modeling bulk systems where the specific details of heat carriers are not important. These theories are generally not applicable to thermal transport at the micro- or nano-scales. Theories based on specific details of energy carriers are now required to model micro- or nano-scale thermal transport. Such theories require the knowledge of the true physics concerning heat carriers and various scattering mechanisms.

This dissertation is divided into several chapters. The first chapter contains the description of the problem that is to be solved in this work. This includes the physical process that will be modeled as well as the motivation for modeling such a problem. The entire modeling strategy in dealing with the physical process will also be discussed. In the second chapter, the transport at the micro/nano-scale levels, particularly, the electron-beam propagation, the electronic thermal conduction, and the phonon transport will be dealt with. This is necessary for the comprehension of the content that will be further discussed.

Once the fundamentals of the heat carriers are unveiled in the first two chapters, we proceed to discussions about the solution methodology used in modeling these transport phenomena. There, one encounters the numerical methods and statistical simulations developed according to the governing equations for these heat carriers. All the basic numerical and simulation procedures will be given in this chapter, which we shall later refer to when we model the physical system of interest in the subsequent chapters. With all the fundamentals and numerical procedures given in the preceding chapters, we are now ready to tackle the problem of interest. In the following two chapters, applications of these principles and methods on the physical process we discussed in the first chapter are unveiled. Results of the simulations of the process will be depicted and discussed in these chapters as well. The final chapter of this dissertation is about conclusions of this

work and future works required to improve the modeling problems encountered in this work.

CHAPTER 1
INTRODUCTION

The prosperity of the art of building small has led to the tremendous production of small devices not visible to the naked human eye. Have you ever taken a peep and observed a chip inside a 10-year old computer? When comparing that chip to one inside a more modern computer, one would be surprised at how much the same chip has shrunk in size over the years owing to the fast-growing nanotechnology. Not surprisingly, both chips can store the exact same amount of information and perform the same tasks. This ability of building small has given birth to new storage media such as Digital Versatile Disc (DVD), which has a storage capacity of 4.7 gigabytes, more than 7 times the storage of a Compact Disc (CD).

Current technology has a good measure of success in producing these microstructures. One excellent example is that of the microprocessor which contains approximately 500,000 devices in an area of 1 cm^2 (Ferry and Goodnick, 1997). The challenge is always there to push the limit of building small to the edge. Consequently, nanostructures have become the current target of all the researchers, and manipulating physics and chemistry at the nano-scale level has created *nanotechnology*. Just how small is a nanostructure? A one-hundred-nanometer device is about one-thousandths of the thickness of a human hair. In fact, it could span hundreds of atoms depending on the type of material.

1.1 The Motivation of Building Small

Material processing with high-power lasers is being used extensively in many industrial applications. They are being used to produce desired structures or patterns on material surfaces, including micrometer size structures. Resolutions of these structures depend greatly on the incident spatial distribution of the beam. However, a laser can only be focused close to its wavelength due to the diffraction limit. This results in the limiting of the smallest resolution of the material processed by using a laser to more than a few hundred nanometers, or, about one-fourth to one-fifth of the laser wavelength. The typical wavelength of a laser used in material processing is on the order of hundreds of nano-meters. Hence, it is not possible to create nanometer-scale indenta-

tions in the size of a few nano-meters using a conventional laser machining approach based on far-field optical arrangements. Even though *x*- or gamma-rays maybe used for nano-scale machining, the cost required for such applications is enormous.

An alternative approach for nano-machining could be achieved by using energized electrons bombarding the target solid and creating localized structural changes. Since electrons have wavelengths much smaller than that of photons, the diffraction effect does not play any role until a size of less than a nano-meter is reached. Focusing the electron-beam down to a few nano-meters can be achieved by using electromagnetic lenses (Egerton, 1996).

Nano-manufacturing is likely to receive significant attention in industry and research institutions due to the ever-growing interest in nanotechnology. Nano-structures are usually manufactured via a two-step process that generates a pattern (e.g. electron-beam lithography) and then develops the pattern (e.g. etching). Recently, the author's group hypothesized that single-step or direct-write nano-scale machining might be achieved by coupling nano-probe field emission with radiation transfer (Vallance et al., 2003). A laser may be used to heat a workpiece within a microscopic region that encloses an even smaller nanoscopic region subjected to a focused electron beam. The electron-beam supplies marginal heat sufficient enough to remove a minute volume of material by evaporation or sublimation. The concept developed in this dissertation emerges as a result of the need of a model describing such a machining process at the nano-scale level. The goal of this dissertation is to focus on various theoretical models that describe nano-scale heat transfer, while the experimental works are being carried by other graduate students within the group.

1.2 The Proposed Physical System – A Brief Information

Recently, Vallance et al. (2003) has proposed a nano-machining tool which is based on the field emission of electrons from a nano-probe. A schematic of the proposed physical system is depicted in Figure 1.1. The system is mainly comprised of an anode and a cathode. The anode is usually referred to as the workpiece since machining will be done on it, while the cathode is referred to as the machining tool or the nano-probe. Voltage is applied between the anode and the cathode, causing energized electrons to flow from the cathode to the anode. A possible nano-

probe candidate for this application would be carbon nanotubes, which are well-known. A sample of the developed nano-probe, which is basically a long Tungsten probe with a carbon nanotube attached at the end of the probe, is depicted in Figure 1.2 (Trinkle, 2003).

The multi-walled carbon nanotubes (MWNTs), which are prepared by a carbon arc process where carbon nanotubes form as a bundle of nanotubes on the negative electrode (Ebbesen, 1994), are generally comprised of 2 to 30 concentric graphitic layers with an outer diameter ranging from 10 to 50 nm (Saito, et al., 1998). The length to diameter ratio of a MWNT is typically in the order of 10^2 to 10^3. For instance, a MWNT with an outer diameter of 10 nm may have a length of 10 μm. The single-walled carbon nanotubes (SWNTs) were first discovered in an arc discharge chamber using a catalyst, such as Fe, Co, and other transition metals, during the synthesis process (Iijima and Ichihashi, 1993; Bethune et al., 1993). Compared to a MWNT, a SWNT is thinner with a diameter of about 1 to 1.4 nm (Saito et al., 1998). The structures of the carbon nanotubes have been studied using high-resolution transmission electron microscopy (TEM) and scanning tunneling microscopy (STM), and it is discovered that these nanotubes are cylinders derived from the honeycomb lattice (graphite sheet). Further discussions of the structure of a nanotube can be found in Burchel (1999).

It is discovered that when a potential difference is applied between the CNTs (cathodes) and an anode, the CNTs emit energized electrons. Generally, the SWNTs are worse emitters than the MWNTs (Bonard et al., 1999). Recently Fransen at al. (1999) investigated the electron field emission from the MWNTs. The MWNTs were mounted on tungsten tips and the emissions from these MWNTs were observed. In these experiments, the detector screen was located 5 cm away from the MWNTs. It was found that the maximum current extracted from a MWNT with a diameter of 9 nm, was about 20 nA for a series of extraction voltages ranging from 550 V to 830 V. This produced a power of 16.6 μW assuming the maximum current occurred at 830V. In addition, a current of 140 nA was detected at 1090 V for a MWNT with a diameter of 44 nm, which was equivalent to a power of 152.6 μW.

Bonard et al. (1998) also investigated the field emission properties of the MWNTs in their experiments where the anode and cathode were separated by 1 mm, and a MWNT was mounted on

the gold tip. The MWNTs used were about 10 nm in diameter. A typical emission current of 1 µA from a MWNT was detected for an applied voltage of 250 V which gave a power of 250 µW. They managed to extract a maximum current of 0.2 mA from a MWNT with an applied voltage of 600 V (a maximum power of 0.12 W), which lasted for a few seconds before the emission current dropped significantly due to the meltdown of the MWNT and the gold tip. This meltdown was due to the extremely high temperature change at the tip of the MWNT as caused by the emission. A temperature change of nearly 3400 K could be possible at 0.1 mA for a 8-nm CNT at the tip, including the temperature change at 0.2 mA, as asserted by Bonard et al. (1998).

Despite the fact that CNTs emit significant power when a voltage difference is applied, the emitted electrons always follow an energy distribution, and this distribution tends to broaden as the voltage increases (Fransen et al. 1999). Apart from that, Saito et al. (1998) discovered a magnification factor of 0.4×10^6 of the emitting area of a CNT for a separation distance of 3 cm between the CNT and the detector screen (based on the inner black spot on the screen as projected by an open-ended MWNT with an inner diameter of 5-10 nm).

Although experiments regarding the emission property of the CNTs have been performed over the years, the full range of applicability of these CNTs remains untested. For instance, the relationships between the maximum current extracted, the maximum voltage applied, the tube diameter, and the magnification of the emitting area on the detector screen need to be addressed. Knowledge of these relationships will be required when choosing the appropriate CNTs later discussed in this work.

1.3 Machining Via Electron Field Emission

The electron-beam processing uses electrons emission from an electron gun. This generates a large amount of energized electrons and projects these electrons onto the solid workpiece to achieve the desirable machining process. The key feature of this method is the use of electrons with large kinetic energies, thus penetrating the lattices of the solid and transferring their energy to the solid via inelastic collisions. This allows melting to be achieved and results in a desirable structure which can be manufactured. The typical energies of the electrons in an electron-beam process are in the order of tens of kilo-electron-volts (keV).

Generally, when energetic electrons strike and interact with a solid material, they are scattered into other directions as a result of elastic and inelastic scatterings. Due to the size of an electron being extremely small, and the scattering nature of propagating electrons by the solid material, the accelerated electrons can easily penetrate the solid material through the lattices. Such penetration depends heavily upon the initial energies of the electrons (see Eq. (1.1)). It is known that the electron-beam processing requires a highly energized electron-beam. Not only does this mean a large penetration depth for the propagating electrons, but it also implies that most of the energies of the penetrating electrons will be absorbed within the penetration depth (not the target surface). This makes the electron-beam processing inappropriate at the micro-scaled level even though the diameter of the incident electron beam is at the same scale. Therefore, an alternative method is to utilize the electron field emission from the CNTs instead of using an electron gun as employed in the traditional electron-beam lithography.

The electron-beam processing, as the name implies, uses electron bombardments between energetic electrons and the workpiece to transfer energies from the electrons to the workpiece. This processing therefore changes the shape or the properties of the workpiece. The physics of the interaction between the propagating energetic electrons and the solid materials is very complex. As the electrons propagate inside the workpiece, they undergo a series of elastic or inelastic scatterings. An elastic scattering refers to the redirection of the propagating electron, while an inelastic scattering not only redirects the propagating direction of the electron, but it also attenuates the energy of the electron. Electrons transfer their energy to the target material by means of inelastic scatterings. Inelastic scattering in this scenario can be classified as an event where an incident electron causes the ionization of the atom by removing an inner-shell electron from its orbit producing a characteristic x-ray or an ejected Auger electron. In addition, inelastic scattering also includes the case where an electron collapses with a valence electron to produce a secondary electron (Joy, 1995).

Some useful features of the electron-beam processing include (a) the possibility of finely focused electron beams, (b) the feasibility of generating high-power-density electron beams, (c) the ability to deflect electron beams rapidly and highly accurately, and (d) the possibility of varying

electron energy with acceleration voltage, hence controlling the electron penetration range (Taniguchi et al., 1989). The disadvantages include (a) the necessity for high vacuum to generate electrons and for work chamber (except for non-vacuum welding and electron reactive processing), (b) the generation of harmful X-rays, and (c) the difficulty in processing electrical insulators (Taniguchi et al., 1989).

There are two practical application areas of electron-beam processing. First is thermal processing, which includes machining, welding, annealing, and heat treatment. The second application is reactive processing, such as electron-beam lithography, electron-beam polymerization and depolymerization (Taniguchi et al., 1989). Our objective in this research involves thermal processing, specifically the machining process. The mechanisms described in the rest of the sections are devoted mainly to electron-beam machining.

The interactions between the electrons and a solid material had been investigated theoretically and experimentally by different researchers. . Some theoretical works include those by Archard (1961), Whiddington (1912) and Kanaya and Okayama (1972). Whiddington (1912) related the electron penetration range R_p (m) with the electron acceleration voltage V (Volt) and the mass density of the metal ρ (kg/m^3), which is given by the following equation:

$$R_p = \frac{aV^2}{\rho},$$
(1.1)

where $a = 2.2 \times 10^{-11}$ kg/V^2-m^2. This is the depth that the penetrating electrons can reach after they are incident on the target surface. This implies that most of the energies of the propagating electrons would be absorbed in this range, but not on the surface of the workpiece. As a result, the heating of the surface of the target cannot be achieved via direct electron bombardments. It requires conduction heat transfer from the adjacent layer of the solid material. Because of this phenomenon in using the electron-beam processing, thermal machining at the micrometer scale (depth) cannot be successful, even though electrons can be formed into a fine beam of several micrometers in diameter.

Due to the complicated interactions between propagating electrons and the solid material, obtaining a physically realistic theoretical analysis is quite a challenging. For this reason, many re-

searchers have adapted statistical approaches, such as the Monte Carlo Method (MCM) to simulate the processes. A MCM models the propagations of a large number of electrons inside a solid material based on certain probability distribution functions and then generates a solution according to the scorings of these electrons.

As asserted by Taniguchi et al. (1989), even with a finely focused electron beam, processing a very small area using the beam is difficult to achieve due to the multiple scattering nature of the electron inside the solid material. This is proven by the results obtained by the MCM simulations (Shimizu et al., 1972; Joy, 1995). The challenge in this dissertation is to model the electron-beam processing using CNTs, which will increase the resolution of machining processing to an even smaller scale.

This research is interested in using the CNTs in nano-machining. To effectively remove atoms from the workpiece, a large amount of energy transfer from the carbon nanotube via electron bombardments is required. One way to overcome this setback is to preheat the workpiece to a certain temperature through a bulk heating, and then use a laser beam for subsequent localized heating. This heating will further increase the temperature of a specified location to nearly the melting point of the workpiece, where the electron bombardments occur, resulting in minimum energy required from the nanotube to process the material. Due to the fact that the electron-beam processing is done in vacuum conditions, the bulk heating can only be achieved by radiative or conductive transfer, but not convective transfer. This limits possible candidates for the bulk heating to laser or resistance heating.

The electron penetration depth on gold (ρ = 19,300 kg/m^3) is about 1 nm for an applied voltage of 1kV and gold's melting temperature is about 1336 K (see Eq. (1.1)). This value is relatively low compared to that of tungsten on which the CNTs will be mounted (Vallance et al. (2001), therefore, gold will be first used as the workpiece. Due to the highly reflective property of gold in all the spectra except within the visible range, a laser beam with a visible wavelength will be used to heat the workpiece. Even though this research will focus its results mostly on aluminum, copper, silver, and gold, the approach presented in this work will not be limited to certain materials and lasers.

9

Note that it is determined that the energy required to remove a single atom from most metals is about 1×10^{-18} Joule (which is equivalent to 10 eV) based on a simple calculation. This suggests that the emission energy from the CNTs alone could be sufficient to complete the removal process. Yet, for the sake of completeness and confirmation, all three heating modes will be accounted for in this work.

It is crucial to understand the structures of the system that are being considered so that appropriate approaches and measures can be chosen to monitor the heat transports. As it was previously emphasized, the solid target is assumed to be made of gold, silver, aluminum, or copper. These materials all have the *face-centered cubic* unit cell lattice structure. The orange spheres on the upper right corner in Figure 1.3 illustrate the lattice structure of a *face-centered cubic* unit cell comprising of 14 atoms. Each atom has a diameter of about 3-4 Å for the selected materials, therefore each cube in the figure represents a collection of atoms with dimensions of about 1 nm x 1 nm x 1 nm. In the figure, a SWNT with a diameter of about 1 nm and a MWNT with a diameter of about 5 nm are shown. A SWNT has a cross-section area comparable to that of a cube (~ 1 nm^2) while the cross-section area of a 5-nm MWNT is about 25 times of that. As one can see, the removal of the atoms can be achieved at the nano-scaled level using these CNTs when the emitted electrons from the CNTs are collimated to some extent.

1.4 The Modeling Tasks

The goal of this dissertation is to perform theoretical modeling tasks on this problem, which will be used later to predict the specific requirements for the machinig probe, such as the current and the voltage, in order to facilitate the nano-machining process. The actual nano-machining experiments and details of the setup are not of concern in this dissertation. They are to be carried out independently by Hii (2006/2007). The following chapters will outline the various transport equations and the simulation technique used in modeling the electron-beam as well as the thermal heat transport. Later, these techniques will be coupled to theoretically predict the behaviors of the nano-machining process. In each chapter, a series of results will be given to show the accuracy of the sub-models.
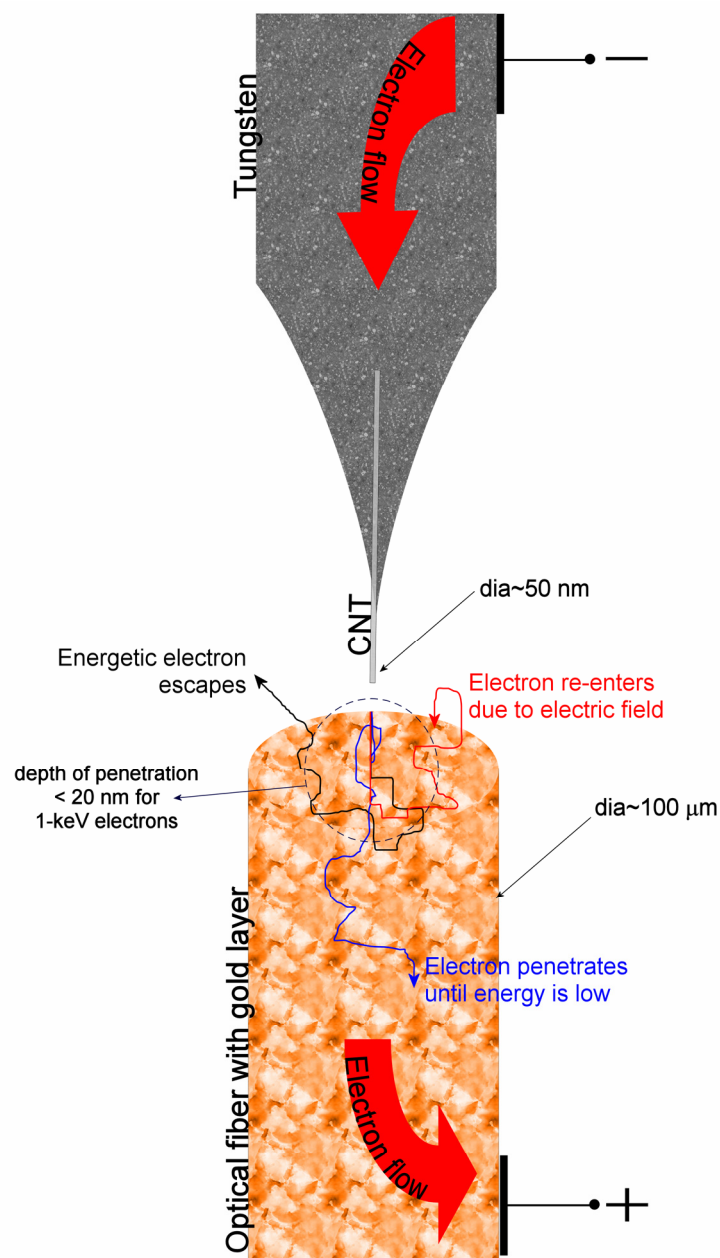
Figure 1.1   The closeup schematic of the proposed machining process using electron field emission from a nano-probe. Note that the figure is not drawn to the correct scales of the objects. The actual size of the carbon nanotube (CNT) is about 50 nm in diameter while the optical fiber has a diameter of hundreds of micrometers. The fiber is considered to be infinite in extent compared to the nanotube.
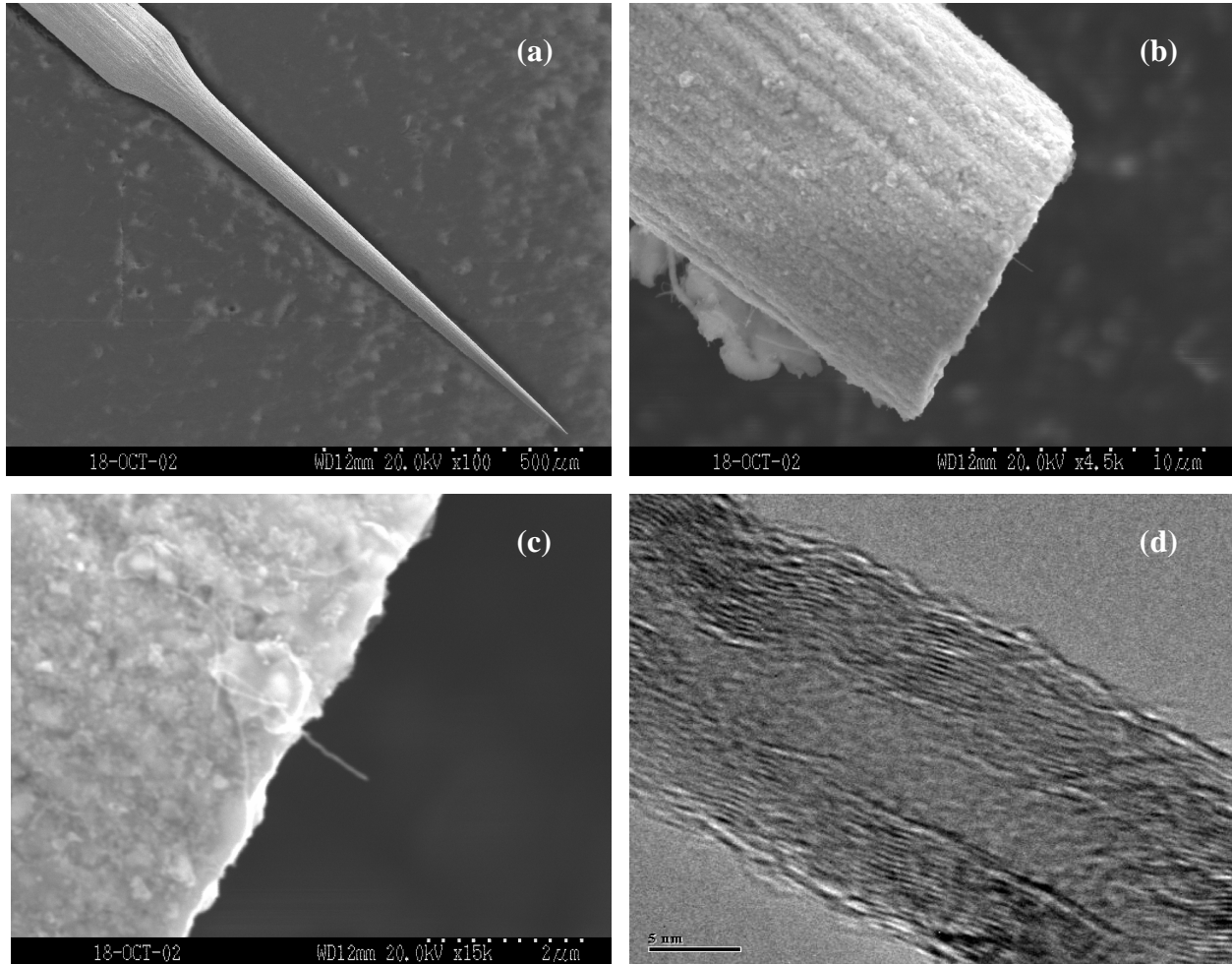
Figure 1.2   Structure of probe tips and mounted carbon nanotubes (CNTs) for demonstrating the feasibility of nano-scale machining. (a) Tungsten probe fabricated using electro-chemical etching, (b) Tungsten probe with mounted single CNT, (c) Enlarged view of the mounted CNT on the probe, and (d) Concentric walls in a multi-walled carbon nanotube (MWNT).
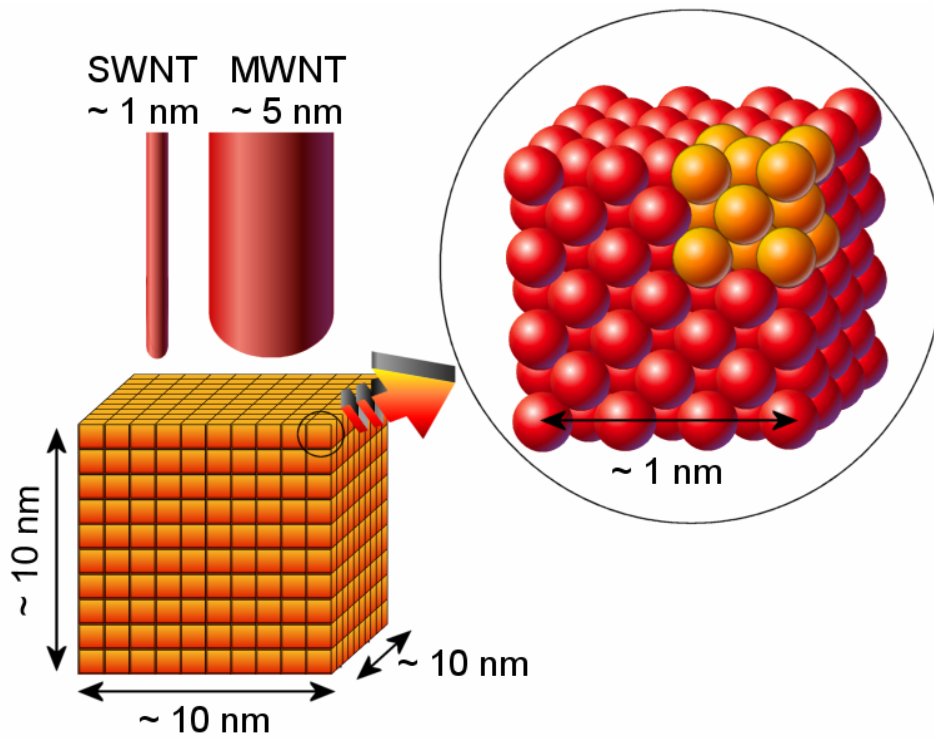
Figure 1.3 The size comparison between a single-walled nanotube (SWNT), a multi-walled nanotube (MWNT), and the workpiece. The lattice structure of the workpiece shown is face-centered cubic (fcc). Examples of elements which possess fcc unit cells are silver (Ag), copper (Cu), and gold (Au).

CHAPTER 2
TRANSPORT EQUATIONS

Many transport phenomena exist in this fascinating world. One of which, for instance, is the radiative transfer or the so-called photon transport. The heat originating from the sun is the most common radiative transfer that we encounter in our daily lives. The electromagnetic waves (or light) coming from the sun suffers attenuations after propagating through atmospheric layers. In terms of an engineering glossary, attenuations refer to the multiple-scattering and absorption of the photons and waves. Due to these intriguing natural absorption and scattering phenomena, the earth is protected against the scorching heat of the sun. Understanding the scattering behavior of these electromagnetic waves has led scientists and engineers to develop various diagnostic tools for analyzing structures of matter and processing materials.

Although there are many so called "particles" which behave as heat carriers, we will consider only electrons, phonons, and photons will be considered in this work. Electrons exist in all matter, they are quantum particles that orbit the nuclei of atoms. The two categories of electrons are inner-shell electrons and outer-shell electrons. The inner-shell electrons are bounded tightly to the nuclei, such electrons are not capable of "wandering" around in the matter. This results in both the nuclei and the inner-shell electrons usually being considered as a whole in most transport phenomena. The inner-shell electrons may also be referred to as the bound electrons. Conversely, the outer-shell electrons can propagate nearly effortlessly around the matter. They are primarily responsible for heat or electrical transport in metals and partially in semi-conductors. Therefore, the outer-shell electrons[1] are often called the conduction electrons as well. Among all other heat carriers, the wavelength of electrons is the shortest, which makes them the best candidate for nanometer-scale machining applications.

Similar to the electron-beam and photon-beam propagations, thermal (heat) conduction also involves the propagation of energy in the form of waves. If there is no resistance, the waves are able to propagate freely and the resultant effect is infinite thermal conductivity. Resistances to

---

[1] Outer-shell electrons may also be named valence electrons.

waves usually come in the form of scatterings, whether they are elastic or inelastic. Elastic scattering refers to re-direction of a heat carrier onto a different path without causing any alteration to its energy[2]. An inelastic scattering not only changes the path of the carrier, but also attenuates its energy assuming that the carrier possesses larger energy than its surroundings.

Generally speaking, there are two different species of heat carriers in solids; they are electrons and phonons. Electrons and phonons follow different dispersion relations[3]. They possess distinct characteristics and dictate the conduction behavior of a material. A material can be a conductor, semi-conductor, or insulator depending on the dispersion relations of the electrons and phonons. For a conductor, the main energy carriers are basically electrons since they propagate at velocities that are several orders larger compared to that of phonons. For a semi-conductor, the transports of both electrons and phonons are equally important in conducting heat. There exits however, band gaps[4] in the electronic band structure where no electrons are allowed to have such energy states. Such gaps can often easily be overcome by electrons in the semi-conductors. When the band gaps are so large that electrons are not moving freely, the material is considered as an insulator.

The thermal conduction inside matter is greatly influenced by the characteristic time and the length of the object of interest, the mean free time of heat carriers, and the mean free path of heat carriers. Depending on these parameters the nature of the thermal wave propagation can vary from purely ballistic to completely diffusion-like, resulting in a temperature distribution that may vary significantly. The mean free time refers to the time interval between two successive collisions suffered by an energy carrier while the mean free path is the distance corresponding to the time interval. They usually depend on the properties of the medium and the wavelength (or energy) of the carriers. Within the mean free time (or the mean free path), the energy carrier travels ballistic without being deflected out of its direction propagation. If one is interested in the transport behavior within the time limit comparable to the mean free time of the heat carriers, then ballistic transport is to be expected. In the following sections, various transport models are stud-

---

[2] A change in energy also implies a change in the wavelength (or wave number).
[3] Dispersion relation for electrons is usually referred to as band structure.
[4] Band gap refers to a discontinuity in the energy spectrum of the carrier.

15

ied under different conditions.

2.1 Wave Theories versus Particle Transport Modelings

There are two important parameters that need to be accounted for to correctly predict the behavior of the transport phenomena. These are the mean free path[5] of the heat carriers and the characteristic length of the object of interest. Depending upon the ratio between these two, various assumptions can be made about the nature of the transport. These assumptions would lead to the correct corresponding governing theory. The transport usually boils down to two approaches. The first is based on the wave theories and the second is based on the particle transport modelings.

Wave theories treat the propagations of particles, such as those of photons, electrons, and phonons, as wavelike. This is where phases and amplitudes of the waves are considered after the scattering events and affect the outcome of the transport. Particles transport theories conveniently replace wave theories when the number of scattering events becomes increasingly significant, and only the scattering rate and the mean free path of the scattering need to be considered,. One can find several wave theories including electromagnetic wave (light) theory, lattice wave theory, and matter wave theory. Most of the particles transport theories are derived from the general form of the Boltzmann Transport Theory (see Section 2.3). The parameter that sets the wave theories and the particles transport theories apart is the ratio of the characteristics length (ℓ) of the object of interest to the wavelength of propagation (λ), Γ (i.e. $\Gamma = \ell / \lambda$). If Γ is much larger than unity, then the particles transport theories can be used. As Γ approaches unity or less, the wave theories play more important roles in solving the energy transfer.

2.2 Time and Length Scales

The time and length scales of the system dictate the theoretical assumptions that we made to solve the heat transports. Accordingly, there are two length scales that lead to the appropriate simplifications of the particle transport theories. They are the mean free path, L_{mfp} and the characteristic size of a volume over which local thermodynamics equilibrium can be defined, L_r (Tien

et al., 1998). Generally, the latter is greater than the former (i.e. $L_r > L_{mfp}$). There are two time-scales associated with with these length scales. These scales are the mean free time, τ_{mfp} and the relaxation time, τ_r. Another important time scale is the collision time (duration of collision), τ_c. To be able to reach a local thermodynamics equilibrium, five to twenty collisions are needed. This corresponds to a maximum total collision time of 20 fs for the electrons (at Fermi energy) and 2 ps for the phonons in a metal (Majumdar, 1998). Since $\tau_r > \tau_{mfp} >> \tau_c$, τ_r is much greater than 20 fs for electrons and 2 ps for phonons in a metal. This yields a value of L_r far exceeding 20 nm for electrons and 2 nm for phonons, assuming the velocities of electrons and phonons are 10^6 m/s and 10^3 m/s, respectively. This also suggests that local thermodynamics equilibrium cannot be assumed for electrons, but it might be achievable for phonons since the thickness of the workpiece considered here is in the order of tens of nanometers. It is assume that the time required for machining processes is much greater than any of the time scales stated. This makes the time-averaged assumption possible for the statistical particle transport equations.

2.3 Boltzmann Transport Equation

When the amplitudes and phases of waves are not important in the energy transport, the transport phenomena can be modeled using particle transport theory. The governing equation for the transport is the Boltzmann Transport Equation (BTE). The BTE describes the evolution of a particle probability distribution over time t, space $\bar{r}$, and wave vector $\bar{k}$ (f may relate to $\bar{v}$ or momentum $\bar{p} = \hbar\bar{k}$), as quantum particles experience a series of scattering events and external forces. In the following derivation, the general form of the BTE is presented. In principle this is applicable to all energy carriers, including electrons, phonons, or photons, as long as the wavelengths of the carriers are small compared to the characteristic length of the object of interest. For example, the BTE should not be used to model energy transfer of a photon beam (i.e. laser) with a wavelength of 532 nm striking a 100-nm dielectric film. However, it is applicable if the photon beam is replaced with an electron-beam with wavelengths in the order of nanometers.

The rate change of a particle distribution f is balanced by the rate at which the distribution is increased or decreased due to collisions with other particles. The conservation equation follows

---

[5] Mean free path is the distance that the heat carrier can travel without altering its path direction and/or energy.

(Ashcroft and Mermin, 1976; Ziman, 1964) that

$$\frac{\partial f\left(\vec{r},\vec{k},t\right)}{\partial t}+\frac{\partial \vec{r}}{\partial t}\cdot\frac{\partial f\left(\vec{r},\vec{k},t\right)}{\partial \vec{r}}+\frac{\partial \vec{k}}{\partial t}\cdot\frac{\partial f\left(\vec{r},\vec{k},t\right)}{\partial \vec{k}}=\left(\frac{\partial f\left(\vec{r},\vec{k},t\right)}{\partial t}\right)_{col}. \tag{2.1}$$

The terms on the LHS are the change of f in time t, the rate of change of f due to advection in space $\vec{r}$, and the rate of change of f due to momentum change while the RHS is the collision term. For the sake of simplicity, $f\left(\vec{r},\vec{k},t\right)$ is abbreviated as f from this point on, however it is understood that f is a function of t, $\vec{r}$, and $\vec{k}$. The conservation of the particle distribution function can then be rewritten using the different notation as:

$$\frac{\partial f}{\partial t}+\vec{v}_{\vec{k}}\cdot\nabla_{\vec{r}}f+\dot{\vec{k}}\cdot\nabla_{\vec{k}}f=\left(\frac{\partial f}{\partial t}\right)_{col}. \tag{2.2}$$

Note that the group velocity of the particles is denoted as $\vec{v}_{\vec{k}}$, which is typically a function of the wave vector $\vec{k}$. The time evolution of the wave vector $\dot{\vec{k}}$, is due to the external applied fields or forces. This is valid for charged particles such as electrons when they are accelerated through the electric field. Although this term will be dropped out for the case where phonons or photons are the energy carriers, it shall be retained in this term for the completeness of the derivation.

According to semi-classical particle dynamics, the rate of change of $\vec{k}$ as a result of the applied electric field $\vec{E}$ and magnetic field $\vec{H}$ is given as (Ashcroft and Mermin, 1976; Ziman, 1960):

$$\dot{\vec{k}}=-\frac{e}{\hbar}\left(\vec{E}+\frac{1}{c}\vec{v}_{\vec{k}}\times\vec{H}\right)=\frac{\vec{F}_{ext}}{\hbar}. \tag{2.3}$$

Inserting this expression into the conservation equation yields the general form of the BTE (Ashcroft and Mermin, 1976; Ziman, 1960):

$$\frac{\partial f}{\partial t}+\vec{v}_{\vec{k}}\cdot\nabla_{\vec{r}}f+\frac{\vec{F}_{ext}}{\hbar}\cdot\nabla_{\vec{k}}f=\left(\frac{\partial f}{\partial t}\right)_{col}. \tag{2.4}$$

If the BTE is to be solved rigorously, the collision term can be evaluated using scattering probabilities. The collision term refers to the rate at which the distribution is increased or decreased. In terms of the physical sense, the collision term consists of transitions (or scatterings) of quantum particles from the wave vector $\vec{k}'$ into $\vec{k}$ or from the wave vector $\vec{k}$ into $\vec{k}'$. This results in

the transition probabilities (or scattering probabilities) being properly accounted for.

For phonons and photons the collision term can be expressed as:

$$\left(\frac{\partial f}{\partial t}\right)_{col} = \sum_{\vec{k}'} W\left(\vec{k}' \to \vec{k}\right) f' - \sum_{\vec{k}'} W\left(\vec{k} \to \vec{k}'\right) f. \tag{2.5}$$

In the right-hand side of Eq. (2.5), $W\left(\vec{k}' \to \vec{k}\right)$ denotes the rate of scattering from $\vec{k}'$ to $\vec{k}$. The first summation is the rate of change of f due to the in-scattering of particles from various locations and directions, while the second is the rate of change of f caused by the out-scattering of particles. The collision term is slightly different for electrons since electrons are obliged to Pauli's exclusion principle, which prevents two electrons with the same state from residing at the same location. In order for an electron to undergo a transition (or scattering) from $\vec{k}'$ to $\vec{k}$, there must be an "empty slot" in the $\vec{k}$ state to accommodate for this scattered electron. If a state is fully occupied by other electrons, then the distribution function f has a value of unity, otherwise, (1–f) represents the available probability. The collision term for electrons is then modified accordingly:

$$\left(\frac{\partial f}{\partial t}\right)_{col} = \sum_{\vec{k}'} W\left(\vec{k}' \to \vec{k}\right) f'\left(1-f\right) - \sum_{\vec{k}'} W\left(\vec{k} \to \vec{k}'\right) f\left(1-f'\right). \tag{2.6}$$

In its general form, the BTE is virtually intractable using analytical methods owing to the various independent variables and its integro-differential form. This is usually resolved by using the statistical methods such as the Monte Carlo method which are commonly used to simulate the propagation of quantum particles according the probability distribution functions.

2.3.1 Relaxation-Time Approximation

Solving the BTE with the integral collision term as given above is not practical for some applications, resulting in approximations to the collision term being made. This is done so that the equation can become tractable analytically, if not, numerically. In order to determine an approximation for the collision term, we need to understand its significance and the function.

Without any simplifications, the collision term in the BTE is understood to be particle transformations from one particular state to another. If one assumes that a large number of electrons

with different energy levels are "poured" into an isolated control volume, the electrons at the higher energy levels would tend to transfer excess energies to those at lower levels through collisions. Over time the entire control volume would eventually come to thermal equilibrium. This is where the amount of energy transfer from electrons possessing higher energy to the lower ones and vice versa, are the same, resulting in an equilibrium distribution function eventually being achieved. According to the above observation, collisions of particles tend to restore equilibrium over a period of time. Based on this concept, a relaxation-time approach can be derived.

In the relaxation-time approach, it is assumed that the perturbed distribution function will eventually relax back to the equilibrium distribution function within a period of time. In terms of mathematical expression, the collision term is then approximated as:

$$\left(\frac{\partial f}{\partial t}\right)_{col} = -\frac{f - f^{eq}}{\tau_r}, \tag{2.7}$$

where f^{eq} is the equilibrium distribution and τ_r is the relaxation time needed to reach the equilibrium state. The solution of f in the above first-order differential equation (if the partial derivative is replaced with ordinary derivative) can be expressed as:

$$f = f^{eq} + \left(f_0 - f^{eq}\right) exp\left(-\frac{t}{\tau_r}\right). \tag{2.8}$$

Note that the solution for f in the above equation is of exponential decaying nature, meaning that if f is increased (or decreased) from its equilibrium distribution, it will decay (or grow) exponentially to the original state with the relaxation time τ_r being the time constant.

Using the relaxation-time approximation, the specific details of the scattering process is lost. For example, the directional dependence of the transitions process is compromised, which may be critical in some applications. Nevertheless, this approximation transforms the BTE into a partial differential equation instead of an integro-differential equation, and hence, the BTE becomes tractable.

2.3.2 The Significance of the Distribution Function f

The BTE describes the evolution of the particle distribution function f. By solving the BTE we

gain the knowledge of how the particles are dispersed or distributed in time, space, and various directions. The *f* by itself may not yield any useful information, however, various physical quantities can be derived from it by performing integrations of the function over the independent variables. The density of particles as a function of time and space can be retrieved by integrating the distribution function over the momentum space $\bar{k}$:

$$n(\bar{r},t)= \int f(\bar{r},\bar{k},t)d\bar{k} .$$ (2.9)

Similarly, the momentum density of particles can also be determined using *f*,

$$p(\bar{r},t)= \int \left[m(\bar{k})v(\bar{k})f(\bar{r},\bar{k},t) \right]d\bar{k} .$$ (2.10)

where *m* is the mass and *v* is the velocity of particles.

2.4 Intensity Form of Boltzmann Transport Equation

2.4.1 Electron-Beam Transport Equation

In the field of the electron-beam processing, free electrons are the energy carriers. The energy of an electron is always characterized by its wave number *k* ($k=2\pi/\lambda$) instead of its frequency or wavelength. Unlike photons, free (propagating) electrons do not undergo absorption by other particles. This implies that inelastic scatterings change the energy of these carriers but dooes not attenuate the number of carriers. Therefore the wave number or the wavelength of the electrons changes as they undergo inelastic scatterings. From the computational standpoint, the scattering cross section changes once the energy of a propagating electron ensemble is altered. The governing equation for the electron-beam transport can be derived from the BTE.

It must be clear that propagations of quantum particles should indeed satisfy the BTE. This research is interested in the details of the scattering mechanisms and the transition processes. Hence, the BTE is to be solved rigorously without taking its moments. The distribution *f* by itself may not yield any useful information, therefore it is best to cast the BTE in terms of intensity. Before attempting to derive the intensity equation from the BTE, it is informative to know that an electron-beam consists of bundles of free electrons traveling along a given line of sight. In principle these free electrons have the same electronic properties of the free-electron model.

These properties do not have directional dependency since the electronic band structure is of a spherical parabolic type. Hence, the electron intensity can be defined as:

$$I_e\left(\bar{r},\hat{s},E_e,t\right)=\frac{1}{4\pi}f_e\left(\bar{r},\hat{s},E_e,t\right)E_eD_e\left(E_e\right)v_e\left(E_e\right),\qquad(2.11)$$

where the electron density of states D_e and the electron velocity v_e are energy (or wave number k) dependent.

If we multiply the BTE by the electron energy, density of states, and group velocity, we obtain

$$\frac{\partial\left(f_eE_eD_ev_e\right)}{\partial t}+\bar{v}_e\cdot\nabla_{\bar{r}}\left(f_eE_eD_ev_e\right)+\left(E_eD_ev_e\right)\frac{\bar{F}_{ext}}{\hbar}\cdot\nabla_{\bar{k}}f_e=\left(\frac{\partial\left(f_eE_eD_ev_e\right)}{\partial t}\right)_{col}.\qquad(2.12)$$

Using the definition of electron intensity, the above equation can be re-written as

$$\frac{\partial I_e}{\partial t}+\bar{v}_e\cdot\nabla_{\bar{r}}I_e+\left(E_eD_ev_e\right)\frac{\bar{F}_{ext}}{\hbar}\cdot\nabla_{\bar{k}}f_e=\left(\frac{\partial I_e}{\partial t}\right)_{col},\qquad(2.13)$$

where it is understood that the intensity is a function of time, energy (or wave number), location, and direction. Note that the third term on the LHS of the equation needs to be expressed in terms of electron intensity. To do so, it is first written as:

$$\left(E_eD_ev_e\right)\frac{\bar{F}_{ext}}{\hbar}\cdot\nabla_{\bar{k}}f_e=\frac{\bar{F}_{ext}}{\hbar}\cdot\left[\nabla_{\bar{k}}\left(f_eE_eD_ev_e\right)-f_e\nabla_{\bar{k}}\left(E_eD_ev_e\right)\right].\qquad(2.14)$$

and then by replacing the gradient in wave vector with partial derivative in energy by using the definition of the group velocity, it is written as:

$$\frac{\bar{F}_{ext}}{\hbar}\cdot\left[\nabla_{\bar{k}}\left(f_eE_eD_ev_e\right)-f_e\nabla_{\bar{k}}\left(E_eD_ev_e\right)\right]=\left(\bar{F}_{ext}\cdot\bar{v}_e\right)\left(\frac{\partial I_e}{\partial E_e}-f_e\frac{\partial}{\partial E_e}\left(E_eD_ev_e\right)\right).\qquad(2.15)$$

It can be shown that the following relation

$$f_e\frac{\partial}{\partial E_e}\left(E_eD_ev_e\right)=\frac{2}{E_e}\left(f_eE_eD_ev_e\right)=\frac{2}{E_e}I_e,\qquad(2.16)$$

holds for the spherical parabolic electronic band structure (or free-electron model). Thus, the electron intensity equation derived from the BTE is now given as:

$$\frac{\partial I_e}{\partial t}+\bar{v}_e\cdot\nabla_{\bar{r}}I_e+\left(\bar{F}_{ext}\cdot\bar{v}_e\right)\left(\frac{\partial I_e}{\partial E_e}-\frac{2}{E_e}I_e\right)=\left(\frac{\partial I_e}{\partial t}\right)_{col},\qquad(2.17)$$

where the first two terms on the LHS describes the variation of intensity in time and in space while the third term is the energy gained or lost as a result of the external applied field on the electron-beam. Note that the electron intensity equation is written along a line of sight, thus, the collision term on the RHS of the equation can be interpreted as intensity lost or gained due to interactions of the electron-beam with the participating medium. Here the term interactions means elastic or inelastic scatterings of the electron beam. Scatterings result in re-directions of electron-beam intensity into and out of a given line of sight. The collision term should consist of in-scattering and out-scattering terms for both elastic and inelastic scatterings.

The out-scattering term that describes the intensity lost of electron-beam, both elastically and inelastically, can be expressed as:

$$
-\frac{1}{4\pi}\int_{E'}\int_{\Omega'}\left[\sigma_e^{inel}(E)\Phi_e^{inel}\left(E,\theta,\phi\to E',\theta',\phi'\right)I_e\left(E,\theta,\phi,t\right)v_e(E)\right]d\Omega'dE'
$$
$$
-\frac{1}{4\pi}\int_{E'}\int_{\Omega'}\left[\sigma_e^{el}(E)\Phi_e^{el}\left(E,\theta,\phi\to E',\theta',\phi'\right)I_e\left(E,\theta,\phi,t\right)v_e(E)\right]d\Omega'dE'.
$$

$$(2.18)$$

Here the concept of phase function (denoted as Φ_e), is analogous to that of photons. It is used to describe the probability of scattering from one energy state to another and from one direction to another. The elastic phase function Φ_e^{el} is totally different from the inelastic phase function Φ_e^{inel} since the inelastic scattering phenomena are rather distinct from the elastic scattering mechanism. The factor of 4π in the expression is used for normalization purposes of the phase functions. The out-scattering term can be further simplified by taking the scattering coefficients and intensities outside the integrals such that

$$
-\frac{\sigma_e^{inel}(E)}{4\pi}v_e(E)I_e\left(E,\theta,\phi,t\right)\int_{E'}\int_{\Omega'}\Phi_e^{inel}\left(E,\theta,\phi\to E',\theta',\phi'\right)d\Omega'dE'
$$
$$
-\frac{\sigma_e^{el}(E)}{4\pi}v_e(E)I_e\left(E,\theta,\phi,t\right)\int_{E'}\int_{\Omega'}\Phi_e^{el}\left(E,\theta,\phi\to E',\theta',\phi'\right)d\Omega'dE'.
$$

$$(2.19)$$

The above expression takes a simpler form as:

$$
-\left[\sigma_e^{inel}(E)+\sigma_e^{el}(E)\right]v_e(E)I_e,
$$

$$(2.20)$$

since

$$\frac{1}{4\pi}\int_{E'}\int_{\Omega'}\Phi_e^{inel}\left(E,\theta,\phi\to E',\theta',\phi'\right)d\Omega'dE'=1,$$

$$\frac{1}{4\pi}\int_{E'}\int_{\Omega'}\Phi_e^{el}\left(E,\theta,\phi\to E',\theta',\phi'\right)d\Omega'dE'=1. \tag{2.21}$$

Alternatively, it can be written in terms of elastic and inelastic mean free paths as:

$$-\left[\frac{1}{\lambda_e^{inel}(E)}+\frac{1}{\lambda_e^{el}(E)}\right]v_e(E)I_e, \tag{2.22}$$

based on the fact that the scattering coefficients are inversely proportional to the mean free paths, for instance,

$$\sigma_e^{inel}(E)=\frac{1}{\lambda_e^{inel}(E)}. \tag{2.23}$$

Similarly to the out-scattering term, the in-scattering of the electron-beam can be expressed as:

$$\frac{1}{4\pi}\int_{E'}\int_{\Omega'}\left[\sigma_e^{inel}(E')\Phi_e^{inel}\left(E',\theta',\phi'\to E,\theta,\phi\right)I_e\left(E',\theta',\phi',t\right)v_e(E')\right]d\Omega'dE'$$

$$+\frac{1}{4\pi}\int_{E'}\int_{\Omega'}\left[\sigma_e^{inel}(E')\Phi_e^{el}\left(E',\theta',\phi'\to E,\theta,\phi\right)I_e\left(E',\theta',\phi',t\right)v_e(E')\right]d\Omega'dE'. \tag{2.24}$$

This term is positive since in-scattering means contributions of electron intensity from all other directions.

Substituting the out-scattering and in-scattering terms into the electron-beam intensity equation yields

$$\frac{\partial I_e}{\partial t}+\vec{v}_e\cdot\nabla_{\vec{r}}I_e+\left(\vec{F}_{ext}\cdot\vec{v}_e\right)\frac{\partial I_e}{\partial E_e}$$

$$=-\left[\sigma_e^{inel}(E)+\sigma_e^{el}(E)\right]v_e(E)I_e+2\frac{\left(\vec{F}_{ext}\cdot\vec{v}_e\right)}{E_e}I_e$$

$$+\frac{1}{4\pi}\int_{E'}\int_{\Omega'}\left[\sigma_e^{inel}(E')\Phi_e^{inel}\left(E',\theta',\phi'\to E,\theta,\phi\right)I_e\left(E',\theta',\phi',t\right)v_e(E')\right]d\Omega'dE'$$

$$+\frac{1}{4\pi}\int_{E'}\int_{\Omega'}\left[\sigma_e^{el}(E')\Phi_e^{el}\left(E',\theta',\phi'\to E,\theta,\phi\right)I_e\left(E',\theta',\phi',t\right)v_e(E')\right]d\Omega'dE' \tag{2.25}$$

In this work, the above equation shall be termed, the *electron-beam transport equation* (EBTE). The EBTE is similar to the *radiative transfer equation* (RTE). Both equations are of integro-differential type, which is typical in the particle transport theory. The EBTE is the BTE in its in-

tensity form. No averaging effect over the electron energy (or wave number) spectrum has been embedded in the equation, therefore in its current form the EBTE is as general as it can be for the case where the free-electron model is assumed. This is justified for the electron-beam modeling. If there are no external forces applied to the electron-beam, then the EBTE reduces to:

$$\frac{\partial I_e}{\partial t} + \vec{v}_e \cdot \nabla_{\vec{r}} I_e = -\left[\sigma_e^{inel}(E) + \sigma_e^{el}(E)\right] v_e(E) I_e$$

$$+ \frac{1}{4\pi} \int_{E'} \int_{\Omega'} \left[\sigma_e^{inel}(E') \Phi_e^{inel}(E',\theta',\phi' \to E,\theta,\phi) I_e(E',\theta',\phi',t) v_e(E')\right] d\Omega' dE' \quad (2.26)$$

$$+ \frac{1}{4\pi} \int_{E'} \int_{\Omega'} \left[\sigma_e^{el}(E') \Phi_e^{el}(E',\theta',\phi' \to E,\theta,\phi) I_e(E',\theta',\phi',t) v_e(E')\right] d\Omega' dE'$$

2.4.2 Radiative Transfer Equation

In radiative transfer, quantum particles are photons, each having energy of $h\nu$ for a given frequency ν (or wavelength $\lambda=c/\nu$). To derive the _radiative transfer equation_ (RTE) describing the conservation of radiant energy along a line of sight of a beam propagating within an absorbing, emitting, and scattering medium, the radiative intensity is defined in terms of the photon distribution fv, the photon energy $h\nu$, the density of states D_ν, and the speed of light c:

$$I_\nu(\vec{r},\theta,\phi,t) = \sum_p f_\nu(\vec{r},p,\theta,\phi,t) h\nu \frac{D_\nu(p)}{4\pi} c . \quad (2.27)$$

The subscript ν is used to indicate that the equation is for a given specific frequency (or wavelength) which corresponds to a monochromatic laser beam. The summation is to be performed over all polarization branches. This implies that the change of polarization of photons is ignored in this case.

Multiplying Eq. (2.4) by the photon energy, the density of states, and the speed of light, and then performing the summation over all the polarization branches, allows the BTE to be cast in terms of the radiative intensity:

$$\frac{\partial I_\nu}{\partial t} + \vec{v}_\nu \cdot \nabla I_\nu = \sum_{\theta',\phi'} W_\nu(\theta',\phi';\theta,\phi) I_\nu'(\theta',\phi',t) - \sum_{\theta',\phi'} W_\nu(\theta,\phi;\theta',\phi') I_\nu(\vec{r},\theta,\phi,t). \quad (2.28)$$

To further simplify the BTE, the in-scattering term is rewritten as:

$$\sum_{\theta',\phi'} W_\nu\left(\theta',\phi';\theta,\phi\right) I_\nu'\left(\theta',\phi',t\right) = \frac{\sigma_\nu}{4\pi} \int_{\Omega'} \Phi_\nu\left(\theta',\phi';\theta,\phi\right) I_\nu'\left(\theta',\phi',t\right) d\Omega', \qquad (2.29)$$

where σ_ν is the scattering coefficient and Φ_ν is the phase function of the medium. The in-scattering term contains all the contributions from within the solid angle Ω'. The out-scattering term can be given as

$$\sum_{\theta',\phi'} W_\nu\left(\theta,\phi;\theta',\phi'\right) I_\nu\left(\vec{r},\theta,\phi,t\right) = \left(\kappa_\nu + \sigma_\nu\right) I_\nu\left(\vec{r},\theta,\phi,t\right), \qquad (2.30)$$

with κ_ν being the absorption coefficient. Therefore, this yields the familiar form of the RTE:

$$\frac{\partial I_\nu}{\partial t} + \vec{v}_\nu \cdot \nabla I_\nu = -\beta_\nu I_\nu + \frac{\sigma_\nu}{4\pi} \int_{\Omega'} \Phi_\nu\left(\theta',\phi';\theta,\phi\right) I_\nu'\left(\theta',\phi',t\right) d\Omega'. \qquad (2.31)$$

Note that β_ν is simply the sum of κ_ν and σ_ν. This form of RTE assumes that the in-scatterings are elastic which means that a photon scattered with its energy (i.e., frequency) remains unaltered. This is not true in the case of Raman scattering. The out-scattering term includes the absorptions and re-emissions of photons, which are considered as inelastic scatterings. From the quantum mechanics point of view, the RTE asserts that the rate of change of the radiant energy of a propagating ensemble of photons in a given direction is equal to the amount of photons attenuated, emitted along the direction, and in-scattered from all other directions into the given direction. One important thing to note for the radiative transfer is that the number of photons does not conserve. In other words, photons can be created and destroyed during inelastic scattering processes. Inelastic scatterings mean that the ensemble of photons is attenuated in terms of the population of the photons, but not the frequency of the photons. This in turn reduces the energy of the entire ensemble.

2.5 Moments of Boltzmann Transport Equation

The BTE can be transformed into a set of governing equations by taking various moments of the equation, conserving the particle number, momentum, and energy. By doing this, one can only obtain averaged effects of the overall system because the computed quantities are averages. The directional dependent of the scattering effect is conveniently removed after the integrations. Although the moments of the BTE remove specific details of scattering process, they still remain as one of the most frequently used approaches for research. This is because the overall effect is

preserved, the statistical average provided is manageable, and the directional dependent of the transport is not pronounced. In the procession of smaller and smaller scales, these two conditions may not hold at all. Under such circumstances, these moments may yield inaccurate results. In the following sections, brief derivations of various conservation equations from the BTE are given. Details of the derivations are available elsewhere (Snowden, 1988; Tomizawa, 1993), so they will not be repeated here.

The overall basic concept on these derivations is to cast the BTE into particle number, momentum, and energy conservation equations and to remove the wave vector dependency of the BTE by taking various order moments of the BTE. If the BTE is multiplied by a function ψ and integrate the entire equation over $\bar{k}$, the following equation is obtained:

$$\int \psi \left(\frac{\partial f}{\partial t} + \bar{v}_{\bar{k}} \cdot \nabla_{\bar{r}} f + \frac{\bar{F}_{ext}}{\hbar} \cdot \nabla_{\bar{k}} f \right) d\bar{k} = \int \psi \left(\frac{\partial f}{\partial t} \right)_{col} d\bar{k} .$$

(2.32)

This equation can be re-written in the following fashion using the simple differentiation rule as:

$$\int \left[\frac{\partial (\psi f)}{\partial t} - f \frac{\partial \psi}{\partial t} + \nabla_{\bar{r}} \cdot (\psi \bar{v}_{\bar{k}} f) - \bar{v}_{\bar{k}} f \cdot \nabla_{\bar{r}} \psi + \psi \left(\frac{\bar{F}_{ext}}{\hbar} \cdot \nabla_{\bar{k}} f \right) \right] d\bar{k}$$
$$= \int \left(\frac{\partial (\psi f)}{\partial t} - f \frac{\partial \psi}{\partial t} \right)_{col} d\bar{k}$$

(2.33)

Equation (2.33) is the general moment equation for ψ (Duderstadt and Martin, 1979). For the following discussions, the spherical energy bands for the particle will be assumed.

2.5.1 Continuity

The continuity equation for particle transport conserves the carrier density. It is obtained by taking the zeroth moment of the BTE with $\psi = 1$. Therefore, Eq. (2.33) becomes:

$$\int \left(\frac{\partial f}{\partial t} \right) d\bar{k} + \int \left[\nabla_{\bar{r}} \cdot (\bar{v}_{\bar{k}} f) \right] d\bar{k} + \int \left(\frac{\bar{F}_{ext}}{\hbar} \cdot \nabla_{\bar{k}} f \right) d\bar{k} = \int \left(\frac{\partial f}{\partial t} \right)_{col} d\bar{k} .$$

(2.34)

Note that the average particle density, denoted as n, is given by:

$$n(\bar{r}, t) = \int f(\bar{r}, \bar{k}, t) d\bar{k} .$$

(2.35)

The first term on the LHS of the equation is simply the time derivative of the average particle

density:

$$\int \left(\frac{\partial f}{\partial t}\right) d\bar{k} = \frac{\partial}{\partial t} \int f d\bar{k} = \frac{\partial n}{\partial t}. \tag{2.36}$$

Before proceeding to simplify the other terms in the equation, it is important to examine the wave-vector dependent velocity, $\bar{v}_{\bar{k}}$, which is the velocity of the particle. Here, it is assumed that:

$$\bar{v}_{\bar{k}} = \langle \bar{v}_{\bar{k}} \rangle + \bar{v}'_{\bar{k}}, \tag{2.37}$$

where $\langle \bar{v}_{\bar{k}} \rangle$ is an average velocity or the drift velocity of the particle, which shall be denoted as $\bar{v}_d$, while $\bar{v}'_{\bar{k}} \left(= \bar{v}_{\bar{k},T} \right)$ is the random velocity due to thermal effects on the particle. The average velocity is expressed as follows:

$$\bar{v}_d = \langle \bar{v}_{\bar{k}} \rangle = \frac{\int \left(\bar{v}_{\bar{k}} f\right) d\bar{k}}{\int f d\bar{k}}. \tag{2.38}$$

Therefore,

$$\bar{v}_{\bar{k}} = \bar{v}_d + \bar{v}_{\bar{k},T}. \tag{2.39}$$

The drift component of the velocity can be viewed as the average velocity that the particles are supposed to possess if there are no thermal effects. The thermal effects cause the particle velocity to fluctuate around this drift velocity, which is called thermal velocity. However, the average thermal velocity over the distribution function is assumed to be zero (Tomizawa, 1993; Majumdar, 1998), that is:

$$\int \left(\bar{v}_{\bar{k},T} f\right) d\bar{k} = 0. \tag{2.40}$$

Also, note that:

$$\int \left(\bar{v}_d f\right) d\bar{k} = \bar{v}_d, \tag{2.41}$$

since $\bar{v}_d$ is already an average quantity over the wave-vector spectrum. According to these observations, the second term on the LHS of Eq. (2.34) can be replaced by the product of the average drift velocity and the average particle density:

$$\int\left[\nabla_{\bar{r}}\cdot\left(\bar{v}_{\bar{k}}f\right)\right]d\bar{k}=\nabla_{\bar{r}}\cdot\int\left[\left(\bar{v}_d+\bar{v}_{\bar{k},T}\right)f\right]d\bar{k}=\nabla_{\bar{r}}\cdot\left(\bar{v}_d n\right). \quad\quad (2.42)$$

The third term on the LHS is zero. This is based on the fact that the divergence theorem can be used to replace the volume integral with surface integral, and the surface integral goes to zero since the integration is to be performed for a surface at a large wave vector where the function f goes to zero (see Snowden, 1988; Tomizawa, 1993). Thus,

$$\int\left(\frac{\bar{F}_{ext}}{\hbar}\cdot\nabla_{\bar{k}}f\right)d\bar{k}=\frac{\bar{F}_{ext}}{\hbar}\cdot\int\nabla_{\bar{k}}f d\bar{k}=0. \quad\quad (2.43)$$

Hence, the zeroth moment of the BTE reads:

$$\frac{\partial n}{\partial t}+\nabla_{\bar{r}}\cdot\left(\bar{v}_d n\right)=\left(\frac{\partial n}{\partial t}\right)_{col}, \quad\quad (2.44)$$

where it is understood that the gradient is that of space $\bar{r}$, and the velocity $\bar{v}_d$ is the averaged drift velocity which varies in space and time. The above equation is the particle number conservation. The rate of change of particle concentration or density, which is the first term on the LHS of Eq. (2.44), and the in-coming and out-going particle fluxes (i.e., the second term on LHS of Eq. (2.44)) is equal to the rate of density generated due to collisions.

2.5.2 Conservation of Momentum

The momentum conservation equation is obtained by taking the first moment of the BTE. Here, ψ is now the particle momentum, $\psi=\bar{p}_{\bar{k}}=m\bar{v}_{\bar{k}}$. Again, referring to Eq. (2.33) and substituting the expression for ψ, the following momentum equation is obtained:

$$\int\left[\frac{\partial\left(m\bar{v}_{\bar{k}}f\right)}{\partial t}\right]d\bar{k}+\int\left[\nabla_{\bar{r}}\cdot\left(m\bar{v}_{\bar{k}}\bar{v}_{\bar{k}}f\right)\right]d\bar{k}+\int m\bar{v}_{\bar{k}}\left(\frac{\bar{F}_{ext}}{\hbar}\cdot\nabla_{\bar{k}}f\right)d\bar{k}=\int\left(\frac{\partial\left(m\bar{v}_{\bar{k}}f\right)}{\partial t}\right)_{col}d\bar{k}. \quad (2.45)$$

The first term on the LHS refers to the rate of change of the average momentum density, the second term is the divergence of the flux density of average momentum of particle, and the last term is the flux density of average momentum due to external applied forces. The RHS is the rate of change of momentum due to particle collisions. The above equation shall be simplified starting from the first term on the LHS. Using Eqs. (2.39) and (2.40), it is observed that:

29

$$\int \left[\frac{\partial \left(m\bar{v}_{\bar{k}}f\right)}{\partial t}\right]d\bar{k} = \frac{\partial}{\partial t}\int \left[m\left(\bar{v}_d + \bar{v}_{\bar{k},T}\right)f\right]d\bar{k} = \frac{\partial}{\partial t}\int \left(m\bar{v}_d f\right)d\bar{k} = \frac{\partial \left(n\bar{p}_d\right)}{\partial t}. \tag{2.46}$$

The second term on the LHS of Eq. (2.45) is rather complicated. It can be rewritten as:

$$\int \left[\nabla_{\bar{r}} \cdot \left(m\bar{v}_{\bar{k}}\bar{v}_{\bar{k}}f\right)\right]d\bar{k} = \nabla_{\bar{r}} \cdot \int \left(m\bar{v}_{\bar{k}}\bar{v}_{\bar{k}}f\right)d\bar{k}$$
$$= \nabla_{\bar{r}} \cdot \int \left[m\left(v_{d,i} + v_{\bar{k},T,i}\right)\left(v_{d,j} + v_{\bar{k},T,j}\right)f\right]d\bar{k}$$
$$= \nabla_{\bar{r}} \cdot \int \left[m\left(v_{d,i}v_{d,j} + v_{d,i}v_{\bar{k},T,j} + v_{\bar{k},T,i}v_{d,j} + v_{\bar{k},T,i}v_{\bar{k},T,j}\right)f\right]d\bar{k}. \tag{2.47}$$
$$= \nabla_{\bar{r}} \cdot \int \left[m\left(v_{d,i}v_{d,j} + v_{\bar{k},T,i}v_{\bar{k},T,j}\right)f\right]d\bar{k}$$
$$= \nabla_{\bar{r}} \cdot \left[mnv_{d,i}v_{d,j} + \int \left(mv_{\bar{k},T,i}v_{\bar{k},T,j}f\right)d\bar{k}\right]$$

The RHS of the above equation are the kinetic and thermal energy tensors, respectively. For the sake of simplicity the off-diagonal elements of the thermal energy tensor shall be ignored. It is related to the temperature such that:

$$nk_B T = \int \left(mv_{\bar{k},T,i}v_{\bar{k},T,i}f\right)d\bar{k}, \tag{2.48}$$

for an ideal gas. Hence, it is observed that:

$$\nabla_{\bar{r}} \cdot \left[mnv_{d,i}v_{d,j} + \int \left(mv_{\bar{k},T,i}v_{\bar{k},T,j}f\right)d\bar{k}\right] = \nabla_{\bar{r}} \cdot \left(nv_{d,i}p_{d,j} + nk_B T\right). \tag{2.49}$$

For the third term in Eq. (2.45), it can be simplified as:

$$\int m\bar{v}_{\bar{k}}\left(\frac{\bar{F}_{ext}}{\hbar} \cdot \nabla_{\bar{k}}f\right)d\bar{k} = \frac{\bar{F}_{ext}}{\hbar} \cdot \int m\bar{v}_{\bar{k}}\nabla_{\bar{k}}f d\bar{k}$$
$$= \frac{\bar{F}_{ext}}{\hbar} \cdot \int \nabla_{\bar{k}} \cdot \left(m\bar{v}_{\bar{k}}f\right)d\bar{k} - \frac{\bar{F}_{ext}}{\hbar} \cdot \int f\nabla_{\bar{k}} \cdot \left(m\bar{v}_{\bar{k}}\right)d\bar{k}. \tag{2.50}$$
$$= \frac{\bar{F}_{ext}}{\hbar} \cdot \int \nabla_{\bar{k}} \cdot \left(m\bar{v}_{\bar{k}}f\right)d\bar{k} - \frac{\bar{F}_{ext}}{\hbar} \cdot \int f\nabla_{\bar{k}} \cdot \left(\hbar\bar{k}\right)d\bar{k}$$

Using the divergence theorem on the first term on the RHS of the above equation to transform the volume integral into surface integral, and performing the integration, the first term vanishes since f goes to zero for large $\bar{k}$. Thus:

$$\int m\bar{v}_{\bar{k}}\left(\frac{\bar{F}_{ext}}{\hbar} \cdot \nabla_{\bar{k}}f\right)d\bar{k} = -\frac{\bar{F}_{ext}}{\hbar} \cdot \int f\nabla_{\bar{k}} \cdot \left(\hbar\bar{k}\right)d\bar{k} = -\bar{F}_{ext} \cdot \int f d\bar{k} = -n\bar{F}_{ext}. \tag{2.51}$$

Collecting all these terms gives the following momentum equation (Snowden, 1988; Tomizawa,

1993):

$$\frac{\partial \left(n\bar{p}_d \right)}{\partial t} + \nabla_{\bar{r}} \cdot \left(n\bar{v}_d \bar{p}_d \right) = n\bar{F}_{ext} - \nabla_{\bar{r}} \left(nk_B T \right) + \left(\frac{\partial \left(n\bar{p}_d \right)}{\partial t} \right)_{col}. \tag{2.52}$$

After the transformation, $\bar{p}_d$ is the average particle drift momentum. It should not be confused with $\bar{p}_{\bar{k}}$, which refers to wave vector dependent particle momentum. For convenience, the momentum conservation is usually written as:

$$\frac{\partial \bar{P}_d}{\partial t} + \nabla_{\bar{r}} \cdot \left(\bar{v}_d \bar{P}_d \right) = n\bar{F}_{ext} - \nabla_{\bar{r}} \left(nk_B T \right) + \left(\frac{\partial \bar{P}_d}{\partial t} \right)_{col}, \tag{2.53}$$

where $\bar{P}_d \left(= n\bar{p}_d \right)$ is the momentum density.

2.5.3 Conservation of Energy

The energy conservation equation is derived by setting ψ to the energy of particles, which shall be denoted as $E_{\bar{k}}$. Note that $E_{\bar{k}}$ is a function of wave vector $\bar{k}$, therefore all the time and space derivatives of it are zeros. Substituting $E_{\bar{k}}$ into Eq. (2.33) yields:

$$\int \left[\frac{\partial \left(E_{\bar{k}} f \right)}{\partial t} \right] d\bar{k} + \int \left[\nabla_{\bar{r}} \cdot \left(E_{\bar{k}} \bar{v}_{\bar{k}} f \right) \right] d\bar{k} + \int E_{\bar{k}} \left(\frac{\bar{F}_{ext}}{\hbar} \cdot \nabla_{\bar{k}} f \right) d\bar{k} = \int \left(\frac{\partial \left(E_{\bar{k}} f \right)}{\partial t} \right)_{col} d\bar{k}. \tag{2.54}$$

Similar to the derivation of the momentum equation, the first term on the LHS is the rate of change of the average energy density, the second term is the divergence of the average energy density flux, and the third term is the average energy generated due to the external forces. The first term on the LHS of the above equation can be expressed as:

$$\int \left[\frac{\partial \left(E_{\bar{k}} f \right)}{\partial t} \right] d\bar{k} = \frac{\partial}{\partial t} \int \left(E_{\bar{k}} f \right) d\bar{k} = \frac{\partial}{\partial t} \left(nw \right), \tag{2.55}$$

while the second term can be written as:

$$\int \left[\nabla_{\bar{r}} \cdot \left(E_{\bar{k}} \bar{v}_{\bar{k}} f \right) \right] d\bar{k} = \nabla_{\bar{r}} \cdot \int \left(E_{\bar{k}} \bar{v}_{\bar{k}} f \right) d\bar{k}$$
$$= \nabla_{\bar{r}} \cdot \left\{ \int \left(E_{\bar{k}} \bar{v}_d f \right) d\bar{k} + \int \left(E_{\bar{k}} \bar{v}_{\bar{k},T} f \right) d\bar{k} \right\}. \tag{2.56}$$
$$= \nabla_{\bar{r}} \cdot \left\{ n\bar{v}_d w + \int \left(E_{\bar{k}} \bar{v}_{\bar{k},T} f \right) d\bar{k} \right\}$$

The second term on the RHS of Eq. (2.56) can be further simplified by assuming that:

$$\begin{aligned} E_{\bar{k}} &= \frac{1}{2} m \left(\bar{v}_{\bar{k}} \cdot \bar{v}_{\bar{k}} \right) \\ &= \frac{1}{2} m \left(\bar{v}_d + \bar{v}_{\bar{k},T} \right) \cdot \left(\bar{v}_d + \bar{v}_{\bar{k},T} \right) \\ &= \frac{1}{2} m \left(\left| \bar{v}_d \right|^2 + 2 \bar{v}_d \cdot \bar{v}_{\bar{k},T} + \left| \bar{v}_{\bar{k},T} \right|^2 \right) \end{aligned} \tag{2.57}$$

and it is given as:

$$\int \left(E_{\bar{k}} \bar{v}_{\bar{k},T} f \right) d\bar{k} = \int \left\{ \frac{1}{2} m \left[\left| \bar{v}_d \right|^2 \bar{v}_{\bar{k},T} + 2 \left(\bar{v}_d \cdot \bar{v}_{\bar{k},T} \right) \bar{v}_{\bar{k},T} + \left| \bar{v}_{\bar{k},T} \right|^2 \bar{v}_{\bar{k},T} \right] f \right\} d\bar{k} . \tag{2.58}$$

The first term vanishes according to the condition given in Eq. (2.40). Again, it shall be assumed that only the diagonal elements of the thermal energy tensor are important and therefore the second term reduces to:

$$\int \left[m \left(\bar{v}_d \cdot \bar{v}_{\bar{k},T} \right) \bar{v}_{\bar{k},T} f \right] d\bar{k} = \int \left(m \bar{v}_d v_{\bar{k},T}^2 f \right) d\bar{k} = n \bar{v}_d k_B T . \tag{2.59}$$

The third term on the RHS of Eq. (2.58) is related to the thermal heat flux, and it is expressed as:

$$\int \left\{ \frac{1}{2} m \left| \bar{v}_{\bar{k},T} \right|^2 \bar{v}_{\bar{k},T} f \right\} d\bar{k} = \bar{q}_T . \tag{2.60}$$

As a result, Eq. (2.56) is given as:

$$\int \left[\nabla_{\bar{r}} \cdot \left(E_{\bar{k}} \bar{v}_{\bar{k}} f \right) \right] d\bar{k} = \nabla_{\bar{r}} \cdot \left(n \bar{v}_d w + n \bar{v}_d k_B T + \bar{q}_T \right) . \tag{2.61}$$

Turning our attention to the third term in Eq. (2.54) :

$$\begin{aligned} \int E_{\bar{k}} \left(\frac{\bar{F}_{ext}}{\hbar} \cdot \nabla_{\bar{k}} f \right) d\bar{k} &= \frac{\bar{F}_{ext}}{\hbar} \cdot \int \left(E_{\bar{k}} \nabla_{\bar{k}} f \right) d\bar{k} \\ &= \frac{\bar{F}_{ext}}{\hbar} \cdot \int \nabla_{\bar{k}} \left(E_{\bar{k}} f \right) d\bar{k} - \frac{\bar{F}_{ext}}{\hbar} \cdot \int f \nabla_{\bar{k}} E_{\bar{k}} d\bar{k} . \\ &= -\bar{F}_{ext} \cdot \int f \bar{v}_{\bar{k}} d\bar{k} \\ &= -n \bar{F}_{ext} \cdot \bar{v}_d \end{aligned} \tag{2.62}$$

Gathering all the reduced terms, the energy conservation equation becomes (Snowden, 1988; Tomizawa, 1993):

$$\frac{\partial (nw)}{\partial t}+\nabla_{\bar{r}}\cdot(n\bar{v}_d w)=n\bar{F}_{ext}\cdot\bar{v}_d-\nabla_{\bar{r}}\cdot(\bar{v}_d nk_B T)-\nabla_{\bar{r}}\cdot\bar{q}_T+\left(\frac{\partial (nw)}{\partial t}\right)_{col}, \qquad (2.63)$$

where w is the average energy of the energy carriers and it is a function of time and space, and $\bar{q}_T$ is the thermal heat flux. Note that the energy density is given as $W=nw$, thus one can write:

$$\frac{\partial W}{\partial t}+\nabla_{\bar{r}}\cdot(\bar{v}_d W)=-n\bar{F}_{ext}\cdot\bar{v}_d-\nabla_{\bar{r}}\cdot(\bar{v}_d nk_B T)-\nabla_{\bar{r}}\cdot\bar{q}_T+\left(\frac{\partial W}{\partial t}\right)_{col}. \qquad (2.64)$$

2.5.4 Conservation of Thermal Heat Flux

Another conservation equation that can be extracted from the BTE is the heat flux conservation equation. This is done by defining $\psi=\bar{v}_{\bar{k},T}E_{\bar{k},T}$ where $\bar{v}_{\bar{k},T}$ and $E_{\bar{k},T}$ are the thermal velocity and energy, respectively. Note that the thermal energy is related to the thermal velocity as follows:

$$E_{\bar{k},T}=\frac{1}{2}m\left|\bar{v}_{\bar{k},T}\right|^2. \qquad (2.65)$$

Substituting this into Eq. (2.33) yields

$$\int\left[\frac{\partial\left(\bar{v}_{\bar{k},T}E_{\bar{k},T}f\right)}{\partial t}\right]d\bar{k}+\int\left[\nabla_{\bar{r}}\cdot\left(E_{\bar{k},T}\bar{v}_{\bar{k},T}\bar{v}_{\bar{k}}f\right)\right]d\bar{k}=\int\left(\frac{\partial\left(\bar{v}_{\bar{k},T}E_{\bar{k},T}f\right)}{\partial t}\right)_{col}d\bar{k}. \qquad (2.66)$$

The external force term is conveniently omitted in the above expression for the sake of simplicity. The equation shall be simplified term by term, starting from the first in the LHS. Note that the thermal heat flux can be expressed as (Tomizawa, 1993):

$$\bar{q}_T=\int\left(\bar{v}_{\bar{k},T}E_{\bar{k},T}f\right)d\bar{k}. \qquad (2.67)$$

Using this expression, the first term on the LHS of Eq. (2.66) is:

$$\frac{\partial}{\partial t}\left[\int\left(\bar{v}_{\bar{k},T}E_{\bar{k},T}f\right)d\bar{k}\right]=\frac{\partial\bar{q}_T}{\partial t}. \qquad (2.68)$$

The second term of Eq. (2.66) is:

$$\int\left[\nabla_{\bar{r}}\cdot\left(E_{\bar{k},T}\bar{v}_{\bar{k},T}\bar{v}_{\bar{k}}f\right)\right]d\bar{k}=\nabla_{\bar{r}}\cdot\int\bar{v}_{\bar{k}}\left(E_{\bar{k},T}\bar{v}_{\bar{k},T}f\right)d\bar{k}=\nabla_{\bar{r}}\cdot\int\left(\bar{v}_d+\bar{v}_{\bar{k},T}\right)\left(E_{\bar{k},T}\bar{v}_{\bar{k},T}f\right)d\bar{k}. \qquad (2.69)$$

The divergence of the integral can be reduced to:

$$\nabla_{\bar{r}} \cdot \int \left[\bar{v}_d \left(E_{\bar{k},T} \bar{v}_{\bar{k},T} f \right) + \bar{v}_{\bar{k},T} \left(E_{\bar{k},T} \bar{v}_{\bar{k},T} f \right) \right] d\bar{k} = \nabla_{\bar{r}} \cdot \left(\bar{v}_d \bar{q}_T + \bar{v}_T \bar{q}_T \right), \quad (2.70)$$

where $\bar{v}_T$ is the average thermal velocity. Since the external force term has already been neglected, it is preferable to ignore the drift velocity term as well. After collecting all the reduced terms for Eq. (2.66), the conservation of heat flux becomes:

$$\frac{\partial \bar{q}_T}{\partial t} + \nabla_{\bar{r}} \cdot \left(\bar{v}_T \bar{q}_T \right) = \left(\frac{\partial \bar{q}_T}{\partial t} \right)_{col}. \quad (2.71)$$

Since the effects imposed by the external forces and by the particle drift on the thermal heat flux are ignored in the derivation, this equation is best suited for describing photon or phonon transport. In the case of electron transport, the above equation may deviate from the actual physics depending on the order of magnitude of the ignored terms. However, with the inclusion of the external forces and the drift velocity in the derivation, the equation is further complicated and may potentially become intractable.

2.6 Macro-Scale Thermal Conduction

Thermal transport in bulk objects is usually termed macro-scale transport. Governing equations for this transport phenomena are considered to be the most simplified form of the BTE. Since the characteristic length scale of the bulk object far exceeds the mean free path of the heat carriers, most of the terms in the moments of the BTE can be neglected. Scales of such length determine that electrons and phonons are always in thermal equilibrium, considering that the relaxation time and length are much smaller than the characteristic behavior of the material. Since only a single temperature exists, the electrons and phonons are considered as a whole. The governing equations for the heat flow are then given by Eqs. (2.63) and (2.71), where the drift velocity and external forces are all negligible. They are:

$$\frac{\partial W}{\partial t} = -\nabla_{\bar{r}} \cdot \bar{q}_T + \left(\frac{\partial W}{\partial t} \right)_{col} + S_T, \quad (2.72)$$

$$\frac{\partial \bar{q}_T}{\partial t} + \nabla_{\bar{r}} \cdot \left(\bar{v}_T \bar{q}_T \right) = \left(\frac{\partial \bar{q}_T}{\partial t} \right)_{col}. \quad (2.73)$$

It is assumed here that there are external neutral heat sources, denoted as S_T, elevating the energy density of the carriers. The collision term is responsible for restoring thermal equilibrium. Since local thermal equilibrium exists between electrons and phonons, the collision term in the energy

conservation equation vanishes. The energy density, which is *nw*, refers to the combined energy density of electrons and phonons and it can be expressed as the product of the specific heat of electrons and phonons, *C*, and temperature, *T*. For macro-scale heat transport there is not a concern with the detailed scattering mechanism in the collision term for the heat flux. So the relaxation-time approach is used (see Section 2.3.1) instead, and the following is obtained:

$$C\frac{\partial T}{\partial t} = -\nabla_{\bar{r}} \cdot \bar{q}_T + S_T,$$ (2.74)

$$\frac{\partial \bar{q}_T}{\partial t} + \nabla_{\bar{r}} \cdot (\bar{v}_T \bar{q}_T) = -\frac{\bar{q}_T}{\tau_q}.$$ (2.75)

The divergence of the product of the thermal velocity and the thermal heat flux can be reduced to account for the temperature variation in space. Referring back to Section 2.3.1,

$$\nabla_{\bar{r}} \cdot (\bar{v}_T \bar{q}_T) = \int \nabla_{\bar{r}} \cdot \left[\bar{v}_{\bar{k},T} \left(E_{\bar{k},T} \bar{v}_{\bar{k},T} f \right) \right] d\bar{k} = \int \left[\left(\bar{v}_{\bar{k},T} \cdot \nabla_{\bar{r}} f \right) E_{\bar{k},T} \bar{v}_{\bar{k},T} \right] d\bar{k}.$$ (2.76)

Since the characteristic length at macro-scale transport is much greater than the relaxation length of the heat carriers (i.e. electrons and phonons), the distribution function *f* should in fact converge to the equilibrium distribution function, denoted as *f*^*eq*. This depends on temperature *T*. The integral can now be re-written as:

$$\int \left[\left(\bar{v}_{\bar{k},T} \cdot \nabla_{\bar{r}} f^{eq} \right) E_{\bar{k},T} \bar{v}_{\bar{k},T} \right] d\bar{k} = \nabla_{\bar{r}} T \cdot \int \left(\bar{v}_{\bar{k},T} E_{\bar{k},T} \bar{v}_{\bar{k},T} \frac{\partial f^{eq}}{\partial T} \right) d\bar{k}.$$ (2.77)

Since the thermal conductivity is defined as (Tomizawa, 1993):

$$k_T = \int \left(\tau_{\bar{k}} \bar{v}_{\bar{k},T} E_{\bar{k},T} \bar{v}_{\bar{k},T} \frac{\partial f^{eq}}{\partial T} \right) d\bar{k},$$ (2.78)

and by assuming that the relaxation time for the thermal heat flux is constant, it can be written that:

$$\nabla_{\bar{r}} \cdot (\bar{v}_T \bar{q}_T) = \frac{k_T}{\tau_q} \nabla_{\bar{r}} T.$$ (2.79)

Using this simplification, the energy and heat flux conservation equations for macroscopic thermal transport become:

$$C\frac{\partial T}{\partial t} = -\nabla_{\bar{r}} \cdot \bar{q}_T + S_T,$$ (2.80)

35

$$\frac{\partial \bar{q}_T}{\partial t} + \frac{k_T}{\tau_q} \nabla_{\bar{r}} T = -\frac{\bar{q}_T}{\tau_q} . \tag{2.81}$$

The above two equations form the so-called hyperbolic heat conduction, where it is diffusive in space but ballistic-diffusive in time. The hyperbolic heat conduction can be expressed in a single equation by taking the divergence of the heat flux equation and substituting the energy equation into it. The equation then takes the form:

$$C\left(\tau_q \frac{\partial^2 T}{\partial t^2} + \frac{\partial T}{\partial t} \right) = \nabla_{\bar{r}} \cdot \left(k_T \nabla_{\bar{r}} T \right) + S_T + \tau_q \frac{\partial S_T}{\partial t} . \tag{2.82}$$

The hyperbolic heat conduction can be reduced to parabolic heat conduction if the time of interest becomes much greater than the relaxation time of the heat flux. Under such a condition, the transient term in Eq. (2.81) drops out and the Fourier law is obtained, that is

$$\bar{q}_T = -k_T \nabla_{\bar{r}} T . \tag{2.83}$$

Inserting this into the energy conservation equation, the parabolic heat equation is then given as

$$C\frac{\partial T}{\partial t} = \nabla_{\bar{r}} \cdot \left(k_T \nabla_{\bar{r}} T \right) + S_T , \tag{2.84}$$

where the conduction is purely diffusive both in time and space.

2.7 Micro-Scale Thermal Conduction

At the microscopic level, which ranges from micrometer to sub-micrometer length scales, electrons and phonons can exist at different thermal energy levels. In other words, local thermal equilibrium does not exist since electrons and phonons possess different temperatures. Typically, the thermalization process first occurs through electrons and then relaxation takes place between hot electrons and phonons until equilibrium is reached. There are quite a number of thermal models available for modeling the microscopic heat transport. Derivations of these models will be discussed in the following sections.

2.7.1 Two-Temperature Model

Interactions between external sources of heating such as the photon- and electron-beams and the target workpiece involve the heating of electron gas inside the target workpiece causing the electron energy to elevate substantially when compared to the lattice energy. One way to model

this phenomenon is to separate temperature into two distinct components, namely the electron and lattice temperatures, though temperature may not be correct term to use. Such a model is referred to as the two-temperature model (TTM). The TTM neglects the kinetic-energy changes of electrons, and assumes interactions between electrons and phonons through a coupling constant G.

To derive the TTM the energy and heat flux conservations for electrons and phonons shall be written using Eqs. (2.63) and (2.71). These conservation equations are written as:

$$\frac{\partial W_e}{\partial t} = -\nabla_{\bar{r}} \cdot \bar{q}_{T,e} + \left(\frac{\partial W_e}{\partial t} \right)_{col} + S_T, \tag{2.85}$$

$$\frac{\partial \bar{q}_{T,e}}{\partial t} + \nabla_{\bar{r}} \cdot \left(\bar{v}_{T,e} \bar{q}_{T,e} \right) = \left(\frac{\partial \bar{q}_{T,e}}{\partial t} \right)_{col}, \tag{2.86}$$

$$\frac{\partial W_{ph}}{\partial t} = -\nabla_{\bar{r}} \cdot \bar{q}_{T,ph} + \left(\frac{\partial W_{ph}}{\partial t} \right)_{col}, \tag{2.87}$$

$$\frac{\partial \bar{q}_{T,ph}}{\partial t} + \nabla_{\bar{r}} \cdot \left(\bar{v}_{T,ph} \bar{q}_{T,ph} \right) = \left(\frac{\partial \bar{q}_{T,ph}}{\partial t} \right)_{col}, \tag{2.88}$$

where subscripts 'e' and 'ph' denote electrons and phonons, respectively. The external heating source, S_T, is assumed to be on electrons. By assuming that the object length far exceeds the relaxation lengths of electrons and phonons, these equations become:

$$\frac{\partial W_e}{\partial t} = -\nabla_{\bar{r}} \cdot \bar{q}_{T,e} + \left(\frac{\partial W_e}{\partial t} \right)_{col} + S_T, \tag{2.89}$$

$$\frac{\partial \bar{q}_{T,e}}{\partial t} + \frac{k_{T,e}}{\tau_{q,e}} \nabla_{\bar{r}} T_e = -\frac{\bar{q}_{T,e}}{\tau_{q,e}}, \tag{2.90}$$

$$\frac{\partial W_{ph}}{\partial t} = -\nabla_{\bar{r}} \cdot \bar{q}_{T,ph} + \left(\frac{\partial W_{ph}}{\partial t} \right)_{col}, \tag{2.91}$$

$$\frac{\partial \bar{q}_{T,ph}}{\partial t} + \frac{k_{T,ph}}{\tau_{q,ph}} \nabla_{\bar{r}} T_{ph} = -\frac{\bar{q}_{T,ph}}{\tau_{q,ph}}. \tag{2.92}$$

Since electrons and phonons are transferring energy between each other, the collision term for electrons include energy lost to phonons while the collision term for phonons involves energy received from electrons. By using the relaxation time approach, the collision terms for electrons and phonons can be written as:

$$\left(\frac{\partial W_e}{\partial t}\right)_{col} = -\left(\frac{\partial W_{ph}}{\partial t}\right)_{col} = C_e \frac{T_{ph} - T_e}{\tau_{e-ph}}, \tag{2.93}$$

where $\tau_{e\text{-}ph}$ is the relaxation time between electrons and phonons. By treating the energy density of electrons and phonons as a function of electron temperature and phonon temperature, respectively, the governing equations are transformed into:

$$C_e \frac{\partial T_e}{\partial t} = -\nabla_{\vec{r}} \cdot \vec{q}_{T,e} - C_e \frac{T_e - T_{ph}}{\tau_{e-ph}} + S_T, \tag{2.94}$$

$$\frac{\partial \vec{q}_{T,e}}{\partial t} + \frac{k_{T,e}}{\tau_{q,e}} \nabla_{\vec{r}} T_e = -\frac{\vec{q}_{T,e}}{\tau_{q,e}}, \tag{2.95}$$

$$C_{ph} \frac{\partial T_{ph}}{\partial t} = -\nabla_{\vec{r}} \cdot \vec{q}_{T,ph} - C_e \frac{T_{ph} - T_e}{\tau_{e-ph}}, \tag{2.96}$$

$$\frac{\partial \vec{q}_{T,ph}}{\partial t} + \frac{k_{T,ph}}{\tau_{q,ph}} \nabla_{\vec{r}} T_{ph} = -\frac{\vec{q}_{T,ph}}{\tau_{q,ph}}, \tag{2.97}$$

where S_T is the volumetric heat generation caused by the external heating sources, C the heat capacity, and k the thermal conductivity. The above four equations shall be called the general TTM where the ballistic nature of electrons and phonons is maintained in the governing equations. The general TTM can be simplified to produce the so-called hyperbolic TTM, parabolic TTM, and even the dual-phase lag model (DPLM).

The hyperbolic TTM can be obtained from the general TTM by ignoring the heat propagation of phonons. This is usually justified when metals are dealt with since the thermal conduction of phonons is weak when compared to that of electrons. Thus, the set of four equations reduces to three:

$$C_e \frac{\partial T_e}{\partial t} = -\nabla_{\vec{r}} \cdot \vec{q}_{T,e} - C_e \frac{T_e - T_{ph}}{\tau_{e-ph}} + S_T, \tag{2.98}$$

$$\frac{\partial \vec{q}_{T,e}}{\partial t} + \frac{k_{T,e}}{\tau_{q,e}} \nabla_{\vec{r}} T_e = -\frac{\vec{q}_{T,e}}{\tau_{q,e}}, \tag{2.99}$$

$$C_{ph} \frac{\partial T_{ph}}{\partial t} = -C_e \frac{T_{ph} - T_e}{\tau_{e-ph}}. \tag{2.100}$$

If the transient behavior of heat flux in the hyperbolic TTM is omitted, the parabolic TTM is formed.

2.7.2 Dual-Phase Lag Model

The hyperbolic TTM can be combined easily to yield the so-called dual-phase lag model (DPLM). This model describes the phonon temperature in a single governing equation. This model requires that all the thermal properties of electrons and phonons are to be considered constant. Therefore, the two of the three unknowns need to be eliminiated from the governing equation. To do so, Eq. (2.98) is first differentiated with respect to time to obtain:

$$\frac{\partial}{\partial t}\left(C_e \frac{\partial T_e}{\partial t}\right) = -\nabla_{\bar{r}} \cdot \frac{\partial \bar{q}_{T,e}}{\partial t} - \frac{\partial}{\partial t}\left(\frac{C_e}{\tau_{e-ph}} T_e\right) + \frac{\partial}{\partial t}\left(\frac{C_e}{\tau_{e-ph}} T_{ph}\right) + \frac{\partial S_T}{\partial t}. \tag{2.101}$$

The divergence of Eq. (2.99) is taken to get:

$$\nabla_{\bar{r}} \cdot \frac{\partial \bar{q}_{T,e}}{\partial t} = -\nabla_{\bar{r}} \cdot \left(\frac{\bar{q}_{T,e}}{\tau_{q,e}}\right) - \nabla_{\bar{r}} \cdot \left(\frac{k_{T,e}}{\tau_{q,e}} \nabla_{\bar{r}} T_e\right). \tag{2.102}$$

Substituting this equation into Eq. (2.101) and rearranging it gives:

$$\frac{\partial}{\partial t}\left(C_e \frac{\partial T_e}{\partial t}\right) = \nabla_{\bar{r}} \cdot \left(\frac{\bar{q}_{T,e}}{\tau_{q,e}}\right) + \nabla_{\bar{r}} \cdot \left(\frac{k_{T,e}}{\tau_{q,e}} \nabla_{\bar{r}} T_e\right) - \frac{\partial}{\partial t}\left(\frac{C_e}{\tau_{e-ph}} T_e\right) + \frac{\partial}{\partial t}\left(\frac{C_e}{\tau_{e-ph}} T_{ph}\right) + \frac{\partial S_T}{\partial t} \tag{2.103}$$

If the relaxation time of the electron heat flux, $\tau_{q,e}$, is assumed constant, then:

$$\frac{\partial}{\partial t}\left(C_e \frac{\partial T_e}{\partial t}\right) = \frac{1}{\tau_{q,e}}\nabla_{\bar{r}} \cdot \bar{q}_{T,e} + \frac{1}{\tau_{q,e}}\nabla_{\bar{r}} \cdot \left(k_{T,e} \nabla_{\bar{r}} T_e\right) - \frac{\partial}{\partial t}\left(\frac{C_e}{\tau_{e-ph}} T_e\right) + \frac{\partial}{\partial t}\left(\frac{C_e}{\tau_{e-ph}} T_{ph}\right) + \frac{\partial S_T}{\partial t} \tag{2.104}$$

Note that the divergence of the electron heat flux can be eliminated by using the electron-energy equation given in Eq. (2.98) where

$$\nabla_{\bar{r}} \cdot \bar{q}_{T,e} = -C_e \frac{\partial T_e}{\partial t} - C_e \frac{T_e - T_{ph}}{\tau_{e-ph}} + S_T. \tag{2.105}$$

Thus, Eq. (2.104) becomes:

$$\frac{\partial}{\partial t}\left(C_e \frac{\partial T_e}{\partial t}\right) - \frac{C_e}{\tau_{q,e}} \frac{\partial T_e}{\partial t} + \frac{\partial}{\partial t}\left(\frac{C_e}{\tau_{e-ph}} T_e\right) - \frac{\partial}{\partial t}\left(\frac{C_e}{\tau_{e-ph}} T_{ph}\right)$$
$$= \frac{1}{\tau_{q,e}}\nabla_{\bar{r}} \cdot \left(k_{T,e} \nabla_{\bar{r}} T_e\right) + \frac{C_e}{\tau_{q,e}}\frac{T_e - T_{ph}}{\tau_{e-ph}} + \frac{S_T}{\tau_{q,e}} + \frac{\partial S_T}{\partial t} \tag{2.106}$$

Next, the phonon energy equation (see Eq. (2.100)) is solved for the electron temperature:

$$T_e = \left(\frac{\tau_{e-ph}C_{ph}}{C_e}\right)\frac{\partial T_{ph}}{\partial t} + T_{ph}. \tag{2.107}$$

Substituting this into Eq. (2.106) to eliminate the electron temperature yields:

$$\tau_{q,e}\frac{\partial}{\partial t}\left(C_e\frac{\partial}{\partial t}\left[\left(\frac{\tau_{e-ph}C_{ph}}{C_e}\right)\frac{\partial T_{ph}}{\partial t}\right] + C_e\frac{\partial T_{ph}}{\partial t}\right)$$

$$-C_e\frac{\partial}{\partial t}\left[\left(\frac{\tau_{e-ph}C_{ph}}{C_e}\right)\frac{\partial T_{ph}}{\partial t}\right] - \left(C_{ph} + \frac{C_e}{\tau_{q,e}}\right)\frac{\partial T_{ph}}{\partial t} + \frac{\partial}{\partial t}\left(C_{ph}\frac{\partial T_{ph}}{\partial t}\right) \tag{2.108}$$

$$= \nabla_{\bar{r}}\cdot\left(k_e\nabla_{\bar{r}}\left[\left(\frac{\tau_{e-ph}C_{ph}}{C_e}\right)\frac{\partial T_{ph}}{\partial t}\right]\right) + \nabla_{\bar{r}}\cdot\left(k_{T,e}\nabla_{\bar{r}}T_{ph}\right) + S_T + \tau_{q,e}\frac{\partial S_T}{\partial t}$$

For the case where the electron-phonon relaxation time, specific heats of electrons and phonons and electron thermal conductivity are constant, the equation takes the form:

$$\tau_{q,e}\tau_{e-ph}C_{ph}\frac{\partial^3 T_{ph}}{\partial t^3} + \left(\tau_{q,e}C_e - \tau_{e-ph}C_{ph} + C_{ph}\right)\frac{\partial^2 T_{ph}}{\partial t^2} - \left(C_{ph} + \frac{C_e}{\tau_{q,e}}\right)\frac{\partial T_{ph}}{\partial t}$$

$$= \left(\frac{k_{T,e}\tau_{e-ph}C_{ph}}{C_e}\right)\frac{\partial}{\partial t}\left(\nabla_{\bar{r}}^2 T_{ph}\right) + k_{T,e}\nabla_{\bar{r}}^2 T_{ph} + S_T + \tau_{q,e}\frac{\partial S_T}{\partial t}. \tag{2.109}$$

2.7.3 Electron-Phonon Hydrodynamic Model

By taking the zeroth-, first- and second-order moments of the Boltzmann transport equation which corresponds to continuity, momentum, and energy conservations, respectively, the so-called hydrodynamic equations can be derived. The hydrodynamic equations are usually useful for simulating heat transport inside electrical devices in sub-micron scale resolution. However, by doing so, the variables such as distribution, velocity, and energy describing the heat carriers in the equations are replaced by the corresponding average quantities. For instance, the energy-dependent velocity of the carriers are neglected and replaced by an averaged velocity. However the physics of the problem are still preserved.

The various conservation equations derived from the moments of the BTE are shown in Section 2.4.2, and they are given by Eqs. (2.44), (2.52), (2.63), and (2.71). It is important to consider that electrically and thermally conducting material consists of electrons and phonons as energy carriers. Using moments of the BTE, continuity, momentum, and energy conservations for elec-

trons are expressed as:

$$\frac{\partial n_e}{\partial t} + \nabla_{\bar{r}} \cdot \left(\bar{v}_{d,e} n_e \right) = \left(\frac{\partial n_e}{\partial t} \right)_c, \tag{2.110}$$

$$\frac{\partial \bar{P}_{d,e}}{\partial t} + \nabla_{\bar{r}} \cdot \left(\bar{v}_{d,e} \bar{P}_{d,e} \right) = -en_e \bar{E} - \nabla_{\bar{r}} \left(n_e k_B T_e \right) + \left(\frac{\partial \bar{P}_{d,e}}{\partial t} \right)_c, \tag{2.111}$$

$$\frac{\partial W_e}{\partial t} + \nabla_{\bar{r}} \cdot \left(\bar{v}_{d,e} W_e \right) = -en_e \bar{v}_{d,e} \cdot \bar{E} - \nabla_{\bar{r}} \cdot \left(\bar{v}_{d,e} n_e k_B T_e \right)$$
$$+ \nabla_{\bar{r}} \cdot \left(k_{T,e} \nabla_{\bar{r}} T_e \right) + \left(\frac{\partial W_e}{\partial t} \right)_c + \dot{W}_{e,gen} \tag{2.112}$$

where it is assumed that an external electric field, $\bar{E}$, is applied. The Fourier law of heat conduction is used for the sake of simplicity. Since Fourier's law is applied, the assumption is that the characteristic length of the geometry far exceeds the mean free path and the relaxation length of electrons. It is also implied that heat conduction by electrons is not ballistic in time. The first equation enforces the particle conservation for electrons. This is where the rate of change of the electrons in time and space equals the rate of increase of electrons due to collisions. The second equation refers to electron momentum conservation. This is when the rate of change of the electron momentum in time and space is equivalent to the forces exerted by the electric field and by the electron pressure, as well as the rate of momentum gain or loss in collisions. The third equation represents the electron-energy conservation. This is where electron energies are conserved in time and space according to the energy supplied by the electric field, the work performed by the electron pressure, the divergence of heat flux, and the rate of change of energy due to collisions.

Similarly, these conservation equations can be written for phonons. However, the continuity equation does not apply for phonons since they can be created and destructed. In addition, the phonon thermal velocity is typically much greater than its drift velocity, implying that the phonon momentum conservation is not needed. Hence, all the terms related to the drift velocity of phonons are dropped out. As a result, energy and heat flux equations remain. Phonons are usually sub-divided into optical phonons and acoustic phonons (Ashcroft and Mermin, 1976; Ziman, 1960). Optical phonons have essentially zero velocity while acoustic phonons propagate and conduct heat. According to the arguments above, the governing equations for optical and acoustic phonons are written as:

$$\frac{\partial W_{LO}}{\partial t} = \left(\frac{\partial W_{LO}}{\partial t}\right)_{col}, \qquad (2.113)$$

$$\frac{\partial W_{A}}{\partial t} = -\nabla_{\vec{r}} \cdot \vec{q}_{T,A} + \left(\frac{\partial W_{A}}{\partial t}\right)_{col}, \qquad (2.114)$$

$$\frac{\partial \vec{q}_{T,A}}{\partial t} + \nabla_{\vec{r}} \cdot \left(\vec{v}_{T,A}\vec{q}_{T,A}\right) = \left(\frac{\partial \vec{q}_{T,A}}{\partial t}\right)_{col}, \qquad (2.115)$$

where the subscript '*LO*' stands for optical phonons and '*A*' for acoustic phonons. In order to present these equations in a simpler manner, the divergence term in the acoustic phonon heat flux equation is approximated by relating it to the phonon thermal conductivity and temperature gradient, as previously shown in Section 2.6.

By using the concept of thermal conductivity, it is assumed that the object is "bulk" in size, enabling conductivity to be defined. By the same token, the internal energy of the phonons can be expressed as a product of the specific heat and temperature. In addition, the ballistic transport of phonons in time shall be ignored. Using these approximations, the above equations for phonon transport are transformed into:

$$C_{LO}\frac{\partial T_{LO}}{\partial t} = \left(\frac{\partial W_{LO}}{\partial t}\right)_{col}, \qquad (2.116)$$

$$C_{A}\frac{\partial T_{A}}{\partial t} = \nabla_{\vec{r}} \cdot \left(k_{T,A}\nabla_{\vec{r}}T_{A}\right) + \left(\frac{\partial W_{A}}{\partial t}\right)_{col}. \qquad (2.117)$$

Next, the various collision terms in the equations need to be addressed. The relaxation time approximation (see Section 2.3.1) will be used to determine these terms. It is important to first discuss what the energy transfer mechanisms are in this electron-phonon system before attempting to express them in terms of mathematical equations as well as the physics of the energy transfer. Due to the external applied electric field, electrons are accelerated where they gain additional energy from the force field. Since the electric field does not directly affect phonon energy, phonons remain cold while electrons are hot. Next, electrons start to relax by transferring excess energy to phonons until thermal equilibrium exists between them. Energy is also transferred between optical phonons and acoustic phonons. Following the detailed explanations given by Blotekjaer (1970), the various collision terms can be approximated as:

$$\left(\frac{\partial n_e}{\partial t}\right)_c = \dot{n}_{e,gen}, \tag{2.118}$$

$$\left(\frac{\partial \bar{P}_{d,e}}{\partial t}\right)_c = -\frac{m_e n_e \bar{v}_{d,e}}{\tau_m}, \tag{2.119}$$

$$\left(\frac{\partial W_e}{\partial t}\right)_c = -\frac{n_e \left(3k_B T_e / 2 + m_e v_{d,e}^2 / 2 - 3k_B T_{LO} / 2\right)}{\tau_{e-LO}}$$
$$-\frac{n_e \left(3k_B T_e / 2 + m_e v_{d,e}^2 / 2 - 3k_B T_A / 2\right)}{\tau_{e-A}}, \tag{2.120}$$

$$\left(\frac{\partial W_{LO}}{\partial t}\right)_{col} = \frac{n_e \left(3k_B T_e / 2 + m_e v_{d,e}^2 / 2 - 3k_B T_{LO} / 2\right)}{\tau_{e-LO}} - \frac{C_{LO}\left(T_{LO} - T_A\right)}{\tau_{LO-A}}, \tag{2.121}$$

$$\left(\frac{\partial W_A}{\partial t}\right)_{col} = \frac{n_e \left(3k_B T_e / 2 + m_e v_{d,e}^2 / 2 - 3k_B T_A / 2\right)}{\tau_{e-A}} + \frac{C_{LO}\left(T_{LO} - T_A\right)}{\tau_{LO-A}}, \tag{2.122}$$

where the electron momentum, $\bar{P}_{d,e}$, and the average electron energy, W_e, are expressed as:

$$\bar{P}_{d,e} = m_e n_e \bar{v}_{d,e}, \tag{2.123}$$

$$W_e = \frac{3}{2} n_e k_B T_e + \frac{1}{2} n_e m_e v_{d,e}{}^2. \tag{2.124}$$

According to the above order, the first collision term corresponds to the number of electrons generated due to the incoming electrons from external sources. The second term describes the relaxation of the momentum between electrons, while the remaining three terms account for the energy exchange between electrons and phonons. The momentum relaxation is assumed to be fully isotropic. Collisions between impinging electrons from any external sources and electrons inside the material itself randomize momentum, resulting in no net momentum transfer during scattering. The premise of this assumption is based on the condition that the incoming electrons from the external sources are at the same energy level as the electrons inside the medium. The third term describes the energy exchanges between electrons and optical and acoustic phonons. The fourth term refers to interactions of optical phonons with electrons and acoustic phonons while the last term is the interactions acoustic phonons with electrons and optical phonons.

Replacing all the collision terms, electron momentum, and electron energy into the conservation equations with the above expressions, the following set of equations is obtained:

(*e-Continuity*)
$$\frac{\partial n_e}{\partial t}+\nabla_{\bar{r}}\cdot\left(\vec{v}_{d,e}n_e\right)=\dot{n}_{e,gen}, \tag{2.125}$$

(*e-Momentum*)
$$\frac{\partial \vec{v}_{d,e}}{\partial t}+\vec{v}_{d,e}\cdot\nabla_{\bar{r}}\vec{v}_{d,e}=-\frac{e}{m_e}\vec{E}-\frac{k_B}{m_e n_e}\nabla_{\bar{r}}\left(n_e T_e\right)-\left(\frac{1}{\tau_m}+\frac{\dot{n}_{e,gen}}{n_e}\right)\vec{v}_{d,e}, \tag{2.126}$$

(*e-Energy*)
$$\frac{\partial T_e}{\partial t}+\nabla_{\bar{r}}\cdot\left(\vec{v}_{d,e}T_e\right)=\frac{1}{3}T_e\nabla_{\bar{r}}\cdot\vec{v}_{d,e}+\frac{2}{3n_e k_B}\nabla_{\bar{r}}\cdot\left(k_{T,e}\nabla_{\bar{r}}T_e\right)-\frac{T_e-T_{LO}}{\tau_{e-LO}}$$
$$-\frac{T_e-T_A}{\tau_{e-A}}+\left(\frac{2}{\tau_m}-\frac{1}{\tau_{e-LO}}-\frac{1}{\tau_{e-A}}+\frac{\dot{n}_{e,gen}}{n_e}\right)\frac{m_e v_{d,e}^2}{3k_B}, \tag{2.127}$$
$$-\left(\frac{\dot{n}_{e,gen}}{n_e}\right)T_e+\left(\frac{2}{3n_e k_B}\right)\dot{W}_{e,gen}$$

(*LO-Phonon Energy*)
$$\frac{\partial T_{LO}}{\partial t}=\frac{n_e m_e v_{d,e}^2}{2C_{LO}\tau_{e-LO}}-\frac{3n_e k_B\left(T_{LO}-T_e\right)}{2C_{LO}\tau_{e-LO}}-\frac{T_{LO}-T_A}{\tau_{LO-A}}, \tag{2.128}$$

(*A-Phonon Energy*)
$$\frac{\partial T_A}{\partial t}=\frac{1}{C_A}\nabla_{\bar{r}}\cdot\left(k_{T,A}\nabla_{\bar{r}}T_A\right)+\frac{n_e m_e v_{d,e}^2}{2C_A\tau_{e-A}}-\frac{3n_e k_B\left(T_A-T_e\right)}{2C_A\tau_{e-A}}-\frac{C_{LO}\left(T_A-T_{LO}\right)}{C_A\tau_{LO-A}}. \tag{2.129}$$

Details of the derivations are given in Appendix A. The above equations are termed the electron-phonon hydrodynamic equations. These are various conservation equations for the heat carriers. It is necessary to go over the physical meaning of each conservation equation and deduce some implications from them.

The electron continuity equation given in Eq. (2.125) refers to the electron number balance. This is the rate of increase of the electron concentration being equal to the rate of advection and diffusion plus the rate of electrons generated. In the electron momentum conservation (see Eq. (2.126)), it is observed that electron velocity tends to increase propagating through decreasing electric field, negative electron concentration gradient, and/or declining electron temperature gradient. The rate of the electron velocity relaxation (or the rate at which the electron reduces its velocity) is dictated by the momentum relaxation time, τ_m, and the rate of increase/decrease of the externally generated electron concentration, $\dot{n}_{e,gen}$. It is normalized by the local electron concentration, n_e. Note that the larger momentum relaxation time means longer time for the electron to reduce its velocity. In addition, when there is additional local electron concentration being generated, the rate of momentum relaxation is elevated by those electrons since an increasing electron concentration increases the frequency of electron-electron collisions.

Proceeding to the electron energy conservation equation in Eq. (2.127), notice that the Joule heating term $\left(-en_e\vec{v}_{d,e}\cdot\vec{E}\right)$ as expressed in the general electron energy equation (see Eq. (2.112)) does not appear in the equation after the simplification given in Appendix A. The Joule heating phenomenon is embedded in Eq. (2.127) even though it is not expressed explicitly in the equation. The same goes for the work done by the electron pressure $\left(-\nabla_{\vec{r}}\cdot\left(\vec{v}_{d,e}n_e k_B T_e\right)\right)$. It would be rather difficult to point out the explicit physical meaning of each term in the current form of the electron energy equation. This claim shall be explored in the next paragraph.

The effects of electron concentration generation (or heating by external electrons) on the electron temperature seem to appear in the last three terms on the RHS of Eq. (2.127). One can increase the electron temperature locally by imposing a strong localized heating source. This effect is given by the last of the three terms mentioned. Judging from the other two terms (i.e., $\left(\dot{n}_{e,gen}/n_e\right)\left(m_e v_{d,e}^2/3k_B\right)-\left(\dot{n}_{e,gen}/n_e\right)T_e$), it looks as if electron heating has mixed effects on the electron temperature. Increasing the rate of electron heating may increase or decrease the electron temperature depending on the ratio of average kinetic energy to local electron temperature. To clarify this, it should be noted that the average drift velocity of the electron decreases when the electron heating rate is large as asserted by the electron momentum equation (see Eq. (2.126)). Therefore, the combination of the increase in the electron concentration due to electron heating and the decrease in the average electron drift velocity decides whether the electron temperature is elevated or not via the average kinetic energy. When electron concentration is increased locally, the electron temperature shall decrease due to the increase in the electronic heat capacity. The product of one-third of the divergence of the electron drift velocity and temperature appears on the RHS of Eq. (2.127) as well. It is indecisive to draw any physical meaning on each of these terms alone. The effects of the Joule heating and the work done by the electron pressure are lumped together in those terms.

Attention shall be focused on the last two phonon energy equations. Based on the dispersion relation of phonons, optical phonons have essentially zero group velocity, while acoustic phonons are capable of propagating through the medium (Ziman, 1960). Therefore the optical phonon energy equation (i.e., Eq. (2.128)) does not have the diffusion term. Optical phonons can

generally be viewed as intermediate energy storage between electrons and acoustic phonons. Therefore, the corresponding conservation equation consists of energy exchanges between these heat carriers. Optical phonons gain energy from electrons (both from average electron kinetic energy and thermal energy), as given by the first two terms on the RHS of Eq. (2.128). The last term describes energy exchange with acoustic phonons. The acoustic phonon energy equation is similar to the optical phonon energy equation except that there is a diffusion term that describes diffusion of acoustic phonon energy.

Until now, the electric field term in the momentum equation has not been addressed. The electric field can be obtained by examining the electric potential and the charge distribution in space. The relationship between these quantities is derived from Maxwell's equations. The resultant governing equation is the Poisson equation. Snowden (1988) has provided a detailed discussion on how the Poisson equation is derived from the Maxwell equations, therefore, the same derivation shall not be repeated here. Instead, it will be assumed that the Poisson equation can readily be used, which is expressed as:

$$\nabla^2 V = \frac{e}{\varepsilon_e}\left(n_e - n_+\right),$$
(2.130)

where n_+ is the density of the positive charges in the material, and the electric field is expressed as

$$\vec{E} = -\nabla V .$$
(2.131)

As a result, the entire electron-phonon hydrodynamic equations are given by Eqs. (2.125), (2.126), (2.127), (2.128), (2.129), and (2.130). These equations are to be solved simultaneously in order to predict the electrical and thermal behavior of a system with electrons and phonons as energy carriers.

The momentum equation in the hydrodynamic equations can be further simplified to yield the so-called drift-diffusion approximation. This is where the velocity transient and inertia terms are neglected. The drift velocity vector of electrons can be conveniently expressed as:

$$\vec{v}_{d,e} = -\frac{e\tau_{eff}}{m_e}\vec{E} - \frac{k_B\tau_{eff}}{m_e n_e}\nabla\left(n_e T_e\right),$$
(2.132)

where

$$\tau_{eff} = \left(\frac{1}{\tau_{e-e}} + \frac{\dot{n}_{e,gen}}{n_e} \right)^{-1}. \tag{2.133}$$

Since the electron drift velocity is explicitly given, it can be substituted into the electron continuity equation to yield:

$$\frac{\partial n_e}{\partial t} - \frac{e}{m_e} \nabla \cdot \left(\tau_{eff} n_e \vec{E} \right) - \frac{k_B}{m_e} \nabla \cdot \left(\tau_{eff} \nabla \left(n_e T_e \right) \right) = \dot{n}_{e,gen}, \tag{2.134}$$

where the second term on the left-hand side represents the drift of electrons in and out of the system while the third term includes the gains or losses due to the electron diffusion.

During the course of obtaining these governing equations, a number of assumptions have been made for the sake of simplicity. These assumptions are by no means unique. If one or more of the assumptions are removed, the hydrodynamic model will take a rather different form than the derived one. It will certainly raise the difficulty level of solving the model substantially.

Thermal Transport Phenomena

Macroscopic Thermal Transport

Fourier Heat Conduction
($L \gg l_{mfp}$, $t \gg t_{mfp}$)

Macro-/Microscopic Thermal Transport

Hyperbolic Heat Equation
($L \gg l_{mfp}$, $t \sim t_{mfp}$)

Microscopic Thermal Transport

Two-Temperature Model
($L \gg l_{mfp}$, $t \gg t_{mfp}$)

Dual-Phase Lag Model
($L \gg l_{mfp}$, $t \sim t_{mfp}$)

Micro-/Nano-scale Thermal Transport

Electron Hydrodynamic
Equations ($L \gg l_{mfp}$, $t \gg t_{mfp}$)

Moments of Boltzmann
Equation ($L \sim l_{mfp}$, $t \sim t_{mfp}$)

Phonon/Photon Boltzmann
Equation ($L \sim l_{mfp}$, $t \sim t_{mfp}$)

Nano-scale Thermal Transport

Maxwell's Electromagnetic
Wave Equations ($L \sim \lambda$)

Electron-Beam Monte Carlo
Simulation ($L \sim l_{mfp}$, $t \sim t_{mfp}$)

Electron Boltzmann Equation
($L \sim l_{mfp}$, $t \sim t_{mfp}$)

Molecular Thermal Transport

Molecular Dynamic
Simulation ($L \ll l_{mfp}$, $t \ll t_{mfp}$)

Figure 2.1   The thermal transport phenomena at various scales (ranging from macroscopic levels to molecular levels) and the corresponding thermal transport models are depicted in the flow diagram. Note that this diagram is not unique since there are some other models that may fit one of the categories listed above.

CHAPTER 3
MONTE CARLO METHODS

The Boltzmann transport equation (BTE) for any particle (e.g., electron, phonon, photon, etc) transport is difficult to solve due to the in-scattering nature of the transfer and the involvement of seven or more independent variables. Although there are some analytical/numerical approaches such as the discrete ordinates method and the spherical harmonics approximation that are capable of solving the integro-differential equation such as the BTE, extensive mathematical knowledge and lengthy derivations are required for one to acquire the solution. This is especially true when anisotropic scattering is involved. There is a relatively simple way of solving the BTE that requires the use of one's imagination and a little effort of derivations. The simple way makes use of a statistical approach called the _Monte Carlo method_ (MCM). Although this method can be powerful in accounting for various complicated situations and conditions, it suffers statistical errors, usually requiring large number of statistical ensembles accompanied with a tremendous amount computational time to remedy. Nevertheless, with the improvement of computer speeds each year, the Monte Carlo Method will become more commonly applied in solving the BTE.

In the context of particle transport phenomena, a MCM refers to the simulation of the propagations of energy carriers such as photons and electrons inside a participating medium. This absorbs and scatters the carriers according to the transport equation. It is similar to playing the game of Monopoly$^{(TM)}$. To play the game correctly, one needs uniformly distributed dices, a good set of game rules, and a game board. In a MCM, one needs a uniformly distributed random number generator, correct scattering probabilities, and a grid system for storing the particle histories. At first glance, one often wonders how the randomness of the particle simulation can generate a correct solution to the transport equation. Strictly speaking, the simulation is not truly random in the sense that particles or energy carriers travel according to the scattering probabilities. These are not random because they are derived based on the laws of physics.

Each bundle is comprised of lots of particles. The simulation procedures are as follows: First, a bundle is released in the medium from its initial location. Then according to some probability distribution functions, the path length and the direction of the bundle are determined. As the

bundle moves in the medium, a fraction of its intensity/energy is absorbed or scattered. Eventually, all of its energy is consumed (attenuated) or the bundle reaches the boundary and contributes to either reflection or transmission distribution. Figure 3.1 depicts sample trajectories of two statistical bundles as they propagate through a scattering medium. It is the contribution of many of these statistical bundles that provides the intensity distributions and solution to the governing equation. It is clear that a MCM treats propagating waves as discrete packets of quantum particles. The assumption that the wavelength of the propagating bundle is negligible compared to the characteristic length of the object is always implied. Should this assumption be violated, then the wave nature of particles needs to be considered.

The MCM has lots of different applications in the field of sciences. In this dissertation, the discussions shall be confined to the simulation procedures applicable to electron-beam transport, radiative heat transfer, and heat conduction in terms of electrons and phonons. The simulation procedures for the MCMs in electron-beam transport and radiative heat transfer are almost identical with a few exceptions. When it comes to the electron or phonon thermal conduction inside matters, the simulation becomes cumbersome since all the heat carriers must be accounted for simultaneously, meaning that all the statistical ensembles are launched at the same time, in order to determine the scattering properties in time and space. Such a simulation requires a tremendous amount of computer memory storage and computational time.

This chapter is devoted to basic simulation procedures of the MCMs since they are somewhat similar in the heat transport modes that are encountered in this work. Specific details about the scattering properties for different heat carriers will not included here as they will be discussed in other chapters.

3.1 Cumulative Probability Distribution Function

The basic principle behind a Monte Carlo technique is the *cumulative probability distribution function* (CPDF). A CPDF of a variable is how frequently a given value of that variable occurs within a fixed function. As an example, consider a blackbody energy distribution over the wavelengths for a given temperature of 1000 K. The plot of the spectral emissive power distribution at the temperature is shown in Figure 3.2. The total emissive power of this object can be expressed

as:

$$E = \int_0^\infty E_\lambda d\lambda \qquad (3.1)$$

and the amount of emissive power if the object emits within the spectral range of 0 - λ (e.g., λ = 2 μm), which is the shaded area in the figure, is given as:

$$C_\lambda = \int_0^\lambda E_\lambda d\lambda \qquad (3.2)$$

Therefore, the CPDF of the object which emits at a wavelength smaller than λ can be sampled as

$$R(\lambda) = \frac{C_\lambda}{E} \qquad (3.3)$$

If $R(\lambda)$ is replaced with a random number *Ran*, then the corresponding wavelength λ can be obtained by inverting Eq. (3.3). Therefore,

$$\lambda = \lambda(Ran) \qquad (3.4)$$

When this process is repeated for N times, a histogram for a range of λ drawn can be obtained. Normalizing this function by N and multiplying by E yields the original spectral emissive power function, E_λ, as N approaches infinity.

The above example can be viewed as a statistical means of representing the wavelength of a given object which radiates at a temperature of 1000 K. If only one wavelength is drawn from Eq. (3.4) using a random number, it will not represent the range of wavelengths that the object is supposed to emit. It would require a generous amount of statistical ensembles to truly represent the distribution, and that is the drawback of a statistical approach. Nevertheless, such an approach easily lends itself to solving the particle transport phenomena, which is described by the BTE.

It is already known how intensity or energy suffers attenuations (i.e., scatterings) along a line of sight according to the BTE. Therefore, we can apply the statistical concept to solving the BTE can be applied by simply "chopping" the intensity into a prescribed number of statistical ensem-

51

bles and allowing each to travel in time and across space independently[6] using the "rules" asserted by the BTE and the CPDFs derived from the scattering properties. For example, the intensity form of the BTE for radiative transfer (that is, the RTE) states that intensity should be attenuated exponentially; therefore, the probability of a statistical ensemble being attenuated must increase exponentially following the equation. The CPDFs will then statistically determine the scattering direction or the scattered energy of an ensemble when it encounters scatterings. Similar to the above example for statistically determining the emission spectrum of a blackbody object, the results are meaningful only when a large number of statistical ensembles are traced. What a MCM really offers in this context is a statistical approximation to the solution of the BTE in time, space, energy spectrum, and/or directions. Having known the concept behind the MCMs, all that is needed to do next is to establish a tracking algorithm which simulates the propagations of these statistical ensembles.

3.2 Monte Carlo Simulation for Particle-Beam Transport

Particle-beam transports that shall be referred to in this dissertation are electron- and photon-beam transports. Both of those have been widely used as non-intrusive[7] diagnostic tools. For example, the most commonly used tool to visualize micro- or nano-scale structures is the scanning electron microscope (SEM). This microscope utilizes the reflected electrons from a specimen to construct images of the targets. Although there are some minor differences in comparing electron-beam scatterings to photon-beam scatterings, the basic MC simulation procedures discussed are applicable to both cases. In this chapter, the details of the scattering properties of electrons or photons will not be discussed. It is presumed that they are taken for granted. The derivations of these properties will be given in other chapters.

3.2.1 Grid Preparation

Any space dependent numerical or statistical simulations require preparation of a grid. In any numerical method, physical domains are usually divided into grids to facilitate the discretization

---

[6] It means that the propagation of a statistical ensemble will not interfere that of another, so interference effects are ignored.

[7] Non-intrusive tools mean that the powers of the beams used are not sufficient to cause structural damage to the specimen. Oppositely, the beams in this dissertation serve as intrusive tools to melt and subsequently evaporate the target.

process. In the case of statistical simulations, grids are used to collect histories of the propagating ensembles. In other words, they are used to tally the contributions of each statistical ensemble to various locations in space. These contributions, in a sense, can be regarded as raw data. When proper normalizations are utilized, they are transformed into useful statistical distributions corresponding to the expected physical quantities.

There is a very distinct property of the grid used in the statistical simulation compared to the regular numerical simulation. The size of the grid possesses no effects on the accuracy of the statistical simulated results, but it does have an effect on the resolution of the distributions. The ultimate factors that control the accuracy of the simulation are actually the number of ensembles used and the number of runs performed. When either a coarse grid or a fine grid is used in the simulation, the resultant distribution is always fluctuating around the statistical mean distribution, provided that the number of statistical ensembles used in each case is sufficient. Using more grid points would produce resultant distributions at higher resolution. Unfortunately, it also means more statistical ensembles are required to reduce the statistical noises.

Since the histories of statistical ensembles are tallied within infinitesimal control volumes for the sake of normalizations, it is better to have grid points centered in each control volume instead of using four grid points to form a control volume.

3.2.2 Random Number Generator

Another important requirement for a statistical simulation is a random number generator. A statistical method is like a "rolling dice" method where one randomly draws a number using the dice to decide the outcome. The random number generator needs to have a uniform probability for the range of numbers required, which is typically between 0 and 1. There are a handful of random number generators given in the literature. The details of each one will not be discussed within this work.

The FORTRAN language is used in coding all the algorithms in this dissertation. It has a built-in random number generator, which goes by the syntax, *ran*(*nseed*). This random number generator requires a large odd integer number, denoted as *nseed*, to be initialized. This number will

change automatically after each time the function is called. However, in order to avoid an exact same series of random numbers being drawn, the initial *nseed* used in the algorithm should be different for different runs. One way to overcome this dilemma is to utilize the total number of seconds calculated using year, date and time as the *nseed*, since it would never be the same at any given moment.

3.2.3 Outlines of the Simulation

There are two ways of approaching the simulation procedures. One is using the so-called *continuous slowing-down approach* (CSDA) and the other is the *discrete inelastic scattering* (DIS). Just as the names imply, the former treats inelastic scattering events as a continuous phenomenon where energy change corresponds to the distance traveled while the latter assumes the events discrete at which energy change depends on the type of scattering mechanism. The flowcharts of these two MCMs are available in Figure 3.3 and Figure 3.4.

A MCM simulation starts by setting up the grid system for storing the particle histories. The simulation proceeds with launching an ensemble of particles one after another, until the last number of ensembles is specified. Each ensemble is treated separately demonstrating that there is no interference factor between any two ensembles. The location and direction of launching the ensembles are defined according to the incident particle beam profile. The most common beam profiles used in the simulation are impulse (or point incident beam), flat (or uniform within a specified area), and Gaussian (i.e. exponential decaying). The location of launching the ensembles needs to be sampled from its probability distribution, except in the case of the impulse beam profile.

The distance of interaction is determined next from a random number. The distance of interaction is equivalent to the mean free path of an ensemble. This indicates the distance the ensemble can travel without being scattered. Once the distance of interaction is set, the ensemble is allowed to propagate from its initial position to the next location following its initial direction. The ensemble is then checked for confinement within the defined control volume. If the condition is met, the ensemble is allowed to scatter, otherwise the contribution of the ensemble to either the transmission or the reflection is tallied. A new ensemble of particles would be initiated according

to the incident beam profile and launched from the appropriate location. If the ensemble is still confined within the medium, its weight (or energy) is updated (or attenuated) and its contribution to the absorption is tallied. Following the attenuation, the ensemble is tested for its remaining weight. If the energy of the ensemble becomes less than the tolerance, it is disregarded and a new ensemble is launched. If this is not done, then it suffers an elastic scattering and changes the direction of propagation. The procedures are continually repeated until a new distance of interaction is determined. Once the simulation is done the tallied particle histories are converted to the desired quantities such as the radial or angular reflectance and transmittance.

3.2.4 Incident Beam Profiles

In this section, the normal incident beam profiles are discussed. They are the flat and Gaussian beam profiles. The particle launching location for a flat circular particle beam will first be determined. For a given source with strength of Λ incident to a circular area with a radius of r_0, the beam profile can be written as:

$$B(r) = \begin{cases} \Lambda/\pi r_0^2 & \forall \; \mathrm{r} \leq r_0 \,, \\ 0 & \forall \; \mathrm{r} > r_0 \,. \end{cases} \tag{3.5}$$

Note that if steady-state simulation is desirable then Λ can be the power of the beam. otherwise Λ would be amount of energy transferred as a function of time. The strength of the beam is not important in determining the launching of the particles. To obtain the CPDF of this beam profile, the principle discussed in Section 3.1 is applied and the following equation is obtained:

$$R(r) = \frac{1}{\Lambda} \int_0^r B(r') 2\pi r' dr' = \left(\frac{r}{r_0}\right)^2. \tag{3.6}$$

Introducing a random number, Ran_r, the radius of launching particles for a flat incident beam profile is given as:

$$r = r_0 \sqrt{Ran_r} \,. \tag{3.7}$$

Translating this into the Cartesian coordinate obtains the following:

$$x = r_0 \sqrt{Ran_r} \, cos(2\pi Ran_{r1}), \tag{3.8}$$
$$y = r_0 \sqrt{Ran_r} \, sin(2\pi Ran_{r1}), \tag{3.9}$$

where Ran_{r1} is a second random number.

For a Gaussian beam profile with a $1/e^2$ radius of r_0, one can write:

$$B(r) = \frac{2}{\pi r_0^2} exp\left[-2\left(\frac{r}{r_0}\right)^2\right]. \tag{3.10}$$

Using the similar procedure as in the flat incident beam case, the radius for launching particles can be written as:

$$r = r_0\sqrt{-ln(1-Ran_r)/2}, \tag{3.11}$$

and therefore the following is obtained in Cartesian coordinate:

$$x = r_0\sqrt{-ln(1-Ran_r)/2}\, cos(2\pi Ran_{r1}), \tag{3.12}$$

$$y = r_0\sqrt{-ln(1-Ran_r)/2}\, sin(2\pi Ran_{r1}). \tag{3.13}$$

3.2.5 Direction of Propagation

In a MCM simulation, there are fixed and moving frames of coordinates. The fixed frame of coordinate is simply the coordinate system that is used to define the grid or the geometry. As the name implies, it is stationary and serves as the reference for the moving coordinate frame. The moving frame of the coordinate is based on the direction of the propagation of the ensemble. It is defined such a way that the direction of propagation coincides with the z'-axis[8] of the moving frame where the scattering polar angle is measured from this axis.

The direction cosines of the scattered ensemble must be calculated from the incident ones. It is easy for the isotropically scattering media since the probability of the isotropically-scattered photons is equal in all directions. Immediately after each scattering event, the direction cosines of the scattered particles are given as:

$$\mu'_x = cos\,\varphi\,sin\,\Theta, \tag{3.14}$$

$$\mu'_y = sin\,\varphi\,sin\,\Theta, \tag{3.15}$$

$$\mu'_z = cos\,\Theta, \tag{3.16}$$

where μ'_x, μ'_y, and μ'_z are the scattered direction cosines in x-, y-, and z-directions, respectively.

---

[8] An orthogonal coordinate system (i.e., $x'y'z'$) is used for defining the moving frame.

For the anisotropic case, the scattered direction cosines can be expressed in terms of the incident direction cosines (μ_x, μ_y, μ_z) and the scattering angles (Θ, φ):

$$\mu_x' = \frac{sin\,\Theta}{\sqrt{1-\mu_z^2}}\left(\mu_x\mu_z\,cos\,\varphi - \mu_y\,sin\,\varphi\right) + \mu_x\,cos\,\Theta\,, \tag{3.17}$$

$$\mu_y' = \frac{sin\,\Theta}{\sqrt{1-\mu_z^2}}\left(\mu_y\mu_z\,cos\,\varphi + \mu_x\,sin\,\varphi\right) + \mu_y\,cos\,\Theta\,, \tag{3.18}$$

$$\mu_z' = -\,sin\,\Theta\,cos\,\varphi\sqrt{1-\mu_z^2} + \mu_z\,cos\,\Theta\,. \tag{3.19}$$

3.2.6 Distance of Interaction

The distance of interaction, which is the path length that a bundle can travel without suffering any attenuation by the medium, can be derived from the intensity form of the BTE. The typical intensity form of the BTE follows that given in Section 2.4. Since this research is interested in the distance of interaction, the transient term can be neglected. In addition, the in-scattering terms are not required, because the tracing of many ensembles in various directions in space is being done and the in-scattering nature of the transport is automatically built-in in the simulation. When these terms in the equation are dropped, the intensity form of the BTE becomes:

$$\frac{dI}{ds} = -\frac{I}{\lambda}, \tag{3.20}$$

where λ is the mean free path and s is the propagation axis. The solution to this equation can be expressed as:

$$I = I_0\,exp\left(-S/\lambda\right), \tag{3.21}$$

where $I = I_0$ at $s = 0$ is taken as the initial condition. According to this solution, the intensity is supposed to decrease exponentially along the path of propagation. Note that the exponential term in the above equation is actually the CPDF for the distance of interaction, ranging from 0 for $S = \infty$ to 1 for $S = 0$, thus the CPDF is:

$$R(S) = exp\left(-S/\lambda\right). \tag{3.22}$$

Continuous Slowing-Down Approach

In the CSDA, the distance of interaction that one needs is the elastic one. The argument behind

57

this hypothesis is that the particle continuously loses energy as it propagates. This means that the inelastic scatterings are included in this way. Consequently, the distance of interaction for inelastic scattering is not required. The CPDF for an elastic scattering can be expressed using Eq. (3.22) as:

$$R(S_{el}) = exp(-S_{el} / \lambda_{el}), \tag{3.23}$$

where λ_{el} is the elastic mean free path. Therefore, the distance of interaction is obtained when $R(S_{el})$ is replaced with a random number Ran_S, which yields:

$$S_{el} = -\lambda_{el} \, ln(Ran_S). \tag{3.24}$$

Discrete Inelastic Scatterings

The DIS treats inelastic scattering events as discrete. This means that energy loss of a particle ensemble occurs at a determined interacting location. This is similar to that of an elastic scattering event. When this method is employed, the CPDF of both elastic and inelastic scatterings can be incorporated into a single equation, which is given as:

$$R(S_{eff}) = exp(-S_{eff} / \lambda_{eff}), \tag{3.25}$$

where λ_{eff} is the effective mean free path computed from both elastic and inelastic mean free path (i.e., λ_{el} and λ_{inel}, respectively):

$$\lambda_{eff}^{-1} = \lambda_{el}^{-1} + \lambda_{inel}^{-1}. \tag{3.26}$$

Therefore, the distance of interaction is given as:

$$S_{eff} = -\lambda_{eff} \, ln(Ran_S). \tag{3.27}$$

This is the distance a particle can travel before the elastic or inelastic scattering event occurs.

3.2.7 Attenuation of Energy

Continuous Slowing-Down Approach

The CSDA assumes that energy is absorbed continuously along the path of propagation. The

amount of absorption depends on the distance traveled by the particles. The larger the distance means more absorption. Such an approach ignores the specific details of the inelastic scattering mechanisms, which greatly simplifies the complexity of the problem. However, one needs to distribute the attenuated energy evenly along the propagation path in this approach. This means that the coordinates of various locations along the path traveled must be calculated in order to enable the operation if the absorption profile is desired.

One important quantity that is required to incorporate this effect into the MC simulation is the amount of energy absorbed per unit distance. For the electron-beam transport, it is quantified as *dE/dS*, which is the change of energy per unit change in distance (see Section 4.3). Except for photons, it is given in terms of the fraction of energy absorbed, and the fraction is expressed as:

$$1 - exp\left(-\kappa S_{el}\right),\tag{3.28}$$

where κ is the absorption coefficient.

Discrete Inelastic Scatterings

In this approach, elastic and inelastic scattering events are discrete, and the distance of interaction is given by Eq. (3.27). Upon interaction, a random number will decide an elastic or inelastic scattering event based upon the following equation. The electron will be scattered elastically if:

$$Ran_\lambda < \frac{\lambda_{el}^{-1}}{\lambda_{eff}^{-1}}.\tag{3.29}$$

Note that in radiative transfer, the above ratio is actually the scattering albedo, this is usually denoted as ω. If an inelastic scattering event occurs for photons, then the entire ensemble is assumed to be absorbed by the medium. Except for electrons, the amount of kinetic energy loss needs to be determined from the probability of inelastic scattering per unit length and energy change (i.e., $d\lambda_{inel}^{-1}/d\left(\Delta E'\right)$). The CPDF for the amount of energy change is then expressed using this probability as:

$$R = \int_0^{\Delta E} \frac{d\lambda_{inel}^{-1}}{d\left(\Delta E'\right)} d\left(\Delta E'\right) \bigg/ \int_0^{E-E_F} \frac{d\lambda_{inel}^{-1}}{d\left(\Delta E'\right)} d\left(\Delta E'\right).\tag{3.30}$$

59

In the limits of the integration, the possible amount of kinetic energy loss of electrons ranges from none to the difference between the current kinetic energy E and the Fermi energy E_F of the target material.

3.3 Monte Carlo Simulation for Electron or Phonon Conduction

The transport phenomena inside matter, for instance, electron or phonon propagation due to thermal gradients or external electric field are discussed in this section. The MC simulations of this sort are usually considered to be more difficult and time-consuming when compared to the particle-beam transports. This is because the nature of the transport involves non-thermal equilibrium phenomena and requires simulations of all the heat carriers simultaneously. The reason all the heat carriers need to be simulated at once is because the thermal condition of the materials depends upon these carriers. Depending on where these heat carriers are populated, some spatial spots on the simulation domain may be hotter than others. This governs the scattering rates of the heat carriers. As shown, the propagation of one heat carrier affects[9] another through determination of the scattering rates. A schematic of the activities of these heat carriers inside the matter is given in Figure 3.5. The concept behind this type of simulation is the initializing of the heat carriers or the statistical ensembles at each control volume inside the medium and then launching all of them at once from their various locations. If the boundary of the domain is heated to a certain temperature, then additional heat carriers are injected from the boundary according to the probability distribution function. Depending upon the type of boundary any heat carrier that encounters the boundary may be absorbed or reflected. For a fixed-temperature boundary, the heat carriers that cross the boundary are terminated (or absorbed); for an insulated boundary, it will be reflected.

3.3.1 Grid Setup

The grid setup in this case is similar to that discussed in Section 3.2.1. In this case, the heat carriers are initialized within each control volume instead of originating from outside the medium. The medium is divided into numbers of infinitesimal control volumes or elements.

---

[9] It does not mean that wave interferences are present in the simulation. Remember that the particle transport theory always neglects the wave interference phenomena. These heat carriers are still independent from each other as far as the propagations in time and in space are concerned.

3.3.2 Initial Particle Distributions

Given a grid element or an infinitesimal control volume with volume V_{CV}, the actual total number of conduction electrons contained inside at a specified temperature T_{CV} under equilibrium can be found according to the following expression:

$$N_{e,CV}^{actual}\left(T_{CV}\right)=V_{CV}\int_{E_F}^{\infty} f^{eq}\left(E,T_{CV}\right)D\left(E\right)dE \tag{3.31}$$

or

$$N_{e,CV}^{actual}\left(T_{CV}\right)=V_{CV}\sum_{i} f^{eq}\left(E_{i},T_{CV}\right)D\left(E_{i}\right)\Delta E \tag{3.32}$$

Since during the simulation, it is often impossible to track that many electrons, a scaling factor is established for each statistical ensemble:

$$W\left(T_{CV}\right)=\frac{N_{e,CV}^{actual}\left(T_{CV}\right)}{N_{e}^{stati}} \tag{3.33}$$

Each infinitesimal control volume or element is initialized with a total of N_e $(= E_e^{stati})$ number of conduction electrons. The electrons have energies distributed according to the Fermi-Dirac statistics where $E \geq E_F$ and T_e is given. The Fermi-Dirac statistics are first approximated by a finite number of columns N_E with a width of ΔE starting from the Fermi energy:

$$N_E = \frac{E_b - E_F}{\Delta E} \tag{3.34}$$

$$E_i = E_F + \left(i+0.5\right)\Delta E, \ i=0, 1, \ ..., N_E - 1 \tag{3.35}$$

N_e should be equal to the area under the curve, therefore each interval will have a number of electrons given by

$$N_{e,i} = \frac{f_i\Delta E}{\Delta E \sum_{j=0}^{N_E-1} f_j} = \frac{f_i}{\sum_{j=0}^{N_E-1} f_j} N_e, \ i=0, 1, \ ..., N_E - 1 \tag{3.36}$$

3.3.3 Launching of Electrons

Electrons of each energy interval in each control volume are launched equally into all directions. This is done by using the isotropic scattering phase function. (Note: sufficient amount electrons in each control volume need to be initialized so that all the neighboring elements when

launched will have a "taste" of the energy spectrum of the current launching control volume.) The isotropic scattering sampling is given as:

$$\Theta = cos^{-1}\left(1 - 2Ran_\Theta\right) \tag{3.37}$$

$$\varphi = 2\pi Ran_\varphi \tag{3.38}$$

Depending upon the energy of an electron, its speed varies according to:

$$v(E) = \sqrt{\frac{2E}{m^*}} \tag{3.39}$$

Electrons are set to travel within a pre-described time interval, namely Δt. Therefore, each electron move from one location to another by following:

$$\vec{r}' = \vec{r} + \left[v(E)\Delta t\right]\hat{s} \tag{3.40}$$

3.3.4 Non-equilibrium Fermi-Dirac Distribution

Throughout the simulation, what is actually known is the number of electrons in each control volume and their associated energies. After each time interval Δt, the non-equilibrium electron distribution must be calculated in order to correctly predict the scattering rates and the Pauli's exclusion principle. To do so, we tally the energy in each level is tallied by:

$$E_{i,total} = E_i \sum_{j=1}^{N_{e,i}} W_j \tag{3.41}$$

This should be given as:

$$V_{CV} f_i^{non-eq} E_i D(E_i) \Delta E = E_{i,total} = E_i \sum_{j=1}^{N_{e,i}} W_j \tag{3.42}$$

Therefore,

$$f_i^{non-eq}(T_{CV}, E_i) = \frac{\sum_{j=1}^{N_{e,i}} W_j}{V_{CV} D(E_i) \Delta E} \tag{3.43}$$

Note that the following expression determines if f_i is fully occupied:

$$\sum_{j=1}^{N_{e,i}} W_j \leq V_{CV} D(E_i) \Delta E \tag{3.44}$$

3.3.5 Pseudo-Temperature Calculation

Somehow, the temperature in each control volume needs to be determined, in order to have a better indication of what the temperature would be if equilibrium is achieved. One way to do this is to use the equilibrium Fermi-Dirac statistics and account for the total electron energy inside the control volume. To determine the pseudo-temperature, we first compute the total energy per unit volume must be computed from the non-equilibrium distribution (Note: $D(E)$ has unit of $[1/m^3\text{-eV}]$). In order to have the identical total energy per unit volume, it is necessary to have:

$$\Delta E \sum_{i=0}^{\infty} E_i f_i^{eq}(E_i) D_i(E_i) = \frac{E_{i,total}}{V_{element}} \tag{3.45}$$

Using the Fermi-Dirac statistics, the equation becomes:

$$\int_{E_F}^{\infty} \frac{ED(E)}{\left[1 + exp\left(\dfrac{E - E_F}{k_B T_{element}^{eq}}\right)\right]} dE = \frac{E_{total}}{V_{element}} \tag{3.46}$$

To determine the temperature, the following equation must be considered:

$$F\left(T_{element}^{eq}\right) = \int_{E_F}^{\infty} \frac{ED(E)}{\left[1 + exp\left(\dfrac{E - E_F}{k_B T_{element}^{eq}}\right)\right]} dE - \frac{E_{total}}{V_{element}} = 0 \tag{3.47}$$

One way to solve the above equation is via the *method of false position* (Wong, 2001). Assuming that both electrons and phonons always have the identical "temperature" the phonon distribution in computing the electron scattering rates will be evaluated at this pseudo-temperature.

3.3.6 Scattering Rates

After traveling for a time interval of Δt, the scattering rates for electrons in each energy level are computed. Since scattering rates depend upon the distribution of electrons in various energy levels, therefore $(1-f_i^{non-eq})$ should be calculated for each energy level in each control volume.

3.3.7 Probability of Scattering

The scattering rate $P(E)$ indicate the frequency of collisions within a unit time for a given energy of E. Therefore, the mean free time τ for a particle (i.e. the free flight time without suffering any collisions) is the inverse of $P(E)$. Accordingly, the cumulative probability distribution func-

tion (CPDF) of the particle for not suffering any collision after time t is given as:

$$R(t) = exp(-t/\tau). \tag{3.48}$$

By replacing $R(t)$ with a random number Ran, the free flight time for the particle corresponds to the following expression:

$$\frac{t}{\tau} = -ln(Ran). \tag{3.49}$$

Note that τ is usually a function of temperature, location, and energy of the particle. Consequently, τ varies along the path that the particle travels. In order to account for the variation of properties of the medium along the path of propagation, the following must be considered:

$$\sum_i \frac{\Delta t}{\tau_i} = -ln(Ran), \tag{3.50}$$

instead of Eq. (3.49). The summation in the above equation is taken over the particle path in the direction of the propagation where $(v \cdot \Delta t)$ is a sub-distance of the entire length $(v \cdot t)$ that the particle is supposed to travel. The direction of the propagating particle remains unaltered unless the following condition is violated:

$$\sum_i \frac{\Delta t}{\tau_i} \leq -ln(Ran). \tag{3.51}$$

3.3.8 Isothermal Boundaries

Electrons that hit an isothermal boundary will be thermalized. To account for the thermalization of electrons, the "identity" of an electron is simply deleted (i.e. its energy upon impact is replaced). The electron will then be re-launched isotropically and its energy is sampled from the Fermi-Dirac statistics at the temperature of the boundary.

$$R(E) = \frac{\int_{E_F}^{E} f(E', T_b) dE'}{\int_{E_F}^{\infty} f(E', T_b) dE'} \tag{3.52}$$

Replacing $R(E)$ by a random number Ran_E, and inverting the equation to obtain E, leads to the energy that the electron should have after re-launching. Note that when the ensemble is re-

launched, it now will have different number of electrons, meaning that W_j for this electron is based on the T_b.

$$N_{e,CV}^{actual}(T_{CV}) = A \cdot \Delta t \int_{E_F}^{\infty} f^{eq}(E, T_{CV})[\vec{v}(E) \cdot \vec{n}]D(E)dE \tag{3.53}$$

or

$$N_{e,CV}^{actual}(T_{CV}) = A \cdot \Delta t \sum_i f^{eq}(E_i, T_{CV})v(E_i)D(E_i)\Delta E \tag{3.54}$$

During the simulation, it is often impossible to track that many electrons, therefore a scaling factor is established for each statistical ensemble:

$$W(T_{CV}) = \frac{N_{e,CV}^{actual}(T_{CV})}{N_e^{stati}} \tag{3.55}$$

3.4 Normalization of the Statistical Results

Whenever a Monte Carlo simulation is performed, histories of the simulated statistical ensembles are obtained. This shall be referred to as the raw data since they do not contain any physical meanings. For instance, when a simulation of energy-beam propagation is performed with 1,000 statistical ensembles, 100 numbers of them are deposited on a particular location in the medium. If another simulation with 10,000 statistical ensembles is carried out for the same structure, one finds that the number of ensembles deposited on the same spot increases to 1,000. This does not imply that the second simulation predicts that the deposition amount in terms of energy is more than in the first case. To compare the two, one needs to normalize the detected deposition with respect to the total number of statistical ensembles used. Therefore, the normalizations of raw data are required in order to deduce the physical quantities.
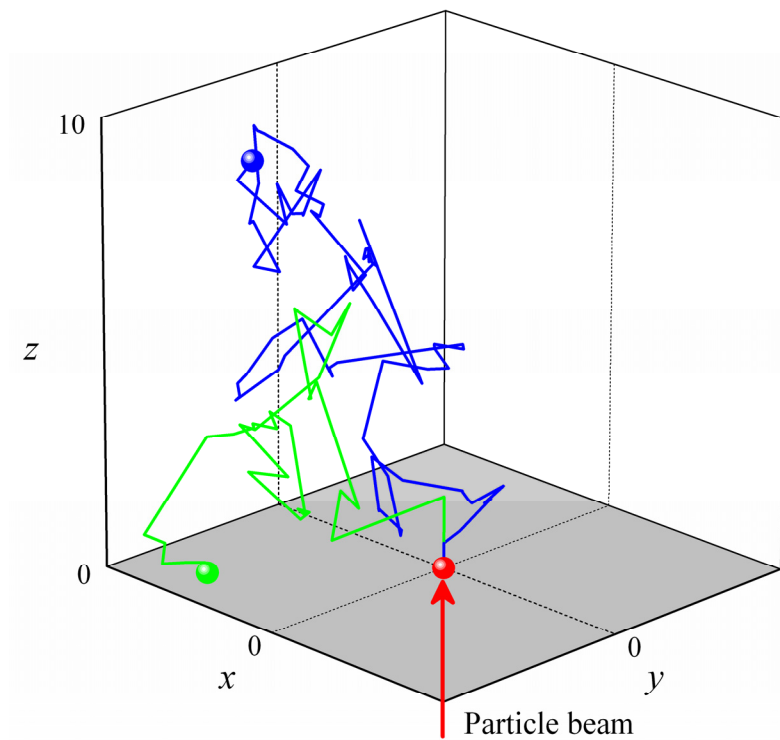
Figure 3.1   The zigzag trajectories of two particles in three dimensions generated using a Monte Carlo simulation are shown. The z-dimension of the medium is set to be 10 units while x- and y-dimensions are infinite in extent.
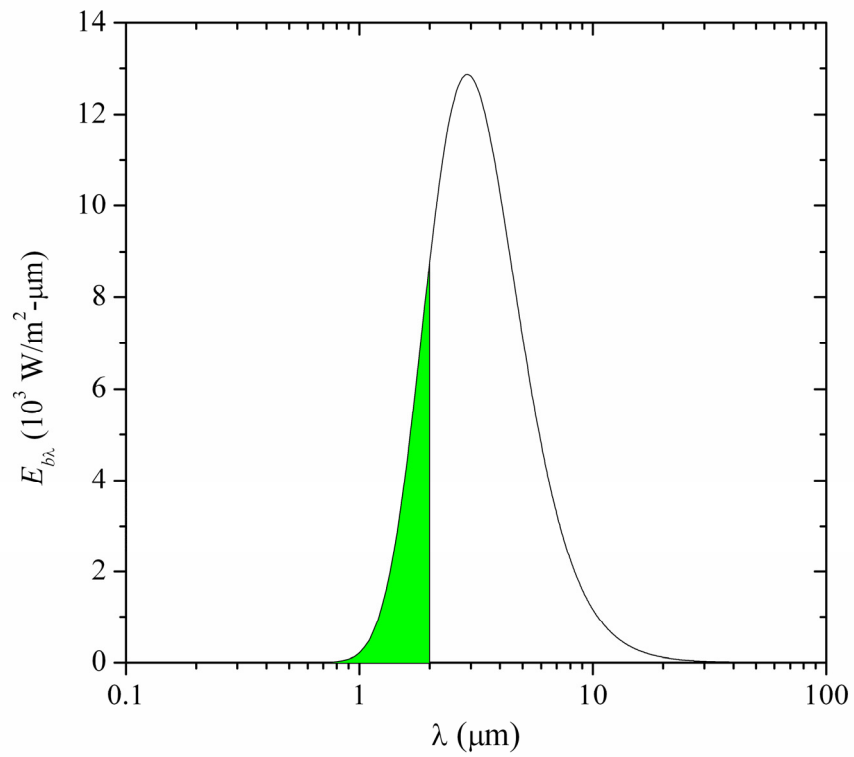
Figure 3.2   The blackbody emissive power as a function of wavelengths at a temperature of T=1000 K is plotted.
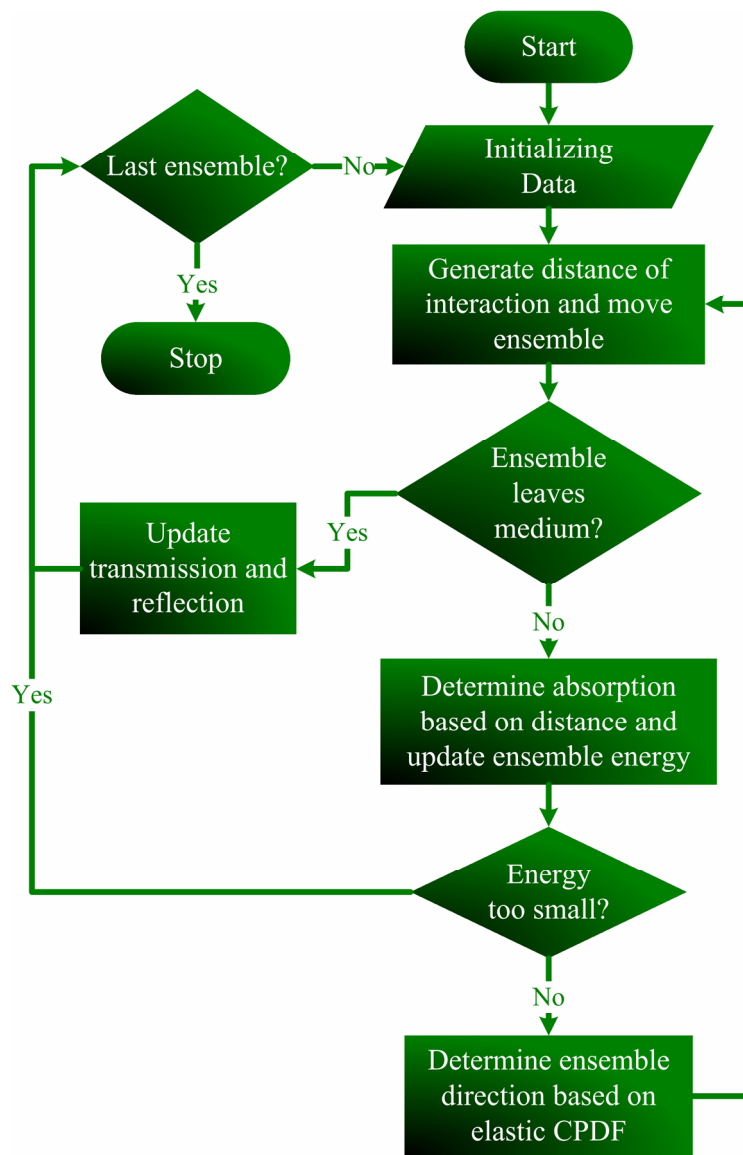
Figure 3.3   The flow diagram for the Monte Carlo simulation using the continuous slowing-down approach (CSDA) is depicted.
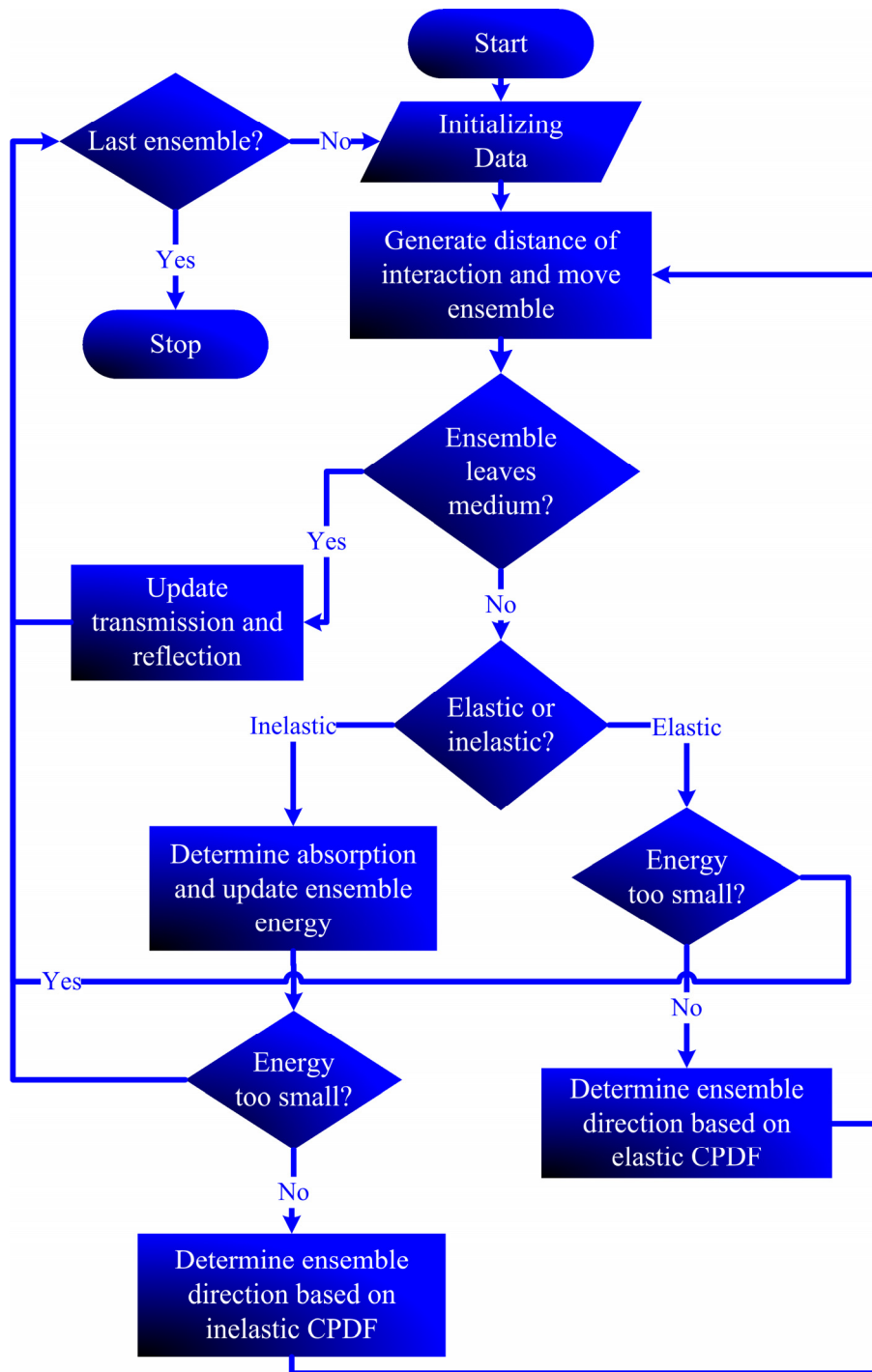
Figure 3.4   The flow diagram for the Monte Carlo simulation using the discrete inelastic scattering (DIS) is depicted.

69
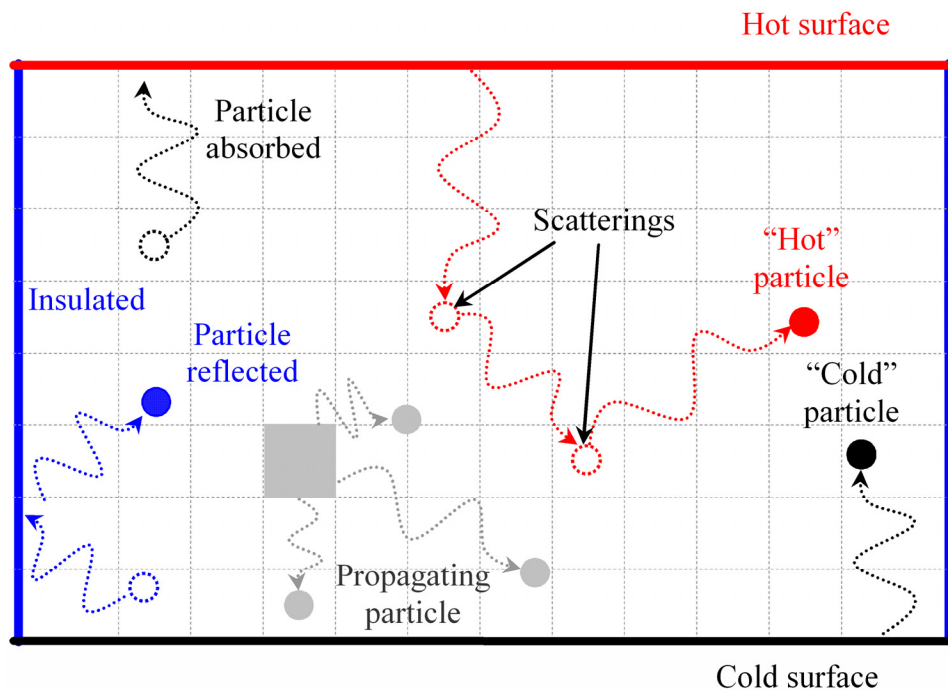
Figure 3.5   The schematic of propagations of particles between two plane-parallel surfaces with one being hot and the other cold. Particles inside the medium are propagating freely and encountering boundaries, and subsequently suffering thermalization or condensation. The "hot" and "cold" particles are propagating and intermixing through scatterings until thermal equilibrium is reached where the rate of generating "hot" particles is equal to that of "cold" particles. Note that "hot" particles refer to particles with higher energies when compared to its surroundings, while "cold" particles are the opposite.
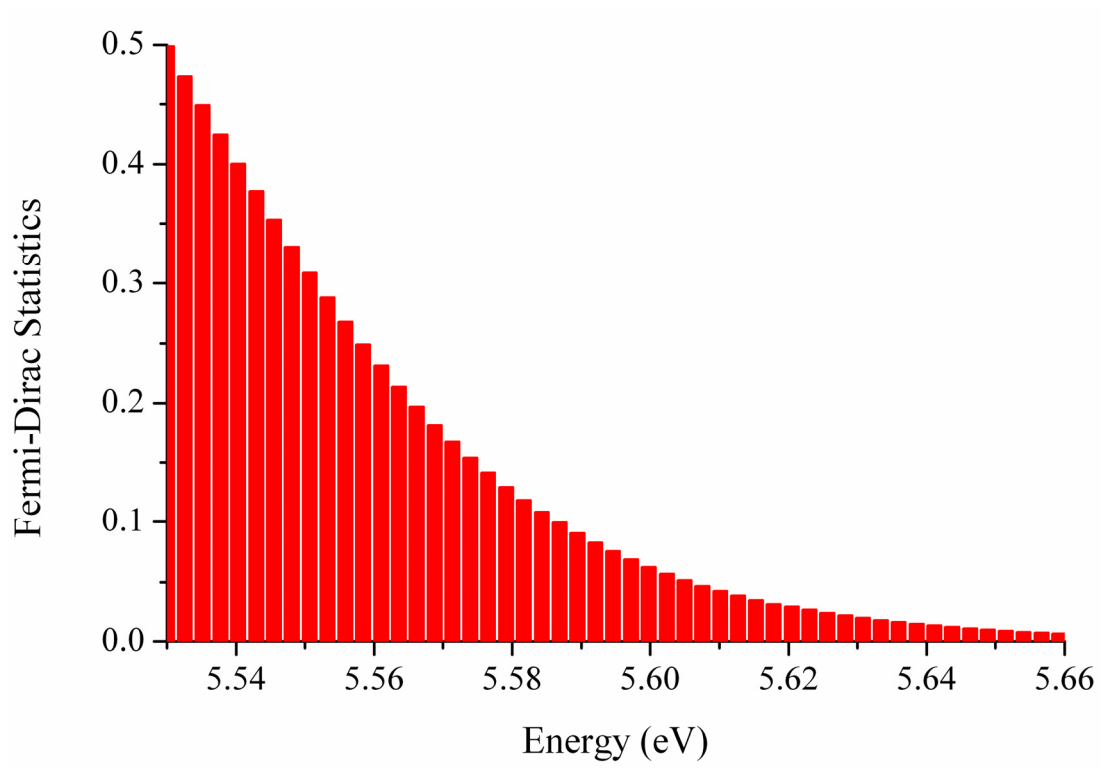
Figure 3.6   Fermi-Dirac statistics for gold at a specified temperature

CHAPTER 4
ELECTRON-BEAM TRANSPORT

In the context of the electron transport inside solids, analytical solutions are virtually impossible to obtain due to the complicated electronic band structures and the scattering probabilities. With the introduction of MCMs, realistic simulations of propagating electrons are therefore easily carried out to better understand the electron transport in such systems. Indeed, electron beam scattering phenomena inside solids have been routinely analyzed via MCMs, leading to high resolution recognition and visualization of nanostructures as done by scanning electron microscopy (SEM), transmission electron microscopy (TEM), and electron energy loss spectroscopy (EELS).

Unfortunately, solving the EBTE is unduly complicated due to the in-scattering nature of the equation. The intensity is to be integrated in the in-scattering term. The integration cannot be easily performed if the intensity is not known. To this end, researchers have been using Monte Carlo simulation to obtain a statistical solution to the EBTE. The drawback to using the Monte Carlo simulation is that it requires a relatively large amount of ensembles to reduce the statistical noise to a desired minimum level. This means that the computational time for the simulation is very long. Although the MC simulation has its weakness, its flexibility in dealing with complex geometries and physics often justifies the end results.

Since the basics of the simulation procedures of a MC simulation for a particle beam have been discussed in Chapter 3. The various scattering mechanisms of the electron inside a participating medium will now be discussed. This will be followed by an overview of the entire simulation steps and the results of the various simulation cases.

4.1 Various Scattering Mechanisms

The interactions between a propagating electron and the matter are very complex. When electrons with high kinetic energy are impinged on a target material, they undergo various transition processes, which are often termed scatterings. These incident electrons are called the primary

electrons. Scatterings are divided into two main types. One is the elastic scattering while the other is the inelastic scattering. The elastic scattering means the alteration of the electron propagating direction without changing its energy. The inelastic scattering refers to changes in both the energy and direction of the electron. However, the deflection caused by the latter case is usually small and negligible compared to the former case.

The elastic scattering of electrons is caused by the positively-charged nuclei of atoms. Unlike elastic scattering, there are a number of distinct modes of inelastic scattering of electrons that exist. The most common ones, which occur in all sort of matters, are: a) excitation of outer-shell electrons or conduction electrons, b) ionization of inner-shell electrons, c) generation of plasmons, d) phonon emission, and e) x-ray emission. The x-ray emission typically occurs when the electron energy is more than tens of kilo-electronvolts. In insulators and semiconductors, the energetic electrons can also lose energy by generating excitons. A schematic of the scattering mechanisms occurring for a penetrating energetic electron inside a material is depicted in Figure 4.1. Next, these scattering mechanisms shall be examined one after another, starting from the elastic scattering.

4.2 Elastic Scattering by an Atom

In the EBTE derivation, it is acknowledged that electrons can be scattered elastically and inelastically. In this section, the elastic scattering of an electron is discussed. Elastic scattering refers to deflections of electrons by positively-charged atoms where the atomic potential is screened by the coulomb cloud (or orbiting electrons). Although the direction of propagation of the electron is altered, the electron maintains its kinetic energy. There are two models available in describing this phenomenon. One is the Rutherford scattering model and the other is the Mott scattering model. The Mott model is usually preferred since it is valid at low electron energy compared to the Rutherford model. However, one can obtain an explicit expression for the electron scattering phase function in the latter model, which simplifies the simulation.

The elastic scattering of electrons is usually characterized by the differential elastic scattering cross section. This is defined as the flux of electrons scattered around an infinitesimal solid angle in a given direction with respect to the total incident electron flux. It is a directional and energy

dependent quantity. The scattering direction is always measured from the center core of the scatterer. When the differential cross section is normalized by its total cross section, the scattering phase function is obtained. In other words, one can view the differential cross section as the probability of an incident electron ensemble being scattered in a given direction. The differential elastic scattering cross section of electrons is typically determined by examining the interaction between the incoming wave function of an electron ensemble and the scatterer. This case involves the atom with a known potential. Similar to most of the scattering phenomena for other quantum particles, the elastic scattering theory for electrons is established based on the assumption that the scattered wave function is a large distance away from the scatterer. This is where the atomic potential vanishes. Such an assumption renders oneself the fact that the scattered wave function can be defined explicitly using a spherical wave.

The lengthy mathematical derivations of the differential elastic scattering cross section for electrons are available elsewhere (Kessler, 1976; Joy, 1995; Dapor, 2003), so it will not be repeated in this context. There are two distinct formulations for elastic scattering of electrons by an atom. The first is the relatively simple model based upon the first Born approximation where the electron spin and polarization are neglected. This results in the Rutherford scattering cross section. The second formulation involves using the relativistic partial wave expansion accounting for the spin and polarization of electrons. The latter case is often referred to as the Mott scattering cross section. The Rutherford cross section works accurately for incident electrons with high kinetic energy because the first Born approximation is a high-energy approximation where the scattering is assumed weak and the scattered wave function has the similar form as the incident one. A typical criterion for using this model is (Dapor, 2003):

$$E \gg \frac{e^2}{2a_0} Z^2 , \qquad (4.1)$$

where E is the kinetic energy of the incident electron, e the electron charge, a_0 the Bohr radius, and Z the atomic number of the target. The Rutherford model is best used in describing the elastic scattering in gold for $E > 85$ keV. Unlike the Rutherford model, the Mott cross section is applicable for both low and high energy scattering. However, since both models assume that the effect of the vibrational motion of the atom on the kinetic energy of the electron is negligible, the Mott model should fail when the electron energy falls within the range of the vibrational energy

of the atom, which is typically less than 10 eV.

4.2.1 Rutherford Cross Section

The differential elastic scattering cross section of the electron by a central potential without considering the spin of the electron and the polarization effect is given as (Egerton, 1996; Dapor, 2003):

$$\frac{dC_e^{el}}{d\Omega} = \left|f(\Theta)\right|^2 ,$$ (4.2)

where C denotes the scattering cross section, Ω the solid angle, and f the scattering amplitude. The scattering amplitude f can be expressed as (Dapor, 2003):

$$f(\Theta) = -\frac{2m}{\hbar^2 q}\int_0^\infty \sin(qr)V(r)r\,dr .$$ (4.3)

The variable q in the above expression refers to the difference between the wave vectors of the electron before and after scattering while $V(r)$ is the potential of the atom as a function of radius r. A Wentzel-like potential is given as:

$$V(r) = -\frac{Ze^2}{r}exp\left(-\frac{r}{a}\right),$$ (4.4)

it can be shown that the differential cross section is expressed as:

$$\frac{dC_e^{el}(\Theta,E)}{d\Omega} = \frac{Z^2 e^4}{4E^2}\frac{1}{(1-\cos\Theta+\alpha_1)^2} ,$$ (4.5)

with the screening parameter defined as:

$$\alpha_1 = \frac{me^4}{4\hbar^2}\frac{Z^{2/3}}{E} .$$ (4.6)

The above cross section is the famous Rutherford cross section where it is explicitly expressed in terms of the atomic number, electron energy, and scattering angle. The differential scattering cross section can be converted into the so-called scattering phase function, which defines the probability of scattering in a given direction per unit solid angle. This is done by normalizing it with the total scattering cross section. Therefore, the phase function Φ_e for the elastic electron scattering can be written as:

$$\Phi_e(\Theta, E) = \frac{4\pi}{C_{e,total}^{el}(E)} \frac{dC_e^{el}(\Theta, E)}{d\Omega}, \tag{4.7}$$

where

$$C_{e,total}^{el}(E) = \int_{\Omega=4\pi} \frac{dC_e^{el}(\Theta, E)}{d\Omega} d\Omega. \tag{4.8}$$

The phase function above is such that the following normalization holds:

$$\frac{1}{4\pi} \int_{\Omega=4\pi} \Phi_e d\Omega = 1. \tag{4.9}$$

For the differential elastic cross section given by Eq. (4.5), the total elastic cross section is determined to be:

$$C_{e,total}^{el}(E) = \frac{\pi Z^2 e^4}{E^2} \frac{1}{\alpha_1(2+\alpha_1)}. \tag{4.10}$$

Thus, the corresponding phase function is expressed as:

$$\Phi_e(\Theta, E) = \frac{\alpha_1(2+\alpha_1)}{(1-\cos\Theta+\alpha_1)^2}. \tag{4.11}$$

Another form of the Rutherford differential cross section can be expressed as (Reimer and Krefting, 1976; Joy, 1995):

$$\frac{dC_e^{el}(\Theta, E)}{d\Omega} = \frac{Z^2 e^4}{4E^2} \left(\frac{E+511}{E+1024}\right)^2 \left(sin^2\left(\frac{\Theta}{2}\right)+\alpha_2\right)^{-2}, \tag{4.12}$$

where the screening parameter is now given as:

$$\alpha_2 = \frac{me^4}{8\hbar^2} \frac{Z^{2/3}}{E}. \tag{4.13}$$

The total elastic cross section in this case is given as:

$$C_{e,total}^{el}(E) = \frac{Z^2 e^4}{4E^2} \frac{4\pi}{\alpha_2(1+\alpha_2)} \left(\frac{E+511}{E+1024}\right)^2. \tag{4.14}$$

The phase function is then expressed as:

$$\Phi_e(\Theta, E) = \frac{\alpha_2(1+\alpha_2)}{\left(sin^2\left(\frac{\Theta}{2}\right)+\alpha_2\right)^2}. \tag{4.15}$$

It is easily shown that this phase function is exactly the same as that given by Eq. (4.11), although the differential scattering cross sections have some minor differences.

The phase functions of gold as a function of scattering angle at various incident electron energies based on the Rutherford formulation are plotted in Figure 4.2. Here, the reference axis for the angles is the direction of propagation, meaning that the zero-degree angle refers to the direction of propagation. Notice that the elastic scattering profile becomes highly forward when the electron energy is increased. This implies that the angular deflection of the electron by an atom decreases in this case. However, when the electron energy is low, elastic scattering is more evenly distributed between the forward[10] and backward directions. Figure 4.3 shows the elastic scattering phase function for different materials, namely copper, silver, and gold, with increasing atomic numbers in the given order. For a material with a higher atomic number, backward scattering can be more pronounced when compared to another material with a lower atomic number.

Another quantity that can be derived from the differential elastic scattering cross section is the elastic mean free path. This describes the separation distance between two successive elastic scattering events. Since the total elastic scattering cross section refers to the effective scattering area for electrons by an atom, the mean free path can be obtained by taking the inverse of the product of the elastic scattering cross section and the number of atoms per unit volume. It can be written as:

$$\lambda_e^{el}(E) = \frac{A}{N_a \rho C_{e,total}^{el}(E)}, \qquad (4.16)$$

where A is the atomic weight, N_a the Avogadro number, ρ the density of the material, and $(N_a\rho/A)$ the number of atoms per unit volume. Note that the elastic scattering coefficient is the inverse of the elastic mean free path as similar to Eq. (2.23). The elastic mean free path derived from the two different forms of the Rutherford scattering cross section is plotted in Figure 4.4. The elastic mean free path is a function of the electron energy for different materials. Both models yield the same mean free path profiles for different materials at low electron energies, yet they deviate from each other when the electron energy is high (i.e., $E > 50$ keV).

The Rutherford scattering phase function shall be re-visited later in this chapter when the Monte Carlo simulation of the electron-beam transport is discussed. The derivations of the Mott scattering phase functions will be shown next.

4.2.2 Mott Cross Section

The Rutherford scattering phase function offers a simple and convenient analytical expression for describing the elastic scattering phenomenon of electrons by an atom. However, due its basis on high-energy approximation, the phase functions predicted using this method often produce errors when it comes to a relatively low energy electron beam. In order to correctly represent the scattering phase functions for both the low- and high-energy electron beams, the Mott scattering cross section should be employed. The reason that the Rutherford model fails to predict the correct elastic scattering phase function is because the spin of the electron is neglected. The spin-orbit coupling between the incident electron and the atom becomes important when the electron energy is low. This is incorporated in the Mott cross section through the Dirac equation.

The Mott elastic differential scattering cross section for an electron beam is typically given in the form of (Mott and Massey, 1965; Kessler, 1976; Czyzewski et al., 1990; Dapor, 2003):

$$
\frac{dC_e^{el}\left(\Theta, \varphi, E\right)}{d\Omega} = |f|^2 + |g|^2 + \frac{-AB^* e^{i\varphi} + A^* B e^{-i\varphi}}{|A|^2 + |B|^2}\left(fg^* - f^* g\right), \tag{4.17}
$$

where the scattering factors f and g are generally functions of a scattering polar angle Θ and wave number of the incident electron beam k, and A and B describe the state of polarization of the beam (e.g. $A=1$ and $B=1$ yield transverse polarization, $A=1$ and $B=0$ or $A=0$ and $B=1$ refer to longitudinal polarization). Note that the third term in Eq. (4.17) represents the dependence of the cross section on the azimuthal angle (i.e. φ), and it vanishes for an unpolarized electron beam. Therefore, scattering of a (partially-) polarized beam generally depends on both Θ and φ, as well as the incident energy of the beam.

---

[10] Forward direction usually refers to angles between 0° and 90° with respect to the propagating direction while backward direction covers angles from 90° to 180° assuming that azimuthal symmetry holds.

The scattering factors are expressed in the following forms (Mott and Massey, 1965; Kessler, 1976; Czyzewski et al., 1990):

$$f(\Theta, k) = \frac{1}{2ik} \sum_{l=0}^{\infty} \left\{ (l+1)\left[exp(2i\delta_{-l-1}) - 1 \right] + l\left[exp(2i\delta_l) - 1 \right] \right\} P_l(\cos \Theta),$$ (4.18)

$$g(\Theta, k) = \frac{1}{2ik} \sum_{l=1}^{\infty} \left[-exp(2i\delta_{-l-1}) + exp(2i\delta_l) \right] P_l^*(\cos \Theta).$$ (4.19)

Here, δ_l's are the Dirac phase shifts, P_l's and P_l^*'s are the ordinary Legendre polynomials and the associated Legendre polynomials, respectively. In the above expressions, k represents the wave number of the electron with energy E. They are related according to:

$$k^2 = \frac{(E^2 - m^2 c^4)}{\hbar^2 c^2}.$$ (4.20)

The phase shifts are to be determined from the Dirac equation, which describes the relativistic behavior of an electron including its spin, the magnetic moment of the electron, and the spin-orbit coupling. In order to satisfy the Dirac equation in the relativistic case, the wave function of the electron should have four components leading to a resultant of four simultaneous first-order partial differential equations (PDEs) as shown by Kessler (1976). These four PDEs can be transformed into two coupled first-order ordinary differential equation (ODEs) (Mott and Massey, 1965), which are given as:

$$\left\{ \frac{1}{\hbar c}(E - V(r) + mc^2) \right\} F_l^{\pm}(r) + \frac{dG_l^{\pm}(r)}{dr} + \frac{(1+j)}{r} G_l^{\pm}(r) = 0,$$ (4.21)

$$-\left\{ \frac{1}{\hbar c}(E - V(r) - mc^2) \right\} G_l^{\pm}(r) + \frac{dF_l^{\pm}(r)}{dr} + \frac{(1-j)}{r} F_l^{\pm}(r) = 0,$$ (4.22)

where $V(r)$ is the atomic potential. The + solutions apply to the electron 'spin up' case while the – solutions apply to the electron 'spin down.' For the + and – cases, j takes the value $-(l+1)$ and l, respectively. The asymptotic solution of G at large r requires that:

$$G_l^{\pm}(r) = J_l(kr)\cos \delta_l^{\pm} - Y_l(kr)\sin \delta_l^{\pm},$$ (4.23)

where $\delta_l^{\pm}$ are the phase shift needed in computing the Mott cross section. The Dirac equations can be further reduced to the following first-order ODE by introducing the change of variables as proposed by Lin et al (1963):

$$F_l^{\pm}(r) = A_l^{\pm}(r) \frac{\sin \phi_l^{\pm}(r)}{r}, \tag{4.24}$$

$$G_l^{\pm}(r) = A_l^{\pm}(r) \frac{\cos \phi_l^{\pm}(r)}{r}. \tag{4.25}$$

Using the proposed transformation, the Dirac equations now read:

$$\frac{1}{A_l^{\pm}} \frac{dA_l^{\pm}}{dr} = -\frac{j}{r} \cos 2\phi_l^{\pm} - \frac{mc^2}{\hbar c} \sin 2\phi_l^{\pm}, \tag{4.26}$$

$$\frac{d\phi_l^{\pm}}{dr} = \frac{j}{r} \sin 2\phi_l^{\pm} + \frac{1}{\hbar c}\{E - V(r)\} - \frac{mc^2}{\hbar c} \cos 2\phi_l^{\pm}. \tag{4.27}$$

It is convenient to work with a dimensionless equation. Equation (4.27) can be non-dimensionlized by letting:

$$\tilde{r} = \left(\frac{m_e c}{\hbar}\right) r, \tag{4.28}$$

$$K = \frac{\hbar k}{m_e c}, \tag{4.29}$$

$$\tilde{E} = \frac{E}{m_e c^2}, \tag{4.30}$$

$$\tilde{V}(\tilde{r}) = \frac{V(\tilde{r})}{m_e c^2}. \tag{4.31}$$

The dimensionless form of the equation is now expressed as:

$$\frac{d\phi_l^{\pm}}{d\tilde{r}} = \frac{j}{\tilde{r}} \sin 2\phi_l^{\pm} + (\tilde{E} - \tilde{V}) - \cos 2\phi_l^{\pm}. \tag{4.32}$$

Note that there is no need to solve for $A_l^{\pm}$ given in the new variables as the phase shifts can be determined by matching the ratio of the derivative of $G_l^{\pm}$ to $G_l^{\pm}$ between the numerical solution of Eq. (4.27) and the required asymptotic solution as given in Eq. (4.23) at large $\tilde{r}$. This ratio can be easily obtained for the numerical solutions by coupling Eqs. (4.21), (4.24) and (4.25) leading to:

$$\frac{1}{G_l^{\pm}} \frac{dG_l^{\pm}}{d\tilde{r}} = -\{\tilde{E} - \tilde{V}(\tilde{r}) + 1\} \tan \phi_l^{\pm} - \frac{(j+1)}{\tilde{r}}. \tag{4.33}$$

Going back to the asymptotic solution as in Eq. (4.23) shows:

$$\frac{1}{G_l^\pm}\frac{dG_l^\pm}{d\tilde{r}} = \frac{KJ_l'(K\tilde{r})\cos\delta_l^\pm - KY_l'(K\tilde{r})\sin\delta_l^\pm}{J_l(K\tilde{r})\cos\delta_l^\pm - Y_l(K\tilde{r})\sin\delta_l^\pm}, \tag{4.34}$$

in the non-dimensional form where $K^2 = \tilde{E}^2 - 1$. The derivative of the Bessel function is given as (Arfken, 1985):

$$J_l'(K\tilde{r}) = \frac{l}{K\tilde{r}}J_l(K\tilde{r}) - J_{l+1}(K\tilde{r}). \tag{4.35}$$

The same relation applies to $Y_l'(K\tilde{r})$ as well. The phase shifts are determined by matching Eqs. (4.33) and (4.34) at large $\tilde{r}$ where $\tilde{V}(\tilde{r}) \approx 0$, and they are given as (Czyzewski et al., 1990):

$$\tan\delta_l^\pm = \frac{KJ_{l+1}(K\tilde{r}) - J_l(K\tilde{r})\left[(\tilde{E}+1)\tan\phi_l^\pm + (1+l+j)/\tilde{r}\right]}{KY_{l+1}(K\tilde{r}) - Y_l(K\tilde{r})\left[(\tilde{E}+1)\tan\phi_l^\pm + (1+l+j)/\tilde{r}\right]}. \tag{4.36}$$

In short, the Mott elastic scattering cross section has the form given in Eq. (4.17) in which the Dirac phase shifts are to be calculated. These phase shifts are determined by solving Eq. (4.32) for $\phi_l^\pm$ at large $\tilde{r}$ where the asymptotic solution is reached using Eq. (4.36). However, solving Eq. (4.32) requires an initial value for $\phi_l^\pm$, these can be obtained by simply employing the power series expansions for $\phi_l^\pm$ and $\tilde{V}(\tilde{r})$ in $\tilde{r}$ near the origin and inserting them into the equation in which all the constant coefficients of the series are unveiled. The procedures are outlined in the following:

First, $\phi_l^\pm$ and $V(r)$ are expanded in terms of r:[11]

$$\phi_l^\pm = \sum_{k=0}^\infty a_k^\pm r^k, \tag{4.37}$$

$$V = -\sum_{m=0}^\infty b_m r^{m-1}, \tag{4.38}$$

where a_k's and b_m's are constant coefficients. Substituting these approximations into Eq. (4.32) and gathering the coefficients of each corresponding power in r, a_k's and b_m's is determined as:

---

[11] For the sake simplicity, the superscript "~" is dropped for the remaining discussion.

$$\sin 2a_0^{\pm} = -\frac{b_0}{j}, \tag{4.39}$$

$$a_1^{\pm} = \frac{E + b_1 - \cos 2a_0^{\pm}}{1 - 2j\cos 2a_0^{\pm}}, \tag{4.40}$$

$$a_2^{\pm} = \frac{2a_1^{\pm}\sin 2a_0^{\pm}\left(1 - ja_1^{\pm}\right) + b_2}{2 - 2j\cos 2a_0^{\pm}}, \tag{4.41}$$

$$a_3^{\pm} = \frac{2a_2^{\pm}\sin 2a_0^{\pm}\left(1 - 2ja_1^{\pm}\right) + 2\left(a_1^{\pm}\right)^2\cos 2a_0^{\pm}\left(1 - \frac{2}{3}ja_1^{\pm}\right) + b_3}{3 - 2j\cos 2a_0^{\pm}}, \tag{4.42}$$

with the condition that:

$$0 \leq 2a_0^{\pm} \leq \frac{\pi}{2} \quad \text{if } j < 0, \tag{4.43}$$

$$\pi \leq 2a_0^{\pm} \leq \frac{3\pi}{2} \quad \text{if } j > 0. \tag{4.44}$$

Using the fourth-order Runge-Kutta method (Matthew and Fink, 1999), the solution of Eq. (4.32) can be approximated as:

$$\phi_{i+1} = \phi_i + \frac{h\left(f_1 + 2f_2 + 2f_3 + f_4\right)}{6}, \tag{4.45}$$

where

$$f_1 = f\left(r_i, \phi_i\right), \tag{4.46}$$

$$f_2 = f\left(r_i + h/2, \phi_i + h/2\, f_1\right), \tag{4.47}$$

$$f_3 = f\left(r_i + h/2, \phi_i + h/2\, f_2\right), \tag{4.48}$$

$$f_4 = f\left(r_i + h, \phi_i + hf_3\right), \tag{4.49}$$

$$f\left(r, \phi\right) = \frac{j}{r}\sin 2\phi + \left[E - V\left(r\right)\right] - \cos 2\phi. \tag{4.50}$$

The electron phase functions in gold computed at different electron energies using the Mott cross section are depicted in Figure 4.5. Notice that there are "humps" over the angular domain for scattering profiles at various electron energies. They are caused by the interferences between the scattered electron waves. The "humps" disappear when the incident electron energy becomes large, since scatterings are weak at various angles except close to the absolute forward direction (i.e. the zero-degree angle). The electron phase functions for three different types of atoms (i.e.

copper, silver, and gold) are given in Figure 4.6. In the high-energy regimen, there is a clear trend that backscattering increases when the atomic number increases, or if the atom becomes heavy. In other words, the magnitude of the phase function is higher for scattering angles larger than 90° for the heavy element. However, the trend disappears at low electron energies since overlappings of phase functions for different elements are quite frequent.

Figure 4.7 shows the comparison computed between the phase functions using the Rutherford scattering model and the Mott cross section. On a regular basis, the Rutherford model is a reasonable approximation to the Mott model, however, this is not enough to yield physical accurate results. This will be evident in the electron-beam Monte Carlo simulation. The predicted electron-energy dependent elastic mean free paths using the Mott total elastic cross section for different metals are illustrated in Figure 4.8. Notice that the elastic mean free path for gold, a heavier element compared to copper and silver, increases for electron energies smaller than 0.1 keV. This is different from those shown by copper and silver at low electron energies. It implies the importance of the spin-orbit coupling phenomena between the incident electron and the atom for a heavy element such as gold. It also shows that the trend of the elastic mean free path predicted using the Rutherford model is inaccurate for heavy elements as evident in Figure 4.9.

4.3 Continuous Inelastic Scattering Approach – The Bethe Theory

Inelastic scatterings involve interactions between propagating electrons and electrons inside the matter. Describing the inelastic scattering phenomena accurately for the electron-beam propagation is a difficult subject for the modeling task since electrons can lose their kinetic energies in a number of ways within matter. Depending on the strength of the electron energy, the physical processes involved must be different. There are a number of theories and formulations available for describing electron energy losses of an energetic electron propagating inside a matter. In this section, the classical approach or the Bethe theory for accounting inelastic scattering based on continuous slow-down approach is discussed.

The Bethe theory treats the interaction between a propagating electron and electrons at rest based on classical interaction where quantum mechanical effects are not strongly present. According to this theory, a propagating electron is supposed to continuously lose its kinetic energy

along the path of propagation. The energy lost along the path is quantified by a quantity called the *stopping power* (usually denoted as *dE/dS*). This refers to the change of electron kinetic energy per unit length of propagation. To derive the stopping power of the electron, one usually starts by examining the repulsion force between a traveling electron and an electron at rest, and then determines the momentum transferred that is induced by this force when the electron passes over the other. After discovering the amount of momentum transferred from the propagating electron to another at rest, the electron stopping power can be obtained by integrating it over a suitable distance at which the momentum transfer is possible between the traveling electron and another electron orbiting the atom. It is important to also take into consideration the density of atoms and the atomic number. One can consult the paper by Bethe (1930) and the book by Dapor (2003) for the detailed mathematical derivations of the stopping power. The stopping power derived via this method has the following form:

$$\frac{dE}{dS} = -\frac{2\pi e^4 N_a \rho Z}{AE} ln\left(\frac{1.166E}{J}\right),$$
(4.51)

where, N_a the Avogadro number, ρ the density, Z the atomic number, A the atomic weight, E the kinetic energy of the incident electron, and J is the mean ionization energy. The above equation is the Bethe equation, which is valid for $E > J$. In an attempt to extend the applicability of the Bethe equation below the mean ionization energy, Joy and Luo (1989) modified the original Bethe equation to:

$$\frac{dE}{dS} = -\frac{2\pi e^4 N_a \rho Z}{AE} ln\left[\frac{1.166(E+0.85J)}{J}\right],$$
(4.52)

in order to match the data obtained by Tung et al. (1979) using a statistical model. This so-called modified Bethe equation is usually valid for $E > 50$ eV.

The Bethe equation is a relatively crude approximation for modeling the electron energy losses since propagating electrons are assumed to lose energy continuously along the traveling path and the ionization of electrons is treated as an averaged effect. Consequently, it is less accurate when compared to the case where inelastic scatterings are considered discretely in terms of the inner-shell ionizations, the outer-shell excitations, and the plasma oscillations.

4.4 Discrete Inelastic Scattering Treatment – The Dielectric Theory

Another method of treating the inelastic scatterings is by using the dielectric theory/formulation. The dielectric formulation uses the energy loss function directly derived from the experimental optical data and generates the differential inelastic scattering cross section accordingly. The energy loss function is a measure of responses to electrons and atoms in a medium as a whole when exposed to an external disturbance, therefore it is typically more accurate compared to the other independent formulations. This is especially true when the electron energy is low. In this way, the inner-shell ionizations and the outer-shell excitations cannot be distinguished clearly. Nevertheless, it is a better approach in determining the inelastic scattering properties of electrons at low energy, considering that the inelastic electron scatterings are not currently well-understood at the low electron-energy regimen.

The double differential inelastic scattering cross section (or the probability for an inelastic scattering event to occur per unit length, energy change, and momentum change) formulated using this method is given as (Pines and Nozières, 1966):

$$\frac{d^2\lambda_{inel}^{-1}}{d(\hbar\omega)dq} = \frac{1}{\pi a_0 E} Im\left[-\frac{1}{\varepsilon(q,\omega)}\right]\frac{1}{q},$$ (4.53)

where a_0 is the Bohr radius and λ_{inel} is the inelastic mean free path. The imaginary part (denoted as $Im[\cdot]$) of the negative inverse of the dielectric function $\varepsilon(q,\omega)$ in the equation describes the probability of energy loss. It is called the energy loss function. The incident energy of the electron is denoted as E while the amount of energy loss is given as $\hbar\omega$ which shall be refered to as ΔE. The energy loss function can be derived from extrapolating the optical dielectric constant as measured by experiments.

Equation (4.53) can be modified via the variable change to account for the Ω-dependent instead of the q-dependent. This is achieved by using the energy and the momentum conservation, which are given as ($E -\Delta E=E'$) and ($\vec{k}' + \vec{q} = \vec{k}$), respectively. Using the cosine law and the parabolic free-electron band structure (i.e., $E=(\hbar k)^2/2m_0$), both the energy and the momentum conservation assert that:

85

$$\frac{(\hbar q)^2}{2m} = 2E - \Delta E - 2\sqrt{E(E-\Delta E)}\cos\Theta, \tag{4.54}$$

where Θ is the angle between the incident and the scattered direction. Therefore, by multiplying Eq. (4.53) with $dq/d\Omega$ (i.e., $d\Omega=2\pi sin\Theta d\Theta$ and $dq/d\Omega$ can be derived by differentiating Eq. (4.54)), the cross section transforms into:

$$\frac{d^2\lambda_{inel}^{-1}}{d(\Delta E)d\Omega} = \frac{1}{(\pi a_0 e)^2 E} Im\left[-\frac{1}{\varepsilon(q,\omega)}\right]\frac{1}{q^2}\sqrt{E(E-\Delta E)}, \tag{4.55}$$

where the definition of the Bohr radius (i.e., $a_0=\hbar^2/me^2$) is used.

If the optical dielectric constant of a given matter is given as $\varepsilon(\omega_0)$, then the q-dependent energy loss function reads:

$$Im\left[-\frac{1}{\varepsilon(q,\omega)}\right] = \frac{\omega_0}{\omega} Im\left[-\frac{1}{\varepsilon(\omega_0)}\right], \tag{4.56}$$

where ω_0 is the positive solution of the plasmon dispersion equation $\omega_q(q,\omega_0)=\omega$, which is given as (Penn, 1987):

$$\omega_q^2(q,\omega_p) = \omega_p^2 + \frac{1}{3}v_F^2\omega_p q^2 + \left(\frac{\hbar q^2}{2m_0}\right)^2, \tag{4.57}$$

or (Ashley, 1991; Kwei and Tung, 1986; Ritchie and Howie, 1977):

$$\omega_q = \omega_p + \frac{\hbar q^2}{2m_0}. \tag{4.58}$$

In the above equations, ω_p stands for the plasma frequency, v_F is the Fermi velocity, and m is the electron mass. Using the quadratic rule, ω_0 is obtained as:

$$\omega_0 = -\frac{v_F^2 q^2}{6} + \frac{1}{2}\sqrt{\frac{1}{9}v_F^4 q^4 - 4\left(\frac{\hbar q^2}{2m_0}\right)^2 + 4\omega^2}, \tag{4.59}$$

using Eq. (4.57), and:

$$\omega_0 = \omega - \frac{\hbar q^2}{2m_0}, \tag{4.60}$$

if the latter plasmon dispersion relation is employed. An example of the energy loss function of

gold is given in Figure 4.11 and its corresponding *q*-dependent energy loss function is depicted in Figure 4.12.

The probability of an electron suffering an inelastic scattering event per unit path length and per unit energy change is obtained through Eq. (4.53) after integration over all possible wave number *q* of the excited plasmons and using the energy and momentum transfer conservation. It is given as (Ding and Shimizu, 1996):

$$
\frac{d\lambda_{inel}^{-1}}{d(\Delta E)} = \frac{1}{\pi a_o E} \int_0^\infty \left\{ \frac{\hbar\omega_p}{\left(\Delta E\right)^2 - \left(\hbar\omega_p\right)^2 + \left[\left(\hbar\overline{q}\right)^2/2m_0\right]^2} Im\left[\frac{-1}{\varepsilon(\omega_p)}\right] \times \right.
$$
$$
\left. \times \Theta\left[\frac{\hbar^2}{2m_0}\left(2k\overline{q} - \overline{q}^2\right) - \Delta E\right] \right\} d\left(\hbar\omega_p\right) \tag{4.61}
$$

when Eq. (4.57) is assumed, and (Ding and Shimizu, 1996):

$$
\frac{d\lambda_{inel}^{-1}}{d(\Delta E)} = \frac{1}{2\pi a_o E\Delta E} \int_0^\infty \left\{ \frac{\hbar\omega_p}{\Delta E - \hbar\omega_p} Im\left[\frac{-1}{\varepsilon(\omega_p)}\right] \Theta\left[\frac{\hbar^2}{2m_0}\left(2k\overline{q} - \overline{q}^2\right) - \Delta E\right] \right\} d\left(\hbar\omega_p\right), \tag{4.62}
$$

if Eq. (4.58) is used. In the above equations, $\overline{q}$ is the positive solution of the dispersion relation $\omega = \omega_q(\overline{q}, \omega_p)$. Note that $E = (\hbar k)^2/2m$ and $\Delta E = \hbar\omega$. Using Eq. (4.62), this probability for gold is plotted and given in Figure 4.13.

The inelastic mean free path of the electron can then be obtained by integrating the cross section over all energy change where the Fermi energy E_F is assumed to be the reference level (i.e. the primary electrons lose energies until they reach energy level E_F). The inverse of the mean free path is given as:

$$
\lambda_{inel}^{-1} = \int_0^{E-E_F} \frac{d\lambda_{inel}^{-1}}{d(\Delta E)} d(\Delta E). \tag{4.63}
$$

Note that λ_{inel} depends on the kinetic energy of the electrons. Therefore, the electron stopping power can be estimated as:

$$
-\frac{dE}{dS} = \int_0^{E-E_F} (\Delta E) \frac{d\lambda_{inel}^{-1}}{d(\Delta E)} d(\Delta E). \tag{4.64}
$$

The inelastic mean free path of hot electrons for gold is depicted in Figure 4.14.

4.5 Electron-Phonon Scattering

The discussions about the electron-energy loss mechanisms up until now are classified as electron-electron collisions where the electron-beam interacts with electrons inside the matter. The electron-beam can lose energy by creating phonons or gain energy by absorbing phonons. The former is more probable than the latter in this case. Phonons are the energy quantas of lattice vibrations. There are two different types of phonons. The first type is the optical phonon while the second type is the acoustic phonon. If the creation of the optical phonon is assumed to be dominant over the absorption of the optical phonon and the dispersion relation of the optical phonon is neglected, then the scattering probability per unit time is given as (Ganachaud et al., 1997):

$$
\frac{1}{\tau_{LO}(E)} = \left(\frac{m^*}{2}\right)^{1/2} \frac{e^2 \omega_{LO}}{4\pi\hbar} \left[\frac{1}{\varepsilon(\infty)} - \frac{1}{\varepsilon(0)}\right] \frac{1}{E^{1/2}} \left(\langle n_{LO}\rangle + 1\right) ln \left[\frac{1 + \left(1 - \frac{\hbar\omega_{LO}}{E}\right)^{1/2}}{1 - \left(1 - \frac{\hbar\omega_{LO}}{E}\right)^{1/2}}\right], \quad (4.65)
$$

where the Bose-Einstein distribution is:

$$
\langle n_{LO}\rangle = \frac{1}{exp\left(\frac{\hbar\omega_{LO}}{k_B T_{LO}} - 1\right)}, \quad (4.66)
$$

and $\varepsilon(0)$ is the static dielectric constant at low frequency and $\varepsilon(\infty)$ at high frequency. The electron-phonon mean free path can be obtained by dividing the above equation by the electron velocity and taking the inverse of the quantity to yield:

$$
\lambda_{e-LO} = \frac{8\pi\hbar E}{m^* e^2 \omega_{LO}} \frac{\varepsilon(\infty)\varepsilon(0)}{\varepsilon(0) - \varepsilon(\infty)} \left[1 - \frac{1}{exp\left(\hbar\omega_{LO}/k_B T_{LO}\right)}\right] \times
$$

$$
\times \frac{1}{ln\left\{\left[1 + \left(1 - \frac{\hbar\omega_{LO}}{E}\right)^{1/2}\right] \middle/ \left[1 - \left(1 - \frac{\hbar\omega_{LO}}{E}\right)^{1/2}\right]\right\}}. \quad (4.67)
$$

4.6 Electron Reflection and Refraction at the Surface

When an electron encounters a surface between a vacuum and the material, it can be reflected

or refracted (or transmitted) depending upon the energy of the electron and the impinging angle with respect to the surface normal, due to the surface barrier of the material. A quantum mechanical expression for describing electron transmission from the material to vacuum is given as (Cohen-Tannoudji et al., 1977):

$$T(E,\beta) = \begin{cases} \dfrac{4\left(1-U_0/E\cos^2\beta\right)^{1/2}}{\left[1+\left(1-U_0/E\cos^2\beta\right)^{1/2}\right]^2} & \text{if } E\cos^2\beta > U_0 \\ 0 & \text{otherwise} \end{cases}, \tag{4.68}$$

where U_0 is the inner potential (which is the sum of the Fermi energy and the work function of the material), and β is the impinging angle with respect to the surface normal. If the electron is transmitted, then β will be altered to β' following the expression below while its energy is reduced by U_0 amount:

$$\sqrt{E-U_0}\,\sin\beta' = \sqrt{E}\,\sin\beta. \tag{4.69}$$

4.7 Monte Carlo Simulation Results and Verifications

In this work, two different Monte Carlo codes are implemented in order to account for the electron-beam propagation inside the material. One is with the Continuous Slow-Down Approach (CSDA) and the other is with the Discrete-Inelastic Scattering (DIS) method. Since the simulation procedures for these methods are well-described in Chapter 3, the details of these simulations will not be repeated. The properties used in the simulations follow those as described in the previous sections. The CSDA treats the elastic scatterings using the Rutherford cross-section or the Mott cross-section (see Section 4.2). The inelastic scattering is accounted for by using the Bethe Theory as given in Section 4.3. As for the DIS method, the Mott scattering cross-section and the dielectric theory are used to account for the elastic and inelastic scatterings, respectively. Details of the dielectric theory are given in Section 4.4.

Since the Monte Carlo codes were built by the author for this research, the verifications of the codes are needed in order to ensure the validity of the simulations. The backscattering yields were calculated using the codes. Backscattering yields are defined as the total number of electrons reflected back normalized by the total number of incident electrons. The simulation results

were compared with the various experimental results. All the data points from different references are given in the database compiled by Joy (2001). Even though the variations of the experimental results are quite large, the computational results seem to coincide with most of them.
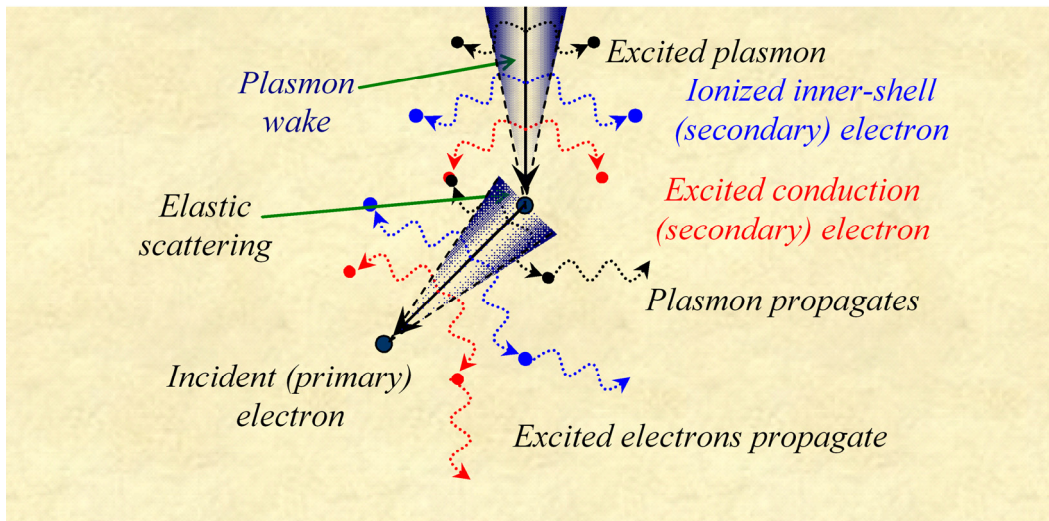
Figure 4.1 Various scattering mechanisms for an incident electron from the field emission source are depicted in this figure. The incident electron is considered primary while the excited atomic (either inner-shell or conduction) electrons are secondary. As an energized electron originates from an external source to penetrate a matter, it loses its energy by undergoing different types of inelastic scattering mechanisms and suffers deflections through elastic scatterings. Inelastic scatterings include excitation of plasmons, ionization of inner-shell electrons, and excitation of conduction electrons.
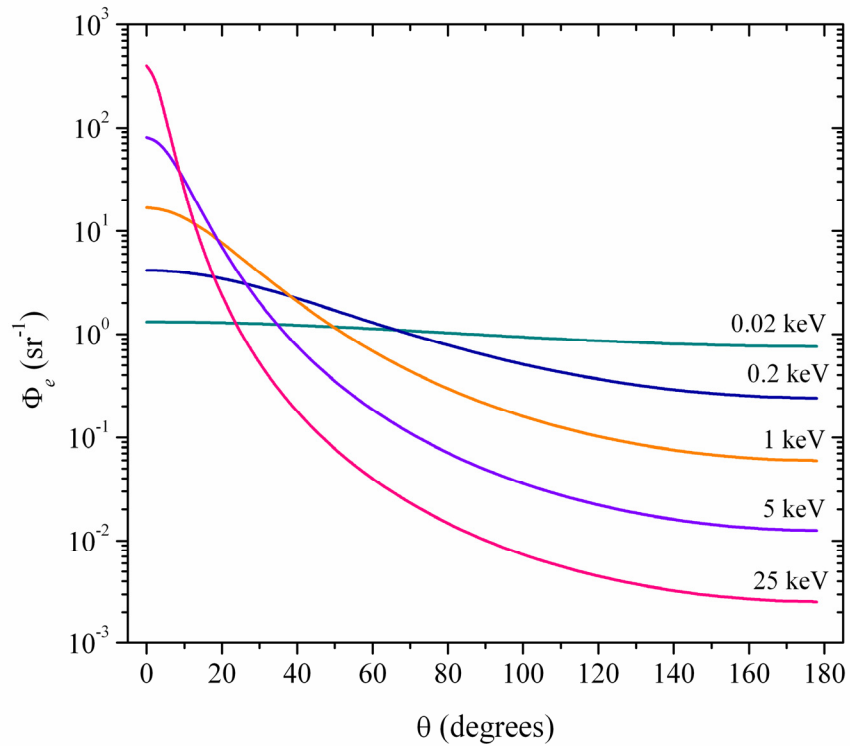
Figure 4.2   Rutherford scattering cross-section of electron by a gold atom at various scattering angles and different electron energies. Note that an electron tends to be scattered by the gold atom almost equally in the forward and backward directions at low energy. When the electron energy is high, scattering becomes highly forward, meaning that the angular deflection is relatively small.
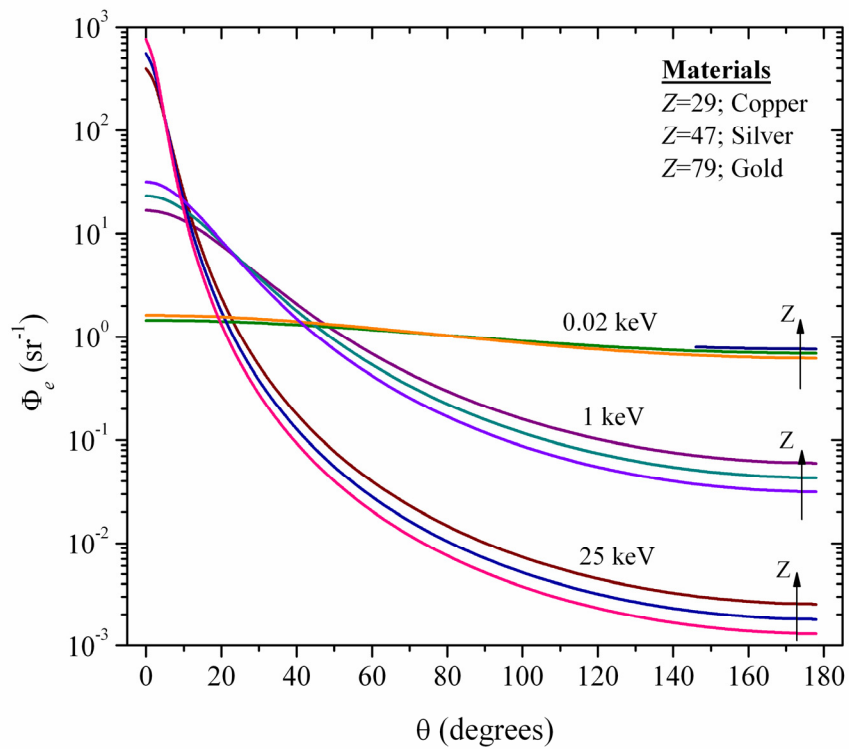
Figure 4.3   Rutherford scattering cross-section of electron by different types of atoms, (i.e., copper, silver, and gold) at various scattering angles and different electron energies. Increasing the atomic number Z tends to enhance backscattering but it weakens forward scattering.
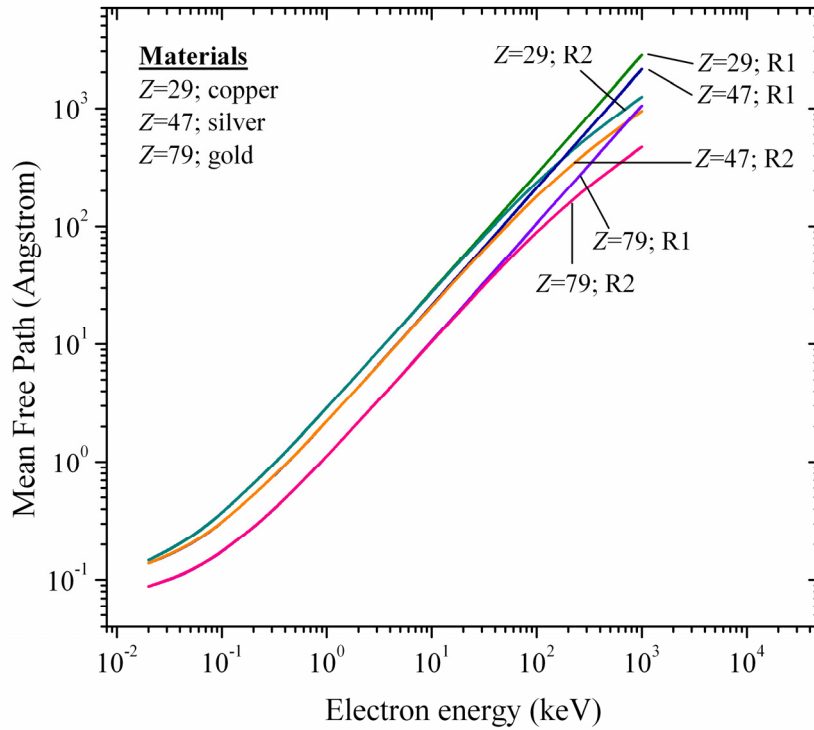
Figure 4.4 The elastic mean free path of electrons derived from the two different forms of the Rutherford scattering cross-section discussed in the text. R1 and R2 refer to the mean free paths derived using Eqs. (4.10) and (4.14), respectively. Both models yield the same mean free path at low electron energies but deviate from each other at high energies. The elastic mean free paths for different materials are also shown in the figure.
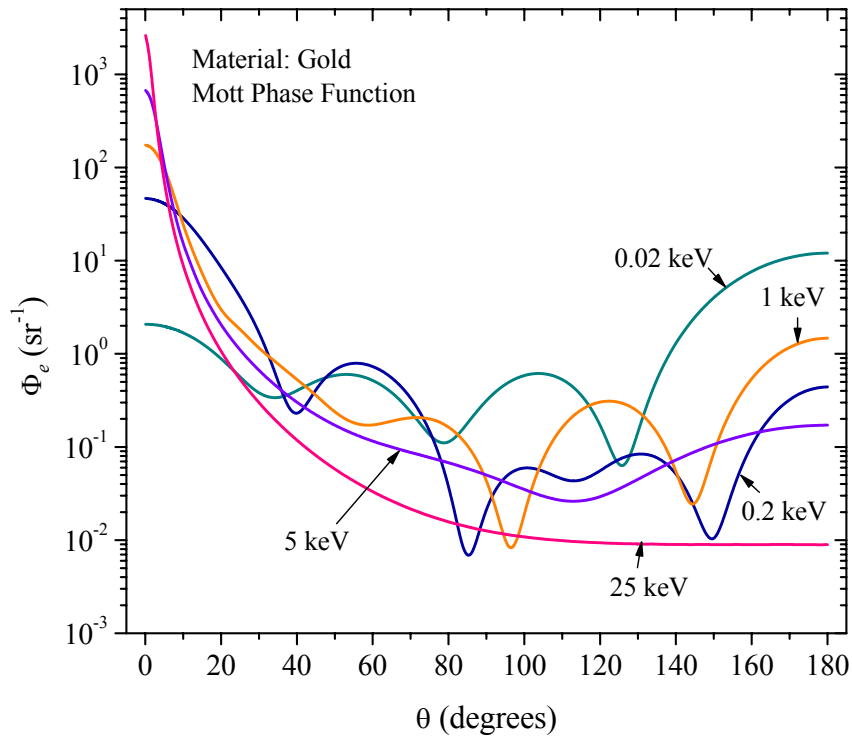
Figure 4.5 Mott scattering cross-section of electrons by a gold atom at various scattering angles and different electron energies. Notice that there are "humps" over the angular domain for scattering profiles at various electron energies. They are caused by the interferences between the scattered electron waves. The "humps" disappear when the incident electron energy becomes large. This is because scatterings are weak at various angles, except when close to the absolute forward direction (i.e. the zero-degree angle).
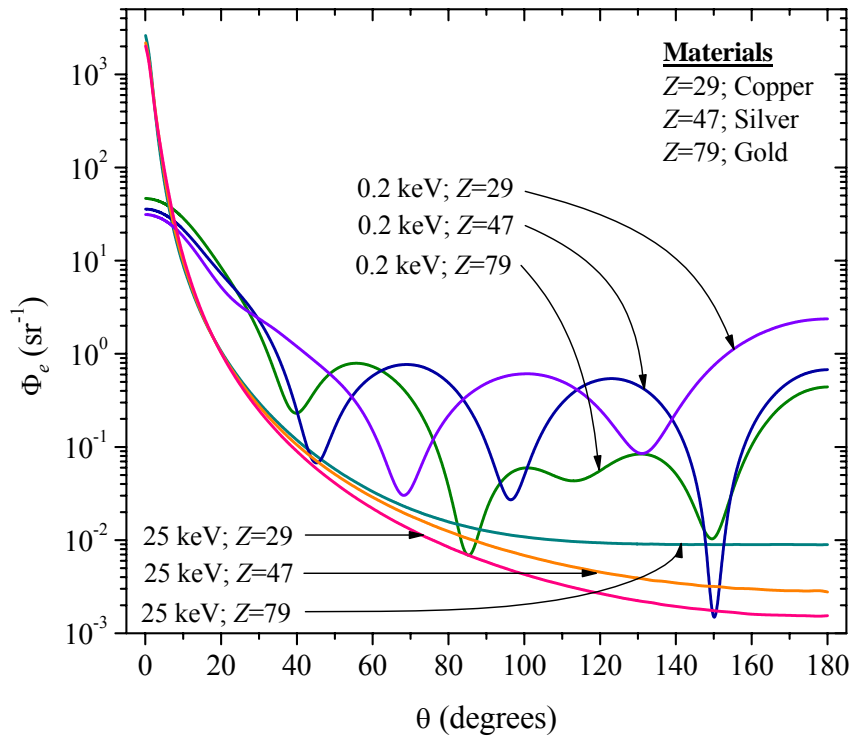
Figure 4.6   The Mott elastic scattering cross section for various materials (i.e. copper, silver, and gold) at various scattering angles and at two different electron energies.
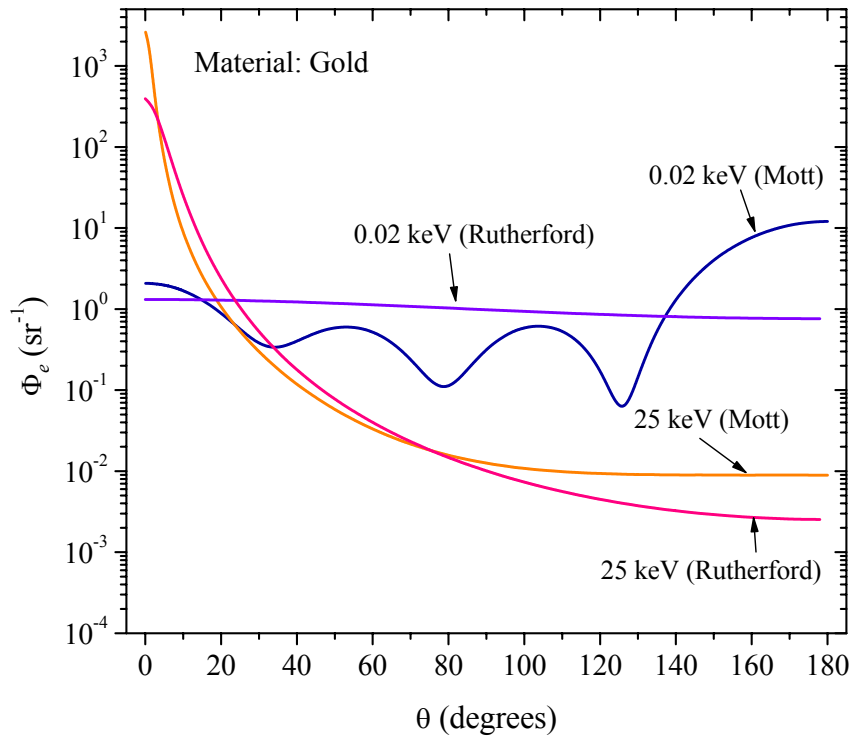
Figure 4.7   Scattering cross-sections of electron computed by Rutherford's model and Mott's model at various scattering angles and different electron energies. It can be seen that the Rutherford model deviates significantly from the Mott model at low electron energy.
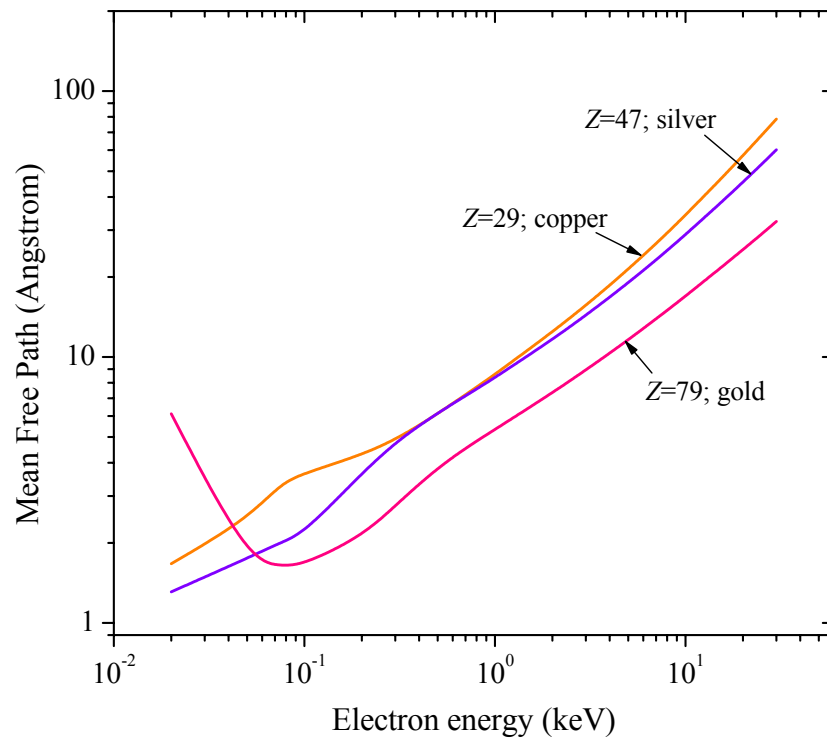
Figure 4.8   Elastic mean free path of electron at various electron energies for the Mott scattering model is given.
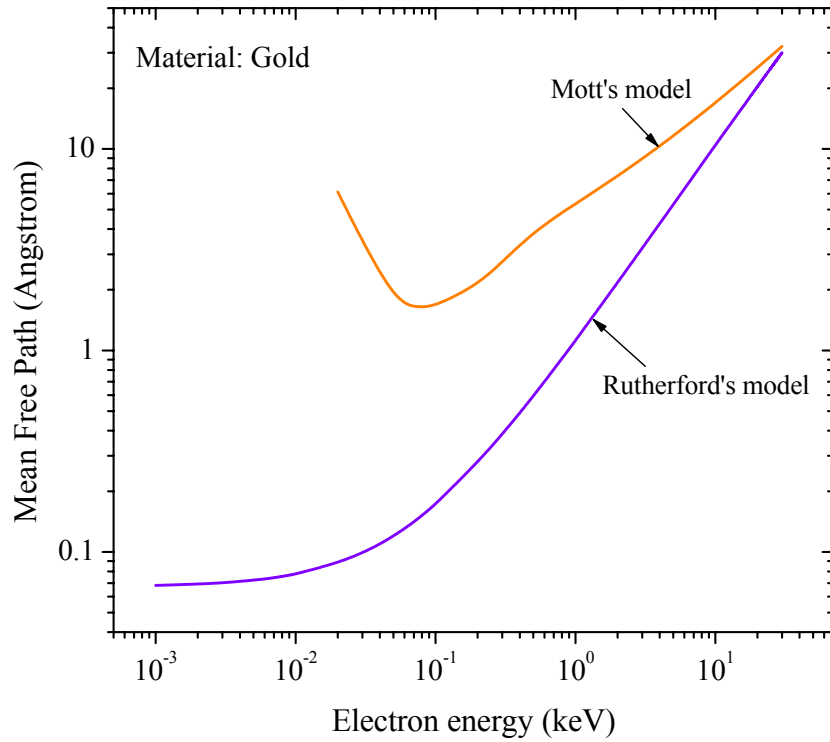
Figure 4.9   Elastic mean free path of electron at various electron energies for the Rutherford scattering model and the Mott scattering model. The Rutherford model always underestimates the elastic mean free path of electron.
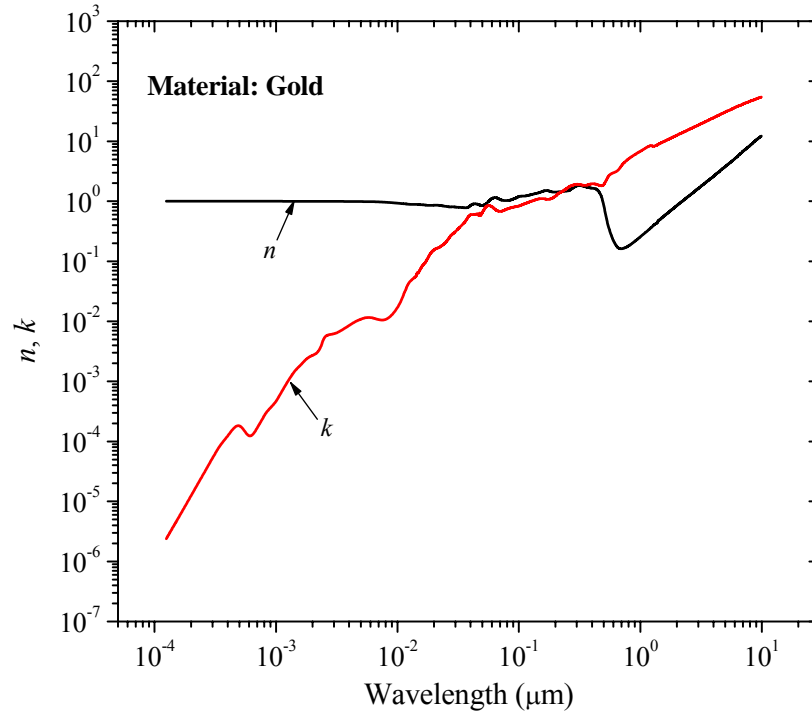
Figure 4.10 The complex index of refraction of gold is shown. *n* is the real part while *k* is the imaginary part of the index. Data is obtained from Palik (1985).
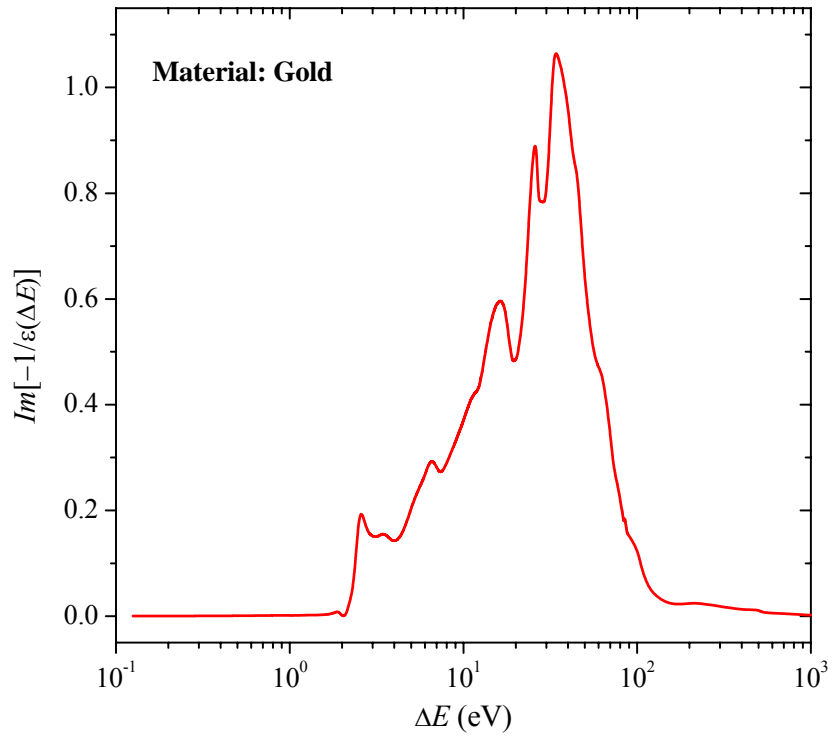
Figure 4.11 The energy loss function of gold derived from the complex index of re-
fraction given in Figure 4.10 is illustrated.
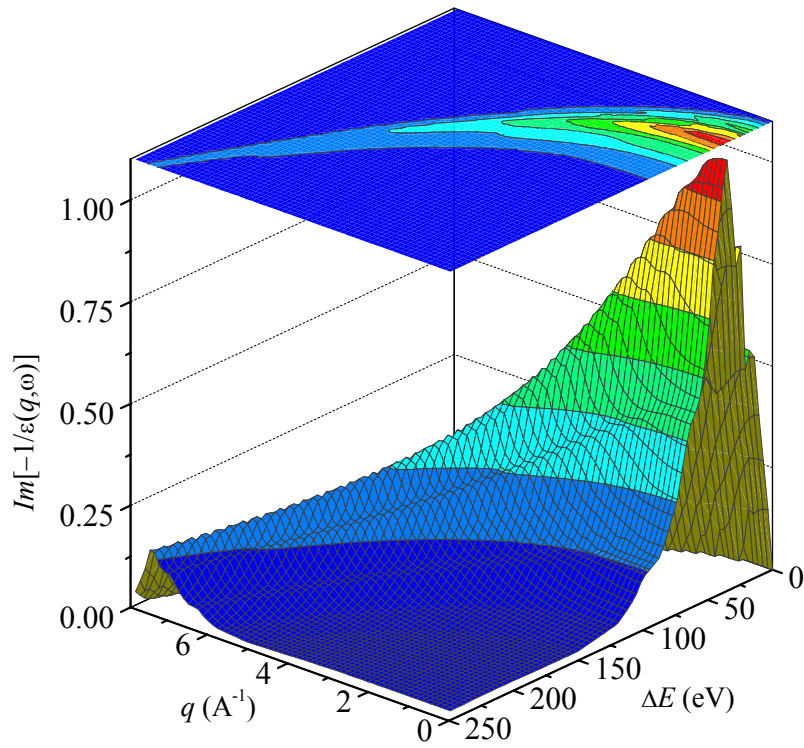
Figure 4.12 The probability of energy loss for hot electrons as a function of incident kinetic energy E and momentum transfer in terms of wave number q in gold.
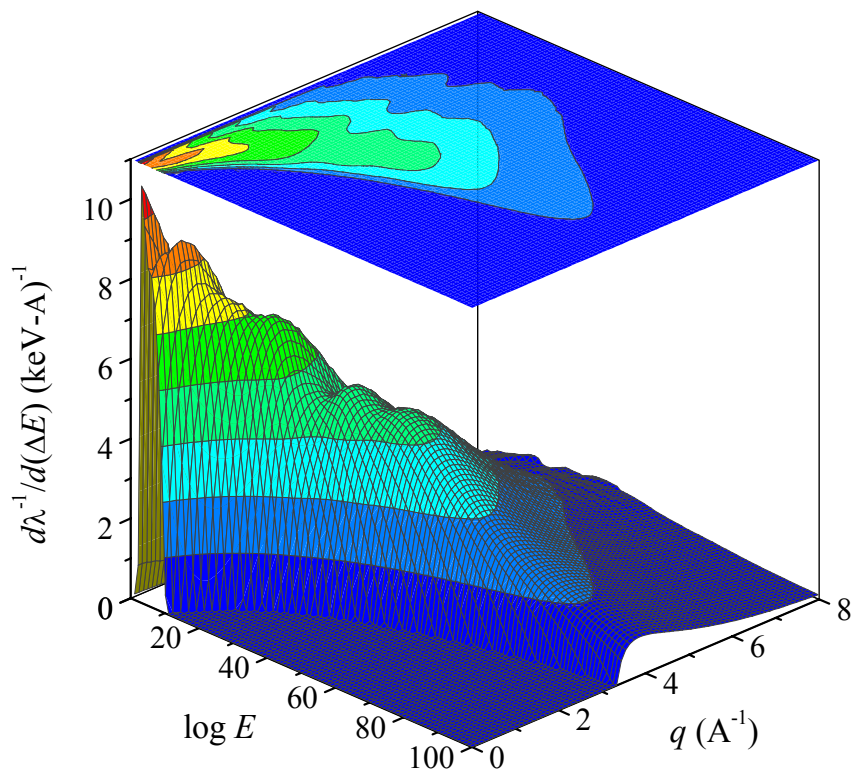
Figure 4.13 The probability of energy loss for hot electrons as a function of incident kinetic energy E and momentum transfer in terms of wave number q in gold.
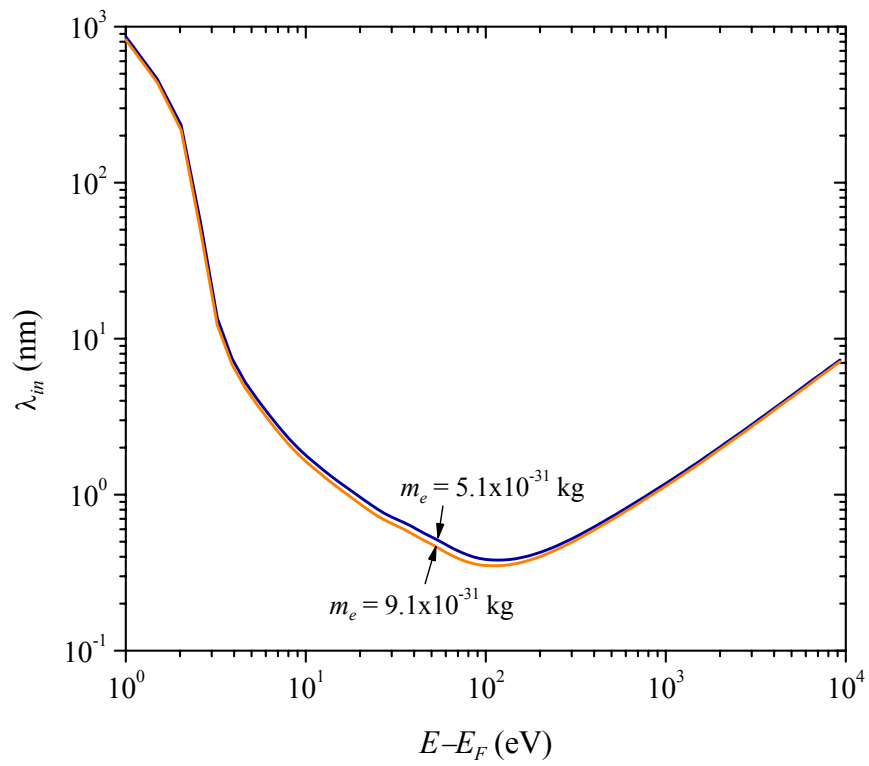
Figure 4.14 The inelastic mean free path of hot electrons for gold.
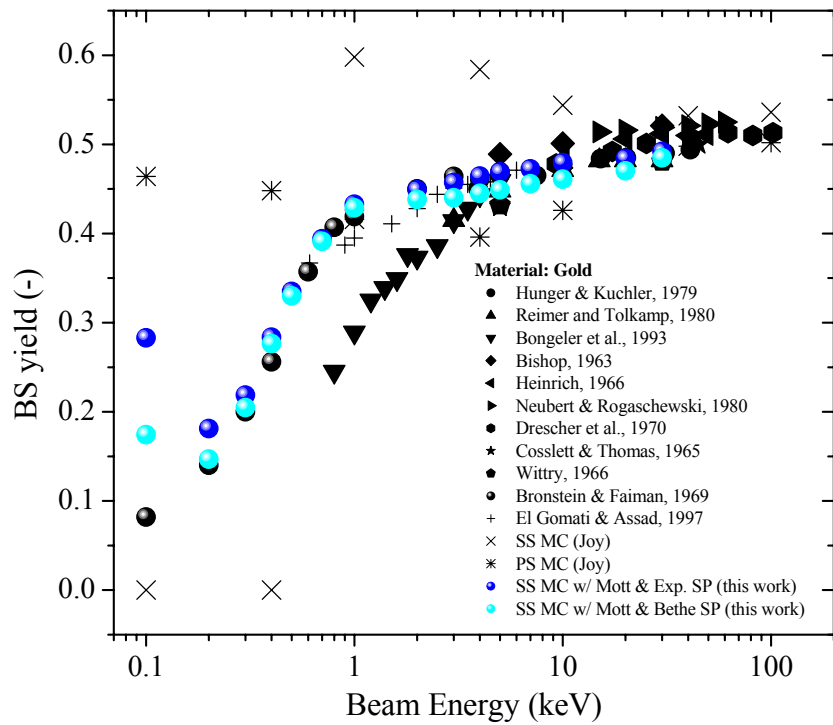
Figure 4.15 Backscattering yields for various incident electron energies. The medium is assumed to have infinite thickness.

CHAPTER 5
ELECTRON-BEAM INDUCED THERMAL CONDUCTION VIA CSDA[12] *E*-BEAM MONTE CARLO AND FOURIER'S LAW

In this chapter, the main focus is on the thermal heat generation and the heat conduction phenomena due to the electron heating. The electron-beam scatterings and the thermal conduction occuring inside the workpiece, due to the electron-beam, are considered in the modeling. Absorptions of photons by electrons inside the matter occur at the area of incidence when a laser beam at a given wavelength is used to heat a matter at micro/nano-scale levels. The transfer between the photons and electrons that is involved is in terms of energy alone. The momentum transfer is negligible because photons possess negligible momentum when compared to that of electrons. There are no additional perturbations to the electric field because photons are non-charged particles. When an electron beam impinges a conducting target, the problem becomes even more complicated since electrons are charged particles. These charged particles create perturbation to the electric field of the material. The surface of the target may be charged positively or negatively depending on the properties of the material and the energy of the beam. This serves as a potential barrier which lowers the kinetic energy of subsequent incoming electrons. Moreover, electrons from an electron-beam typically have significant amounts of momentum. This why momentum transfers between these electrons and electrons inside the matter cannot be neglected.

Before presenting any modeling of these phenomena, the transfer mechanisms involved in this process shall be explored. There are three physical phenomena present in this picture. They are electron-beam propagation, photon-beam propagation, and thermal conduction inside the target.

5.1 Modeling the Unknowns

Although the machining process (i.e. nano-machining using a nano-probe) described is an ingenious concept, the actual modeling of such a process is quite difficult and complicated. If this process were to occur within the "macro" world of engineers, then the task would be rather sim-

---

[12] CSDA stands for Continuous Slow-Down Approach.

ple since all the required material properties and the governing equations for thermal heat conduction are well-known and well-documented. However, when the entire dimension of the process is reduced down to the nano-scale levels, the numerical modeling requires a further detailed understanding of the physics.

The most important aspect of this modeling task is to find the correct governing equation. It is rather difficult to estimate the nature of the transport without knowing the exact transport properties of the material of interest. If the transport phenomenon is of a wave nature, then the wave theory should be employed, if not, the particle transport theory can be followed. Since the interest of this research is in modeling the nano-machining process using a nano-probe, it is expected that with the use of an electron-beam, a small well-defined area of the target material will undergo evaporation, which will yield the material removal, and result in the machining process. The temperature involved in this process may range from the room temperature (i.e. 300 K) to the evaporation temperature (i.e. ~3000 K for metals)[13], if the concept of temperature is still applicable at such a scale. Most of the properties known up-to-date as a function of temperature and air pressure are documented before melting temperature of the material. The transport properties beyond the melting temperature are unknown and not available even for the macro-scale thermal transport, not to mention at the nano-scale level. However, since the temperature range involved in this type thermal transport is considered wide and high, the thermal transport (or heat conduction) for the heated material is assumed to be diffusive due to the highly scattering of heat carriers caused by the highly-elevated temperature. Under such a condition, the intense scatterings of the heat carriers cause the phase information of the particle waves to be unimportant. This will result in no need to utilize the wave theory, and the particle transport theory will be sufficient. One of the best candidates for modeling the particle transport is the Boltzmann Transport Equation (BTE).

The BTE in its general form can be considered the best candidate for assuming that the range of the wavelengths of the heat carriers involved are much smaller than the physical dimension of

---

[13] The evaporation temperature at macroscopic level is assumed here. Melting and evaporation temperatures for nano-structures are different from those defined at macro-scale level. They vary depending on the air pressure as well. Further details of the nano-scale melting will be provided by J. Sanchez.

the object of interest. Nevertheless, solving the general BTE is extremely difficult. One possible way of solving the equation is to use the Monte Carlo (MC) simulation. The drawback of this method is that it requires large computational costs and resources if the machining problem is to be solved rigorously. The two types of heat carriers involved are electrons and phonons. Electrons are categorized into two kinds: a) primary electrons originating from the electron-beam and, b) the electrons inside the material itself. This means that there are three BTEs to be solved (i.e., two for electrons and one for phonons). The ultimate simulation would involve three MC simulations simultaneously and progressing dependently in time. This can be done provided that the required computer resources are readily available.

What is the real challenge of the modeling task for the nano-machining process if the MC simulation is the answer to the problem? It should be understood that MC simulations can be quite powerful when it comes to solving complicated physical problems involving integro-differential equations. This is true only if the physics are correctly implemented in the simulation procedures. It is very easy to construct a MC simulation and to create the "rules" for the heat carrier propagations based on some intuitive thinking. These "rules" may lead to unique resultant statistical distributions, which can be considered as the solution to the problem. However, a MC simulation is very similar to an experimental setup. It could produce errors and wrong results without the proper calibrations. This truth applies to all sorts of numerical modeling methods available that are for nano-scale level heat transport. This is because the fundamental research on the physics at such a scale is still early in its infancy.

5.2 Modeling Thermal Conduction due to Single *e*-Beam Heating

5.2.1 Problem Description and Assumptions

The origin of the coordinate frame is set at the point where the electron bombardments first occurred. Note that the *y*-axis is oriented perpendicular to the figure, pointing outward. In modeling the energy transfers to the workpiece, it is assumed that the workpiece is infinitely long in extensions in both *x*- and *y*- directions. Such assumption is justified if all the reflected, transmitted, and absorbed electron energy distributions are well confined within the workpiece dimensions. The thickness of the workpiece is denoted as *L*. As far as the distances between the CNT,

laser beam, and the workpiece are concerned, they are not as critical at this stage since they only affect the incident profiles of the electrons and photons at the boundaries. Those can easily be accounted for in the analyses later. For the sake of simplicity, a single CNT will be used for the machining process. The machining process involving multi CNTs will be included later.

Another important assumption to be made is the absolute purity of the material for the workpiece. This means that the medium is homogeneous and is free of defects and cracks. Such an assumption simplifies the analyses in the heat transports. This is because electron, photon and phonon scatterings become extremely complicated when there are impurities in the medium.

As mentioned, there are three modes of heating in this problem: 1) an overall heating of the workpiece, which is denoted as the bulk heating, 2) a local heating using a laser beam to raise the energy of the location of interest, and 3) energy transfer to the workpiece by electron bombardment using carbon nanotubes. To be able to model these three modes of heat transport, the correct and appropriate approaches need to be chosen. This choice strongly depends on the wavelengths of the energy carriers and time and length scales of the system.

The objectives are: a) to model the electron-beam transport, b) to predict the temperature field in the workpiece, and c) to determine the electron-beam power to effectively remove atoms from a workpiece. The end result is to achieve nano-machining. The sufficient number of energized electrons supplied per unit time (or current) needed to elevate local workpiece temperatures near the melting, evaporation, or sublimation temperature is necessary. It should be realized that the concepts of "melting," "evaporation," and "sublimation" at the nano-scale are used loosely here. They require further investigation, particularly in conjunction with detailed experiments. The models and predictions developed in this work will subsequently serve as experimental guidelines for finding suitable nano-probes for nano-machining.

A schematic of the problem is depicted in Figure 5.3. Two possible scenarios are considered. The first scenario uses only the electron-beam as the source of heating, which is illustrated in Fig. 1(a). In the second scenario auxiliary heating using a laser at the interface between the workpiece and the substrate is considered in addition to the electron-beam heating (see Fig.

1(b)). For the current investigation, the type of the electron source used in the simulations is irrelevant as long as the probe can emit sufficient amount of electrons without failing. In simplifying the current investigation, it is assumed that there are no electron sources or drains imposed on the workpiece. Additional applied voltages across the workpiece would alter the propagation of penetrating electrons from the electron-beam and may also cause non-uniform joule heating within the workpiece. These details will be included in future models as joule heating can serve as a means of assisting the nano-machining process by providing additional heat beside the electron-beam and laser.

A thin gold film is chosen as the solid target (or workpiece). This is deposited on a 10-μm semi-transparent substrate (quartz). Both the workpiece and the substrate are assumed to have a radial dimension of 10 μm. The thickness of the gold film is considered to be either 200 nm or 500 nm. Although in the experiments the actual thickness of the substrate could possibly be a few hundred micrometers thick, it would not affect the final results since the 10-μm quartz is "infinitely thick" with respect to heat waves (as well as a 100-μm quartz substrate). It is assumed that quartz does not absorb any radiant energy (i.e. it is transparent to the laser). A single electron source is considered to emit electrons, with predetermined initial kinetic energies, directly onto the top surface of the workpiece. A laser with a wavelength of 355 nm is chosen to heat the workpiece from the bottom of the substrate. The laser wavelength is selected to minimize reflection of the incident radiation, as gold reflects radiation significantly at wavelengths beyond 355 nm. Although the workpiece and the laser are specified in the calculations, the numerical approach presented in this work is general and can be extended to other materials or laser wavelengths.

The origin of the coordinate frame is set at the point where electron bombardment occurs. A cylindrical coordinate system is used for the computations since both the electron-beam and the laser normally impinge on the workpiece and the solution will be axisymmetric along the z-direction. The choice of distances between the electron-beam, the laser, and the workpiece are not so critical at this stage of simulations because they only affect the incident profiles of the electrons and photons at the boundaries. These parameters can easily be modified in later studies. The current interest focuses on material removal using a single probe, therefore only a single

electron-beam is used for the machining process. Machining paradigms based on multiple beams are under consideration, and these will be discussed in a future work.

In a vacuum, the only two possible heat transfer mechanisms are radiation and conduction. The emission of radiation from the workpiece at high temperatures is inevitable and needs to be considered. However, radiation heat transfer at nano-scale levels requires more detailed investigation. The radiative properties (i.e. emissivity and absorptivity) at nano-scale, and temperatures beyond melting, are not readily available for gold. In addition, since the emission of radiation depends greatly on surface areas (which are extremely small in this problem), therefore they may not have any impact in the energy balance at all. For these reasons emission is omitted in this study.

It is assumed that the top of the workpiece, the bottom of the transparent substrate, and the side walls are considered insulated. The problem of this sort is naturally unsteady since there are no heat losses. In terms of the computational domain, the overall geometry is a dual layer of cylinders. If the computed temperatures near the side wall of the cylinder are equal to the room temperature, then the solution is physically equivalent to a plane-parallel workpiece with infinite side walls at room temperature.

5.2.2 Grid Setup

The computational grid is expressed in cylindrical coordinates with the grid index m corresponding to the radial direction r, and the grid index n corresponding to the axial direction z. The MC simulations for the electron-beam transport are performed in the uniform grid, which is the domain given by $(r \times z) = (R_1 \times L_1)$ and spans from $m = 0$ to $N_{R1}-1$ and $n = 0$ to $N_{L1}-1$. Since the boundary conditions are defined far away from the incident electron-beam and laser, the use of a uniform grid within the entire computational domain for the conduction problem would be impractical. To overcome this, the grid spacing is increased as it is moved away from the origin. Since the radial distribution of the laser would be larger than that of the electron-beam, the uniform grid is extended from $(R_1 \times L_1)$ to $((R_1+R_2) \times (L_1+L_2))$ when the conduction is modeled. The extended uniform grid is then connected to the non-uniform grid with stretching factors in both r- and z-direction. The grid is set up so that the thickness of the workpiece is described as L_1+L_2

(i.e. $n = 0$ to $N_{L1}+N_{L2}-1$) while the thickness of the substrate is denoted as L_3 (i.e. $n = N_{L1}+N_{L2}$ to $N_{L1}+N_{L2}+N_{L3}-1$). The number of grid points required for the calculations, (i.e. N_{R1}, N_{R2}, N_{R3}, N_{L1}, N_{L2}, and N_{L3}) can be easily determined using the R's, the L's, and the ratios of the two adjacent grid spacing (particularly, the latter over the former) for the r- and z-directions.

A schematic of the grid structure used is given in Figure 5.4. Note that the thicknesses of the workpiece and the substrate are denoted as L_w and L_s, respectively. They are given as:

$$L_w = L_1 + L_2, \tag{5.1}$$
$$L_s = L_3. \tag{5.2}$$

The radial dimension of the workpiece is given by:

$$R_{obs} = R_1 + R_2 + R_3. \tag{5.3}$$

The numbers of grid points required for uniform-grid regions A and B are determined from the following expressions:

$$N_{z1} = \frac{L_1}{\Delta z}, \tag{5.4}$$

$$N_{z2} = \frac{L_2}{\Delta z}. \tag{5.5}$$

As for region C, the grid spacings are stretched linearly (i.e. multiplied by a constant factor, ξ, consecutively) between adjacent grids along the z-direction, so that:

$$L_3 = \Delta z \sum_{l=1}^{N_{z3}} \xi^l. \tag{5.6}$$

Note that L_3 may not be precisely as specified by user because of the rounding error at the last stretched grid spacing. Therefore, if a 1-μm thick workpiece is desired, the actual length of the object will be slightly off depending on the stretching factor used.

Once all the required numbers of grid points are determined, the grid spacing and the coordinate of each computational element in the z-direction follows:

$$\Delta z_n = \begin{cases} \Delta z & \forall \quad n = 0,\dots,N_w - 1, \\ \xi^{n+1}\Delta z & \forall \quad n = 0,\dots,N_s - 1, \end{cases} \tag{5.7}$$

$$
z_n = \begin{cases}
(n+0.5)\Delta z & \forall \quad n = 0,\ldots,N_w - 1, \\[2mm]
N_w \Delta z + \dfrac{1}{2}\xi\Delta z & \forall \quad n = N_w, \\[2mm]
N_w \Delta z - \dfrac{1}{2}\xi^{n+1}\Delta z + \displaystyle\sum_{l=0}^{n}\xi^{l+1}\Delta z & \forall \quad n = 1,\ldots,N_s - 1.
\end{cases}
\tag{5.8}
$$

Similarly, the grid spacing and the coordinate of each computational element in the *r*-direction can be obtained following those in the previous discussion. As a result:

$$
\Delta r_m = \begin{cases}
\Delta r & \forall \quad m = 0,\ldots,N_{uni} - 1, \\[2mm]
\zeta^{m+1}\Delta r & \forall \quad m = 0,\ldots,+N_{non} - 1,
\end{cases}
\tag{5.9}
$$

$$
r_m = \begin{cases}
(m+0.5)\Delta r & \forall \quad m = 0,\ldots,N_{uni} - 1, \\[2mm]
N_{uni}\Delta r + \dfrac{1}{2}\zeta\Delta r & \forall \quad m = N_{uni}, \\[2mm]
N_{uni}\Delta r - \dfrac{1}{2}\zeta^{n+1}\Delta r + \displaystyle\sum_{l=0}^{m}\zeta^{l+1}\Delta r & \forall \quad m = 1,\ldots,N_{non} - 1,
\end{cases}
\tag{5.10}
$$

where $N_{uni} = N_{r1} + N_{r2}$, $N_{non} = N_{r3}$, $N_{r1} = \dfrac{R_1}{\Delta r}$, $N_{r2} = \dfrac{R_2}{\Delta r}$, and $R_3 = \Delta r \displaystyle\sum_{l=1}^{N_{r3}}\zeta^{l}$. Note that the

stretching factor along the *r*-direction for the uniform-grid region is denoted as ζ.

5.2.3 Monte Carlo Method (CSDA) for the Electron-Beam Transport

The distribution of energy deposited in a workpiece due to electron bombardment can be determined using the Monte Carlo Method (MCM). For the case of electrons penetrating a workpiece, a MCM simulates the propagation of electrons inside a workpiece based on cumulative probability distribution functions (CPDFs). The MCM treats an electron-beam as discrete electrons. This is where all the electrons have equal energy. Each electron undergoes a series of elastic and inelastic scatterings inside the workpiece. The histories of many propagating electrons form the resultant profile of absorbed energy.

MCM is used extensively for the solution of the Radiative Transfer Equation (RTE). However, the propagations of photons follow different scattering and absorption probability distributions than electrons (Wong and Mengüç, 2002; Wong and Mengüç, 2004). The scattering characteristics of electrons in a solid target based on MCMs are well outlined in the literature (Murata et al.,

1971; Shimizu et al. 1972; Joy, 1995; Wong and Mengüç, 2004).

The MCM simulation starts by initializing data including the number of ensembles, the location of emission, the initial launching direction, etc. An ensemble represents a bundle of quantum particles (i.e. electrons or photons). Each ensemble is launched, one after the complete propagation of another, assuming that interferences between ensembles do not exist. The distance of interaction, which is the distance the ensemble can propagate before interacting with the medium, is drawn according to the material properties of the medium. The ensemble is then moved from its current position to the next, covering the distance of interaction with its initial direction of emission. If it exits the medium, then it will either contribute to the reflection or transmission. If it does not exit, its weight or energy is altered accordingly and a new propagating direction is determined. The above procedures are then repeated with drawing another distance of interaction.

The energy absorbed from the electron-beam is modeled as internal heat generation when solving the heat conduction problem. The result of the MCM simulations is the energy absorbed from the electron-beam at elements within the grid. The energy is adapted into a normalized energy density $\Psi_{m,n}$ by dividing the absorbed energy by the volume of the element and the total energy of incident electron ensembles. It is mathematically expressed as:

$$\Psi_{m,n} = \frac{\psi_{m,n}}{2\pi r_m \Delta r_m \Delta z_n N_{en} E_0},$$
(5.11)

where $\psi_{m,n}$ is the total kinetic energy of electrons deposited at the (m,n) element, N_{en} is the total number of electron ensembles used (i.e. for the statistical MC simulation, not the actual number of electrons incident on the solid target), E_0 is the initial energy of the electrons, and the quantity $2\pi r_m \Delta r_m \Delta z_n$ is the volume of the (m,n) element. The internal heat generation at a given element (m,n), $\dot{q}_{m,n}^{\text{elec}}$, is then computed with the following expression:

$$\dot{q}_{m,n}^{\text{elec}} = \dot{E} \Psi_{m,n},$$
(5.12)

where $\dot{E}$ is the input power of the electron-beam.

5.2.4 Auxilary Heating using Laser Beam

A collimated laser is considered for the additional heating of the workpiece within a specified radius R_{laser} (see Figure 5.5). It is assumed that the substrate is transparent to the incident laser beam (i.e. no absorption within the substrate) while the metal layer is absorbing. Since the absorption cross-section in a metal is much larger than the scattering cross-section, the laser heating is analyzed in one dimension along the direction of incidence.

The Fresnel reflections at the mismatched interfaces (i.e. different indices of refraction) where the laser is incident need to be considered. For the normal incident case, the fraction of the incident radiant energy reflected, $R_{i \to t}$, as the laser propagates from medium i to t, is given as (Hecht, 1998):

$$R_{i \to t} = \left(\frac{\tilde{n}_t - \tilde{n}_i}{\tilde{n}_t + \tilde{n}_i} \right) \left(\frac{\tilde{n}_t - \tilde{n}_i}{\tilde{n}_t + \tilde{n}_i} \right)^*, \tag{5.13}$$

where $\tilde{n}_i$ and $\tilde{n}_t$ are the complex indices of refraction of the incident and the transmitted media, respectively. In the simulations, the initial heat flux q_0'' of the laser beam propagating through the substrate is prescribed (see Figure 5.5). As the laser first hits the quartz-gold interface, a fraction of the heat flux, $R_{s \to w}$ (= 0.75) is reflected, while the remainder is transmited through the interface. When the laser propagates within the gold film, its energy decreases exponentially with respect to the distance traveled due to absorption. Therefore, the radiant heat flux as a function of depth in the z-direction within the radial area of incidence is given as:

$$q''(z) = \left(1 - R_{s \to w}\right) q_0'' e^{-\kappa(L_w - z)}, \tag{5.14}$$

where κ is the absorption coefficient of the workpiece. The absorption coefficient is determined using the imaginary refractive index of the workpiece, $n_{I,w}$, according to the expression (Modest, 1993):

$$\kappa = \frac{4 \pi n_{I,w}}{\lambda_o}, \tag{5.15}$$

where λ_o is the wavelength of the laser in vacuum. Normally, the incident photons are strongly absorbed within the first few tens of nanometers in a metal. For a $\lambda_o = 355$ nm laser, κ of gold (i.e., $n_{I,W} = 1.848$ (Palik, 1985)) is about 0.0654 nm^{-1} so that 95% of the penetrating photons are

absorbed within 46 nm into the gold film. The thickness of the film considered in this work is sufficiently large enough that the penetrating photons would never reach the other surface of the workpiece. Hence, there is no need to consider the interference effect between the incoming photons from one end and the reflected ones (if there is any) from the other.

To determine the amount of radiant energy per unit volume absorbed by a computational element in the workpiece within a radius of R_{laser}, the radiant heat flux is divided by the Δz_n and is expressed as:

$$\dot{q}_{m,n}^{\text{rad}} = \frac{q''(z)}{\Delta z_n},$$

(5.16)

for $m = 0, 1, \ldots, N_{R\text{laser}} - 1$ and $N_{R\text{laser}}$ is the radial index at R_{laser}.

5.2.5 Thermal Conduction Induced by Electron and Laser Beam

Heat conduction refers to the transport of energy by electrons and phonons. Electrons are the dominant energy carriers in metals while phonons are solely responsible for heat transport in insulators. In semiconductors, both electrons and phonons are equally important. Phonons exist in all materials, and they serve as the main source of electron scattering in metals although their heat capacities are much smaller than those of electrons. In this problem, electrons originated from the electron-beam and photons from the laser penetrate the target workpiece. Therefore, significant amounts of energy and momentum are transferred to the electrons inside the workpiece causing these electrons to become "hot" while the phonons remain "cold." Through scatterings between these propagating electrons and phonons, the incident energies are distributed (or conducted) within the workpiece. Both electrons and phonons eventually reach thermal equilibrium.

The mean free path and the mean free time of the energy carriers are important in the heat transport analysis (Majumdar, 1998). The mean free path of an energy carrier is the average distance that the carrier travels without involving any collision with other carriers. The mean free time of an energy carrier is the average time that the carrier is "free" (i.e. the time required to penetrate a distance equivalent to the mean free path). If the size of the physical domain far exceeds the mean free path, and the time scale is much larger than the mean free time, then macro-

116

scopic model, such as Fourier's law, are used to solve the heat transport phenomena. If the physical length scales are at the same order of magnitude as the mean free path or the observation time is comparable to the mean free time, then special attention should be paid to the propagation of individual energy carriers, especially the collisions and scatterings between carriers (Cahill et al., 2003).

Mean free paths of electrons in materials are usually less than a few nanometers, and speeds of electrons are on the order of 10^6 m/s. Both the mean free paths and the speeds depend on the energies of the electrons (Ashcroft and Mermin, 1976). This leads to mean free times for electrons on the order of femto-seconds. Unlike electrons, mean free paths of phonons span from nanometers to micrometers depending on the temperature. Their mean free times range from picoseconds to nanoseconds since phonons travel at about the speed of sound (i.e. 10^3 to 10^4 m/s) (Tzou, 1997). In this work, the thicknesses of the gold film and the quartz substrate are 200 or 500 nm and 10 μm, respectively. For the metal where the electrons are of concern, the thickness considered far exceeds the electron mean free paths, therefore the transport behavior is spatially diffusive-like. Due to the interest in machining within nano-second intervals, which is at a time-scale much larger than mean free times of the electrons, the ballistic behavior of electrons is not important. As a result, the electronic thermal conduction may be assumed to be macroscopic within the gold film. Unfortunately, because mean free paths for phonons can be comparable to the thickness of the workpiece depending on the temperature, questionable results are produced if the macroscopic approach is employed. In the context of this work, the temperature range (i.e. 300 K-3129 K) involved is vast and mean free paths of phonons at the higher temperatures can easily be as small as a few nanometers or even less. This means that the phonon transport is likely to be diffusive.

Of the concerns regarding heat conduction at nano-scales, especially those for phonons, more detailed theoretical approaches and experiments are required to clarify and prove the validity of various approaches. This is beyond the scope of this work. Since temperatures in this application are high so that both the electron transport and the phonon transport can be diffusive, and since electrons play the major role in heat transport within metals (although electrons and phonons can exist at different temperatures), it is assumed the Fourier law is acceptable for the heat conduc-

tion. Consideration of other models for more accurate electron-phonon transport will be carried out in future works.

The derivation of the energy balance for each element within the workpiece and the substrate is shown next. The heat generation term at each element (*m,n*) in the computational domain will include the sum of both the deposition of electron energy and the absorption of radiant energy:

$$\dot{q}_{m,n} = \dot{q}_{m,n}^{\text{elec}} + \dot{q}_{m,n}^{\text{rad}}. \tag{5.17}$$

5.2.6 Fourier Heat Conduction – Energy Balance for an Element in the Workpiece or Substrate

The energy balance for each computational element is performed according to the convention described in Figure 5.6. Note that the non-uniform grid spacings are portrayed in the schematic. The energy balance for the uniform grid follows in a similar way except that all the Δz's (or Δr's) are constant. To be consistent, all the heat is assumed to be transferred into the node of interest, (*m,n*), and the heat generation term as a result of heating by external means (i.e. laser or electron beam) is denoted as $\dot{E}_{sto}$. The thermal properties (i.e. conductivity, *k*, heat capacity, *C*, and density, ρ) are assumed varying from one element to another due to the transient and spatial temperature variation.

According to the Fourier law of conduction, the heat coming into a computational element is expressed as the the product of the thermal conductivity, *k*, the cross-sectional area, *A*, and the negative gradient of the temperature in the direction of interest. In terms of mathematical description, it is given as:

$$\dot{Q} = -kA\nabla T. \tag{5.18}$$

After accounting for the proper areas, the variation in thermal properties and the temperature gradient, heat propagates into the node (*m,n*) from all four directions, as discussed in Figure 5.6, and can be expressed as:

$$\dot{Q}_1 = 2\pi\left(r_m - \frac{\Delta r_m}{2}\right)\Delta z_n \left(\frac{\Delta r_{m-1}/2}{k_{m-1,n}^{P+1}} + \frac{\Delta r_m/2}{k_{m,n}^{P+1}}\right)^{-1} \left(T_{m-1,n}^{P+1} - T_{m,n}^{P+1}\right), \tag{5.19}$$

$$\dot{Q}_2 = 2\pi \left(r_m + \frac{\Delta r_m}{2} \right) \Delta z_n \left(\frac{\Delta r_m/2}{k_{m,n}^{P+1}} + \frac{\Delta r_{m+1}/2}{k_{m+1,n}^{P+1}} \right)^{-1} \left(T_{m+1,n}^{P+1} - T_{m,n}^{P+1} \right), \tag{5.20}$$

$$\dot{Q}_3 = 2\pi r_m \Delta r_m \left(\frac{\Delta z_{n-1}/2}{k_{m,n-1}^{P+1}} + \frac{\Delta z_n/2}{k_{m,n}^{P+1}} \right)^{-1} \left(T_{m,n-1}^{P+1} - T_{m,n}^{P+1} \right), \tag{5.21}$$

$$\dot{Q}_4 = 2\pi r_m \Delta r_m \left(\frac{\Delta z_n/2}{k_{m,n}^{P+1}} + \frac{\Delta z_{n+1}/2}{k_{m,n+1}^{P+1}} \right)^{-1} \left(T_{m,n+1}^{P+1} - T_{m,n}^{P+1} \right), \tag{5.22}$$

where the superscript '*P*' denotes the time step. Accordingly, the heat generation and the unsteady energy terms are given as:

$$\dot{Q}_{gen} = 2\pi r_m \Delta r_m \Delta z_n \dot{g}_{gen}, \tag{5.23}$$

$$\dot{E}_{sto} = 2\pi \rho_{m,n}^{P+1} C_{m,n}^{P+1} r_m \Delta r_m \Delta z_n \left(\frac{T_{m,n}^{P+1} - T_{m,n}^{P}}{\Delta t} \right). \tag{5.24}$$

Note that at each new time step (*P*+1) the thermal conductivity for various nodes are unknowns. This is because temperatures at that particular instance are to be solved numerically. Therefore, it needs to be extrapolated based on the known previous value in such a way that:

$$k_{m,n}^{P+1} = k_{m,n}^{P} + \left(\frac{\partial k_{m,n}^{P}}{\partial t} \right) \Delta t = k_{m,n}^{P} + \left(\frac{\partial k_{m,n}^{P}}{\partial T} \right) \left(\frac{\partial T_{m,n}^{P}}{\partial t} \right) \Delta t. \tag{5.25}$$

The derivative of *k* in temperature can be easily determined using the data provided in the literature while the derivative of *T* in time is to be approximated as:

$$\frac{\partial T_{m,n}^{P}}{\partial t} = \frac{T_{m,n}^{P} - T_{m,n}^{P-1}}{\Delta t}. \tag{5.26}$$

Equation (5.25) applies not only to thermal conductivity but also to the specific heat and density of the material in the differenced equation. Hence, the energy balance for the element (*m,n*) reads:

$$\dot{Q}_1 + \dot{Q}_2 + \dot{Q}_3 + \dot{Q}_4 + \dot{Q}_{gen} = \dot{E}_{sto}, \tag{5.27}$$

and additional simplifications lead to:

$$\dot{Q}_1 = A_1^{m-1 \to m} \left(T_{m-1,n}^{P+1} - T_{m,n}^{P+1} \right) ; A_1^{m-1 \to m} = \left(\frac{K_{m-1 \to m,n}^{P+1}}{\rho_{m,n}^{P+1} C_{m,n}^{P+1}} \frac{\Delta t}{r_m \Delta r_m} \right), \tag{5.28}$$

$$\dot{Q}_2 = A_2^{m+1 \to m} \left(T_{m+1,n}^{P+1} - T_{m,n}^{P+1} \right) ; A_2^{m+1 \to m} = \left(\frac{K_{m+1 \to m,n}^{P+1}}{\rho_{m,n}^{P+1} C_{m,n}^{P+1}} \frac{\Delta t}{r_m \Delta r_m} \right), \tag{5.29}$$

$$\dot{Q}_3 = A_3^{n-1\to n}\left(T_{m,n-1}^{P+1} - T_{m,n}^{P+1}\right) \; ; \; A_3^{n-1\to n} = \left(\frac{K_{m,n-1\to n}^{P+1}}{\rho_{m,n}^{P+1}C_{m,n}^{P+1}}\frac{\Delta t}{\Delta z_n}\right), \tag{5.30}$$

$$\dot{Q}_4 = A_4^{n+1\to n}\left(T_{m,n+1}^{P+1} - T_{m,n}^{P+1}\right) \; ; \; A_4^{n+1\to n} = \left(\frac{K_{m,n+1\to n}^{P+1}}{\rho_{m,n}^{P+1}C_{m,n}^{P+1}}\frac{\Delta t}{\Delta z_n}\right), \tag{5.31}$$

$$\dot{Q}_{gen} = A_5\dot{g}_{m,n}^{\,gen} \; ; \; A_5 = \left(\frac{\Delta t}{\rho_{m,n}^{P+1}C_{m,n}^{P+1}}\right), \tag{5.32}$$

$$\dot{E}_{sto} = T_{m,n}^{P+1} - T_{m,n}^{P}, \tag{5.33}$$

where:

$$K_{m-1\to m,n}^{P+1} = \left(r_m - \frac{\Delta r_m}{2}\right)\left(\frac{2k_{m-1,n}^{P+1}k_{m,n}^{P+1}}{\Delta r_{m-1}k_{m,n}^{P+1} + \Delta r_m k_{m-1,n}^{P+1}}\right), \tag{5.34}$$

$$K_{m+1\to m,n}^{P+1} = \left(r_m + \frac{\Delta r_m}{2}\right)\left(\frac{2k_{m+1,n}^{P+1}k_{m,n}^{P+1}}{\Delta r_{m+1}k_{m,n}^{P+1} + \Delta r_m k_{m+1,n}^{P+1}}\right), \tag{5.35}$$

$$K_{m,n-1\to n}^{P+1} = \left(\frac{2k_{m,n-1}^{P+1}k_{m,n}^{P+1}}{\Delta z_{n-1}k_{m,n}^{P+1} + \Delta z_n k_{m,n-1}^{P+1}}\right), \tag{5.36}$$

$$K_{m,n+1\to n}^{P+1} = \left(\frac{2k_{m,n+1}^{P+1}k_{m,n}^{P+1}}{\Delta z_{n+1}k_{m,n}^{P+1} + \Delta z_n k_{m,n+1}^{P+1}}\right). \tag{5.37}$$

Subsequently, the overall differenced equation for a node (m,n) is everywhere inside the work-piece or the substrate but the interfaces between the two gives:

$$-A_3^{n-1\to n}T_{m,n-1}^{P+1} - A_1^{m-1\to m}T_{m-1,n}^{P+1} + \left(1 + A_1^{m-1\to m} + A_2^{m+1\to m} + A_3^{n-1\to n} + A_4^{n+1\to n}\right)T_{m,n}^{P+1}$$
$$- A_2^{m+1\to m}T_{m+1,n}^{P+1} - A_4^{n+1\to n}T_{m,n+1}^{P+1} = T_{m,n}^{P} + A_5\dot{g}_{m,n}^{\,gen} \tag{5.38}$$

Depending upon the location of the node, all A's are to be evaluated according to the corresponding properties of the material.

5.2.7 Fourier Heat Conduction – Energy Balance for an Element of the Workpiece and the Substrate at the Interface of Two Distinct Materials

In the previous derivations, transient and spatial variations of the thermal physical properties were accounted for and the differenced equation for a computational element inside either the workpiece or the substrate was derived. The energy balance at the interface between the workpiece and the substrate can be obtained in a similar fashion. It is necessary to take into consideration the contact resistance between the two materials and to incorporate the correct thermal properties into the differenced equation. A schematic of the energy balance of a computational ele-

ment of the workpiece one top of the substrate is depicted in Figure 5.7.

Note that the various terms in the energy balance equation are identical to those derived in the previous section except that $\dot{Q}_4$ is to be modified to account for the contact resistance and the thermal properties of the substrate. It is expressed as:

$$\dot{Q}_4 = 2\pi r_m \Delta r_m \left(\frac{\Delta z_n / 2}{k_{m,n}^{P+1}} + R_c'' + \frac{\Delta z_{n+1}/2}{k_{m,n+1}^{P+1}} \right)^{-1} \left(T_{m,n+1}^{P+1} - T_{m,n}^{P+1} \right). \tag{5.39}$$

Following the similar derivations as discussed, the energy balance equation for a node in the workpiece adjacent to that in the substrate becomes:

$$-A_{3w}^{n-1\to n}T_{m,n-1}^{P+1} - A_{1w}^{m-1\to m}T_{m-1,n}^{P+1} + \left(1 + A_{1w}^{m-1\to m} + A_{2w}^{m+1\to m} + A_{3w}^{n-1\to n} + \widehat{A}_{4w,s}^{n+1\to n} \right) T_{m,n}^{P+1}$$
$$- A_{2w}^{m+1\to m}T_{m+1,n}^{P+1} - \widehat{A}_{4w,s}^{n+1\to n}T_{m,n+1}^{P+1} = T_{m,n}^{P} + A_{5w}\dot{g}_{m,n}^{\text{gen}} \tag{5.40}$$

where

$$\widehat{A}_{4w,s}^{n+1\to n} = \left| \frac{\left(\widehat{K}_{m,n+1\to n}^{P+1} \right)_{w,s} \frac{\Delta t}{\Delta z_n}}{\left(\rho_{m,n}^{P+1} C_{m,n}^{P+1} \right)_{w}} \right|, \tag{5.41}$$

$$\left(\widehat{K}_{m,n+1\to n}^{P+1} \right)_{w,s} = \left(\frac{2\left(k_{m,n+1}^{P+1} \right)_s \left(k_{m,n}^{P+1} \right)_w}{\Delta z_{n+1}\left(k_{m,n}^{P+1} \right)_w + \Delta z_n \left(k_{m,n+1}^{P+1} \right)_s + 2\left(k_{m,n}^{P+1} \right)_w \left(k_{m,n+1}^{P+1} \right)_s R_c''} \right). \tag{5.42}$$

The subscripts 'w' and/or 's' in the A's require that the properties of the workpiece and the substrate be used when calculating the coefficients, respectively.

For the case where the substrate element is of interest at the interface of the two materials, the energy balance equation for the element is similar to those given in Figure 5.6 with the exception that $\dot{Q}_3$ needs to be modified. An illustration of the notations used is given in Figure 5.8. Accordingly, the energy balance equation for this node should read:

$$-\widehat{A}_{3w,s}^{n-1\to n}T_{m,n-1}^{P+1} - A_{1s}^{m-1\to m}T_{m-1,n}^{P+1} + \left(1 + A_{1s}^{m-1\to m} + A_{2s}^{m+1\to m} + \widehat{A}_{3w,s}^{n-1\to n} + A_{4s}^{n+1\to n} \right) T_{m,n}^{P+1}$$
$$- A_{2s}^{m+1\to m}T_{m+1,n}^{P+1} - A_{4s}^{n+1\to n}T_{m,n+1}^{P+1} = T_{m,n}^{P} + A_{5s}\dot{g}_{m,n}^{\text{gen}} \tag{5.43}$$

with

$$\hat{A}_{3w,s}^{n-1\to n} = \left|\frac{\left(\hat{K}_{m,n-1\to n}^{P+1}\right)_{w,s}\Delta t}{\left(\rho_{m,n}^{P+1}C_{m,n}^{P+1}\right)_s\Delta z_n}\right|, \tag{5.44}$$

$$\left(\hat{K}_{m,n-1\to n}^{P+1}\right)_{w,s} = \left(\frac{2\left(k_{m,n-1}^{P+1}\right)_w\left(k_{m,n}^{P+1}\right)_s}{\Delta z_{n-1}\left(k_{m,n}^{P+1}\right)_s + \Delta z_n\left(k_{m,n-1}^{P+1}\right)_w + 2\left(k_{m,n}^{P+1}\right)_s\left(k_{m,n-1}^{P+1}\right)_w R_c''}\right). \tag{5.45}$$

5.2.8 Fourier Heat Conduction – The System of Equations and Matrices

In order to solve the temperature distributions within the workpiece and the substrate, it is important to collect all the differenced equations for all the nodes and form the system of equations. For the sake of simplicity, the following quantities are defined as:

$$N_r = N_{r1} + N_{r2} + N_{r3} - 1, \tag{5.46}$$
$$N_z = N_{z1} + N_{z2} + N_{z3} - 1, \tag{5.47}$$

The boundary conditions are given as:

$$\begin{aligned}
T_{-1,n}^{P+1} &= T_{0,n}^{P+1} & \forall\ n &= 0,\ 1,\ldots,N_z-1,\\
T_{m,-1}^{P+1} &= T_{m,0}^{P+1} & \forall\ m &= 0,\ 1,\ldots,N_r-1,\\
T_{m,N_z}^{P+1} &= T_{m,N_z-1}^{P+1} & \forall\ m &= 0,\ 1,\ldots,N_r-1,\\
T_{N_r,n}^{P+1} &= 2T_0 - T_{N_r-1,n}^{P+1} & \forall\ n &= 0,\ 1,\ldots,N_z-1.
\end{aligned} \tag{5.48}$$

When all the nodal equations are gathered, a system of equations can be constructed in the form of $A\vec{T} = \vec{B}$ where A is a $(N_r{\times}N_z){\times}(N_r{\times}N_z)$ matrix. Details about matrices A and B can be found in Appendix A.

If the radiation interaction needs to be incorporated into the system, then the boundary conditions will change accordingly. For any boundary exchanging radiant heat with the surroundings, the energy balance at the boundary should read:

$$-k\frac{\partial T}{\partial n} = \varepsilon\sigma\left(T^4 - T_{surr}^4\right). \tag{5.49}$$

Applying this to the top surface of the workpiece and discretizing the equation yield:

$$2\pi r_m\Delta r_m\left(\frac{k_{m,n}^{P+1}}{\Delta z_n/2}\right)\left(T_{m,n}^{P+1} - T_{m,n-1/2}^{P+1}\right) = \varepsilon_{m,n}^{P+1}\sigma\left[\left(T_{m,n}^P\right)^4 - T_{surr}^4\right]. \tag{5.50}$$

Note that the non-linearity in the temperature has been conveniently removed by assuming the

radiation loss is given by the previous time step P. Next, the temperature at the node $(m,n-1/2)$ shall be approximated as the mean value between two adjacent nodes, namely nodes $(m,n-1)$ and (m,n), and it is expressed as:

$$T_{m,n-1/2}^{P+1} = \frac{1}{2}\left(T_{m,n-1}^{P+1} + T_{m,n}^{P+1}\right). \tag{5.51}$$

As a result, the boundary condition at the top of the workpiece is given as:

$$2\pi r_m \Delta r_m \left(\frac{k_{m,n}^{P+1}}{\Delta z_n/2}\right)\left(T_{m,n}^{P+1} - \frac{1}{2}\left(T_{m,n-1}^{P+1} + T_{m,n}^{P+1}\right)\right) = \varepsilon_{m,n}^{P+1}\sigma\left[\left[\frac{1}{2}\left(T_{m,n-1}^{P} + T_{m,n}^{P}\right)\right]^4 - T_{surr}^4\right]. \tag{5.52}$$

$$
\begin{aligned}
T_{-1,n}^{P+1} &= T_{0,n}^{P+1} & \forall \; n &= 0,\, 1,\dots,N_z - 1, \\
T_{m,-1}^{P+1} &= T_{m,0}^{P+1} & \forall \; m &= 0,\, 1,\dots,N_r - 1, \\
T_{m,N_z}^{P+1} &= T_{m,N_z-1}^{P+1} & \forall \; m &= 0,\, 1,\dots,N_r - 1, \\
T_{N_r,n}^{P+1} &= 2T_0 - T_{N_r-1,n}^{P+1} & \forall \; n &= 0,\, 1,\dots,N_z - 1.
\end{aligned}
\tag{5.53}
$$

5.2.9 Solving the System of Equations and Accounting for "Melting" and "Evaporation"

After discretizing the entire computational domain, the differenced equations for all the nodal points are collected to form a system of linear equations. It is given in matrix representation as:

$$B\vec{T} = \bar{D}, \tag{5.54}$$

where B is a $(N_R \times N_L) \times (N_R \times N_L)$ matrix, $\vec{T}$ is the temperature field, and $\bar{D}$ is known from the discretizations. This contains temperatures at the previous time step and heat generation terms at various nodes. Equation (5.54) is solved for $\vec{T}$ using the point successive overrelaxation (SOR) numerical scheme (Matthews and Fink, 1999).

In order to properly account for "melting" and "evaporation", the latent heats of fusion and evaporation need to be included in the solution scheme. In solving the system of equations, the point SOR sequentially solves the nodal temperature, which can be modified to account for "melting" and "evaporation." In the current solution scheme, the code detects any nodal temperatures beyond the prescribed "melting" or "evaporation" temperature at any given time step. If there are any nodal temperatures computed at a given time step beyond the specified temperatures, the code re-solves the system of equations with those nodal temperatures fixed at either one of the temperatures, accordingly. After the temperature field is solved, the energy balance is

performed at each node to determine the heat generation term q_{gen}. Each calculated q_{gen} is the energy required to maintain that particular nodal temperature at the "melting" or "evaporation" temperature. Note that during this particular time step, energies are still supplied by electrons from the electron-beam to those nodes. A fraction (i.e. the calculated q_{gen}) of the supplied energy is then used for sustaining the specified temperature while the rest is stored at the corresponding node to overcome the latent heat of fusion, followed by the latent heat of evaporation.

Once a node has enough latent heat, its temperature is allowed to increase at the next time step. The stored heat never exactly equals the specified latent heats of fusion and evaporation because of the increment time interval, so the energy supplied is fixed. Therefore, when an element overcomes the latent heat at a given time step, the excess energy from the electron-beam is added to the same element at the next time step, preventing unrealistic energy destruction.

5.2.10 Computational Parameters

In principle, the material properties such as the thermal conductivity, the specific heats, etc. are temperature-dependent. This is especially the case in this application where the variation of temperatures across the workpiece is large. They also may change depending upon air pressure. Unfortunately, these properties at temperatures beyond melting and at various air pressures are not readily available either theoretically or experimentally. Therefore, constant material properties at the ambient condition are used. In this work, gold is the selected workpiece, which has a density (ρ_w) of 19,300 kg/m^3, a specific heat (C_w) of 129 J/kg-K, and a conductivity (k_w) of 317 W/m-K at room temperature. The melting temperature of gold is given as 1,336 K while its evaporation temperature is 3,129 K (Incropera and DeWitt, 1996). The complex index of refraction of gold at the wavelength of 355 nm is given as 1.74-i1.848 (Palik, 1985). Its atomic number (Z) and the atomic weight (A) are 79 and 196.97 g/mol, respectively. The corresponding mean ionization potential (J) is 0.790 keV (Joy, 1995). For the transparent substrate quartz is selected, which has a ρ_s = 2,650 kg/m^3, C_s = 765.85 J/kg-K, and k_s = 1.77 W/m-K (Incropera and DeWitt, 1996). A typical value of 1.5 is assumed for the index of refraction of quartz (Modest, 1993).

The incident profile of the electron-beam is a Gaussian distribution with a $1/e^2$ radius of $R_{electron}$ (Jacques and Wang, 1995). In this work, two beam profiles are assumed. One of which is

with $R_{electron}$ = 50 nm, and the second is twice the former (i.e. $R_{electron}$ = 100 nm). The initial energies of electrons originating from the electron-beam are considered to be either 4 or 6 keV. All the temperature distributions are determined after about one nano-second (ns) of the machining process.

5.2.11 Selection of Computational Time Steps, Grid Spacings and Tolerances

If very fine grid spacing were adapted in the simulations, a significant amount of computational time would be needed for both the Monte Carlo and the conduction heat transfer simulations to converge. Since the computational domains for both models need to overlap, a finer grid on the MC simulation would lead to an over-refined grid for the conduction problem.

The computational grid requirements are determined after a number of preliminary numerical experiments are conducted. An effective grid scheme can be constructed where Δr = 1.25 nm and Δz = 1.25 nm with 10% increases in the r- and 5% increases in the z-grid spacings starting from $m = N_{R1} + N_{R2}$ and $n = N_{L1} + N_{L2}$, respectively (see Figure 5.4). The size of the uniform grid is taken to be either ($r \times z$) = (400 nm x 200 nm) or (400 nm x 500 nm) when the thickness of the gold film considered is 200 nm or 500 nm. These values keep the computational time reasonable while maintaining acceptable resolutions for the MCM predictions. A change of temperature in the order of 1 K is observed when halving the grid spacings, while still holding the other computational variables constant. Decreasing the grid stretching effect inflicts a temperature change of order 1 K. The Δt's in the various simulated cases are chosen in such a way that accurate (i.e. within O(1K)) temperature distributions are obtained. In addition, the convergent tolerance for the SOR scheme is chosen to be 10^{-6}, guaranteeing a convergence of the temperature distribution to within O(1K). As a result, an overall uncertainty is expected in the order of 1 K for the temperature field in all of the calculations.

5.2.12 Normalized Energy Density Deposited Due to Electron Beam

Figure 5.9 depicts the electron energy deposited within gold as determined by the MCM for two selected beam profiles (i.e. $R_{electron}$ = 50 nm and 100 nm) and two initial kinetic energies of electrons (i.e. E_0 = 4 keV and 6 keV). Each of the sub-figures depicts the average result of five separate MC runs and the number of statistical ensembles was about 10 x10^6 for each run to en-

sure smooth spatial distributions. One important observation is that by decreasing the incident E_0, the peak amount of electron energy deposited per unit volume within the workpiece increases although the penetration depth decreases (see (a) and (c) in Figure 5.9). This may seem rather confusing since one might expect electrons with higher initial energy to deposit more energy per unit volume within the workpiece. Although more energy is deposited within the workpiece, it is distributed over a wider space since electrons penetrate deeper into the workpiece with higher initial energy.

Similarly, when the incident electron-beam profile is wide, the incident electrons are more dispersed compared to the case when the incident beam profile concentrates at the point of incidence. Subsequently, this causes the dispersion of the electron energy absorbed within the metal over a wider range. Therefore, it is observed that the energy deposited per unit volume within gold in Figure 5.9(a) is less than that in Figure 5.9(b) near the axis of the incident beam.

5.2.13 Temperature Distribution Due to Electron Beam

Using the normalized energy densities obtained from the MC simulations, the temperature distributions were determined with the Fourier law. Interest is in the material removal during a period of about one nano-second. The conduction code runs until the element at the origin evaporates (i.e. latent heat of evaporation is overcome and $T > T_{evap} = 3129$ K). The temperature distribution due to the electron energy deposited within gold for the case where $R_{beam} = 100$ nm and $E_0 = 4$ keV (see Figure 5.9(a)) is illustrated in Figure 5.10(a). The evaporated region is portrayed in the white color. The time required for evaporation to occur is found to be about $t = 0.9$ ns for an electron-beam power of 0.5 W. The required current, or the number of electrons needed per unit time equals 125 μA or 7.8 x 10^{14} electrons/s for a power of 0.5 W at 4 keV. Since a 500-nm gold layer on top of a 10-μm transparent substrate is assumed, the isotherms bend sharply at $z = 500$ nm as the material properties change at the interface. Note that the figure only portrays the portion of the computational domain where the highest temperatures exist. The element at the origin where evaporation occurs is removed as shown by a white spot in the upper left-hand corner.

Using the MC result given in Figure 5.9(b), the temperature distribution for an incident electron-beam of $R_{electron} = 50$ nm is computed and depicted in Figure 5.10(b). The power of the elec-

tron-beam was 0.305 W and evaporation started at $t = 0.7$ ns. Note that the beam has less power, yet evaporation occured sooner when compared to the previous case (i.e. $R_{electron} = 100$ nm). This demonstrates that the required power for evaporation can be reduced when the beam is narrow. It also indicates that the temperature of gold film can be increased much faster at the origin if the electron-beam is more focused. If a wider machining area is desired, then a wider beam should be used even though this slows down the process and may require greater beam power.

Figure 5.10(c) shows the temperature distribution within gold film at $t = 1$ ns for an incident electron-beam of 6 keV with an input power of 0.615 W. It is obvious that increasing the applied voltage tends to spread the electron energy over a deeper range since the penetration depth is also increased. This elevates the input power required from the beam, nad is evident from the comparison between (a) and (c) in Figure 5.10. To compare the current required between the two (i.e. $E_0 = 4$ keV versus 6 keV with the same R_{beam}), the evaporation time should be identical in both cases. Therefore, it is essential to determine the required input power for the 6-keV beam needed to cause evaporation at $t = 0.9$ ns instead of 1 ns. An extra simulation with a beam power of 0.625 W was performed, and it was determined that the evaporation time is at 0.8 ns. Assuming a linear relationship between the time for evaporation and the power, it takes approximately 0.62 W for the 6-keV electron-beam to start evaporation at 0.9 ns as opposed to 0.5 W for the 4-keV one. This leads to a current of 103 µA for the former and 125 µA for the latter. The current required for achieving evaporation is actually reduced when the beam energy increases. However, this preliminary conclusion should not be generalized since there are other factors affecting the outcome, including the evaporation time and the thicknesses of the film. In-depth calculations and explorations are needed for further clarification of the affects of other parameters.

Note in Figure 5.10(c) that evaporation first occurs in the layers beneath the surface, creating the gold vapor, which is expected. It is clear from Figure 5.9(c) that the region with the highest density of energy deposited by the electron beam is not at the surface, but a few nanometers beneath it. However, the vapor is trapped inside the material since the surface has not been evaporated. The instant the element at the origin is removed, the vapor is released, leaving a noticeable evaporated region as seen in the figure. Further examination on the temperature distributions reveals a similar trend in both (a) and (b) in Figure 5.10, except that the evaporated regions are

smaller. Though it may be informative to compare among the electron-beam powers or currents required for various cases to evaporate the exact volume and shape, it is impractical since the penetration depth varies depending on the incident kinetic energy of the electron-beam.

5.2.14 Temperature Distribution Due to Electron-Beam and Laser

An alternative to reduce the power required from the CNT is to supply additional heat via a laser. To investigate this, additional numerical simulations were carried out. Figure 5.11 shows the temperature distribution obtained with laser heating for the same conditions used in Figure 5.10(a). To be consistent with other cases, the result given here is at the instance where the element at the origin evaporates. With the help of a laser heat flux of 5.09 $\mu W/nm^2$ ($= q_0''$) incident on the bottom of the gold layer within an area of a radius of $R_{laser} = 300$ nm measured from the z-axis, the time required for evaporation is shortened from $t = 0.9$ ns (as in Figure 5.10(a)) to 0.5 ns. By coupling the laser heat flux required, the incident area, and the Fresnel reflection when the laser first enters the vacuum-substrate interface, the laser power needed for this specific case is calculated to be about 1.5 W. Although this approach can reduce the power required from the electron-beam, the thickness of the workpiece is a limiting factor since the laser heats from the back of the workpiece. In addition, the absorption of radiant energy in a metal is strong, therefore the gold film thickness needs to be as small as possible in order for the laser heating to affect the material in the vicinity of the incident electron-beam.

For the simulation results depicted in Figure 5.12, the thickness of the gold layer is 200 nm. The specifications of the electron-beam and the laser remain the same as in Figure 5.11. In this case, the laser heating is more effective in reducing the power required from the electron-beam. Figure 5.12(a) is the temperature field at about 1 ns where evaporation occurs at the origin for a reduced electron-beam power of 0.25W, while Figure 5.12(b) depicts the time required for evaporation as a function of various powers of the electron-beam (with or without the use of a laser) for a 200-nm layer of gold film. One obvious observation from the figure is that the time of evaporation is reduced when the laser is employed for heating from the back of the workpiece. Notice that the evaporation time increases as the electron-beam power is decreased. For a strong electron-beam, using a laser would not be necessary since the evaporation time is so short. The workpiece starts to evaporate before the heat provided by the laser is conducted to the top.

If both the electron-beam and the laser are directed towards the same point of incidence, the laser heating is used to its greatest advantage. This would require that both beams be obliquely oriented, which would require revisions to the model. This can be investigated in future work.

5.2.15 Transient Temperature of the Origin

Figure 5.13 shows the transient temperatures of the element at the origin around an infinitesimal radius of $\Delta r = 1.25$ nm and a depth of $\Delta z = 1.25$ nm, under different conditions. The descriptions of the various cases can be found in the figure caption. In short, *Case* 1 sets the standard for the remaining four cases, *Case* 2 refers to a more focused electron-beam, *Case* 3 refers to the inclusion of laser heating, *Case* 4 refers to the reduced gold thickness with laser heating, and *Case* 5 is for an electron-beam with higher incident kinetic energy.

It is observed that the transient curve shifts to the left as the electron-beam is focused narrower (see *Cases* 1 and 2), indicating that the transient temperature at the origin is always higher for the latter case. This shows that a highly-focused electron-beam is desired when elevating local temperatures in this application, resulting in shortened evaporation time. When the laser heating is used simultaneously with the electron-beam, it has no effect on the temperature of the origin until $t = 0.15$ ns at which the temperature starts to increase compared to that of the case where it is excluded (see *Cases* 1 and 3). The starting time for the laser to aid the heating process at the origin can be reduced by decreasing the thickness of the workpiece. This is evident from the transient curve of *Case* 4. Note that all the cases have the same input power for the electron-beam except the final case where the incident beam energy is lowered to 6 keV. This is because the computational cost required for the case where a 6-keV electron-beam of 0.5 W is used is relatively expensive. The power was increased to 0.615 W to reduce the cost while maintaining the trend that the temperature at the origin, as heated by a lower-energy beam is lower at all time (see *Cases* 1 and 5).

5.2.16 Comments

In this section, the possibility of achieving nano-scale machining on a thin metallic film deposited on a transparent substrate was investigated. The effects of simultaneous electron and photon

processing were considered. The propagation of the electron-beam inside the gold film was modeled using a MC simulation while the laser heating was treated as a one-dimensional problem. Both the electron and photon energy accumulated inside the workpiece were considered as heat generation in the conduction heat transfer model. The temperature field inside the workpiece was predicted. The results show that a power input of half-a-watt supplied from an electron-beam alone is sufficient enough to start local evaporation during about 1 ns. This can be achieved by using either a 4- or 6-keV electron-beam, provided the spatial distribution of the emitted electrons from the electron-gun is no greater than 100 nm and closely resembles a Gaussian distribution. With the help of focused laser heating, the power required from the electron-beam can be reduced by a factor of 50% if the workpiece is sufficiently thin. Although a comprehensive theoretical frame work is presented here for predicting the power and current required for nano-scale machining, the model needs further modifications and improvements for applications to real systems. Some of these requirements are briefly outlined below.

The accuracy of the electron energy deposition profiles predicted using the MC simulation for the electron-beam transport can be further improved by employing a Discrete Inelastic Scattering Approach (DISA) (see Ding and Shimizu, 1996 for further details) instead of a Continuous Slowing-Down Approach (CSDA), which was adapted here. The DISA uses the experimental optical data for the workpiece to treat all the scattering events discretely, which is more accurate than using the stopping power as in the CSDA. This is especially true if the incident energy of the electron-beam is around 1 keV. The propagations of secondary electrons as a result of the inelastic scatterings (i.e. energy lost from the primary electrons of the electron-beam to the electrons inside the workpiece) would further spread the incident energy from the electron-beam over a wider volume. This is not accounted for in the current MC model.

The radiation losses and the pressure- and temperature-dependent material properties need to be incorporated in the conduction modeling. When these effects are included, the required power for the electron-beam could either be lower or higher. If radiative losses were added, the required power would be higher since the workpiece would lose heat (if it is significant). However, it is known that materials become more temperature-resistant as the temperature increases, therefore it implies that heat loss by conduction at the heating region would be reduced. As a result, the

input power needed from the electron-beam would be reduced as well, which benefits the case of using only the electron-beam.

The use of the Fourier heat conduction model implies that both electrons and phonons are at the same temperature. This approximation needs to be replaced by a two-temperature model (TTM) (Tzou, 1997). The TTM allows electrons and phonons to exist at different temperatures. This is important because the electron-beam first transfers energy to electrons inside the workpiece and then causes elevation of the electron temperature. Consequently, electrons exist at a temperature much higher than that of phonons. Interactions between electrons and phonons then establish equilibrium at which both immerse at a single temperature (Hohlfeld, 2000).

5.3 Sequential Nano-Patterning Using Electron and Laser Beams – A Numerical Methodology

5.3.1 Problem Description and Assumptions

In the previous modeling of laser assisted material processing using an electron-beam, the feasibility of machining at nano-scale level was studied (Wong et al., 2004). The problem was similar to that given in Figure 5.14 except that the electron-beam was stationary and a simple 2-D axisymmetric assumption was employed. The electron-beam propagation inside the workpiece (i.e. a thin gold film) was modelled using a MCM, which treats electron energy losses continuously along the path of propagation. The laser propagation was treated as a one-dimensional problem in a non-scattering medium since absorption of radiation is strong inside metals. The Fresnel reflection at the mismatched boundary between the substrate and the workpiece was taken into consideration. It was found that an electron-beam with a power of about 0.5 W was sufficient to initialize evaporation at nano-scale level within a nano-second. This requirement could easily be halved if a laser was used simultaneously. These observations were based on the premise that there were no radiation losses at the boundaries and material properties were not temperature-dependent.

In this section, these assumptions are removed and the solution of the electron-beam transfer and heat conduction problems are extended to a realistic 3-D case. In addition, temperature-dependent thermophysical properties are considered, which change during the course of the pat-

131

terning process. The problem presented is a time-dependent one the electron-beam is allowed to move from one location to another to create a desired pattern of nano-indentations.

The computational domain, which has a square cross-sectional area ($L_x \times L_y$), consists of a workpiece and a transparent substrate where the former rests on top of the latter, as shown in Figure 5.14. The workpiece is assumed to be gold on which the electron-beam impinges from the top, while the laser heats it from the bottom. The substrate is assumed to be quartz and transparent to the incident laser. The thicknesses of the workpiece and the substrate are denoted L_w and L_s, respectively. The entire object is assumed to be placed inside a vacuum chamber.

An electron source is considered to emit electrons, with predetermined initial kinetic energies, directly onto the top surface of the workpiece. A laser with a wavelength of 355 nm is chosen to heat the workpiece from the bottom of the substrate. The laser wavelength is selected to minimize reflection of the incident radiation. This is because gold reflects radiation significantly at wavelengths beyond 355 nm. In addition, a 355 nm wavelength corresponds to the third harmonic of commercially available Nd:YAG lasers. The type of the electron source used in the simulation is irrelevant as long as it can emit sufficient focused electrons. In simplifying the current investigation, it is assumed that there are no electron sources or drains imposed on the workpiece. Such additional applied voltages across the workpiece would alter the propagation of penetrating electrons from the electron-beam and may also cause non-uniform joule heating within the workpiece.

The 3-D Cartesian coordinate system is used in this case since the electron-beam is moved along the workpiece surface to create a desired pattern, and the solution will be entirely non-symmetric. This feature makes the solution of the problem quite different and more realistic than the one presented in our previous approach (Wong et al., 2004). The selections of distances between the electron-beam, the laser, and the workpiece are not critical at this stage of simulations since they only affect the incident profiles of the electrons and photons at the boundaries. These parameters can easily be modified in later studies. It is assumed that the top of the workpiece, the bottom of the transparent substrate, and the side walls exchange energy with the surroundings via radiation transfer, and these effects are included in the heat conduction modeling. Temperature

dependent properties are considered throughout the simulations. However, we assume that the medium is homogeneous and free of defects and cracks. This is necessary for such fine application purposes. Such an assumption simplifies the heat transfer analysis, as electron and photon scatterings become extremely complicated when there are impurities in the medium.

5.3.2 Computational Methodology

To account for all three heat transfer phenomena simultaneously (i.e. electron-beam transport, laser propagation, and heat conduction) for relatively large dimensions of the geometry, the grid is stretched away from the origin at which the electron-beam first hits. Here, 'relatively' refers to the comparison between the spatial energy spread of the incident electron-beam and the overall dimension of the geometry. The structure of the computational grid employed is depicted in Figure 5.15. The grid spacings in all three directions are uniform at the center of the cross-section area and near the top of the domain. The MC simulation for the electron-beam transport is performed within the uniform grid. Since the laser enters the geometry from the back through the transparent substrate, the grid in the depth direction is stretched starting from the interface between the workpiece and the substrate towards the bottom of the substrate.

The overall goal is to determine the transient temperature distribution of the material while the electron-beam and the laser are heating it and to observe the heating requirement to evaporate the material. The modeling of this problem involves three steps. First, the thermal energy deposited by penetrating energetic electrons inside the workpiece needs to be computed. It is assumed that the kinetic energy that electrons lose is converted instantaneously into thermal energy and stored in the workpiece. Second, the radiant energy absorbed by the workpiece from the incident laser is determined. Finally, all the thermal energy deposited in the workpiece via electron bombardments and laser heating are considered as heat generation in the heat conduction equation.

Energy Deposition due to Electron-Beam

The governing equation of the electron-beam propagation inside solids, which shall be called the *Electron Transport Equation* (ETE), closely resembles the *Radiative Transfer Equation* (RTE) including both extinction and in-scattering. The only difference between these two equa-

133

tions is that the absorption and scattering properties of the medium vary according to the energy of the propagating electrons for the ETE. Once the energy of the electrons changes, the scattering probability in the governing equation changes as well. This is not the case for the RTE. This means that the ETE has to be solved in a dynamic fashion, because after each scattering event there is a new set of values for the properties. Casting in terms of intensity of electrons, the ETE can be written as (Wong and Mengüç, 2004):

$$
\frac{1}{v_e}\frac{\partial I_e}{\partial t} + \hat{s} \cdot \nabla I_e = -\left[\sigma_e^{inel}(E) + \sigma_e^{el}(E)\right]I_e \\
+ \frac{1}{4\pi}\sum_{E'}\int_{\Omega'}\sigma_e^{el}(E')\Phi_e(E',\theta',\phi';E,\theta,\phi)I_e'(E,\theta',\phi',t)d\Omega'
$$
(5.55)

The MC simulation used in the radiative transfer can be easily modified for electron-beam transport. Details about these simulations are already outlined in this work (Wong and Mengüç, 2004). The distribution of energy deposited in a workpiece due to the electron bombardment can be determined using such a MCM (Wong and Mengüç, 2004; Wong et al., 2004). The MCM used here simulates the propagation of electrons inside a workpiece based on probability distribution functions and treats an electron-beam as discrete electrons, where all electrons have equal amount of energy upon entering the workpiece. Each electron undergoes sequential elastic and inelastic scatterings before exiting the medium or being absorbed. It is the contribution of all the remaining energy of the exited electrons that provides the reflected and absorbed energy of the incident electron beam.

In order to include the heating effect due to the energy deposition by electrons from the electron-beam in the heat conduction equation, the amount of heat generated in the elements exposed to the beam needs to be determined. Using the MCM, the energy deposited from the electron-beam at any element (m,n,o) within the grid can easily be tallied. This energy (denoted as $\psi_{m,n,o}$) is then converted into a normalized energy density $\Psi_{m,n,o}$ by dividing it by the volume of the element and the total energy of incident electron ensembles. This is mathematically expressed as:

$$
\Psi_{m,n,o} = \frac{\psi_{m,n,o}}{\Delta x_m \Delta y_n \Delta z_o N_{en} E_0},
$$
(5.56)

where N_{en} is the total number of electron ensembles used (i.e. for the statistical MC simulation purposes, not the actual number of electrons incident on the solid target), E_0 is the initial energy

134

of the electrons, and the quantity $\Delta x_m \Delta y_n \Delta z_o$ is the volume of the (m,n,o) element. The internal heat generation at a given element (m,n,o), $\dot{q}_{m,n,o}^{elec}$, is then computed using the expression:

$$\dot{q}_{m,n,o}^{elec} = \dot{E}\Psi_{m,n,o}, \tag{5.57}$$

where $\dot{E}$ is the input power of the electron-beam.

Absorption of Laser Energy

A collimated laser is considered for additional threshold heating of the workpiece within a specified radius R_{laser} (see Figure 5.16). The assumption is made that the substrate is transparent to the incident continuous laser beam (i.e. no absorption within the substrate), while the metal layer is absorbing. Since the absorption cross-section in a metal is much larger than the scattering cross-section, the laser heating is analyzed in one dimension along the direction of incidence, and the scattering is neglected. The Fresnel reflections at the mismatched interface (i.e. due to different indices of refraction) where the laser is incident need to be considered for accurate representation of laser heating. For the normal incident case, the fraction of the incident radiant energy reflected, $R_{i \to t}$, as the laser beam propagates from medium i to t, is given as (Hecht, 1998):

$$R_{i \to t} = \left(\frac{\tilde{n}_t - \tilde{n}_i}{\tilde{n}_t + \tilde{n}_i}\right)\left(\frac{\tilde{n}_t - \tilde{n}_i}{\tilde{n}_t + \tilde{n}_i}\right)^*, \tag{5.58}$$

where $\tilde{n}_i$ and $\tilde{n}_t$ are the complex indices of refraction of the incident and the transmitted media, respectively. In the simulations, the initial heat flux q_0'' of the laser is prescribed (see Figure 5.16). As the laser beam first hits the quartz-gold interface, a fraction of the heat flux, $R_{s \to w}$ (= 0.75), is reflected while the remainder is transmitted through the interface. When the laser propagates within the gold film, its energy decreases exponentially with respect to the distance traveled due to absorption. Therefore, the radiant heat flux as a function of depth in the z-direction within the radial area of incidence is expressed as:

$$q''(z) = (1 - R_{s \to w})q_0'' e^{-\kappa(L_w - z)}, \tag{5.59}$$

where κ is the absorption coefficient of the workpiece. The absorption coefficient is determined using the imaginary refractive index of the workpiece, $n_{I,w}$, according to the expression (Modest, 1993):

135

$$\kappa = \frac{4\pi n_{\mathrm{I,w}}}{\lambda_{\mathrm{o}}}, \tag{5.60}$$

where λ_{o} is the wavelength of the laser in vacuum. Normally, the incident photons are strongly absorbed within the first few tens of nanometers in a metal. For a $\lambda_{\mathrm{o}} = 355$ nm laser, κ of gold is about 0.0654 nm^{-1} (corresponding to $n_{\mathrm{I,W}} = 1.848$ (Palik, 1998)) so that 95% of the penetrating photons are absorbed within 46 nm into the gold film. The thickness of the film considered in this work is large enough, so the penetrating photons would never reach the other surface of the workpiece. Hence, there is no need to consider the interference effect between incoming photons from one end and the reflected ones (if there are any) from the other.

For simulations, the amount of radiant energy (i.e. $\dot{q}_{m,n,o}^{\mathrm{rad}}$) absorbed per unit volume within a computational element in the workpiece is needed. To determine this value, the radiant heat flux is divided by the Δz_o and expressed as:

$$\dot{q}_{m,n,o}^{\mathrm{rad}} = \frac{q''(z)}{\Delta z_o}, \tag{5.61}$$

for any index m in the x-axis and n in the y-axis inside the area heated by the laser, and o is the index of the element along the z-direction.

Heat Conduction

Heat conduction refers to the transport of energy by electrons and phonons. Electrons are the dominant energy carriers in metals while phonons are solely responsible for heat transport in insulators. In semiconductors, both electrons and phonons are equally important. Phonons are based on lattice vibrations and exist in all materials. They serve as the main source of electron scattering in metals, although their heat capacities are much smaller than those of electrons. In this application, electrons originating from the electron-beam and photons from the laser are assumed to penetrate the target workpiece. A significant amount of energy and momentum are transferred to electrons inside the workpiece causing these electrons to become "hot" while the phonons remain "cold." Through scatterings between these propagating electrons and phonons, the incident energies are distributed (or diffused) within the workpiece. Both electrons and pho-

nons eventually reach thermal equilibrium.

It is hypothesized that thermal electronic heat conduction inside the workpiece in this application is diffusive in space and time. The Fourier law of conduction should apply without significant error (Wong et al., 2004). However, phonon transport in this case may not be entirely diffusive depending on the temperature. The lower the temperature, the longer the wavelength of phonons which could easily exceed the object dimension in this problem. This would result in semi-ballistic or ballistic transport of the phonons inside the workpiece (Wong et al., 2004). Such thermal transport phenomena deviate significantly from the traditional diffusive heat conduction and cannot follow the Fourier Law. Despite the arguments, the Fourier law of conduction was chosen. The electron and phonon temperatures are treated as a whole and described using a single temperature. This is the initial effort of modeling such a complicated transport phenomenon. In the next chapter, the electron temperature will be separated from the phonon temperature, allowing the concept of the so-called two-temperature model to be incorporated into the modeling. Eventually, the electric field induced by the penetrating electrons will be considered as well by using the electron-phonon hydrodynamic approach.

The derivation of the energy balance for each element within the workpiece and the substrate is not outlined as they are fairly standard and well-known (Incropera and DeWitt, 1996). The exception is that the treatment of the heat generation term in each energy balance equation will include the sum of both the deposition of electron energy from the electron-beam and the absorption of radiant energy from the laser. Since material properties vary according to temperature, it is assumed that each computational element will be assigned different thermal properties, such as thermal conductivity and specific heat, based on its temperature at the previous time step. In addition, the radiation exchange between the surfaces of the entire object and the surroundings is also included to account for radiation losses. It is observed, however, that radiation losses are not significant enough to cause any changes in the temperature field. This is mostly due to the fact that the emitting and absorbing surface areas are extremely small. The system of equations derived by collecting all the energy balances of each control volume is solved by using the point Successive Over-Relaxation (SOR) numerical scheme (Matthews and Fink, 1999).

137

To properly account for melting and evaporation, the latent heats of fusion and evaporation need to be included in the solution scheme. The way these effects are incorporated in the SOR scheme is described in the previous section. Basically, the algorithm is constructed in such a way that once a given nodal temperature exceeds the melting or evaporating temperature, its temperature ceases to increase until the latent heat of fusion or evaporation is overcome. At the same time, the code determines the amount of heat needed to be supplied to that node in order to maintain it at the fixed temperature. It then subtracts it from the actual heat provided by the electron-beam and the laser while the excess energy is stored for overcoming the latent heat.

In this section, cooling phenomena such as condensation and solidification are encountered since the electron-beam is moved from one location to another. Once the beam is re-positioned, the previously heated spot would cool since there is no energy source for sustaining the heating. Accounting for such effects is similar to that of melting and evaporation, except that the processes are reversed. The algorithms used for melting and evaporation are also used for condensation and solidification except that the processes are reversed. In other words, as a computational node cools to condensation/freezing temperature, it remains at the fixed temperature until all of its latent heat is lost.

After conducting extensive numeral simulations, what was observed was heating by the electron-beam tends to first evaporate layers beneath the surface since electrons are capable of penetrating deep into the material. However, computational elements that have temperatures beyond the evaporating temperature and enough latent heats of fusion and evaporation are considered trapped inside the material and they continue to increase their thermal energy. Only when the elements above them (up to the surface) are evaporated are those computational elements assumed to go through evaporation and thus be removed. In the code, the evaporated nodes are assumed to have zero thermal conductivity (i.e. insulated). There are two reasons for this assumption. First, the observed radiation losses from the boundaries are negligible since the surface areas involved are extremely small. Second, free heat convection does not exist in vacuum conditions and does not need to be accounted for. Hence, whenever a computational element at the surface is evaporated, the adjacent nodes are exposed to vacuum and their boundaries act as insulated since there are no heat loss mechanisms, therefore it is mathematically correct to replace

the conductivity of the evaporated elements with zero value.

5.3.3 Computational Parameters

In this work, an electron-beam of 0.25 W is assumed to achieve the nano-machining process. The electron-beam has an initial kinetic energy of 4 keV and a spatial Gaussian distribution with a $1/e^2$ radius of 25 nm, while the laser has a wavelength of 355 nm and a power of 0.35 W. The laser beam is assumed to be collimated within a radius of 150 nm, which is extremely difficult to achieve considering the wavelength of the laser. The reason for choosing such an extreme number is because the uniform grid that is used in the simulation has lateral dimensions of (350 nm × 350 nm). This was necessary to maintain the computational costs within the limit of the current computing power. The laser heating needed to be within this grid to avoid excessive computational errors. Even though such a small radius of laser heating is considered, this assumption does not really affect the outcome of the current simulations. The entire computational domain is assumed to be within the laser heating zone, and even if a much larger laser heating domain is realized, the electron-beam based machining predictions would not be altered at all.

The simulations with the Monte Carlo approach are performed using ten-million electron bundles in order to produce sufficiently smooth resultant statistical distributions. The final results reported below are the average of five such runs. Five nm for spatial grid size was used within the uniform grid. The grid size was then stretched beyond the uniform grid with a 10% increment with respect to the previous step size. The time step used in the simulation was set to 3.125 femto-seconds (fs). Details and reasons for choosing such parameters are discussed below.

Since the interest is in material processing, the temperature range involved is large, ranging from the room temperature 300 K to the evaporating temperature 3129 K for gold. As a result, the material properties vary widely between these two limits. However, the thermal properties of gold beyond melting temperature are not readily available in the literature. For the sake of simplicity, these properties are linearly extrapolated beyond the melting temperature based on the existing data points given in the literature. The material properties of gold and quartz, as a function of temperature, are shown in Figure 5.17. During the heating process, the substrate is assumed to stay as solid (i.e. $T < \sim 2000$ K for quartz).

Note that all the properties mentioned and given in this work are at standard air pressure. Under the ultra high vacuum condition, these properties ought to vary since atoms would not be packed as closely as they would be in atmospheric pressure. Unfortunately, this data, especially for gold, is not readily available in the literature, neither experimentally nor theoretically. The thermophysical data available for gold at temperatures beyond melting and at various vacuum conditions is extremely scarce and does not allow for a comprehensive sensitivity study. Therefore, the predictions given in this work can be considered as conservative in terms of the power of the electron-beam required to evaporate gold, since the actual evaporating temperature of gold in vacuum is expected to be lower.

The simulations given below were carried out on a personal computer with an Intel Pentium 4 processor of 3 GHz with a total of 2-GB memory, which is more than sufficient for this work. A typical run takes about three days, including both the Monte Carlo simulation and the heat conduction, on the dedicated computer depending on the time and space steps chosen. Eventually similar cases are expected to be run on more than one computer or even a cluster of computers.

5.3.4 Results and Discussions

Monte Carlo (MC) Simulations for Electron-Beam Transport

The results obtained from the MC simulation are discussed in the previous work (Wong et al., 2004), where the effect of various input parameters such as the electron-beam energy, the spatial distribution of electrons, etc. on the electron energy deposition profile and the temperature distribution was shown. Here, the electron-beam is used to pattern nano-holes which have sizes around 5-10 nm wide and deep while the laser acts as the additional heating mode in order to reduce the input power from the electron-beam.

Instead of making random nano-holes in the workpiece using an electron-beam, the attempt was made to create a more complex pattern, for which the letters 'UK' was chosen. However, there were several issues to be addressed in machining such a complex pattern. First, whenever a

region is evaporated by the electron-beam, the boundary of the geometry changes. The current MC simulation of the electron-beam propagation is based on the fact that the geometry remains intact throughout the entire process. Therefore, if the electron-beam were to impinge on or near the evaporated region, the electron energy deposition profile would be different compared to that before evaporation occurred. This would require a re-run of the MC simulation according to the new geometry. Since the change of the boundary could be dynamic in real time if the electron-beam were dragged along the surface, this situation was avoided in this work as the simulation procedures could get fairly complicated and increase computational costs.

Using the spatial energy deposition profile of an electron-beam as calculated by the MC simulation, the positions that the electron-beam needs for drilling were determined. This was done in order to create the UK pattern and to avoid any drilled nano-holes confining within the profile. Figure 5.18 shows all the electron energy deposition profiles at various locations. Note that there is only one electron-beam available at a time for machining, therefore the distribution shown in Figure 5.18 is a hypothetical situation where there exists 21 beams impinging on the workpiece at once. This is for visualization of various beam locations purpose only.

Heating Sequences

Based on the numerous initial numerical experiments conducted, it was observed that the most effective way of using a laser in assisting the machining process was by preheating the workpiece with the laser and without the electron-beam. Due to the strong absorption of laser energy inside gold, direct radiant heating of the top surface of the workpiece (which is desired to lower the heat input from the electron-beam) would not be possible. The experimental approach that was adapted required the laser beam to enter the workpiece through the backside, therefore heating the top surface required a conduction mechanism. For this reason, it was discovered that the laser had to be turned on first to elevate the temperature of the workpiece, since it took time for the heat to conduct to the top surface.

The time required to initialize the thermal electronic heating remains arbitrary. The longer the heating process, the hotter the surface becomes, and the additional heat input required from the

electron-beam to create evaporation is further minimized. In the current analysis, once the top center of the workpiece reaches to a temperature of 700 K after being heated by the laser, the electron-beam is activated to achieve nano-scale evaporation on the surface.

The heating sequence considered here follows the numerical sequence depicted in Figure 5.18(c). Upon the forming of a nano-hole, the electron-beam is switched off and moved instantaneously to the next location. In the actual experiment, there would be some delay in the heating process from one spot to another due to the mechanical or electrical control mechanism of the probe that produces the electron-beam. These details need to be discussed with the actual experiments. The heating spots are separated far enough apart that two adjacent sequential electron beam profiles do not overlap. Therefore, by turning off the electron-beam and moving it to the next location, the beam will not interact with the voids created previously.

The temperature distribution of the workpiece and the substrate at 0.42 ns are depicted in Figure 5.19 where the laser is used to heat the workpiece for the first 0.12 ns. The temperature distribution given in Figure 5.19 is at the instant where the last nano-hole at the upper right corner is formed, so the temperature is high at that location right after the evaporation occurred. It should be pointed out that the dark blue dots within the high temperature field do not correspond to the lowest temperature given in the contour legend. They are evaporated regions or empty voids.

Figure 5.19(b) shows the top view of the workpiece where the desired UK pattern is clearly visible. However, it is observed that the nano-holes created are not uniform in size, some are wider than others. In order to visualize the depth of each structure, two cross-sections (i.e. A-A and B-B) of the workpiece are plotted in Figure 5.19(c) and Figure 5.19(d). The structures created seem to be non-uniform in depth as well. One reason is the fact that the heating by the laser is non-uniform across the space resulting in a variation of heat received by each location in the space. However, this effect seems to be minor compared to that imposed by the electron-beam itself. Notice that the first nano-hole created for the letter 'U' is the smallest while the width and the depth of the subsequent ones increase along the A-A direction. Close examination of the structures created, reveals that the third, fourth and fifth holes are equal in size. When the elec-

tron-beam turns perpendicularly to create the sixth and the seventh, the dimensions of the created structures appear to change once again, as portrayed in Figure 5.19(d). All of these imply that in order to create uniform structures in one constant direction using this approach, the first few would deviate from the others as the process progresses. As the direction changes, it alters the dimensions of the subsequent indentations due to the previously non-uniform local heatings at various spots. If both the electron-beam and the laser were to switch off after each indentation, and if the workpiece were permitted to cool down, then all the evaporated spots would be more uniform in size and depth provided the electron-beam and the laser are synchronized spatially as well as temporally.

The Transient Behavior and Convergence Tests

The transient behaviors of various locations, namely points 1-5 and 17-21, on the surfaces of the workpiece are depicted in Figure 5.20. The laser is turned on for the first 0.12 ns until the top center of the workpiece reaches over 700 K and then the electron-beam is then activated. It can be seen in Figure 5.20(a) that the temperatures of all the points increase steadily during that interval of time. When the electron-beam starts to bombard the workpiece, the temperature increases drastically as a result of energy transfer from electrons to the material. During the course of the machining process in creating the pattern, the heating is highly localized at various locations during a given time period. Therefore, the surface of the workpiece experiences heating and cooling depending upon the location. This is evident in Figure 5.20(b).

The convergence tests for the numerical model of heat conduction have been carried out in this work in order to access the numerical errors. Both temporal and spatial convergence tests have been performed on the conduction model. The temporal convergence test is carried out by first computing results starting from a time step of $\Delta t =12.5$ fs, and subsequently halving the time step to compare the difference between the two sets of results. The transient temperatures as a function of time steps at three different locations on the top surface are depicted in Figure 5.21. The transient temperatures computed using various time steps agree, implying that the errors due to the temporal discretization is negligible. This can be evident in Figure 5.21(a), which is the transient temperature at Point 1, the first targeted spot. For other targeted spots, for example, Points

10 and 21, the transient temperature profiles converge slower compared to that of Point 1, as illustrated by Figure 5.21(b) and Figure 5.21(c). Overall, the transient temperature trends computed using various time steps are identical. Since reducing the time step to obtain an extremely accurate temperature profile is not of interest here, therefore the results presented in the previous sections are based on a time step of 3.125 fs.

The spatial convergence test is rather difficult to perform compared to the temporal convergence test. This is due to the way the machining sequence was implemented. The program is coded in such a way that the e-beam stops machining whenever a target element is entirely evaporated. It then proceeds to machine the next spot. This means that the machining process is accelerated when a smaller grid element is utilized and the evaporated region becomes smaller as well. This can be seen in the transient temperature profiles of Point 21 given for two different grid sizes in Figure 5.22(b) and Figure 5.22(c). However, the results demonstrate that the transient temperatures at various spots converge when Point 1 is being machined, as evident in Figure 5.22 for the first 0.15 ns. Based on this observation, using a spatial step size of 5 nm is sufficient to suppress the numerical errors caused by the spatial discretization.

Note that the time duration of the machining process proposed here is considerably small (i.e. less than 1 ns). It is always a concern whether or not one can have a sufficient number of electrons to permit the use of a statistical approach such as the Monte Carlo method to model the electron-beam propagation in such a short period. A closer examination at the machining reveals that each target spot is typically exposed to the e-beam for about 0.02 ns before evaporation is achieved. For an electron-beam with a power of 0.25 W and an initial electron energy of 4 keV, the number of electrons supplied per unit time is roughly 4×10^{14} per second. The number of electrons impinged on the target within 0.02 ns is about 7,800. In the simulations, tens of millions of statistical bundles have been used to reduce the statistical noise to a satisfactory level, even though the actual number of electrons available is much less than that. In dealing with this concern, the Monte Carlo simulation was performed for a single electron beam with only 7,800 statistical bundles. As expected, the deposition distribution was not as smooth as that simulated using millions of bundles, however, the order of magnitude and the distribution itself were comparable in both cases. This means that if an actual experiment is to be carried out, the evaporated

regions may not be as organized and clean as those predicted by the theory. Nevertheless, the overall machining trend predicted here shall prevail and serve as a moderate study tool for understanding nano-machining using electron beams.

5.3.5 Comments

A methodology of using an electron-beam coupled with a laser for forming nano-structures in a sequential fashion is demonstrated numerically. A Monte Carlo Method used in typical radiative transfer applications was transformed to model the electron-beam transport to determine the electron-energy deposition distribution rates within a thin gold film. A 355-nm wavelength laser was utilized as the additional heating source for aiding in the machining process. It is shown that by using this methodology a complicated pattern can be written within 0.5 ns actual time with an electron-beam of 0.25 W assisted by a 0.35 W laser. The dimensions of the pattern created are about 200 nm × 300 nm. This would not be possible if the laser was used alone since the lateral spread of photons at the given wavelength covers roughly the entire pattern.

The use of the Fourier heat conduction model implies that both electrons and phonons are at the same temperature. This approximation needs to be replaced by a two-temperature model (TTM) (Tzou, 1997). The TTM allows electrons and phonons to exist at different temperatures, which is important since the electron-beam first transfers energy to electrons inside the workpiece, and then causes elevation of the electron temperature. Consequently, electrons exist at a temperature much higher than that of phonons. Interactions between electrons and phonons subsequently establish equilibrium at which both immerse at a single temperature (Hohlfeld et al., 2000). Future studies are planned to develop and incorporate this model with the Monte Carlo Method in electron-beam transport to describe the heating process more efficiently.
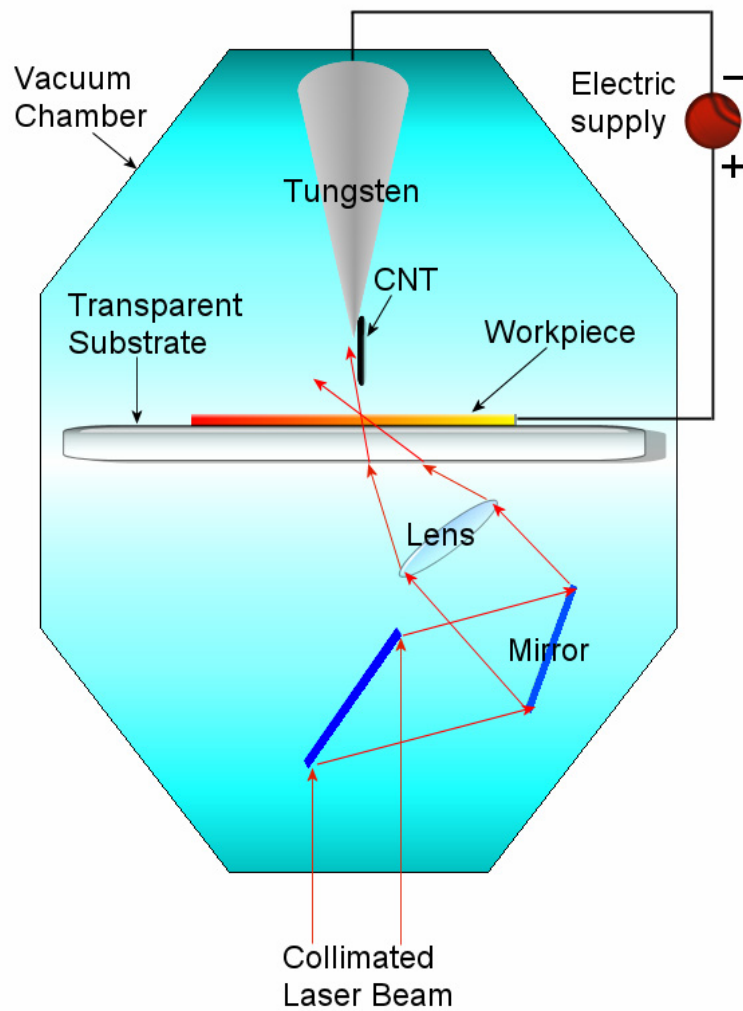
Figure 5.1   The schematic of the proposed machining process using electron field emission from a nano-probe is given.

146
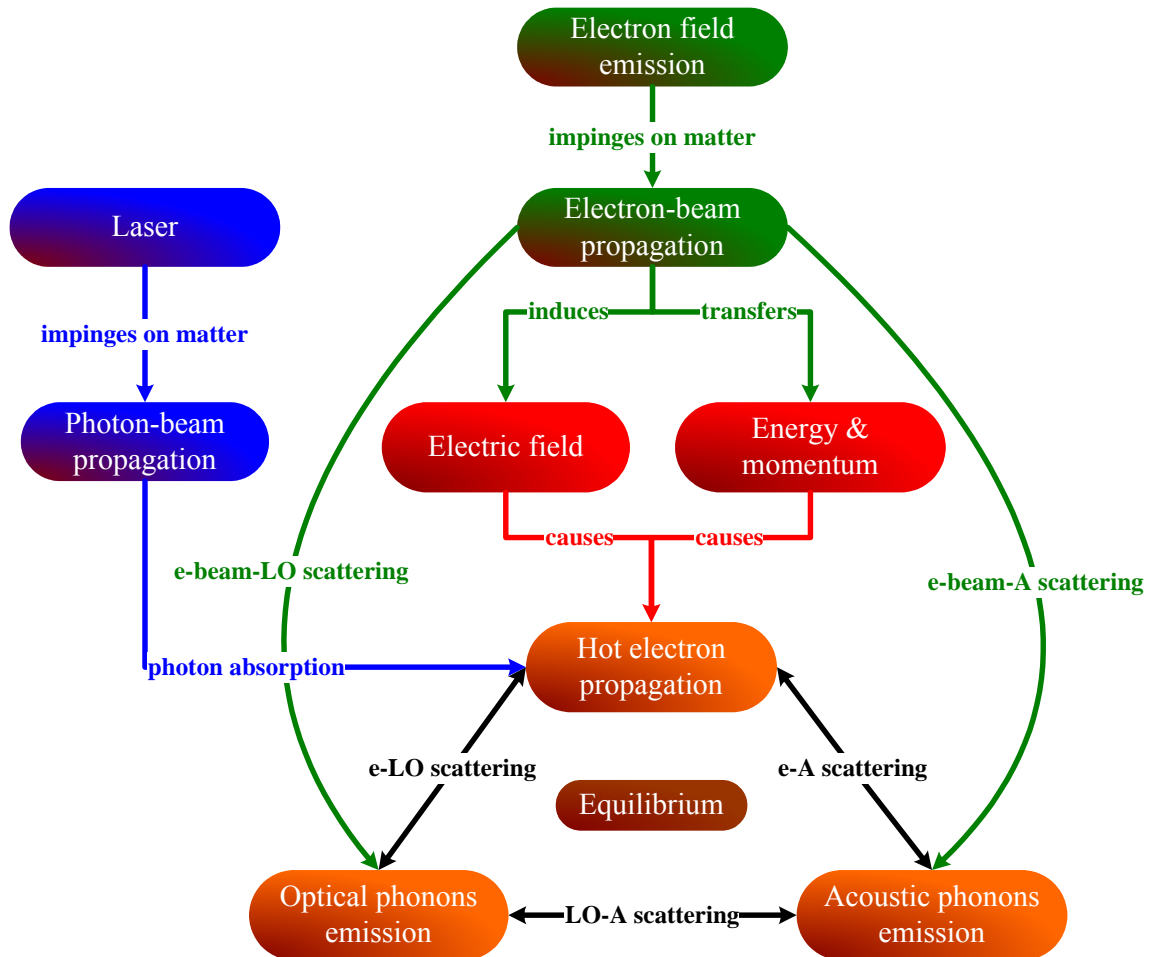
Figure 5.2   Thermal transport mechanisms during electron- and laser-beam heating of a workpiece are illustrated. The region heated by photons originating from the laser-beam, and electrons originating from the electron-beam do not overlap each other. This prevents heating of the electron-beam by the laser.
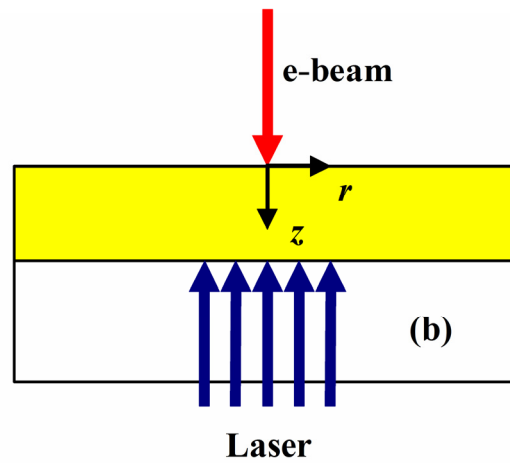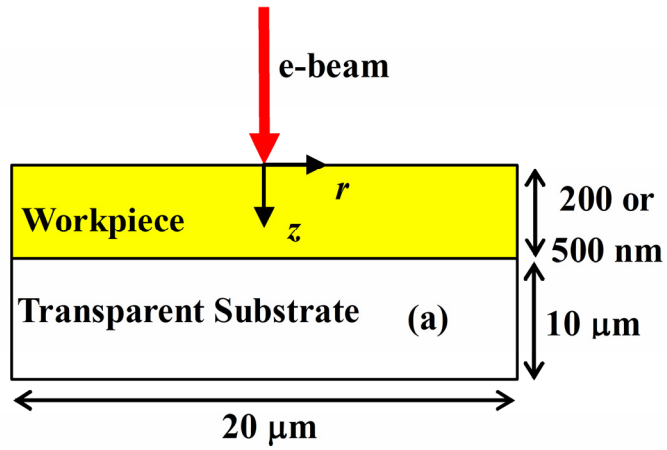
Figure 5.3   Schematic for the nano-scale machining process considered. A work-piece is positioned on top of a substrate. The substrate is assumed to be transparent to the incident laser. Two different evaporation methods are considered: (a) Electron-beam impinges perpendicularly on the top of the workpiece, and (b) Electron-beam and laser impinge normally on the workpiece at opposite directions.
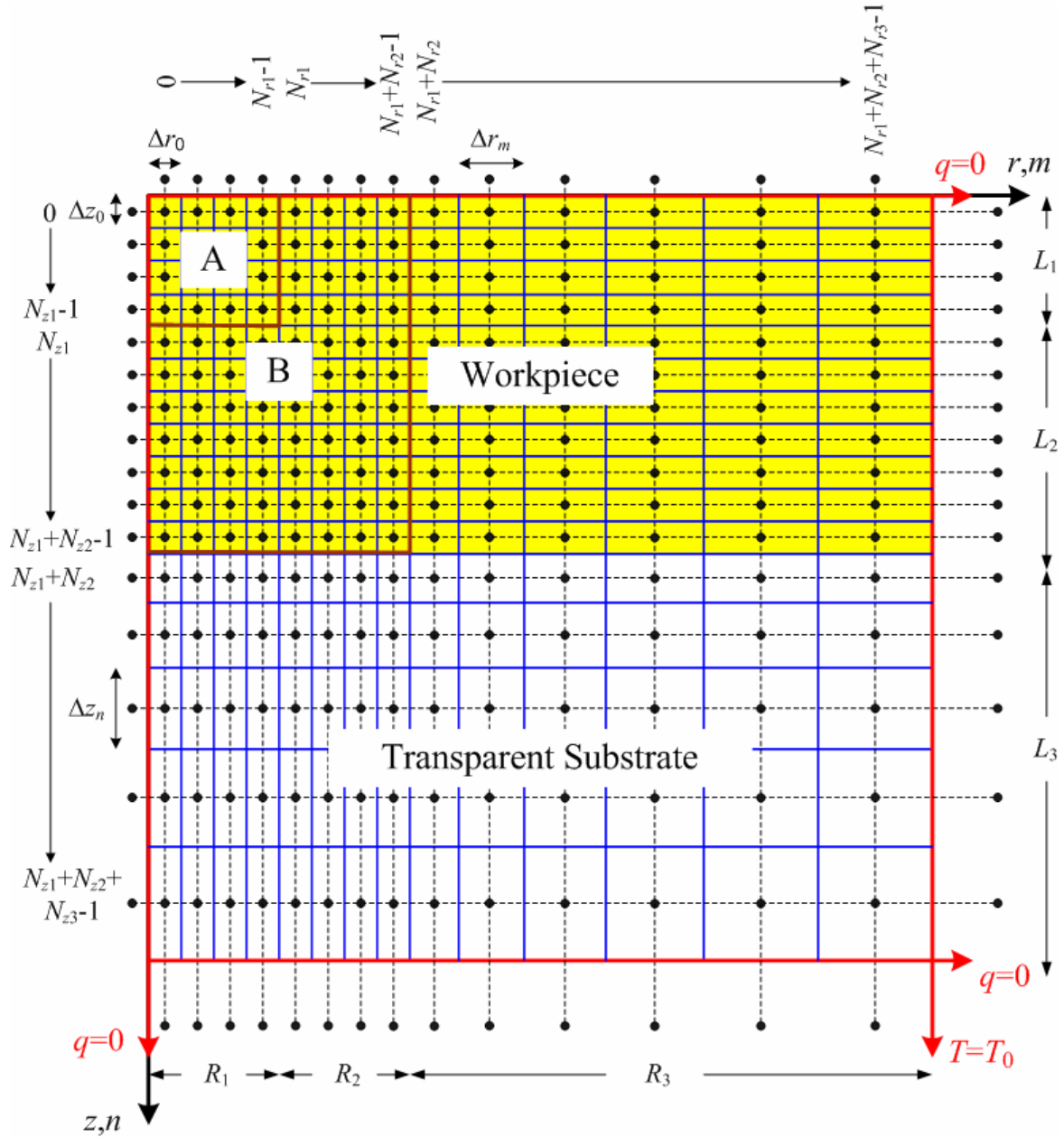
Figure 5.4   The grid setup used in modeling the electron-beam transport, the laser propagation, and the heat conduction inside the workpiece. The grid is sub-divided into two zones: 1) A and B with uniform spacings in both r- and z-directions, 2) C and D with non-uniform spacings where the grid is stretched along r- and z-directions with independent factors. A is where the MC simulation in the electron-beam transport is performed while B extends A uniformly in both r- and z-directions in order to account for the laser heating. The boundary conditions are (a) adiabatic at $r = 0$ due to symmetry and (b) adiabatic at $r = R_1 + R_2 + R_3$, $z = 0$ and $z = L_1 + L_2 + L_3$ since it is assumed that there are no convection and radiation losses.
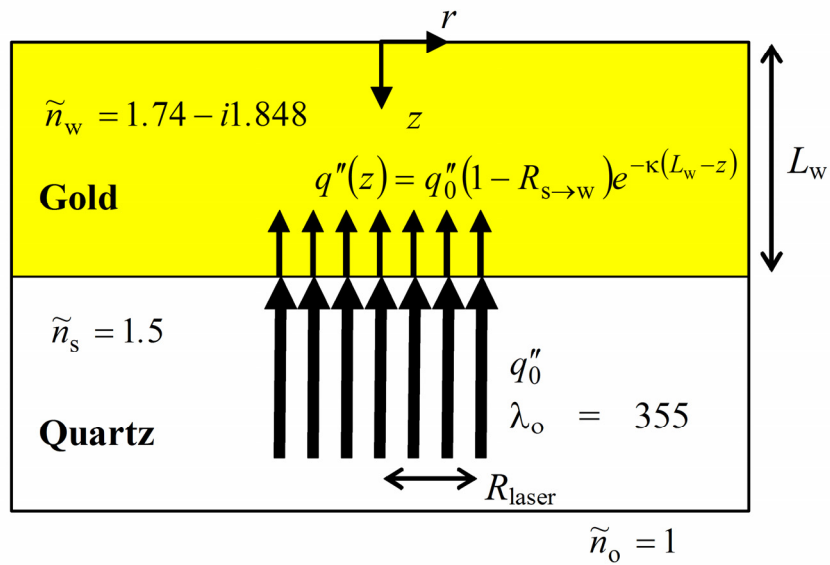
Figure 5.5   Schematic for the radiative transfer inside the workpiece. The impinging laser has a radial dimension of R_{laser} and a wavelength of 355 nm. Since the absorption of radiant energy in a metal is strong, a 1-D radiation model with exponential decaying of radiant energy in the direction of propagation is employed. The scattering of photons is neglected. The complex index of refraction of gold is at the wavelength of the laser. $R_{s \to w}$ is the reflectivity at the interface between gold and quartz when the incident direction is from quartz to gold.
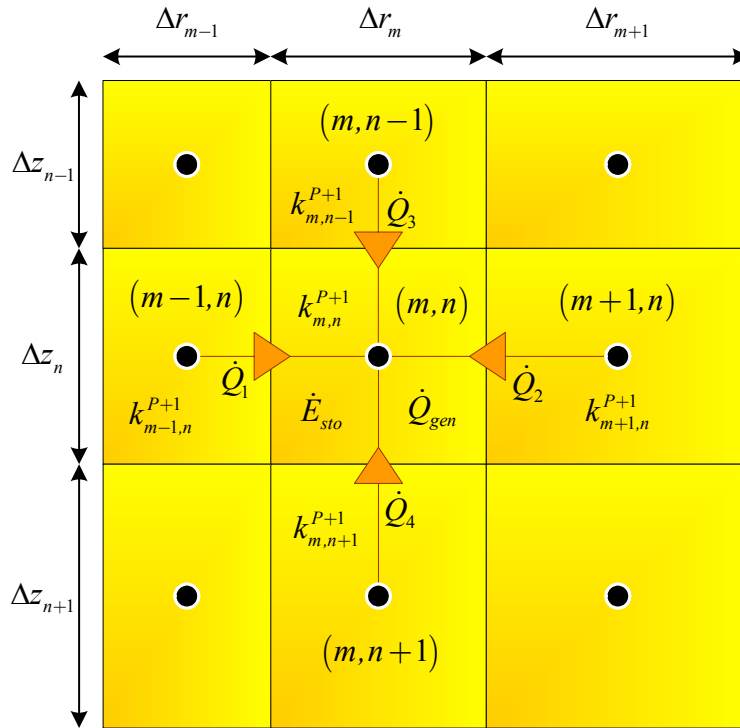
Figure 5.6   The energy balance of a computational element inside the workpiece or the substrate (except at the interfaces between the two) is given. Note that the non-uniform grid spacings are portrayed in the schematic. The energy balance for the uniform grid follows similarly except that all the Δz's (or Δr's) are constant. To be consistent, all the heat is assumed to be transferred into the node of interest, (m,n). The heat generation term as a result of heating by external means (laser or electron beam) is denoted as $\dot{E}_{sto}$. The thermal properties (i.e., conductivity, k, heat capacity, C, and density, ρ) are assumed varying from one element to another due to the transient and spatial temperature variation.
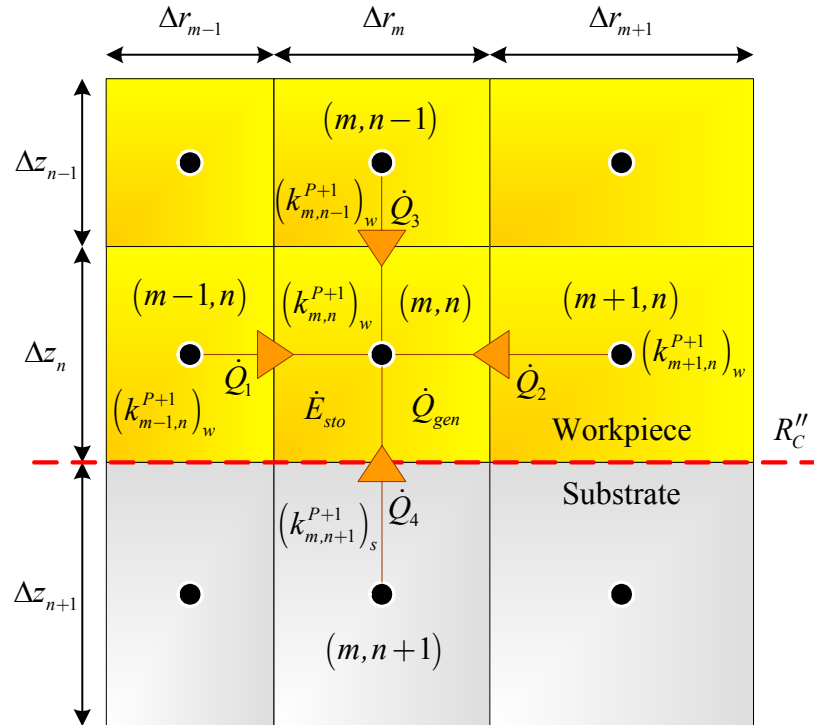
Figure 5.7   The energy balance of a computational element of the workpiece at the interface between the workpiece and substrate is depicted. The subscript 'w' refers to that of the workpiece while 's' refers to the substrate. There exists a contact resistance between two different types of materials, here it is denoted as R_c''.
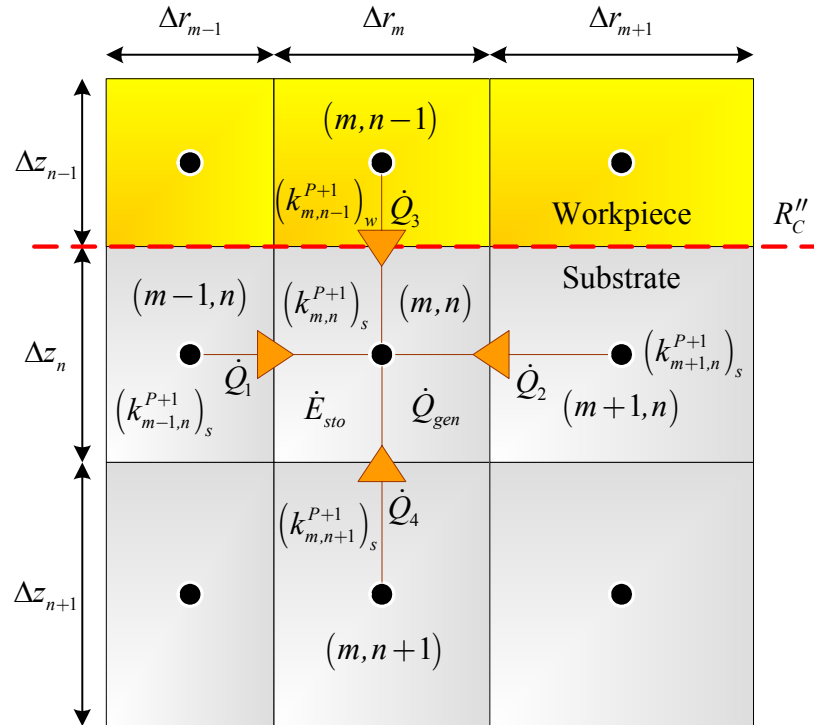
Figure 5.8   The energy balance of a computational element of the substrate at the interface between the workpiece and substrate is depicted.
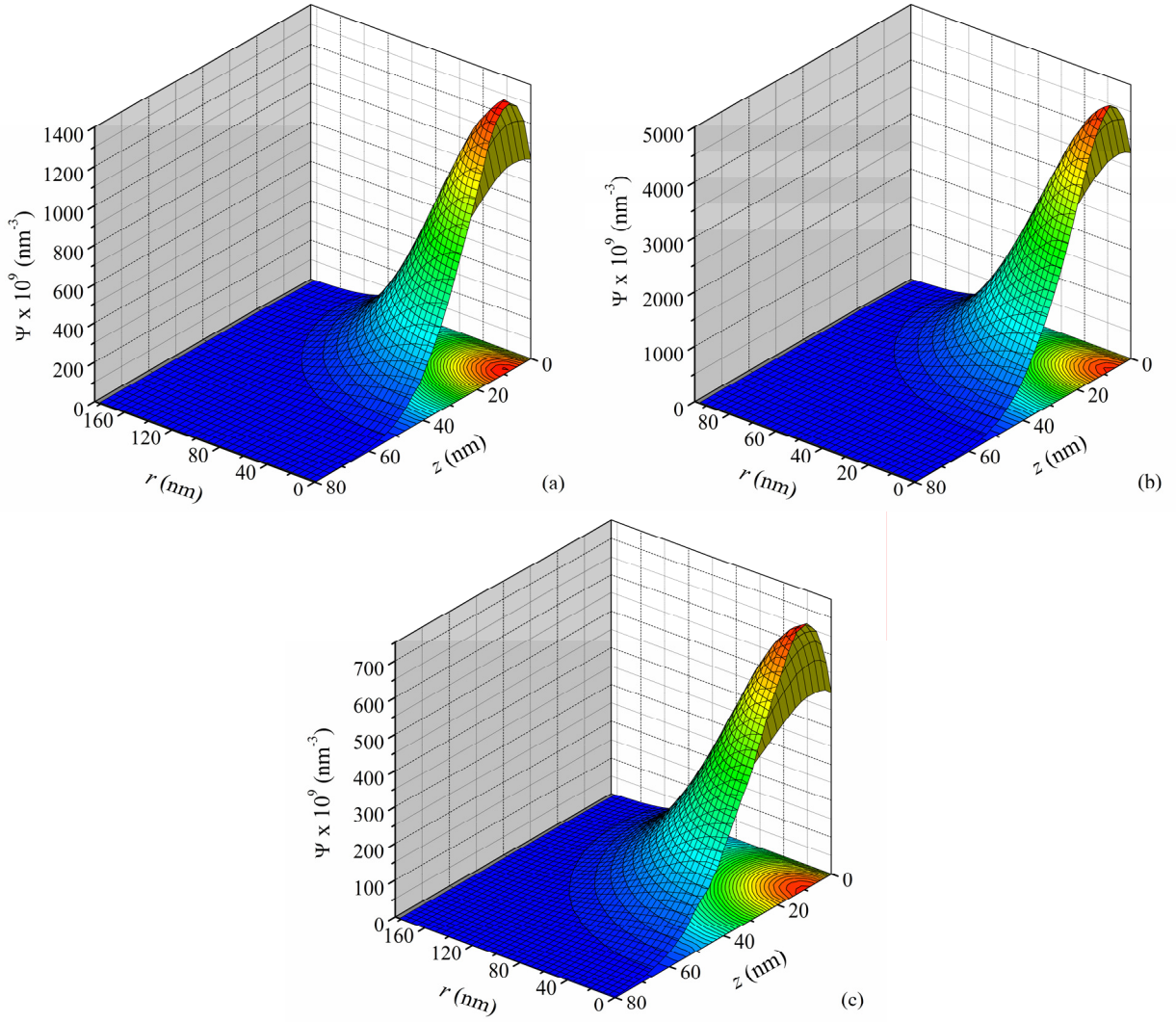
Figure 5.9   Normalized electron energy $\Psi \times 10^9$ (nm^{-3}) (see Eq. (11)) deposited inside gold film. Results are obtained from the Monte Carlo simulation in the electron-beam transport. The incident beam has a Gaussian profile in the r-direction with (a) a $1/e^2$ radius of $R_{electron} = 100$ nm and the initial kinetic energy of $E_0 = 4$ keV, (b) $R_{electron} = 50$ nm and $E_0 = 4$ keV, and (c) $R_{electron} = 100$ nm and $E_0 = 6$ keV.
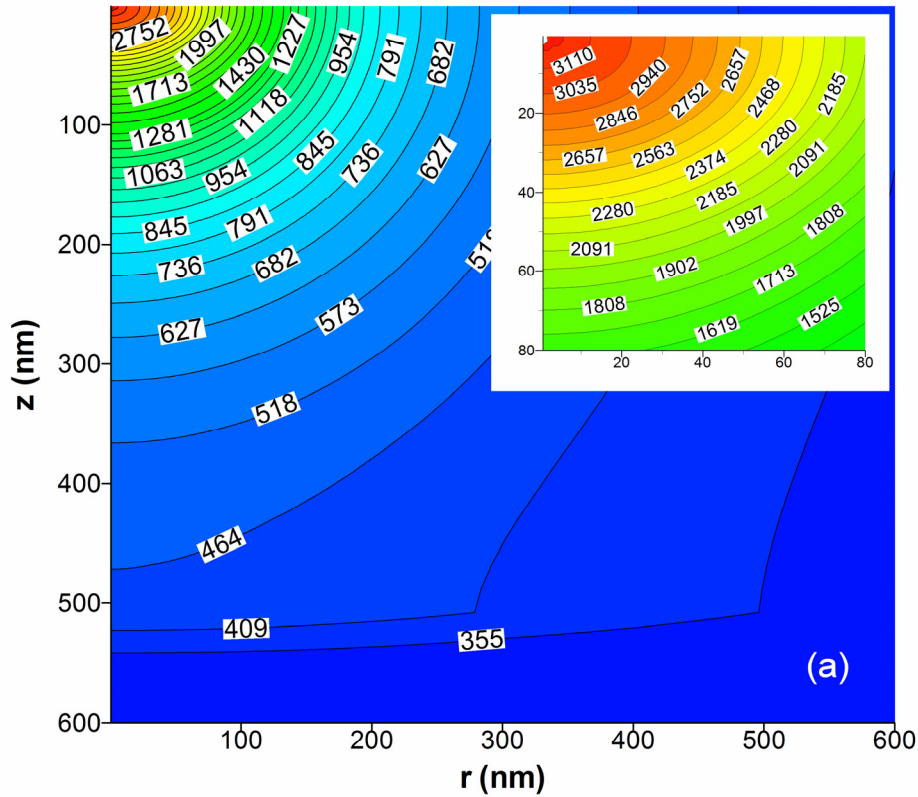
Figure 5.10 (a) Temperature distribution (K) within gold film at $t = 0.9$ ns. The electron-beam impinges on the top of workpiece (i.e., $z = 0$). A Gaussian beam profile is considered with a $1/e^2$ radius of $R_{electron} = 100$ nm and an initial kinetic energy of $E_0 = 4$ keV. The power of the beam is set to $\dot{E} = 0.5$ W. The Δt used in the simulation is 0.005 ps. The thicknesses of the workpiece and the substrate, which are gold and quartz, are assumed to be 500 nm and 10 μm, respectively. In the figure there is a sharp bending of the isothermal lines at $z = 500$ nm, which is where the two different materials interface. Note that this is the snapshot of the temperature field right at the moment when the first computational element nearest to the origin overcomes the latent heat of evaporation and starts to evaporate. The small inset in the top right-hand corner portrays an up-close temperature field for the area of $(r \times z) = (120$ nm $\times 120$ nm) near the origin.
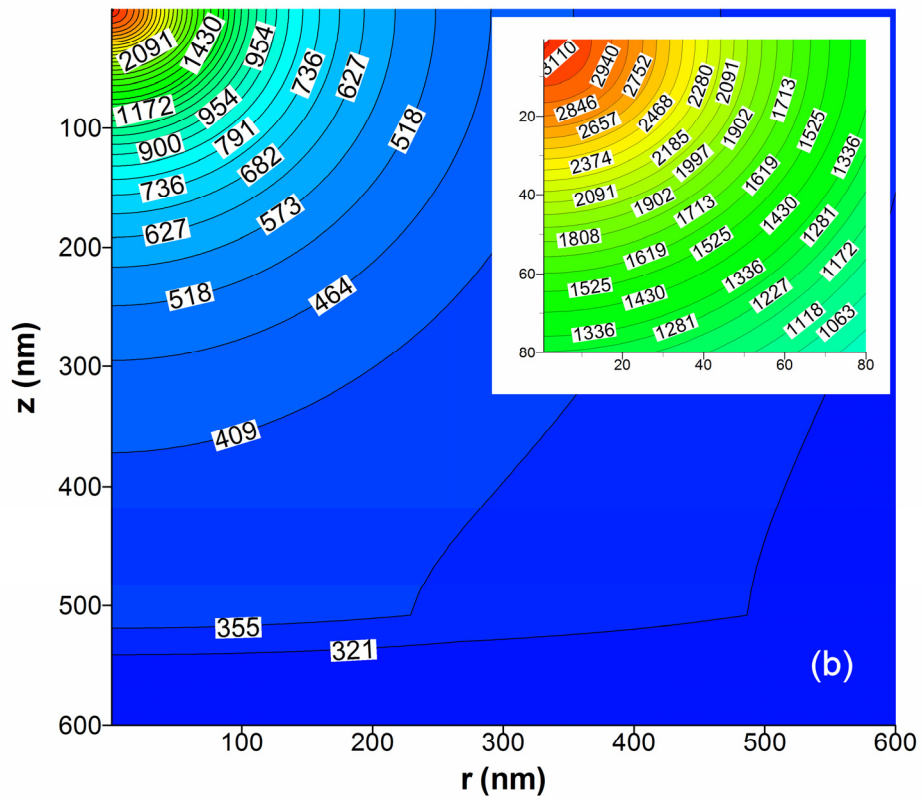
Figure 5.10 (b) Temperature distribution (K) within gold at t = 0.7 ns using the same conditions in (a) except that $R_{electron}$ = 50 nm, E_0 = 4 keV, and $\dot{E}$ = 0.305 W.
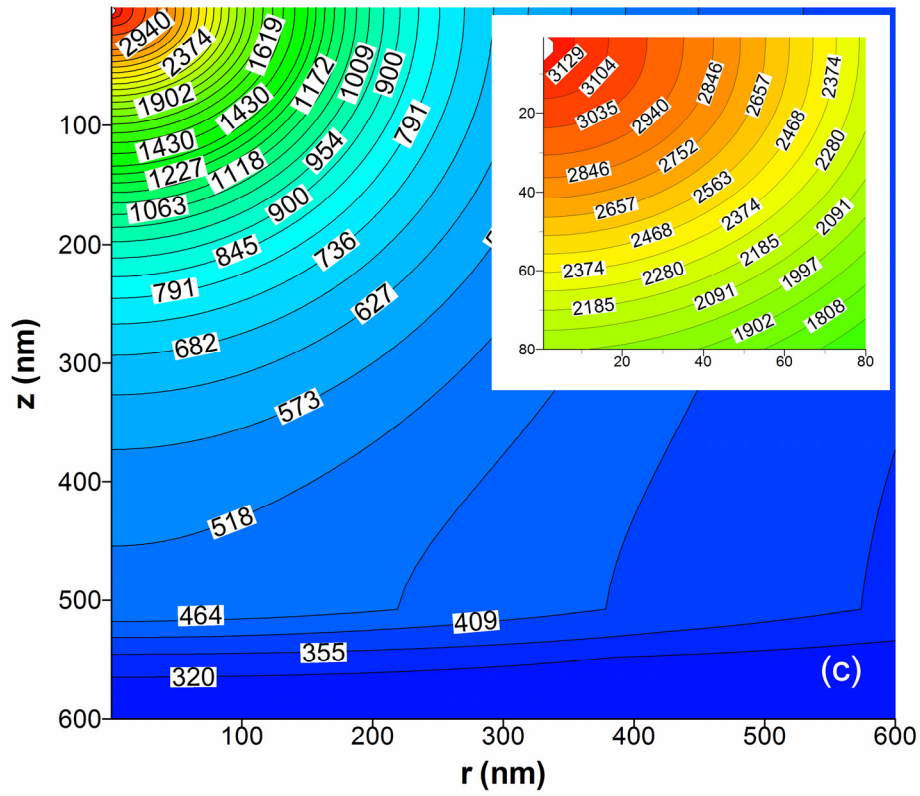
Figure 5.10 (c) Temperature distribution (K) within gold at $t = 1.0$ ns using the same conditions in (a) but with $R_{electron} = 100$ nm, $E_0 = 6$ keV, and $\dot{E} = 0.615$ W.
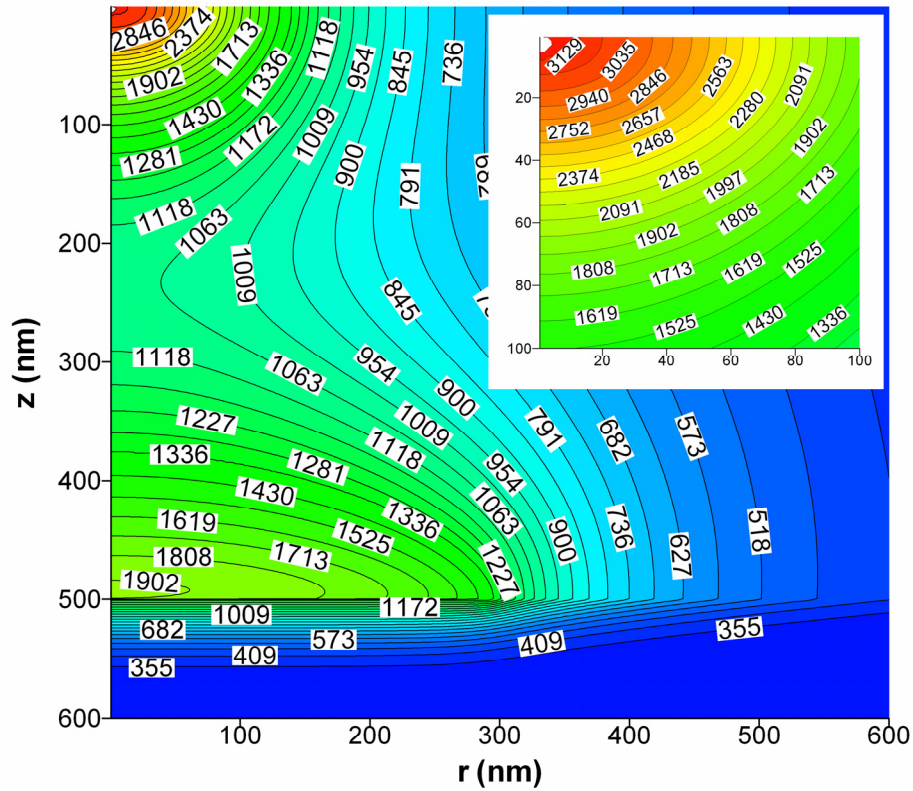
Figure 5.11 Temperature distribution (K) within gold film at $t = 0.5$ ns. Both the electron-beam and the laser are considered. The input parameters are the same as those in Figure 5.10(a). The power of the laser is 1.5 W and it covers a radius of R_{laser} = 300 nm from the z-axis. With the assistance from the laser, the time required for the first element at the origin to evaporate is improved from $t = 0.9$ ns (as in Figure 5.10(a)) to 0.5 ns.

158
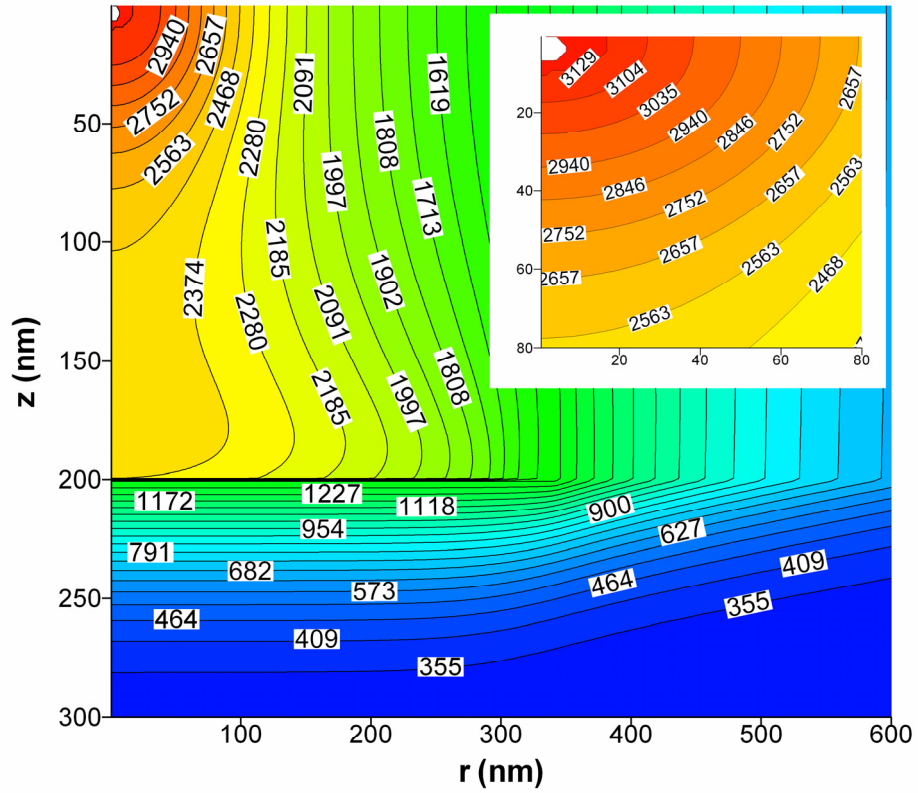
Figure 5.12 (a) Temperature distribution (K) within gold at $t = 1$ ns. Both the electron-beam and the laser heating are considered. The thickness of the gold film is reduced to 200 nm and the power of the electron-beam is set to 0.25 W. The rest of the input parameters follow those given in Figure 5.11. (b) The time required for evaporation as a function of the input power from the electron-beam for the 200-nm gold film
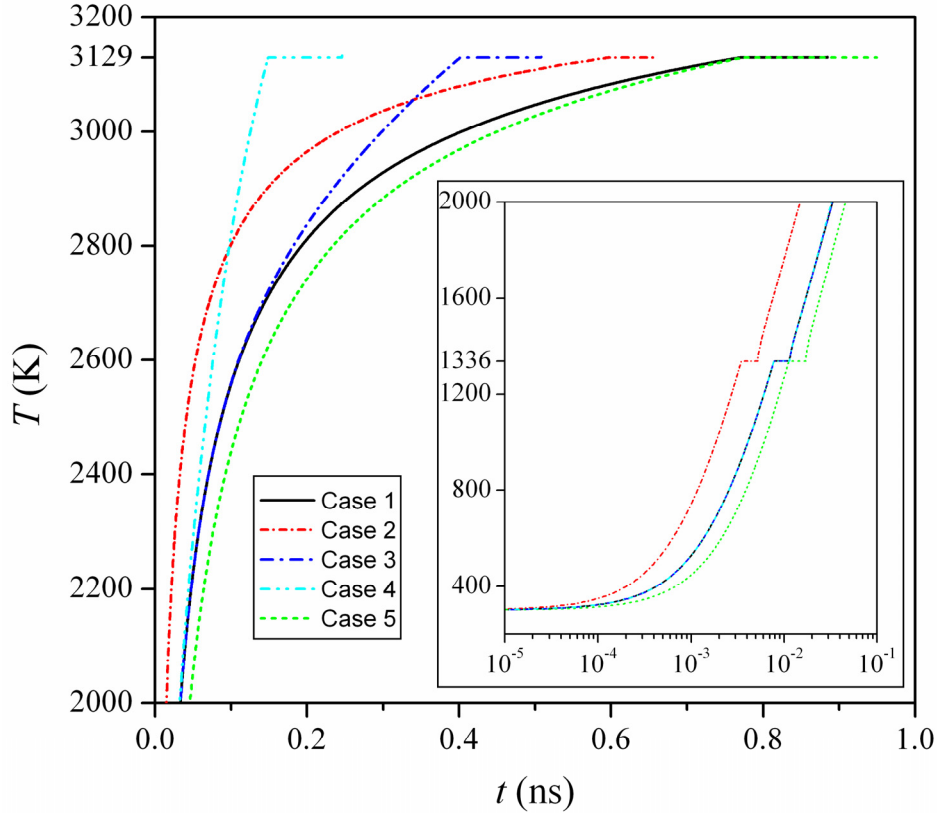
Figure 5.13 Transient temperatures at the origin around an infinitesimal area with radius of $\Delta r = 1.25$ nm and depth of $\Delta z = 1.25$ nm. The first case is set as the reference at which the inputs for the electron-beam are $R_{electron} = 100$ nm, $E_0 = 4$ keV and $\dot{E} = 0.5$ W. The gold film thickness is assumed to be 500 nm. The second case has the same inputs as the reference except that the beam is focused narrower with $R_{electron} = 50$ nm. The third case is the same as the first case but with laser heating. The power of the laser used is 1.5 W. The fourth case has a gold film thickness of 200 nm while the rest of the inputs are the same as the third case. The electron-beam of the final case has $R_{electron} = 100$ nm, $E_0 = 6$ keV and $\dot{E} = 0.615$ W with the laser turned off.
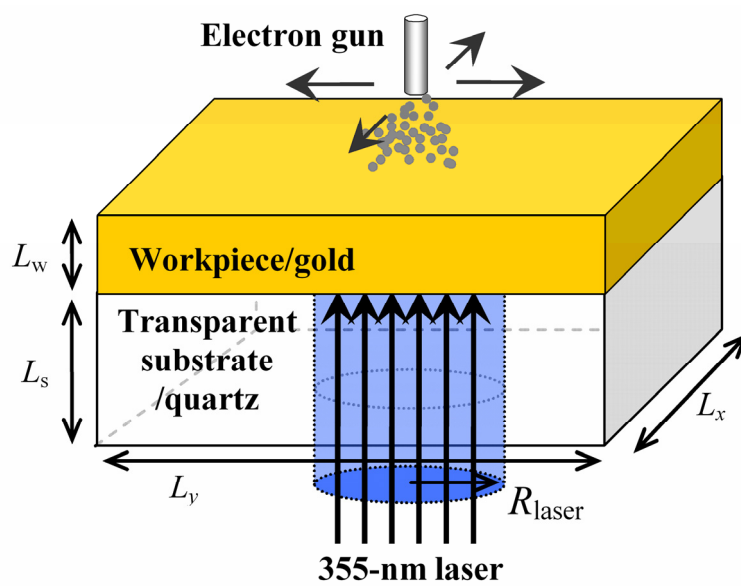
Figure 5.14 The 3-D schematic of material processing using an electron-beam and a laser.
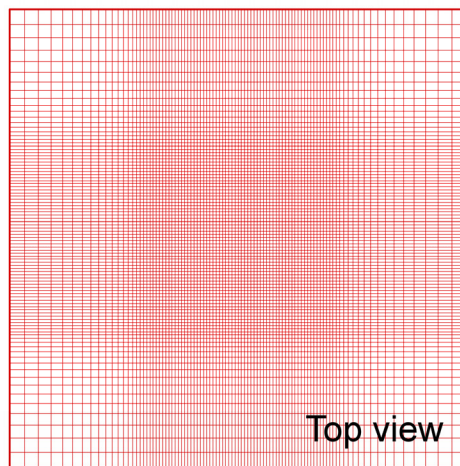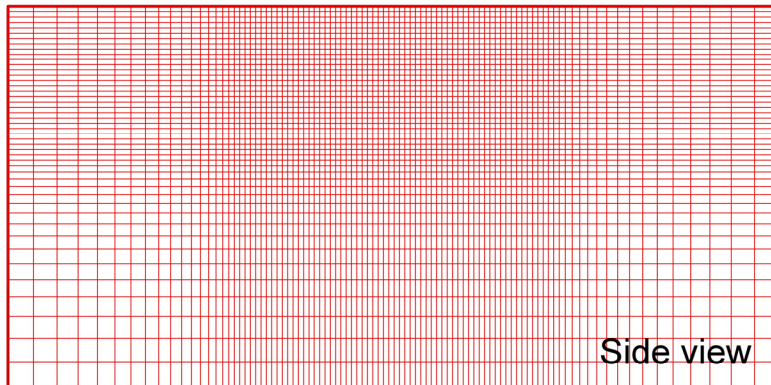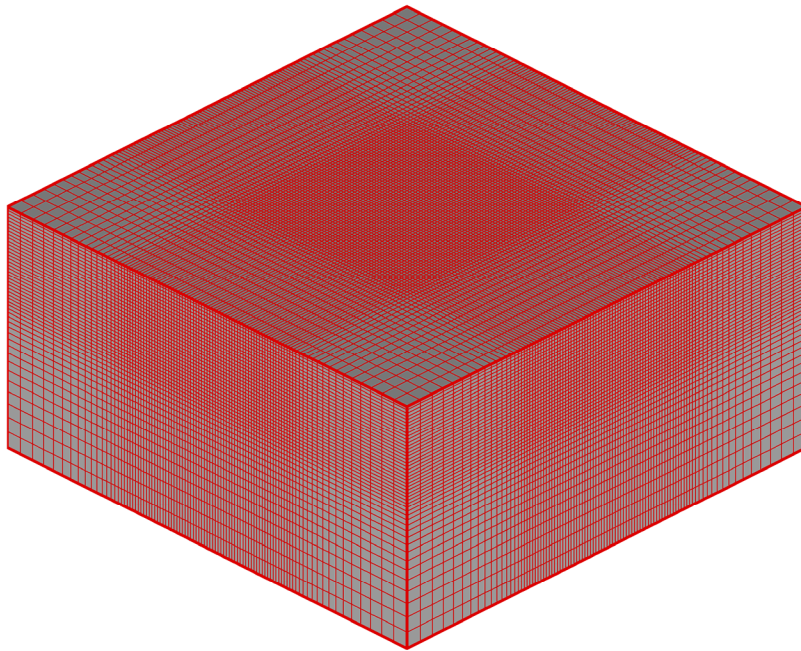
Figure 5.15 A sample of the structure of the grid. These are not the actual grid spacings, they have been adjusted for display purposes.
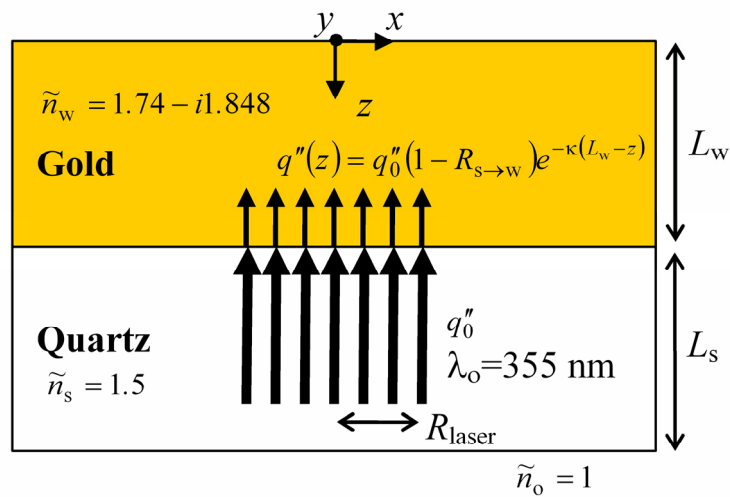
Figure 5.16 Laser propagation inside the transparent substrate and the workpiece. The heat generation inside gold is assumed to be one-dimensional since absorption of photons is strong compared to scattering.
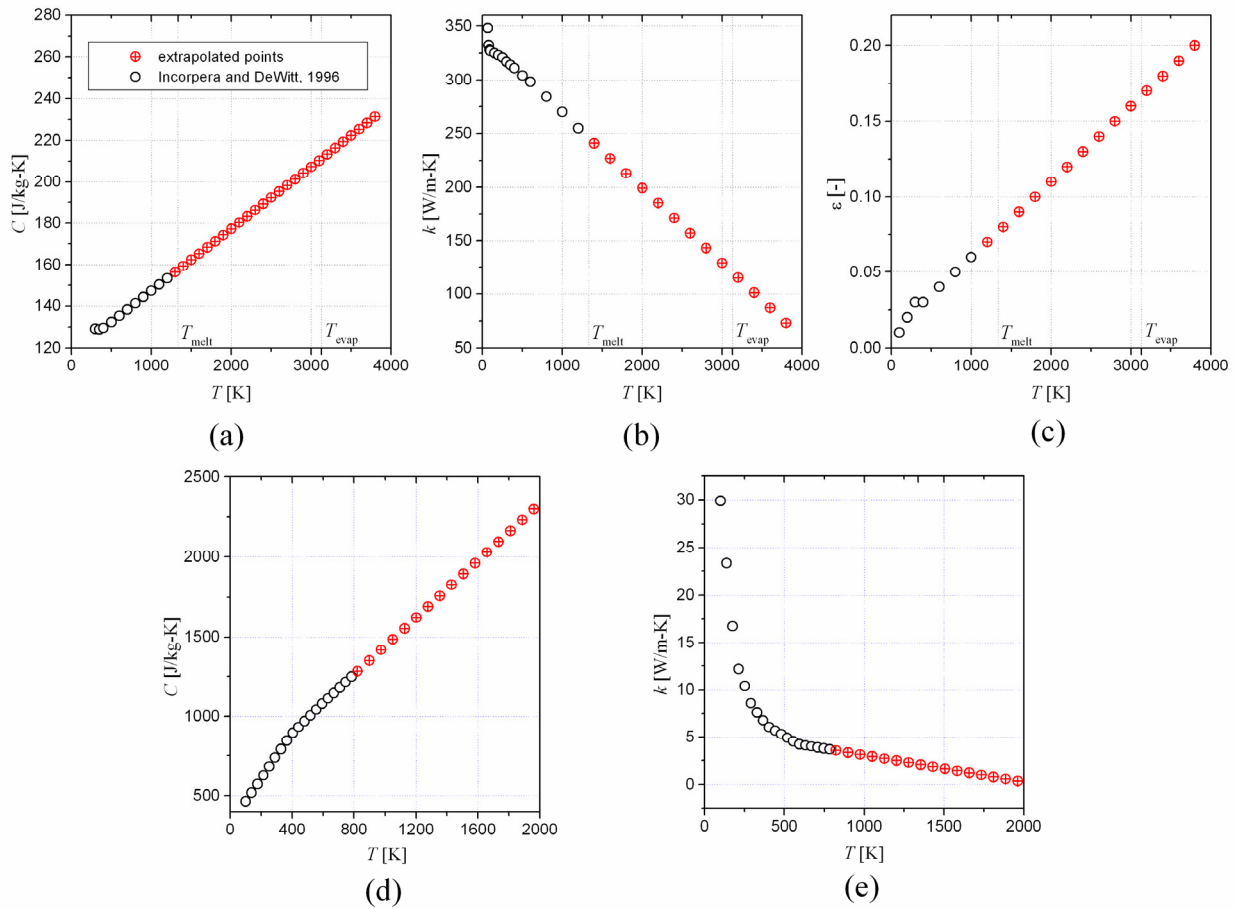
Figure 5.17 The thermal properties of gold and quartz as a function of temperature used in the simulations: (a) Specific heat of gold, (b) Thermal conductivity of gold, (c) Hemispherical emissivity of gold, (d) Specific heat of quartz, and (e) Thermal conductivity of quartz. The red data points (or symbols with a circle and a cross inside) are the extrapolated values.
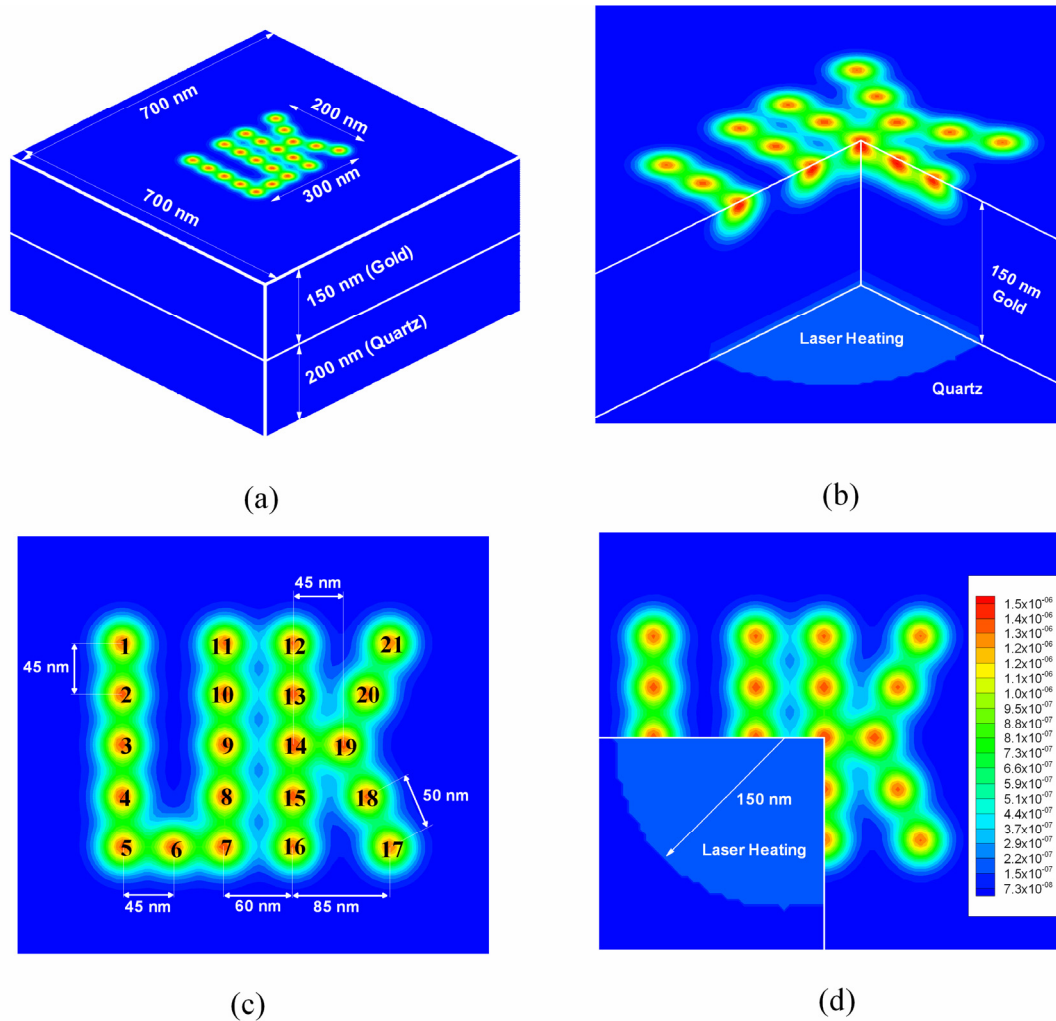
Figure 5.18 Normalized electron energy deposition distributions (in units of nm^{-3}) predicted using Monte Carlo Method in the electron-beam transport. (a) The intended machining locations for the electron-beam as to create the UK pattern are shown. Note that there is only one electron-beam used for machining and it is moved from one location to another. The figure shows an imaginary heat generation profile as if all of the heat generation profiles generated by the electron-beam at various locations are combined together. (b) The internal electron energy deposition profile, including that by the laser, is depicted. (c) The dimensions of the structures are given. (d) The dimension of the laser heating is illustrated.
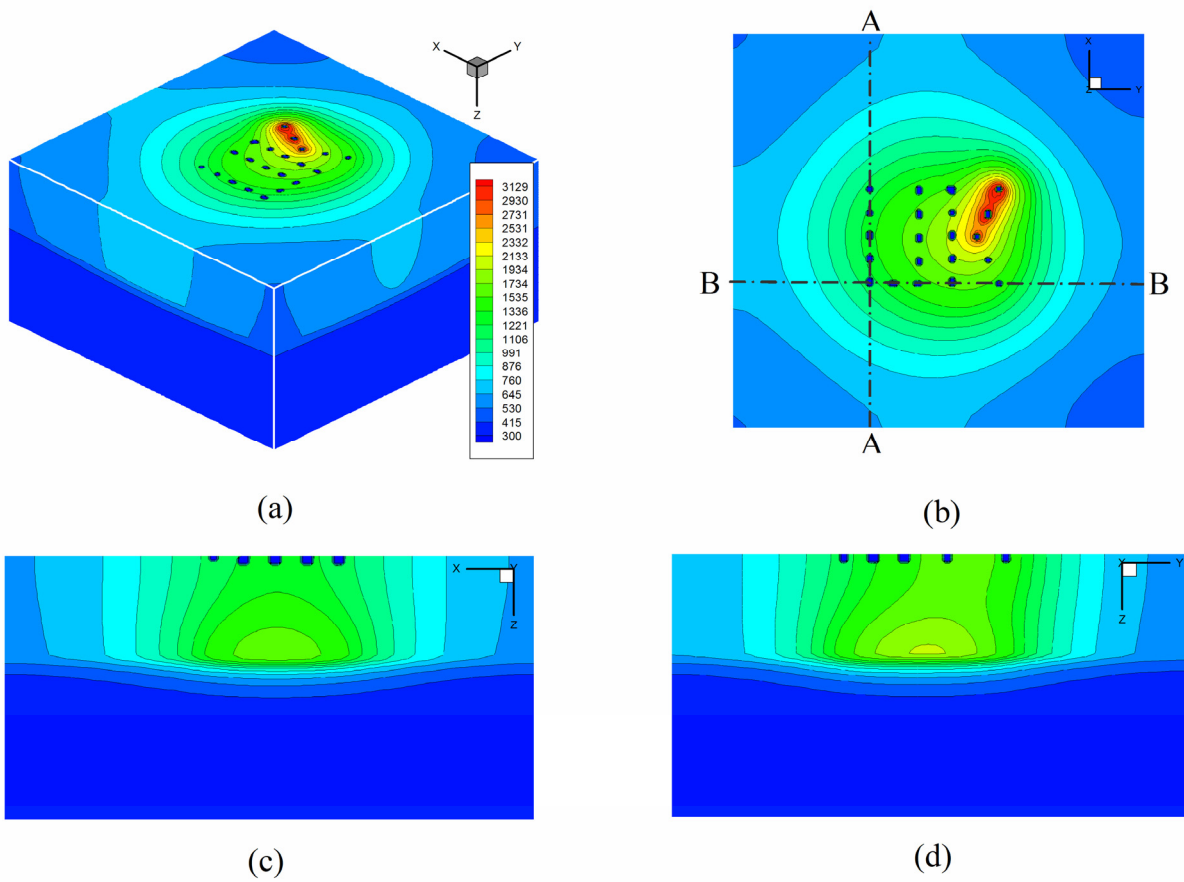
Figure 5.19 Temperature distribution (K) of the workpiece on top of the substrate at 0.42 ns after heated by the laser and then the electron-beam. The electron-beam is turned on after the laser heats the workpiece for about 0.12 ns. (a) The 3-D temperature distribution is given. (b) The top view of the geometry is depicted. (c) The A-A cross-section is shown. (d) The B-B cross-section is shown.
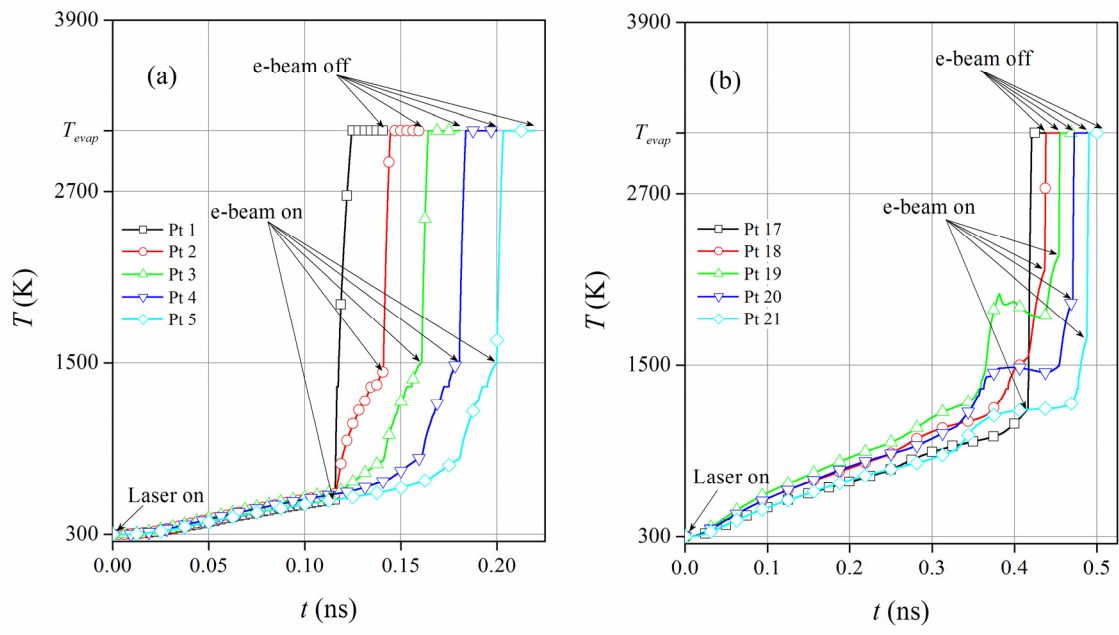
Figure 5.20 Transient temperature (K) of (a) Points 1-5, and (b) Points 17-21.
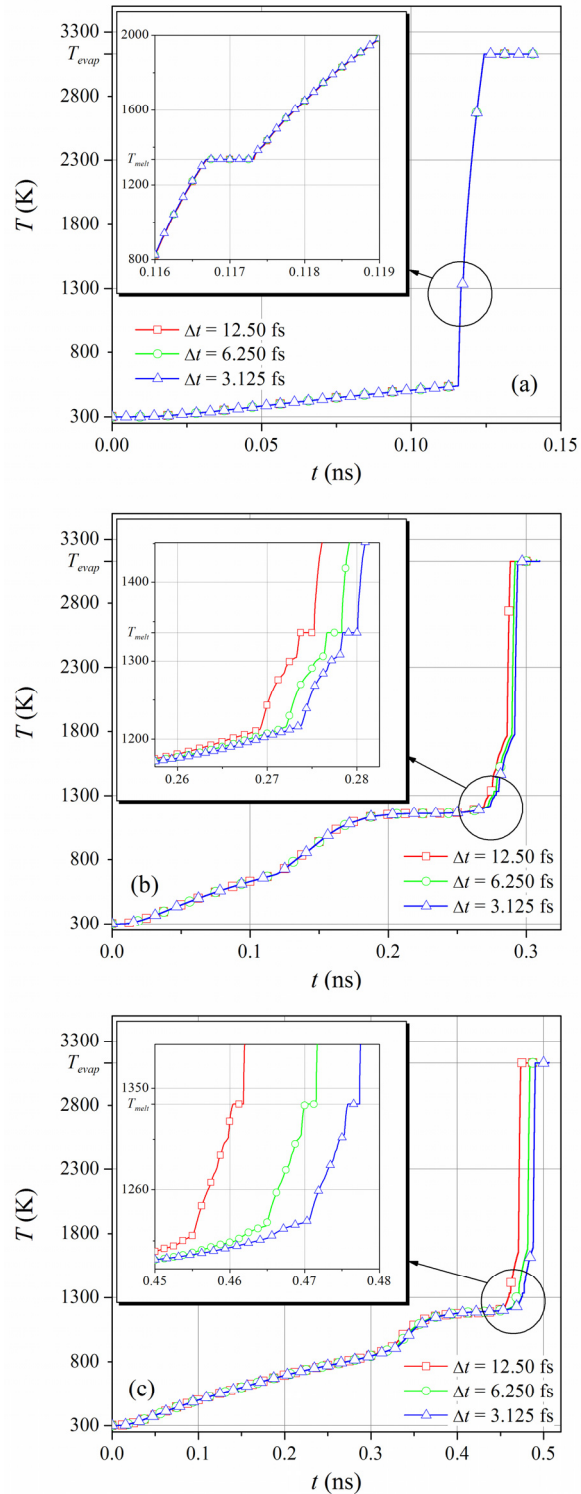
Figure 5.21 Transient temperature (K) of (a) Point 1, (b) Point 10, and (c) Point 21, as a function of various time steps. Each time step is half of its previous one. The uniform spatial step used here is 5 nm ($=\Delta x=\Delta y=\Delta z$) with a 10% increment for non-uniform spatial steps.
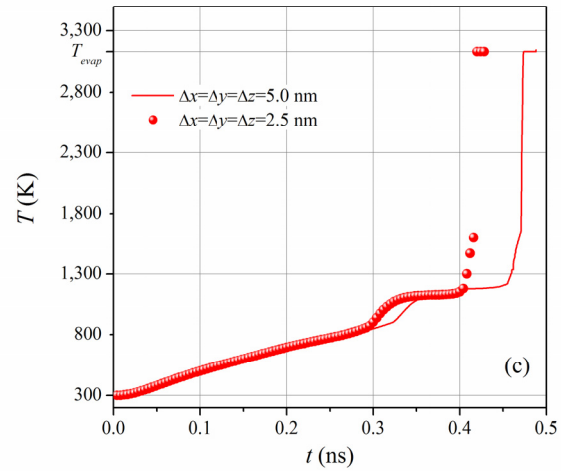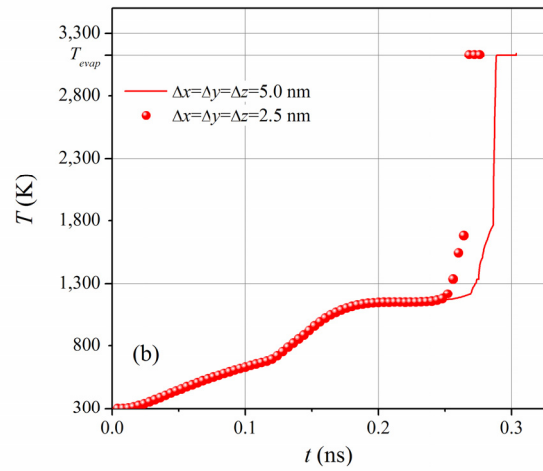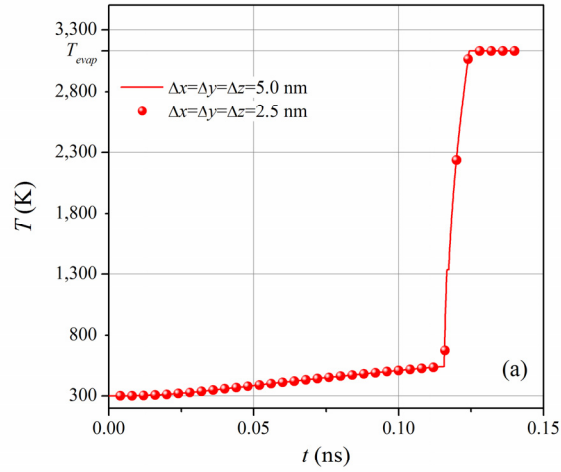
Figure 5.22 Transient temperature (K) of (a) Point 1, (b) Point 10, and (c) Point 21, for spatial step sizes of 5 nm and 2.5 nm. The time step used here for both cases is about 10 fs.

ELECTRON-BEAM INDUCED THERMAL CONDUCTION VIA DIS *E*-BEAM MONTE
CARLO AND THE TWO-TEMPERATURE MODEL

In the previous chapter, the possibility of nano-machining using an *e*-beam based on the Fourier law of heat conduction and the Monte Carlo simulation based on the Continuous Slow-Down Approach (CSDA) was explored. In this chapter, the heating phenomena, and hence nano-machining, inside a conducting object due to the injection of external hot electrons from a source using the electron-phonon conduction equations will be explored. In Chapter 5, the phonon and electron temperatures were assumed to be the same. Now, they will be separated into two different temperatures, one for electrons and the other for phonons.

The Monte Carlo simulation used in this chapter is called the Discrete Inelastic Scattering (DIS) MC simulation as opposed to the Continuous Slow-Down Approach (CSDA) as employed in the previous chapter. The DIS method is considered to be more accurate that the CSDA since it employs the experimentally determined optical data to describe the scattering phenomena. The main difference between the two methods lies within the inelastic scattering treatment in the simulation procedures. The inelastic scattering events refer to the energy loss mechanisms for the propagating particles. The CSDA assumes that particle energy is lost along the traveling path, as the name implies, while the DIS method distinctively describes the particle energy loss at a randomly drawn inelastic scattering distance (i.e. following some cumulative probability distribution). The simulation procedures are rather similar to those given in the CSDA. For further information regarding this method, the reader can refer to Section 3.2 where the details were given.

6.1 The *e*-Beam Monte Carlo Simulation and the Two-Temperature Model (TTM)

Electron-beam induced thermal conduction was previously analyzed by coupling the MCM simulation in electron-beam and the Fourier law of heat conduction. The Monte Carlo/Fourier law approach did not account for the electron transport within the workpiece. An electron-phonon model that distinguishes between the electron and the phonon temperatures, as opposed to the single-temperature approach found in the traditional heat equation will now be considered. The MCM simulation provides the electron-energy deposition profile, which then serves as the

heat source term in the heat diffusion equation. The MCM simulation used is the <u>C</u>ontinuous <u>S</u>low-<u>D</u>own <u>A</u>pproach (CDSA). This treats the energy loss of those penetrating electrons (from the electron-beam) inside the workpiece as continuous phenomena along the line of propagation. In this work, the problem is approached with different computational models. An alternative MCM simulation, which included secondary electron generations, replaced the CDSA in simulating the electron-beam propagation. As a result, the temperature distribution could be computed accordingly. Details on these models are discussed in the following sections.

6.2 Problem Descriptions

A single electron-beam impinging perpendicularly on a 3-D rectangular geometry (workpiece) is considered. A simple schematic of the problem is shown in Figure 6.1(b). When the electron-beam hits the workpiece, "hot" electrons spread inside the workpiece, as depicted by the dark region in the figure. When these electrons transfer their energy to the workpiece, a high temperature region is created (i.e. the red shaded region in the figure). The target workpiece is assumed to have perfect lattice structures and be free from any sort of physical defect. The electron-beam has a Gaussian spatial distribution when incident on the surface of the workpiece. The workpiece has finite dimensions in all three directions, which are defined in section 3.3. The entire system is assumed to be placed inside a vacuum chamber.

In traditional Fourier law, there is no temperature difference between electrons and phonons because there is no differentiation between the two energy carriers. When the energized electrons, which originated from the electron-beam, penetrate the workpiece, kinetic energies from these electrons are assumed to be transferred to both electrons and phonons simultaneously. In this work, a distinct difference between the electron and the phonon temperatures is assumed. When electrons from the electron-beam enter the target, energies are first transferred between these electrons and electrons inside the workpiece, elevating the electron temperature. Subsequently, the phonon temperature also increases through the electron-phonon collisions.

6.3 Grid Setup

To solve this problem numerically, the electron-energy deposition profile is first developed

using a Monte Carlo simulation. This profile is treated as the heat source in the electron-temperature equation. This equation is then coupled with the phonon-temperature equation, and both are solved simultaneously in order to predict the temperature distributions. The workpiece is assumed to be gold, and the electron-beam bombarded the target from above. To account for electron-beam transport and heat conduction for the relatively large dimensions of the geometry, the grid was stretched away from the origin. The 'origin' is where the electron-beam first hits and is located at the top center of the geometry. Here, 'relatively' describes the comparison between the spatial energy spread of the incident electron-beam and the overall dimension of the geometry. The structure of the computational grid employed is depicted in Figure 5.15. The grid spacing in all directions is uniform at the center of the cross-sectional area, as well as near the top of the domain. The MCM simulation for the electron-beam transport was performed within the uniform grid. The uniform grid section was chosen in such a way that the electron-energy deposition profile was well-confined within it.

6.4 Electron-Beam Monte Carlo Method Simulation

In previous publications (Wong et al., 2004; Wong et al., 2006), a MCM simulation was adapted from the CSDA. The basics of this method are similar to a typical Monte Carlo simulation in which ensembles are launched and forced to propagate according to certain cumulative probability distributions derived from the governing scattering phenomena. In this method, the propagating ensembles of electrons are assumed to lose kinetic energy along the path of propagation. The amount of energy lost is proportional to the distance traveled, and this amount is equally divided along the path. In this chapter, the MCM simulation used is slightly different, and it is called the Discrete Inelastic Scattering (DIS) method. The major difference between this method and the other one is the treatment of the inelastic scattering events while the procedures of simulating elastic scattering remain unaltered. As the name implies, the DIS method treats the inelastic scatterings as point scattering events. An inelastic scattering mean free path is employed. Ding and Shimizu (1996) outlined this method in an orderly fashion, and their procedures were followed.

The simulation procedures of the DIS method are similar to that of the CSDA or any typical MCM simulation in particle-beam transport (Wong and Mengüç, 2004). The simulation starts by

172

sampling the launching location of the ensemble. The ensemble is then launched with its known initial energy, and later scattered continuously by the workpiece until its energy becomes low. The scattering distance includes both mean free paths of the elastic and inelastic scattering events. Upon arriving at the distance, a random number is drawn to decide the type of scattering, elastic or inelastic. After that, the scattering direction is determined according to the type of scattering event. The cumulative probability distribution function (CPDF) of the elastic scattering is derived from the Mott scattering cross-section, while that of the inelastic scattering requires the use of the dielectric theory.

Another method of treating the inelastic scatterings is through the use of the dielectric theory/formulation. The dielectric formulation directly employs the energy loss function derived from the experimental optical data, and generates the differential inelastic scattering cross section accordingly. Since the energy loss function is a measure of the responses of electrons and atoms in a medium as a whole (when exposed to an external disturbance), it is typically much more accurate when compared to the other independent formulations. This is especially true when the electron energy is low. In this way, the inner-shell ionizations and the outer-shell excitations cannot be distinguished clearly. Nevertheless, it is a better approach in determining the inelastic scattering properties of electrons at low energy. This takes into consideration that the inelastic electron scatterings are not currently well-understood at the low electron-energy regime. Details on these procedures are quite elaborate, and will therefore not be further expressed here. Interested readers are referred to the paper by Ding and Shimizu (1996).

In the modified MCM simulations, the secondary electrons are accounted for. Whenever an inelastic scattering event occurs, a secondary electron will be "born" *if* the amount of energy transferred to the electron inside the material is greater than the Fermi energy level. The propagations of these secondary electrons are treated in the same way to account for those of the primary electrons (i.e. electrons originated from the electron-beam). The electrons undergo a series of elastic and inelastic scattering events, and additional secondary electrons emerge due to energy transfer from these electrons. This cascade effect can prolong the simulation due to these additional simulated electrons. All the electron ensembles are allowed to propagate until they either exit the medium or their energies fall below that of the surface barrier. Further details of these

equations and simulation procedures can be found elsewhere (Ding and Shimizu, 1996).

The electron-energy deposition distribution within the workpiece can be obtained when all of the propagations of electron ensembles are terminated and recorded, in their respective locations. In the simulation, the energy of the electron ensembles is recorded while maintaining energy conservation at all times. After the MCM simulation is completed, the electron-energy distribution within the material is determined in terms of unit energy. Each computational element is normalized by the total amount of electron-energy supplied from the electron-beam and its elemental volume accordingly. Therefore, in order to use this distribution later in the two-temperature model, it was necessary to provide the power of the electron-beam or the emission current of the beam. This is because the voltage (which determines the initial kinetic energy of the electrons emerging from the electron-beam) is fixed when the MCM simulation starts.

6.5 Two-Temperature Model

Interactions between external heating sources, such as the photon- and electron-beams, and the target workpiece involve the heating of electron gas inside the target workpiece. This causes the electron temperature to elevate substantially when compared to the lattice temperature. One way to model this phenomenon is to separate the temperature into two distinct components, namely the electron and lattice temperatures. Such a model is usually referred to as the two-temperature model (TTM) (Tzou, 1997). The TTM can be expressed as follows:

$$C_e \frac{\partial T_e}{\partial t} = -\nabla \cdot \left(k_e \nabla T_e \right) - C_e \frac{T_e - T_{ph}}{\tau_{e-ph}} + S_T , \tag{6.1}$$

$$C_{ph} \frac{\partial T_{ph}}{\partial t} = -C_e \frac{T_{ph} - T_e}{\tau_{e-ph}} , \tag{6.2}$$

where subscript '*e*' and '*ph*' denote that of electrons and phonons, respectively. The *C*'s are the heat capacities of the energy carriers, and *k* is the thermal conductivity. The electron-phonon relaxation time is denoted as $\tau_{e\text{-}ph}$. The first equation in the model is the electron-energy conservation equation, while the second is the phonon-energy equation. Note that the external heat generation term, denoted as S_T, is included in the first equation. In this work, this heat generation term is the electron-energy deposition distribution obtained from the Monte Carlo simulation for

174

the electron-beam. The TTM is solved numerically using a finite-difference method where first-order time and second-order space discretization schemes are used. The target material is 1 μm thick and 8.5 μm wide in both lateral directions. The properties used in the simulations are summarized in Table 7.1.

In this work, the workpiece is assumed to be gold under vacuum condition (10^{-8} torr). Therefore, the temperature range involved in these simulations is between room temperature and the sublimation temperature of the material. The melting temperature for gold is around 1336 K (Incropera and Dewitt, 1996), however, the sublimation temperature for gold is around 1080 K for a vacuum pressure of 10^{-8} torr (Honig, 1962). As a result, gold is likely to sublimate before melting is actually achieved. To implement this scenario in the TTM, the code is allowed to simulate the temperature field, starting from room temperature and elevating it to a temperature just below sublimation temperature. Once a computational element has reached the sublimation temperature, its phonon temperature is held fixed while the additional energy, supplied from the electron-beam, is used to overcome the latent heat of sublimation. The electron-temperature equation is solved with the fixed phonon temperature at that given time step. After the solution is obtained, the amount of additional energy conducted from electrons to phonons is calculated by:

$$\text{Energy stored as latent heat} = -C_e \left(\frac{T_{ph} - T_e}{\tau_{e-ph}} \right) dt , \qquad (6.3)$$

which is in units of energy per unit volume. This step is repeated until the element has enough latent heat of sublimation at which material removal starts occurring. The computer code is stopped whenever this happens, as the main goal is to find the power required to initiate material removal.

6.6 Results and Discussions

6.6.1 Electron-Energy Deposition Distributions

In numerical simulations, the electron-energy deposition profiles for various cases are first computed, as discussed in Section 6.4. These results are displayed in Figure 6.2 and Figure 6.3. A Gaussian-shaped incident beam profile is used for incident electrons with $1/e^2$ radius at R_{beam},

175

which varies from case to case. For the case shown in Figure 6.2, the initial kinetic energy of the electron-beam is 500 eV and R_{beam} is 500 nm. The unit given in the figure is normalized with respect to the total electron-energy supplied from the electron-beam and the corresponding volume of the infinitesimal element. A series of numerical experiments is carried out to find out that a 20% grid stretching beyond the uniform grid is acceptable for the simulations. While it is possible to solve the problem in the cylindrical coordinate system, which would reduce the computation to two dimensions (the electron-beam impinges normally on the workpiece), it was decided to solve the problem in three dimensions, so that an oblique and/or moving incident electron-beam could be easily implemented without imposing numerous modifications to future computational codes.

In a typical electron-energy deposition distribution, the deposition amount is usually at a maximum below the workpiece surface. This is evident in Figure 6.2 and Figure 6.3. In Figure 6.3, the distributions are shown in the x-z plane for the ease of visualization, although they are actually in three dimensions. Two important parameters that can be adjusted in the code are the initial incident kinetic energy, E_0, and the $1/e^2$ Gaussian radius, R_{beam}, of the electron-beam. Figure 6.3(a) shows the case where $E_0 = 500$ eV and $R_{\text{beam}} = 250$ nm and the deposition amounts are in the order of 10^{-5} per unit nm^3. When the radius of the beam is increased by two times (i.e. $R_{\text{beam}} = 250$ nm $\rightarrow$ 500 nm), the deposition amounts drop to the order of 10^{-7} per unit nm^3, as shown in Figure 6.3(b). This is as expected since electrons are more widely spread when the radius of the beam is broadening. This results in a wider spatial energy spread and lower deposition amounts. In Figure 6.3(c) and (d), the R_{beam} is fixed while E_0 varies. The deposition profiles start to shrink in the z-direction when the energy of the beam decreases. This is because the electron penetration depth becomes shallower when the initial kinetic energy is lower. However, the maximum deposition amount increases as the electron-beam energy is lowered.

6.6.2 Thermal Heating and Sublimation Using an Electron-Beam

Using the electron-energy deposition distributions obtained in the previous section, the heating phenomena subjected to the electron-beam was simulated. In order to obtain accurate temperature simulations, various numerical experiments were carried out with the code. First, the time step was varied while holding other parameters fixed. It was found that a time step of 10^{-12} sec-

onds is sufficient to obtain a converged temperature field. Similarly, the same investigations were done for the spatial steps, and *dx*, *dy*, and *dz* are determined to be 40 nm, 40 nm, and 0.25 nm, respectively. As mentioned before in the discussion, the reasonable grid stretching in the simulation is 20%.

Figure 6.4 shows the typical temperature distribution of the workpiece as heated by the electron-beam. The figure depicts the instant snapshot of the electron-temperature field at a total elapsed time of 3 ns. The power of the electron-beam used in this case is 10 mA while the electron-energy deposition profile is given in Figure 6.3(b). The phonon-temperature is exactly the same as the electron-temperature plot. These temperatures are similar because both the electron-temperature and the phonon-temperature converged into a single temperature after 3 ns of heating. The time that these two temperatures are the same, is the instance at which material removal begins to occur. In other words, the target workpiece, at this time, has reached the sublimation temperature and overcome the latent heat of sublimation locally. Therefore, for an electron-beam with an initial kinetic energy of 500 eV, a power of 10 mA, and a Gaussian beam radius of 500 nm, the sublimation of a gold workpiece (with a dimension of 1 μm × 8 μm × 8 μm) is possible at 3 ns under vacuum pressure of 10^{-8} torr. This is a specific situation, and occurs only when all the above criteria are met. These numbers are determined from the various runs of numerical experiments, and they fall within the computational time limits. For example, 1 μW as the power of the electron-beam could have been used. This delays sublimation until a time later than 3 ns. However, this may require weeks of computational time on a single PC computer (a Pentium 4 3 GHz with 2GB of RAM). Expanding the code to parallel computing can be carried out in the future. Current settings will permit the study of the basic behavior of heating phenomena due to an electron-beam, which lies within the goal of the current work.

Most of the electron-temperature and the phonon-temperature plots are similar in these figures, so plotting the 3-D contour of the temperature fields is not beneficial in understanding the heating behavior. Instead, the maximum transient electron-temperature and phonon-temperature were recorded and compared to various cases as the simulation progressed. These results are depicted in Figure 6.5. The computational parameters used in these results are the same as those discussed for Figure 6.4 (unless mentioned otherwise in the figure caption). A typical transient electron-

temperature and phonon-temperature plot can be seen in Figure 6.5. The main thing to consider is that both electrons and phonons start to exhibit the same temperature profile when the time is beyond ~10 ps. This is expected because the electron-phonon relaxation time for gold is on the order of 0.1 ps or smaller, therefore electrons and phonons tend to reach equilibrium at a time much larger than that. Another phenomena observed from the computations is that when the temperature reaches the sublimation temperature (i.e. 1080 K), the phonon-temperature stays constant (while the electron-temperature increases) until the latent heat of sublimation is overcome. All the profiles in the figure demonstrate this type of behavior due to the implementation of the code, although some profiles are difficult to visualize because of the scales of the axes.

By holding other computational parameters constant and varying the thickness of the workpiece, one can observe how the workpiece thickness effects transient temperature behavior (Figure 6.5(a)). All transient electron and phonon temperature profiles for various thicknesses are identical until about 0.1 ns, at which point they start to deviate from one another. This deviation time implies that the boundary effect is not evident before 0.1 ns, when the heat waves are still emerging and propagating towards the boundary. Intuitively, it is expected that the material will sublimate faster for a thinner workpiece when compared to a thicker one. This can be seen in Figure 6.5(a) where the sublimation time increases as the thickness of the workpiece is increased from 500 nm to 2 μm.

The effect of the initial kinetic energy of the electron-beam on the transient behavior of the temperature is also examined. Three different choices of initial kinetic energy of the electron-beam are considered: 350 eV, 420 eV, and 500 eV. These values do not significantly change the transient temperature profiles. The only effect the initial kinetic energy has on the transient behavior is that one can delay the sublimation in the workpiece by lowering the initial energy of the beam, as shown in Figure 6.5(b). Similarly, one can produce the same effect of delaying the sublimation by lowering the power of the electron-beam, which is evident in Figure 6.5(c).

6.6.3 Comments

In this section, the details of heat transfer for the nano-scale machining due to field emission of electrons from a nano-scale probe have been simulated. The propagation of electrons in the

workpiece and their interaction with the lattice are considered separately by solving a MCM code for the electron-beam (via the Discrete Inelastic Scattering approach) and the two-temperature model for the electron-phonon equation. It was observed that a 500-eV electron-beam with a $1/e^2$ Gaussian radius of 500 nm and a power of 10 mA is capable of sublimating gold under a vacuum pressure of 10^{-8} torr, where the gold workpiece dimensions are 1 μm × 8 μm × 8 μm. A brief parametric study was also outlined to understand the effects of these parameters on the transient behavior of the maximum temperature in the workpiece. It is important to note that the dimensions of the workpiece were chosen to accommodate the computational resources. These numbers can be increased for larger workpieces, although increased computational resources will be required.

The numerical experiments revealed that for time-durations longer than approximately 50 ps, temperatures between electrons and phonons are always in equilibrium. This implies that the Fourier law of heat conduction is acceptable for machining times beyond this range.

Table 6.1 Computational parameters used in the simulation.

Property	References
$C_e = 70 T_e \ \ [\text{J/m}^3\text{-K}]$	(Ziman, 1972)
	(Ashcroft and Mermin, 1976)
	(Tzou, 1997)
	(Ivanov and Zhigilei, 2003)
$k_e = C\vartheta_e \dfrac{\left(\vartheta_e^2 + 0.16\right)^{5/4}\left(\vartheta_e^2 + 0.44\right)}{\left(\vartheta_e^2 + 0.092\right)^{1/2}\left(\vartheta_e^2 + 0.16\vartheta_l\right)} \ ;$	(Ivanov and Zhigilei, 2003)
$\vartheta_e = T_e/T_F \ ; \ \ \vartheta_l = T_l/T_F$	
$C_l = 8.33 \times 10^3 T_l \ \ [\text{J/m}^3\text{-K}]$	(Ziman, 1972)
	(Ashcroft and Mermin, 1976)
	(Tzou, 1997)
$\tau_{e-ph} = 8.1 \times 10^{-12}/T_l \ \ [\text{s}]$	(Ziman, 1972)
	(Ashcroft and Mermin, 1976)
	(Tzou, 1997)

Figure 6.1   (a) The close-up schematic of the proposed machining process using electron field emission from a nano-probe. Note that the schematic is not drawn to scale. The actual size of the carbon nanotube (CNT) is about 50 nm in diameter while the optical fiber may have a diameter of more than one hundred micron meters. The fiber is considered to be infinite compared to the nanotube. (b) The simple schematic of the case study of a workpiece as it is exposed to the electron-beam heating.
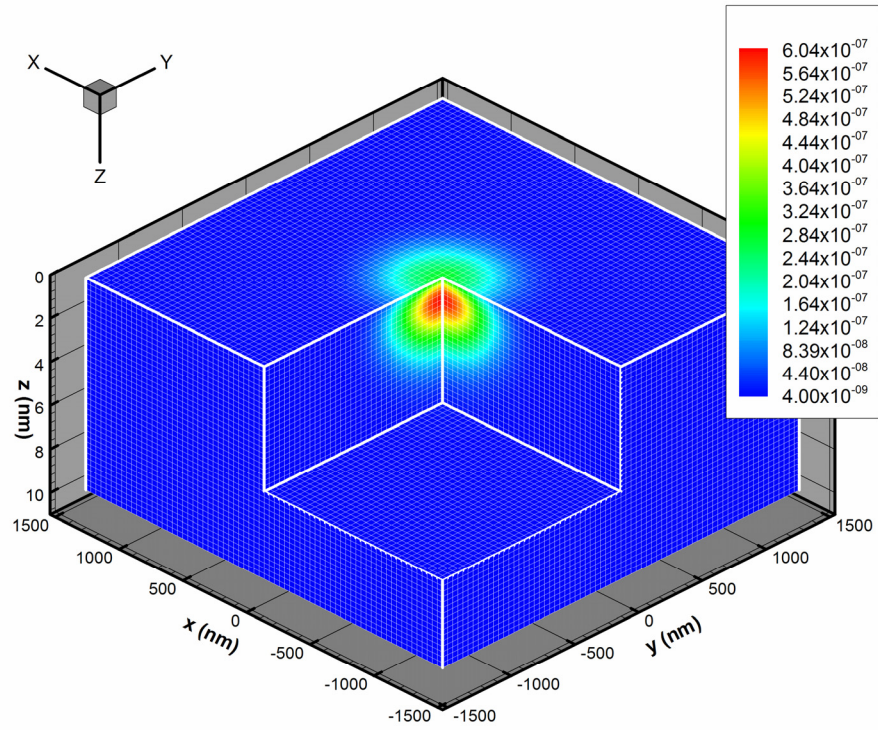
Figure 6.2 Electron-energy deposition distribution for $R_{\text{beam}} = 500$ nm and $E_0 = 500$ eV is shown. The numbers given in the figure are in terms of normalized quantitie, per unit nm^3.
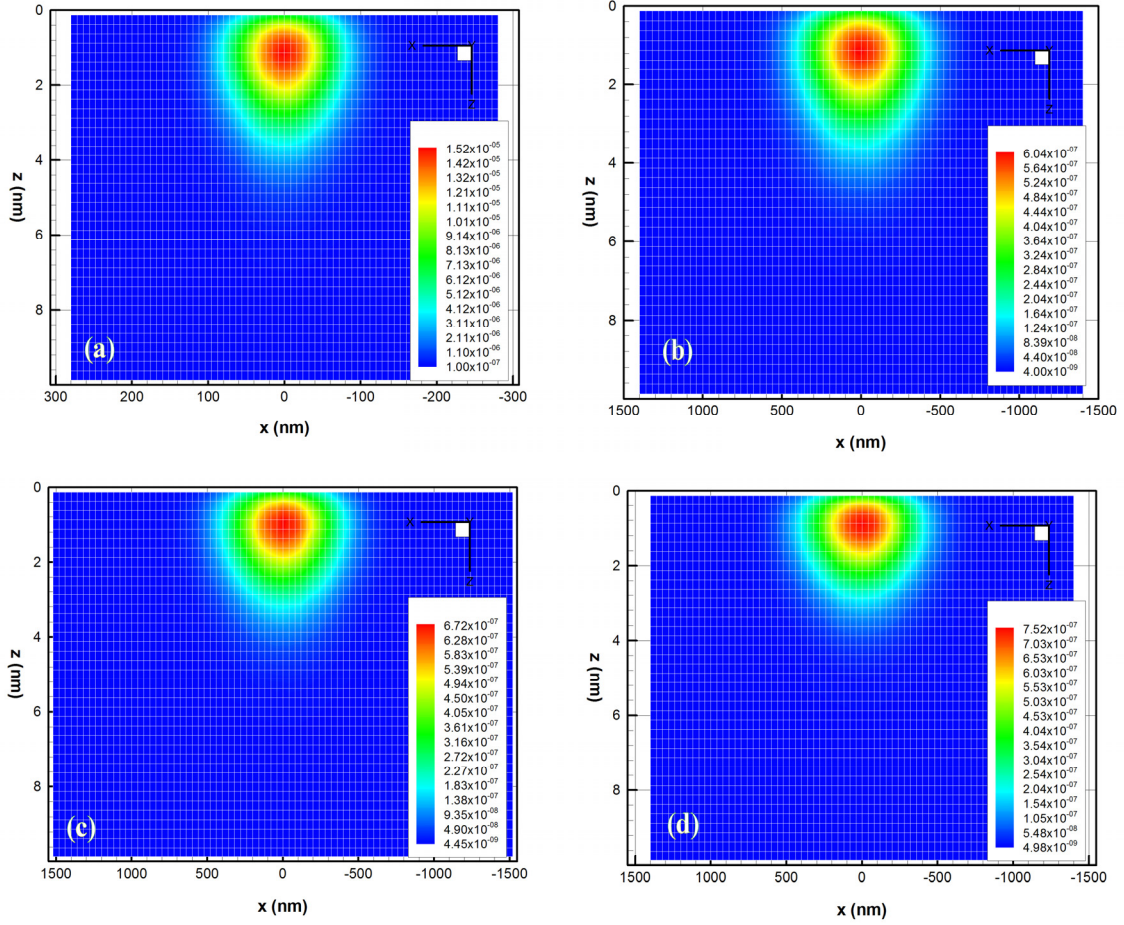
Figure 6.3   Electron-energy deposition distributions for four different cases are depicted: (a) $R_{beam} = 250$ nm and $E_0 = 500$ eV, (b) $R_{beam} = 500$ nm and $E_0 = 500$ eV, (c) $R_{beam} = 500$ nm and $E_0 = 420$ eV, and (d) $R_{beam} = 500$ nm and $E_0 = 350$ eV. The numbers given in the figure are in terms of normalized quantitie, per unit nm^3.
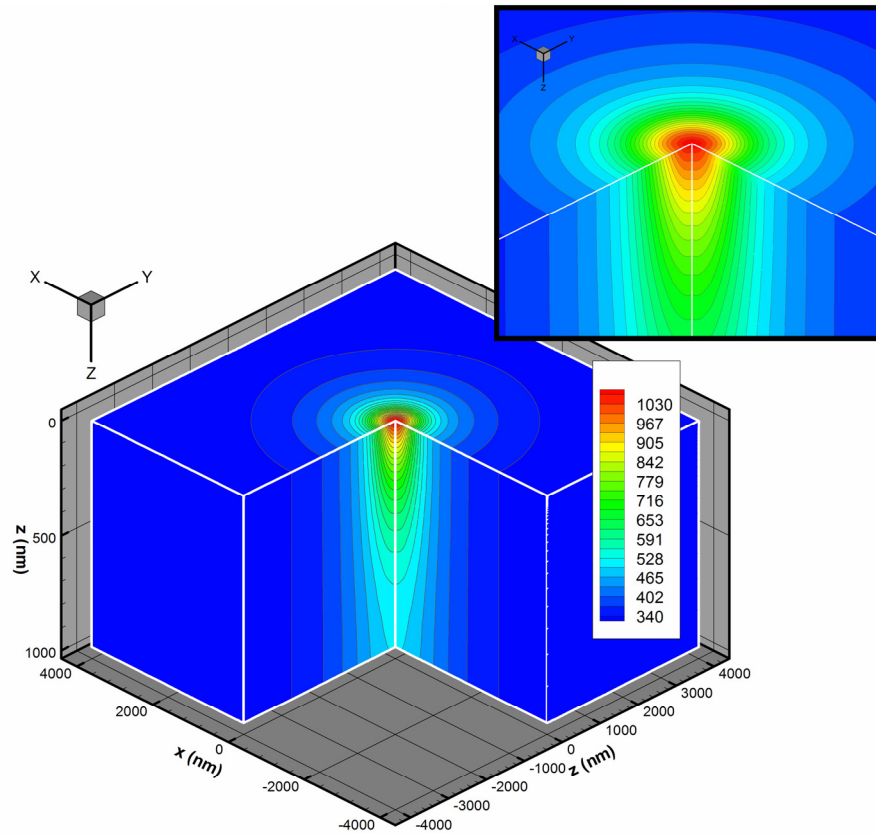
Figure 6.4   The electron-temperature distribution of the target workpiece in unit of Kelvin for R_{beam} = 500 nm and E_0 = 500 eV is shown. The power of the electron-beam used is 10 mA, and the temperature profile shown is the snapshot at t = 3 ns.
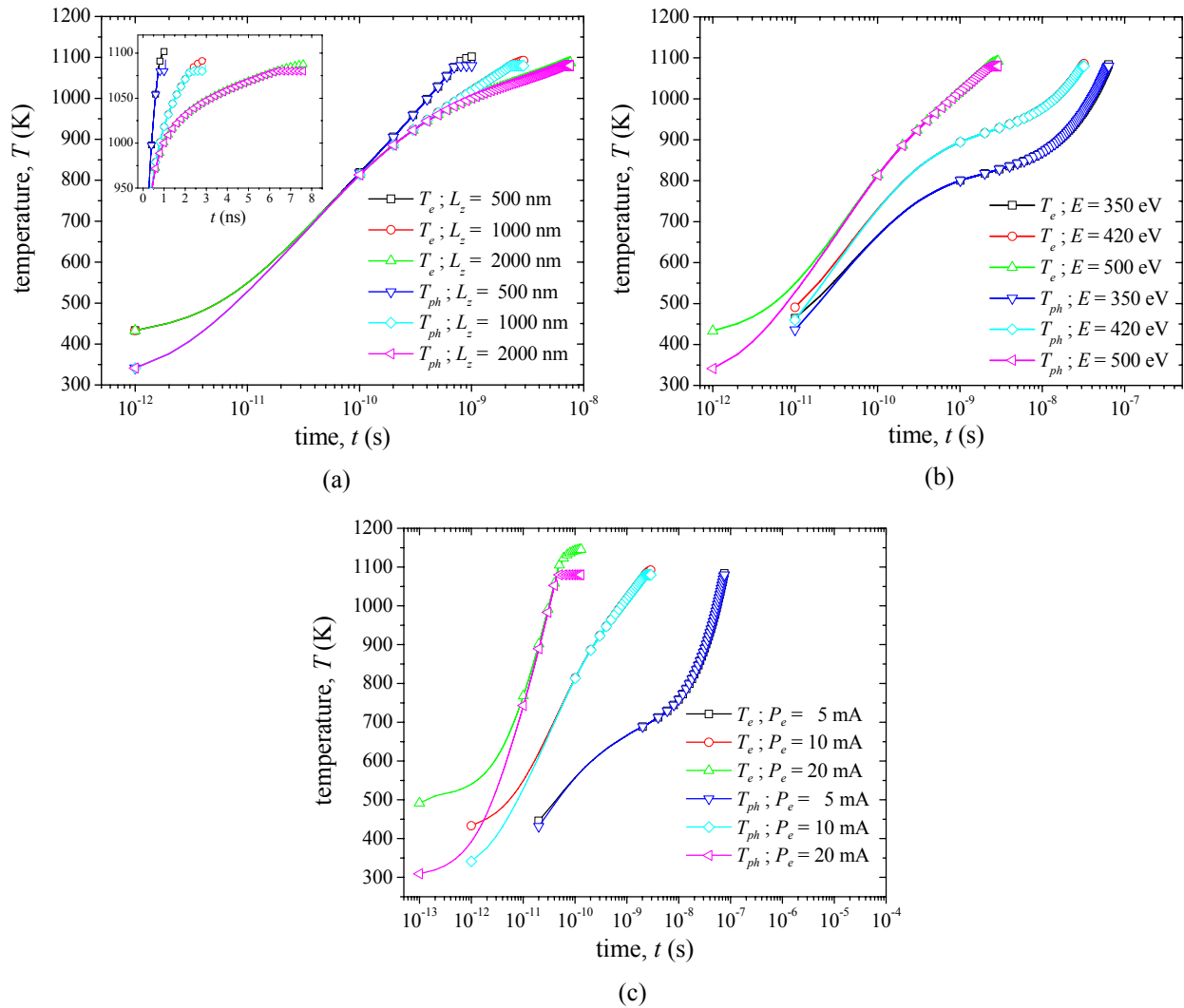
Figure 6.5 The maximum transient electron temperature and phonon temperature for various cases are given.

CHAPTER 7
ELECTRON-PHONON HYDRODYNAMICAL MODEL AND MONTE CARLO
SIMULATION IN ELECTRONIC THERMAL CONDUCTION – FOUNDATIONS FOR
FUTURE WORK

Another transport mechanism that this dissertation is interested in is the electron-phonon transport. The electron-phonon transport at the micro/nano-scale is very different from the traditional macroscopic view. One difference is that local thermal equilibrium in terms of electrons and phonons does not exist when it comes to nano-scale transport where electron transport and phonon heat conduction can no longer be described using the Fourier law. Another important observation for transport at nano-scale is that definitions for all those bulk properties of the transport become obsolete since they are established based on the existence of temperature, which may not exist at the nano-scale.

The properties that are ultimately required to facilitate modeling at nano-scale are the various rates of scattering or the probabilities of different transition processes for quantum heat carriers. Although one may be able to define "effective transport properties" to compare with the bulk ones, these "properties" are not required in the modeling itself. This is different from the macroscale modeling where they play a major role in predicting the physics. Certainly, in some circumstances, it is highly probable that one can establish curve-fitting models which use these "effective properties" to predict the overall behavior of the system, however, specific details of the energy carriers are often needed to explain the physics at nano-scale. That is where the "effective" quantities will fail.

In this chapter, we will discuss modeling electron-phonon transport phenomena at micro/nano-regimen will be discussed. This will include the electron-phonon hydrodynamic equations that are used to describe the electrical and thermal behaviors of the _metal semiconductor field effect transistors_ (MESFETs), and the construction of a Monte Carlo simulation to describe the electronic thermal conduction and to predict the so-called pseudo-temperature profiles of electrons at nano-scale.

7.1 Electrical and Thermal Modeling of MESFETs

Nano-machining involves propagations of electrons inside a target material, for instance, a semiconductor or a metal. These electrons possess huge momentums and energies initially when emitted from the electron gun. The collisions of these incoming energetic electrons with electrons circulating atomic nuclei (i.e. outer-shell electrons and conduction electrons) and lattices (i.e. phonons) require consideration of momentum and energy transfers between these quantum particles.

Modeling such a problem requires a separation of the electron temperature from the phonon temperature since the electron temperature will be thrown far out of equilibrium. This happens as the incoming electrons from an electron source strike the workpiece transferring energy to electrons inside the workpiece. Although the TTM and the DPLM are capable of differentiating the electron temperature from the phonon temperature, the momentums of electrons, and the electrical behavior of the material are simply neglected. In addition, electrons are negatively charged, therefore the incoming electrons (i.e. originated from the electron gun) induce an electric field inside the material due to locally unbalanced positive and negative charges. This not only affects the electron propagations from within, but it also alters the energy transfers between electrons and phonons. A suitable candidate for modeling this problem is the HDM where all the thermal and electrical characteristics of the material are accounted for in the governing equations.

To solve this problem, a numerical HDM is required. The HDM frequently used for modeling semiconductor devices, is first developed numerically to ensure that the simulation produces the correct trend as given in the literature. Next, the developed numerical model will be modified to include momentum transfers between incident electrons from an electron gun and those inside the material.

7.1.1 The Physical Domain

The physical domain under consideration in modeling a MESFET is given in Figure 7.1. The MESFET under consideration in this case consists of two layers. They are the active layer and the semi-insulating layer. The former is deposited on top of the latter. The active layer has an electron concentration in the order of 10^{17} cm^{-3}. The semi-insulating layer is three orders less in

magnitude than that of the active layer. There are three terminals on top of the active layer. They are the source, the drain, and the gate terminals. Each terminal is 500 nm wide. The active layer has a thickness of 150 nm while the semi-insulating layer is 250 nm thick. It is assumed that the MESFET is made of Gallium Arsenide (GaAs).

7.1.2 The Governing Equations

On way to describe the electrical behavior of a MESFET is by using the hydrodynamic equations, which are derived in Section 2.7.3. The details will be repeated here. For the electron flow, these equations consist of the Poisson equation, the electron continuity (or the charge conservation), the electron momentum conservation, and the electron energy conservation:

(*Poisson's Equation*)
$$\nabla^2 V = -\frac{e}{\varepsilon_s}\left(N_D - n_e\right);\ \vec{E} = -\nabla V,\tag{7.1}$$

(*e-Continuity*)
$$\frac{\partial n_e}{\partial t} + \nabla_{\vec{r}}\cdot\left(\vec{v}_{d,e}n_e\right) = 0,\tag{7.2}$$

(*e-Momentum*)
$$\frac{\partial \vec{v}_{d,e}}{\partial t} + \vec{v}_{d,e}\cdot\nabla_{\vec{r}}\vec{v}_{d,e} = -\frac{e}{m_e}\vec{E} - \frac{k_B}{m_e n_e}\nabla_{\vec{r}}\left(n_e T_e\right) - \frac{\vec{v}_{d,e}}{\tau_m},\tag{7.3}$$

(*e-Energy*)
$$\begin{aligned}\frac{\partial T_e}{\partial t} + \left(\vec{v}_{d,e}\cdot\nabla_{\vec{r}}T_e\right) = {}&-\frac{2}{3}T_e\nabla_{\vec{r}}\cdot\vec{v}_{d,e} + \frac{2}{3n_e k_B}\nabla_{\vec{r}}\cdot\left(k_e\nabla_{\vec{r}}T_e\right) - \frac{T_e - T_{LO}}{\tau_{e-LO}}\\ &-\frac{T_e - T_A}{\tau_{e-A}} + \left(\frac{2}{\tau_m} - \frac{1}{\tau_{e-LO}} - \frac{1}{\tau_{e-A}}\right)\frac{m_e v_{d,e}^2}{3k_B} + \left(\frac{2}{3n_e k_B}\right)\dot{W}_{e,gen}\end{aligned}\tag{7.4}$$

The phonon thermal conduction in the MESFET involves the optical phonons and the propagation of the acoustic phonons. The governing equations for these two types of phonons are given as (see Section 2.7.3):

(*LO-Phonon Energy*)
$$\frac{\partial T_{LO}}{\partial t} = \frac{n_e m_e v_{d,e}^2}{2C_{LO}\tau_{e-LO}} - \frac{3n_e k_B\left(T_{LO} - T_e\right)}{2C_{LO}\tau_{e-LO}} - \frac{T_{LO} - T_A}{\tau_{LO-A}},\tag{7.5}$$

(*A-Phonon Energy*)
$$\frac{\partial T_A}{\partial t} = \frac{1}{C_A}\nabla_{\vec{r}}\cdot\left(k_A\nabla_{\vec{r}}T_A\right) + \frac{n_e m_e v_{d,e}^2}{2C_A\tau_{e-A}} - \frac{3n_e k_B\left(T_A - T_e\right)}{2C_A\tau_{e-A}} - \frac{C_{LO}\left(T_A - T_{LO}\right)}{C_A\tau_{LO-A}}.\tag{7.6}$$

Details of the boundary conditions used for these equations are given in Figure 7.1.

7.1.3 Electrical and Thermal Properties

The properties that one needs in order to solve the hydrodynamic equations are the various re-

laxation times and the thermal conductivities for electrons and phonons. The relaxation times are typically derived from the Monte Carlo simulations. These values are obtained from several references in the literature. The thermal conductivity of electrons can be expressed as (Majumdar et al., 1995):

$$k_e = (r+2.5)\frac{n_e k_B^2 \tau_m T_e}{m_e^*},$$ (7.7)

where r is a parameter which varies depending on the material of interest. Note that the thermal conductivity of electrons is a function of the electron density, the electron momentum relaxation rate, and the temperature. Since all these quantities vary locally, the electronic thermal conductivity is a local property as well.

The electron momentum relaxation rate, τ_m, for GaAs as a function of the electron energy, w_e, can be determined using the following expression (Tomizawa, 1993):

$$\tau_m(w_e) = \frac{1+(w_e/w_c)^6}{C_{imp} + C_1 + D_1(w_e + w_0)(w_e/w_c)^6},$$ (7.8)

where

$$C_{imp} = 1.6\left(\frac{N_I}{10^{19}}\right)^{0.4} \times 10^{13} \quad [1/s].$$ (7.9)

Here, N_I is the impurity concentration in the layer in units of cm^{-3}, and the values for C_1, D_1, w_c and w_0 are given as 2.9×10^{12}, 1.7×10^{14}, 0.3eV, and 0.039eV, respectively. The electron energy can be determined from its thermal and velocity components via the following equation:

$$w_e = \frac{3}{2}k_B T_e + \frac{1}{2}m_e v_e^2.$$ (7.10)

Note that the electron momentum relaxation time given above is for constant lattice temperature of 300K. For non-constant lattice temperature, it is assumed that the relaxation rate is inversely proportional to the lattice temperature such that:

$$\tau_m(w_e) = \frac{300}{T_{ph}}\left[\frac{1+(w_e/w_c)^6}{C_{imp} + C_1 + D_1(w_e + w_0)(w_e/w_c)^6}\right].$$ (7.11)

Tomizawa (1993) also provides a similar expression for the electron-phonon relaxation rate given as:

$$\tau_{e-ph}(w_e) = \frac{(w_e + 0.2)\left[1 + (w_e/w_c)^8\right]}{F_1 + G_1(w_e/w_c)^8},$$ (7.12)

where F_1 and G_1 are given as 0.4×10^{12} and 2.8×10^{12}, respectively.

Carnez et al. (1980) provides some data regarding the electron momentum relaxation time and the electron-phonon relaxation time. However, it is not as explicit as those expressed by Tomizawa (1993). Accordingly, both relaxation times are computed using the following formula:

$$\tau_m(w_e) = \frac{m^*(w_e)v_{ss}(w_e)}{qE_{ss}(w_e)},$$ (7.13)

$$\tau_{e-ph}(w_e) = \frac{w_e - w_0}{qE_{ss}(w_e)v_{ss}(w_e)}.$$ (7.14)

Three curves/figures are provided by the authors, they are w_e versus E_{ss}, v_{ss} versus E_{ss}, and m^* versus E_{ss}. In order to determine the relaxation times, one first needs to know the electron energy, w_e. Using the figure plotted as w_e versus E_{ss}, the quantity E_{ss} can be determined. With E_{ss} known, v_{ss} and m^* can be obtained from the other two curves. Unfortunately, the source data for all those curves could not be obtained, therefore the figures were used as is and interpolated as needed to obtain the necessary data points, in order to determine the relaxation times. The results for the relaxation times according to the two sources are plotted in Figure 7.2 and Figure 7.3.

The expressions for the heat capacities of optical and acoustic phonons that were used in this work are given as (Majumdar et al., 1995):

$$C_{LO} = 3.06 \times 10^5 - 2.40 \times 10^4 \left(\frac{\theta_{LO}}{T_{LO}}\right)^{1.94} \quad [\text{J/m}^3\text{-K}],$$ (7.15)

$$C_A = 9.17 \times 10^5 - 4.40 \times 10^4 \left(\frac{\theta_D}{T_A}\right)^{1.948} \quad [\text{J/m}^3\text{-K}],$$ (7.16)

where the values for θ_{LO} and θ_A are assumed to be 429K and 344K, respectively.

7.1.4 Results and Discussions

In order to numerically predict the electrical and thermal behavior of MESFET, Eqs. (7.1)-(7.6) need to be solved simultaneously, with all the properties listed above. For the sake of sim-

plicity, it is assumed that electrons are first transferring energy to optical (LO) phonons, and the acoustic (A) phonons subsequently gain energy through the hot optical phonons. Hence, the electron-phonon relaxation time (i.e. $\tau_{e\text{-}ph}$) given above is assumed to be the electron-optical phonon relaxation time (i.e. $\tau_{e\text{-}LO}$). According to the governing equations, there are four parameters involving the relaxation time. They are τ_m, $\tau_{e\text{-}LO}$, $\tau_{e\text{-}A}$, and $\tau_{A\text{-}LO}$, which are the momentum, the electron-optical phonon, the electron-acoustic phonon, and the acoustic-optical phonon relaxation times, respectively. In deriving the governing equations, all these parameters are included for the sake of completeness. However, $\tau_{e\text{-}A}$ will be omitted in the following simulation since there is no information regarding the magnitude of this relaxation time. For $\tau_{A\text{-}LO}$, 8 ps were chosen (Fushinobu et al., 1995). The discretizations of the governing equations are given in Appendix D. Systems of equations are obtained and solved accordingly using the point successive-overrelaxation (SOR) numerical scheme. Solving equations of this kind may not be efficient using the SOR method, however at this point, the interest is in obtaining the solution. Increasing the speed of the convergence of the computational code can be done in future works.

In order to verify the validity of the numerical solution, the drain currents are computed for various drain voltages and gate voltages. The source voltage in this case is always fixed at 0 V in the simulation. For all the cases, the simulation is run until a steady-state condition is reached. The steady-state condition occurs when the source current and the drain current reach the same magnitude. Figure 7.4 depicts the drain current as a function of the drain voltage and the gate voltage. The lattice temperature (i.e. both the optical phonons and the acoutics phonons) is set to room temperature throughout the simulation and the entire MESFET. The reason for employing such an assumption is that the intention is to generate results that are comparable to the ones given by Yoganathan and Banerjee (1992) in order to verify simulation. Since it was impossible to obtain any publications that indicated standard experimental and numerical results, this verification offers some degree of correctness in the simulation. The results given in the figure closely represent those obtained by Yoganathan and Banerjee (1992) in their publication. Sample figures for the electron temperature, the electron density, the potential, the electric field, the Joule heating rate, the current density, the optical phonon temperature, and the acoustic phonon temperature of the case where the drain voltage and the gate voltage are set to 3V and 0V, respectively, are given from Figure 7.5 to Figure 7.8. These are typical simulation results for a MESFET oper-

191

ating at a given set of conditions.

7.2 Electronic Thermal Conduction – A Monte Carlo Approach

Electron transport inside a semiconductor is a well-established research area due to the rapid development of electronic chips at the micro- or nano-scale size. In addition, most electron transports in these applications are studied at relatively low temperatures (i.e., a few Kelvin to a few hundred Kelvin). On the contrary, electron transport in noble metals at the nano-scale level is still under heavy investigation owing to the peculiar overlapping of the electronic band structures (see Figure 7.9). The overlapping behaviors of this kind present a major challenge in determining the rates of scattering events for electrons, as well as for phonons. This is true even at low temperature applications where the Umklapp scattering processes are frozen out (Ashroft and Mermin, 1976; Ziman, 1960). In this section, the electron transport in thin gold films is investigated using a Monte Carlo Method (MCM) to better understand these mechanisms at nano-scale level. The MC simulation procedures used in this case are discussed in Section 3.3, which will not be repeated here. The properties used in the simulation will be given.

In the following simulations, the parabolic band structure of gold is taken into consideration as well as the electron-electron scattering rates and the electron-phonon scattering rates. The scattering nature of electrons in gold is based on the selection rules presented according to the time-dependent perturbation theory. Using the MC simulations the electron transport phenomena is investigated inside gold at the nano-scale. The effectiveness of electron propagation inside gold are then evaluated based on the scattering rates.

7.2.1 Electron Band Structure

The electronic band structure of electron in any material is obtained through solving the Schrödinger equation. The electronic band structures of transitional elements such as silver, copper, and gold are generally complicated owing to the peculiar overlapping and the anisotropic characteristics of the d-bands. Incorporating these band structures, such as that of gold given in Figure 7.9, into the Monte Carlo (MC) simulation requires extensive computing resources and power. The numerical procedures involved are not difficult but they are tedious. In this work, the goal is to establish the Monte Carlo procedures for simulating the electron transport in a medium

192

or a solid with temperature variation as opposed to the charge transport in a constant temperature field. The approximations of the properties of solid are used. Accurate derivations of the medium properties can be carried out later to improve the accuracy of the MC simulation using the band structure given in Figure 7.9. In this work, a parabolic band structure with an effective electron mass is assumed and the band is supposed to be independent of the wave number, but not of the electron wave vector. It is given as:

$$E(k) = \frac{\hbar^2 k^2}{2m^*},$$ (7.17)

where $\hbar$ is the Planck constant, k is the wave number, and m^* is the effective mass of electron. In this case, m^* is the effective mass of electron in gold which is 0.6515 m_o and m_o is the electron rest mass (i.e., 9.1095×10^{-31} kg).

In the simulation, electrons with energies larger than the Fermi energy, E_F are allowed to propagate, otherwise, electrons with smaller energies than E_F are assumed to be bonding strongly with atoms and not moving.

7.2.2 Electron-Electron Scattering

There are two categories of electron-electron (e-e) scatterings: conduction[14] electron-inner shell[15] electron and conduction electron-conduction electron. It is a well-known fact that coulomb forces of electrons pose long range effects and an electron is capable of influencing other electrons far from its current location. Thus, deriving the electron-electron scattering rate is unduly complicated and the subject is still under intensive investigations and studies. In this work, only the electron-electron (e-e) scattering among the conduction electrons as being the short range interaction is considered. Accordingly, such rate of scattering is expressed as (Ziman, 1960):

$$P_{e-e}\left(\vec{k},\vec{k}';\vec{k}_1,\vec{k}_1'\right) = \frac{2\pi}{\hbar}\left| M\left(\vec{k},\vec{k}';\vec{k}_1,\vec{k}_1'\right)\right|^2 \delta\left(\vec{k}'-\vec{k}+\vec{k}_1'-\vec{k}_1+\vec{g}\right)\delta\left(E_{\vec{k}'}-E_{\vec{k}}+E_{\vec{k}_1'}-E_{\vec{k}_1}\right),$$ (7.18)

where M is the transition matrix element. To compute the e-e scattering as a function of the en-

---

[14] Note that conduction electrons or outer-shell electrons are electrons with energies larger than the Fermi energy, and behave as free electron-like. These are the electrons that are being simulated using the Monte Carlo approach.

ergy of a propagating electron, the following integrations are performed:

$$P_{e-e}(\bar{k}) = \iiint P_{e-e}(\bar{k}, \bar{k}'; \bar{k}_1, \bar{k}_1') f_{\bar{k}_1}(1 - f_{\bar{k}'})(1 - f_{\bar{k}_1'}) d\bar{k}' d\bar{k}_1 d\bar{k}_1' . \tag{7.19}$$

The integrations are performed using the assumption that the spherical parabolic electronic band structure prevails and refers to the analyses given by Ziman (1960). Thus, the scattering rate for the e-e N-processes is expressed as:

$$P_{e-e}^{N}(k) = 2\pi \aleph k^2 \int_0^{2k} \frac{1}{\left(q^2 + q_s^2\right)^2} dq , \tag{7.20}$$

where

$$\aleph = -\frac{\Xi^2 e^4 (k_B T)^2}{\pi^3 \hbar^4 v_k^3} \int_{-\infty}^{\infty} \frac{z}{\left(e^{-(E_k - E_F)/k_B T} e^{-z} + 1\right)(e^z - 1)} dz , \tag{7.21}$$

$$q_s^2 = \frac{4\pi n e^2}{k_B T} . \tag{7.22}$$

Similarly, the U-processes for e-e scattering is derived as:

$$P_{e-e}^{U}(k) = 2\pi \aleph k^2 \int_{g-2k}^{2k} \left[\frac{z'}{2g} \int_{g-q}^{2k} \frac{1}{\left(K^2 + q_s^2\right)^2} dK \right] dq . \tag{7.23}$$

For N-processes, $\Xi^2 \approx 1$ while $\Xi^2 \approx 0.01$ for U-processes. In the process of deriving the above expression, it is assumed that the scattering is absolutely elastic. This may not be entirely justified from the physical point of view for the electron-electron interactions. However, it shall be complied with, since deriving more realistic e-e scattering is a challenging task and requires more elaborated work.

The e-e scattering rate as a function of temperature for gold is depicted in Figure 7.10. The e-e scattering rates at different temperatures converge into a single curve for electron energy exceeds 6.0 eV, as the integral given in Eq. (7.21) converges to a single value regardless of the magnitude of E_k. Compared to the e-ph scattering rate near the Fermi energy, the e-e scattering rate is several orders smaller in magnitude, showing that the e-e interaction is not of importance for electron transport near Fermi level.

---

[15] Inner-shell electrons are electrons packed closely with nuclei, combinations which are referred to as atoms and they are usually not able to propagate freely.

In this work, it is assumed that there are no external sources being used, (i.e. short-pulsed laser or electron gun) that are capable of causing an energy increase of several electron-volts to electrons. The simulation is performed for electrons with energy in the order of $k_B T$ above the Fermi level following the Fermi-Dirac statistics.

7.2.3 Electron-Phonon Scattering

The electron-phonon (*e-ph*) interaction involves the collision of a propagating electron with an atom which leads to the creation or destruction of a phonon. This is where the electron can gain or lose energy. Accurate calculation of the electron-phonon scattering rate requires the actual electronic band structure. These procedures involved are usually quite tedious due to encountering complicated integrations, and the numeric evaluations of the scattering rates. With the assumption of an isotropic, parabolic band structure, obtaining the electron-phonon scattering rate is relatively simple, as given by Ziman (1960).

Generally, the probability of electron-phonon scattering per unit time can be obtained from the time-dependent perturbation theory as (Ziman, 1960):

$$P_{e-ph}\left(\vec{k},\vec{k}';\vec{q},p\right) = \frac{2\pi}{\hbar}\left| M\left(\vec{k},\vec{k}'\right)\right|^2 \delta\left(E_{\vec{k}'} - E_{\vec{k}} \pm \hbar\omega_{\vec{q},p}\right)\delta\left(\vec{k}' - \vec{k} \pm \vec{q} - \vec{g}\right) . \qquad (7.24)$$

Here, M is the scattering matrix element. The Bardeen's self-consistent form for the scattering matrix element is emplyoed. Note that there are two delta functions appearing in Eq. (7.24). The first implies the energy conservation of the electron-phonon collision, while the second indicates the momentum conservation of the process. In the MC simulation, the scattering rate as a function of incident electron wave vector $\vec{k}$ is required. This can be achieved by performing two integrations over the scattered electron wave vector $\vec{k}'$ and the entire phonon wave vector $\vec{q}$ and then summing up the results for all three phonon polarization branches (i.e., two transverse and one longitudinal polarizations). The electron-phonon scattering rate becomes:

$$P_{e-ph}\left(\vec{k}\right) = \sum_p \iint_{\vec{k}',\vec{q}} P_{e-ph}\left(\vec{k},\vec{k}';\vec{q},p\right)\left(1 - f_{\vec{k}'}\right) d\vec{k}' d\vec{q} . \qquad (7.25)$$

Following the details given by Ziman and employing the isotropic, parabolic band structure assumption, the expression for the scattering rate accounting for the electron-phonon Normal (N)

scatterings can be derived as:

$$P^N_{e-ph}(k) = \frac{(1-f_k)}{4\pi mN\hbar v_k} \int_0^Q \left(\frac{1}{\omega_q}\right)(2\langle n\rangle_q + 1)\left|\tilde{P}_q(K)\right|^2 qdq, \qquad (7.26)$$

while for the Umklapp (U) processes, it is determined as:

$$P^U_{e-ph}(k) = \frac{z'(1-f_k)}{8\pi gmN\hbar v_k} \int_{g-2k}^Q \int_{g-q}^{2k} \left(\frac{q}{\omega_q}\right)(2\langle n\rangle_q + 1)\left|\tilde{P}_q(K)\right|^2 dKdq, \qquad (7.27)$$

where $\tilde{P}_q(K)$ is the overlap factor and $K = |\vec{k}' - \vec{k}|$. It is assumed that electrons are scattered only by phonons in the longitudinal branch and the scattering is elastic (i.e. $|\vec{k}'| = |\vec{k}|$). This is fairly justified since the energy of a phonon in a metal is generally small compared to that of an electron. The above two expressions are evaluated numerically by using Bardeen's form of over-lap factor and Debye's model for the phonon dispersion relation (i.e. $\omega_q = v_g q$ where v_g is the group velocity of phonon) with a cutoff wave vector Q. The longitudinal phonon group velocity can be determined by finding the slope of the dispersion curve for the longitudinal branch given in the paper published by Singh and Prakash (1973).

The electron-phonon scattering rate for gold is depicted in Figure 7.11. Generally, the scattering rate increases as electron energy increases. Although it is not shown here, the scattering rate for N-processes increases rapidly for electron energy near the Fermi level, and then decreases gradually as energy increases. The further increases in all the curves beyond 6 eV (as portrayed by Figure 7.11) is because the possibility of U-processes occurring increases when the energy of electron becomes high. Details about N- and U- processes can be found elsewhere (Ziman, 1960; Ziman, 1964).

7.2.4 Monte Carlo Simulation Results

Using the simulations, the range of applicability of the Fourier law for the steady-state thermal transport at nano-scale in thin metallic films can be determined. The temperature profiles for various thicknesses of gold films subject to isothermal boundary conditions are obtained using the simulation. The number of energy intervals used in the simulations is 20 and each has 50 electron ensembles. Each computational element possesses a total of 1000 ensembles initially. The geometry is always set to be L × L × L where L is the thickness of the film that is divided

196

into 1000 computational cubic elements. As a result, the total number of ensembles in the entire domain adds up to 1,000,000. In the simulations, the time interval is chosen in a way that electrons do not propagate through two computational elements at each time step. Several other runs with different computational parameters were performed and the results indicated that the above chosen values are sufficient enough to resolve reasonable temperature profiles where fluctuations in temperature are within 10 degrees or less. The computational time required for each simulation was not documented. It was observed that a simulation requires several clock hours to reach a steady-state condition. In the following results, each temperature profile is constructed by calculating the mean values of temperature at various film locations after 5 independent MC simulations with standard deviations depicted as error bars in the figures.

The one-dimensional temperature profiles for gold thicknesses of 1 m and 100 nm are depicted in Figure 7.12. The straight lines in the figure illustrate the results that one would obtain if the Fourier law is used. The prediction of the linear temperature profile by the model for the thicker gold film shows the correct physical background of the model at the diffusion limit where the electron scattering probability is always 100 percent for any ensemble at any time. According to Figure 7.12, the heat transport is still diffusive in a 100-nm gold film, meaning that the Fourier law is still valid at such scale. This is not surprising given that the total electron collision rate is about 0.2 fs^{-1} near 300-400 K. This implies that the mean free time of electrons is approximately 5 fs. On the average, electrons are capable of traveling at about 1 nm/fs. Therefore, the mean free path of electrons is roughly 5 nm. As expected, a film thickness of 100 nm should demonstrate diffusion-like heat transport.

The temperature profiles for film thicknesses of 1 nm and 10 nm are shown in Figure 7.13, where the semi-ballistic nature of the transport is evident. At such thicknesses, the temperature profiles no longer follow the Fourier law. Note that the temperatures near the upper edge start to decrease when the gold thickness decreases, while at the other end the temperature increases with decreasing film thickness. This suggests that the diffusive behavior of the film starts fading when the mean free path of electrons becomes comparable to the medium thickness, and where the ballistic nature of the electrons starts surfacing. Therefore, electrons are capable of transferring energy ballistically from one end to the other, causing the temperature near the upper

boundary to drop and the temperature near the lower surface to increase.

It can be said that at 1-10 nm regime the transport is semi-ballistic because some[16] of the electrons inside the gold with higher energy levels still "see" the medium as diffusive. In other words, their rate of collision is high. This is evident from the temperature profiles near the upper and lower edges. If the transport were completely ballistic, the temperature profile should be flat as that reported for phonons by Mazumder and Majumdar (2001).

7.2.5 Comments

The Boltzmann transport equation is solved using a Monte Carlo approach to investigate the electronic thermal conduction in thin gold-films. Both the electron-phonon and electron-electron scattering rates are included in the simulations. These results show that a thin gold film of a thickness of 100 nm exhibits a diffusion-like heat transport due to the small mean free path (i.e. ~ 5 nm) of electrons. The semi-ballistic nature of the electronic thermal transport is also captured using this statistical computational scheme. The results extended to 10 nm show that Fourier law loses its accuracy at such small scale.

---

[16] Due to the high temperature at the upper boundary (i.e. 1300 K) and the Fermi-Dirac statistics at this temperature, high-energy electrons are still part of the transport mechanism.

Geometry

Boundary conditions
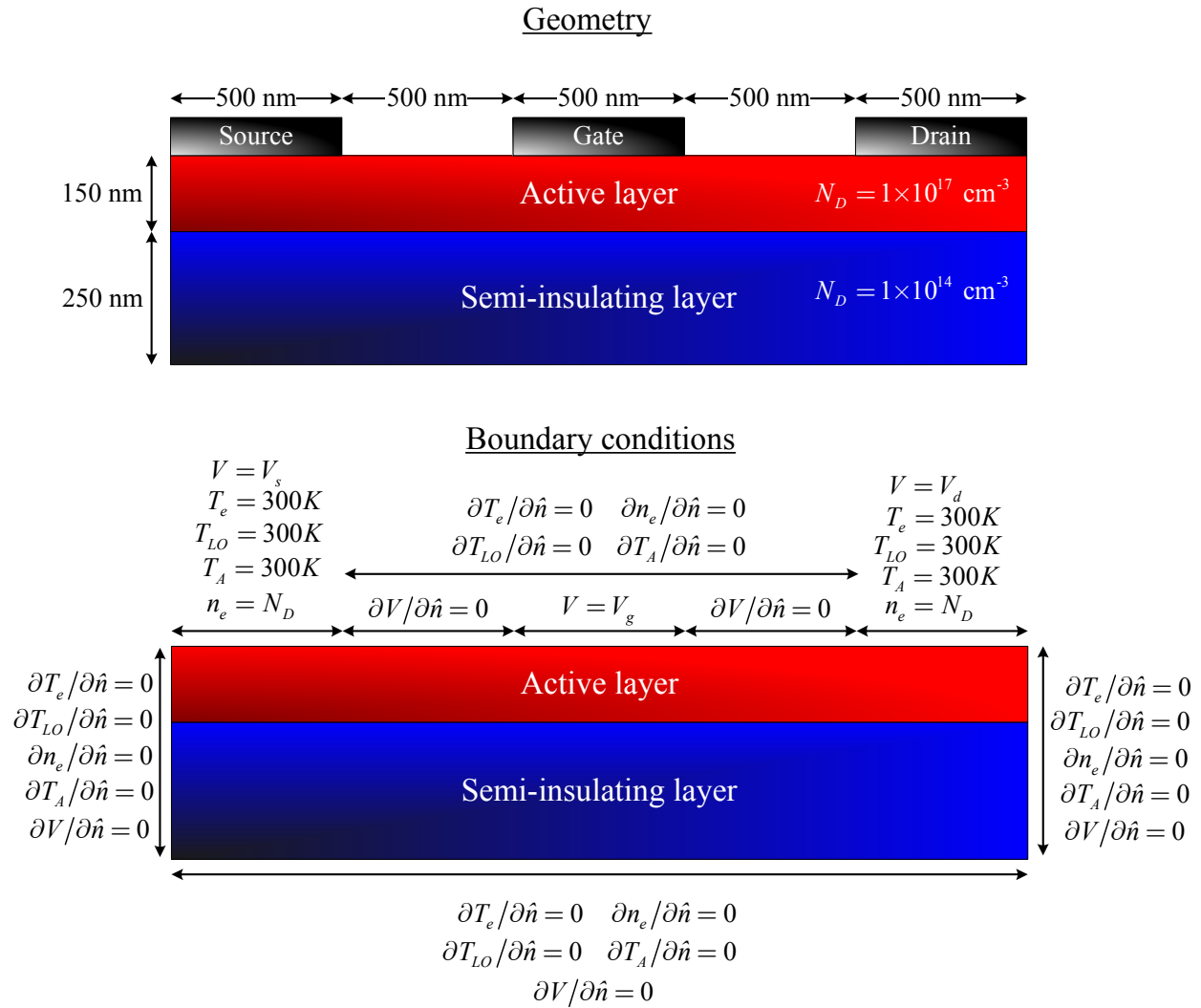
Figure 7.1 (a) A two-dimensional view of a MESFET with an active layer deposited on top of a semi-insulating layer, and (b) the corresponding boundary conditions given in the figure.
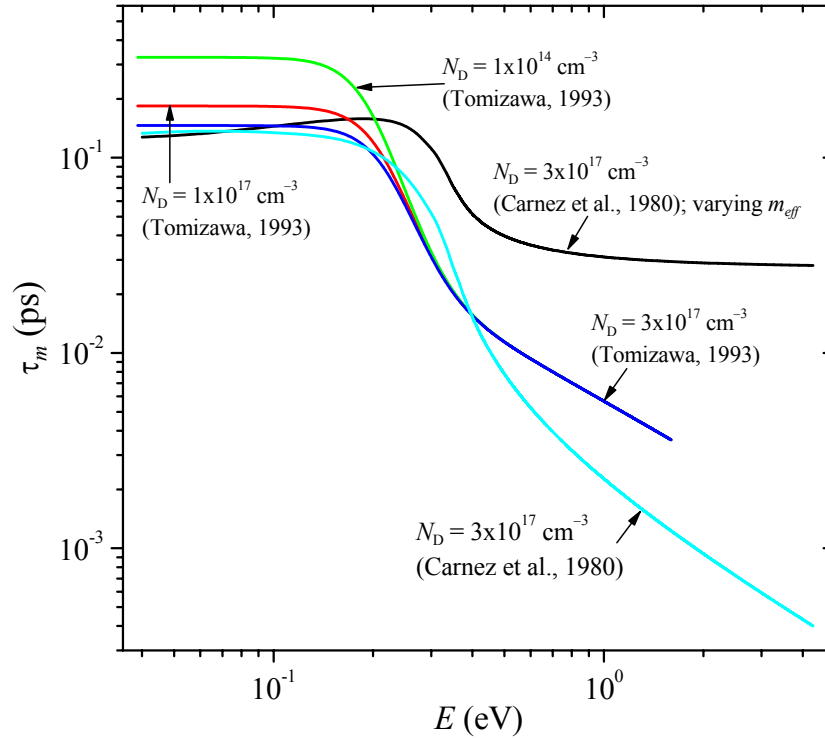
Figure 7.2   The electron momentum relaxation rates as a function of electron energy for various electron concentrations are depicted. The relaxation rates are derived from the Monte Carlo simulation of the electron propagation. The material is Gallium Arsenide (GaAs) and the effective mass used in the simulation is $0.067m_0$, unless otherwise specified.
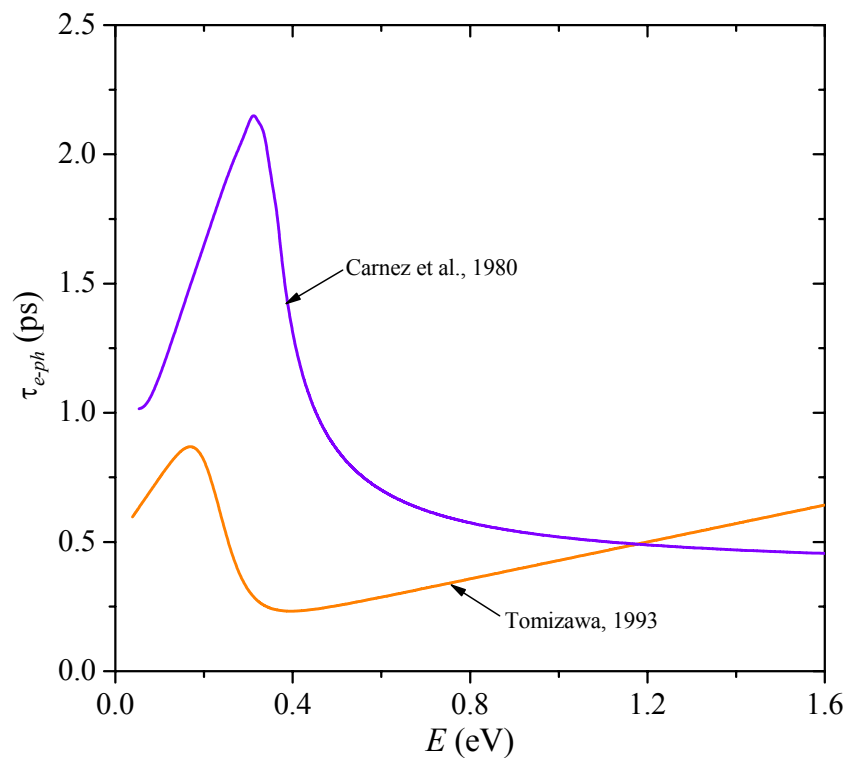
Figure 7.3   The electron-phonon relaxation rates as a function of electron energy obtained from two different sources are depicted. The relaxation rates are derived from the Monte Carlo simulation of the electron propagation. Note that there is a large discrepancy between the results of the two simulations.
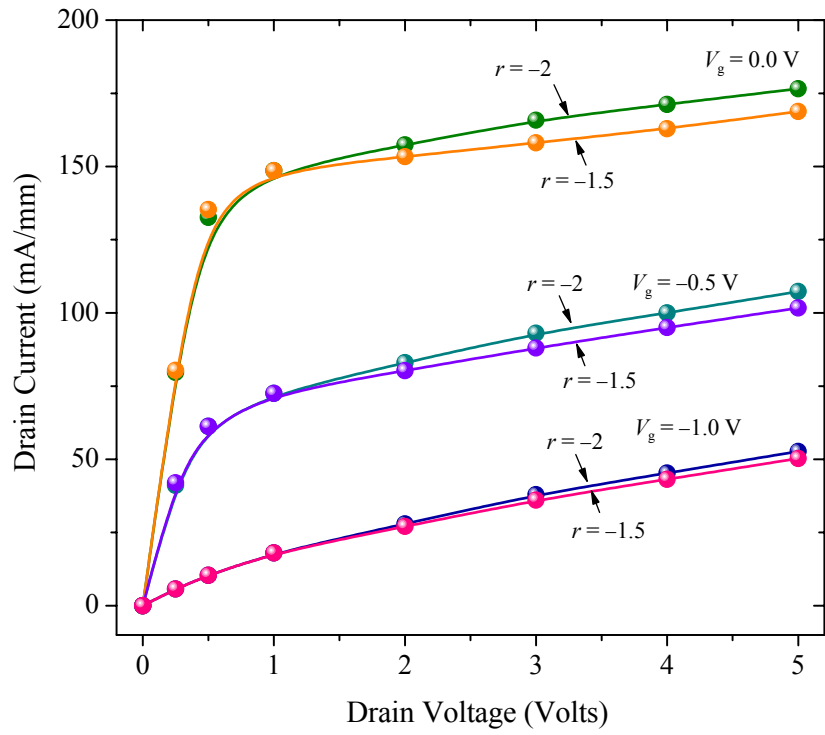
Figure 7.4   The drain current versus the drain voltage characteristic of a MESFET is shown. The lattice temperature is assumed to be constant, which is at 300 K.
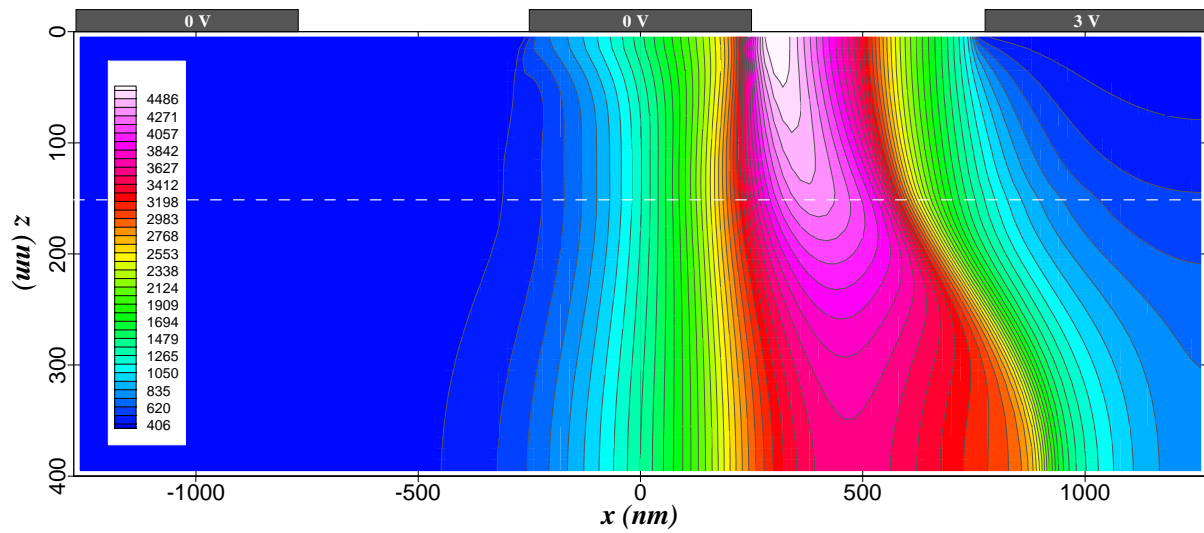
(a)
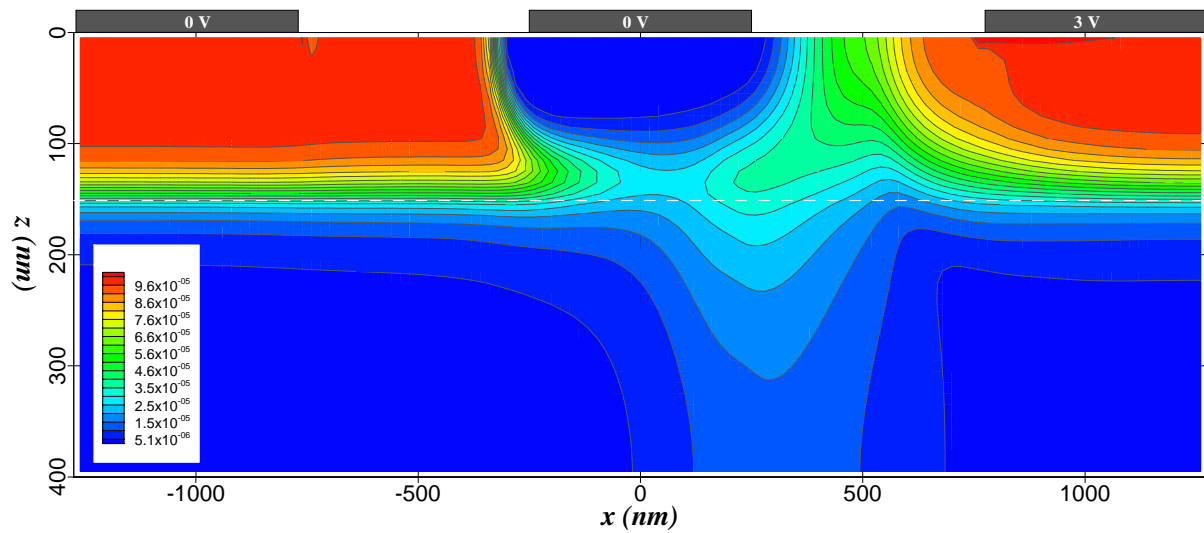
(b)

Figure 7.5   The electron temperature field and the electron concentration inside the MESFET after 40 ns are illustrated.

203
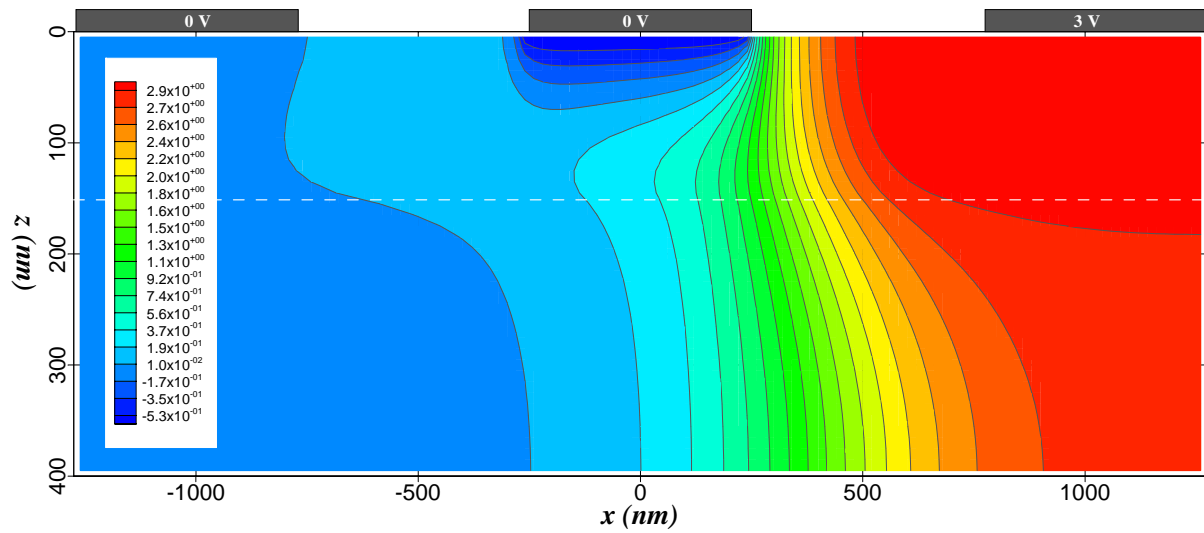
(a)
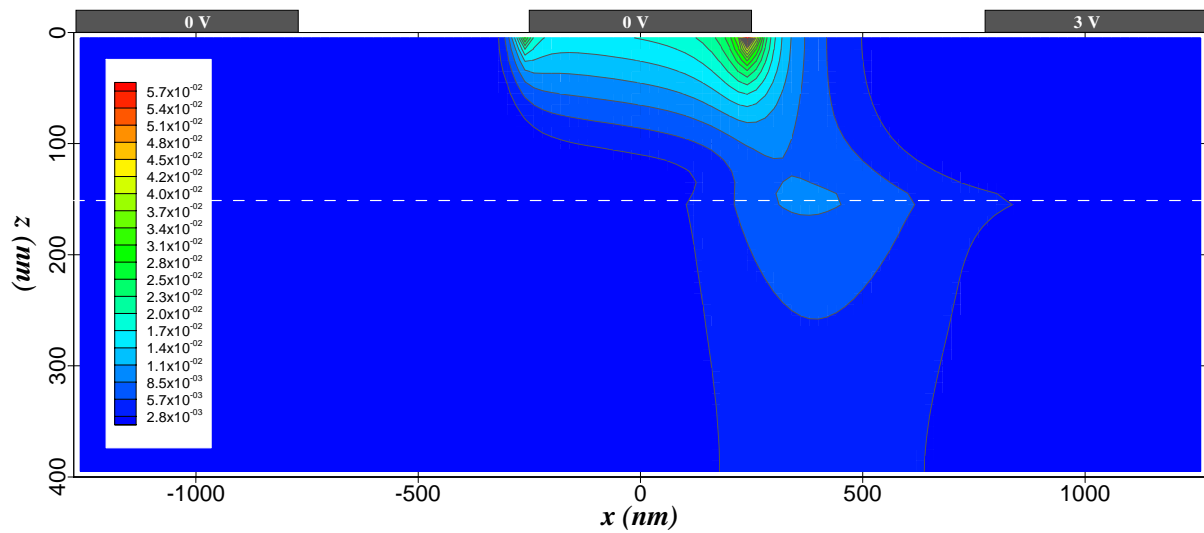
(b)

Figure 7.6   The potential distribution and the electric field distribution inside the MESFET after 40 ns of running the simulation are given.
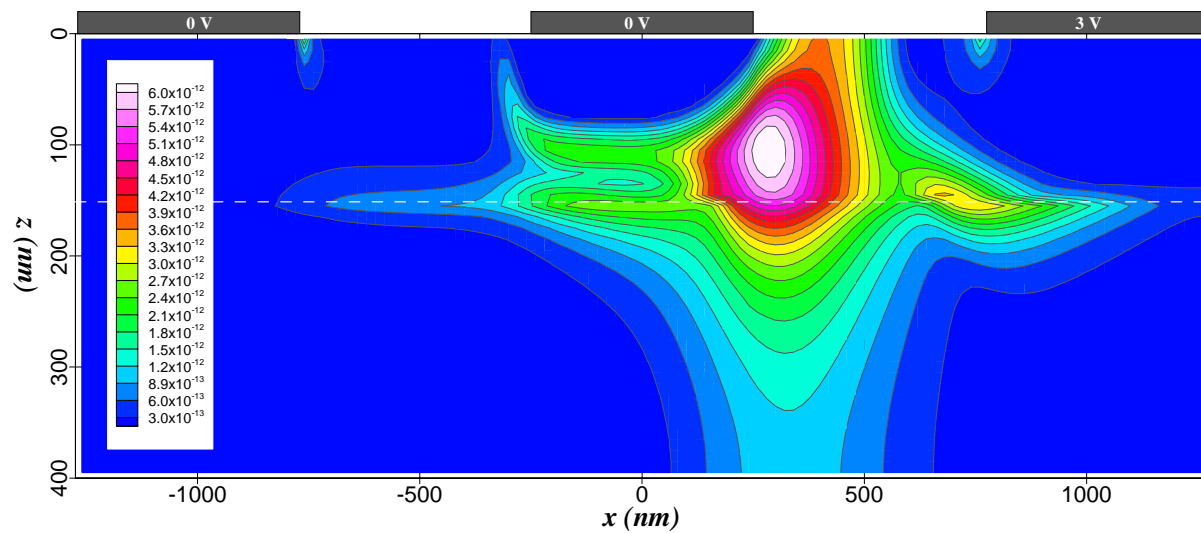
(a)
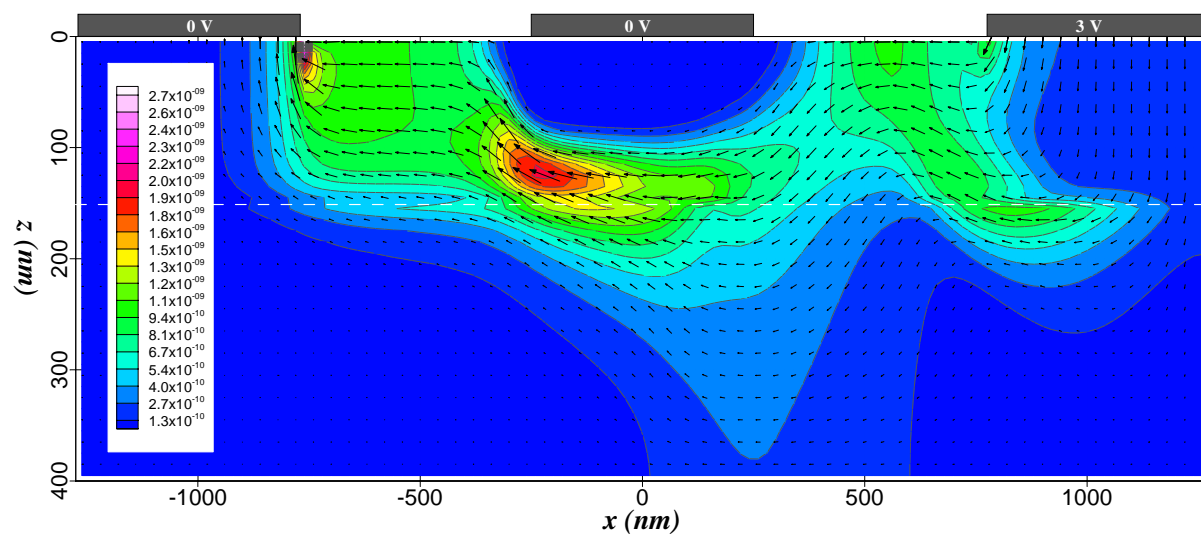
(b)

Figure 7.7   The Joule heating rate and the electron current density inside the MES-FET after 40 ns of running the simulation are given.

205
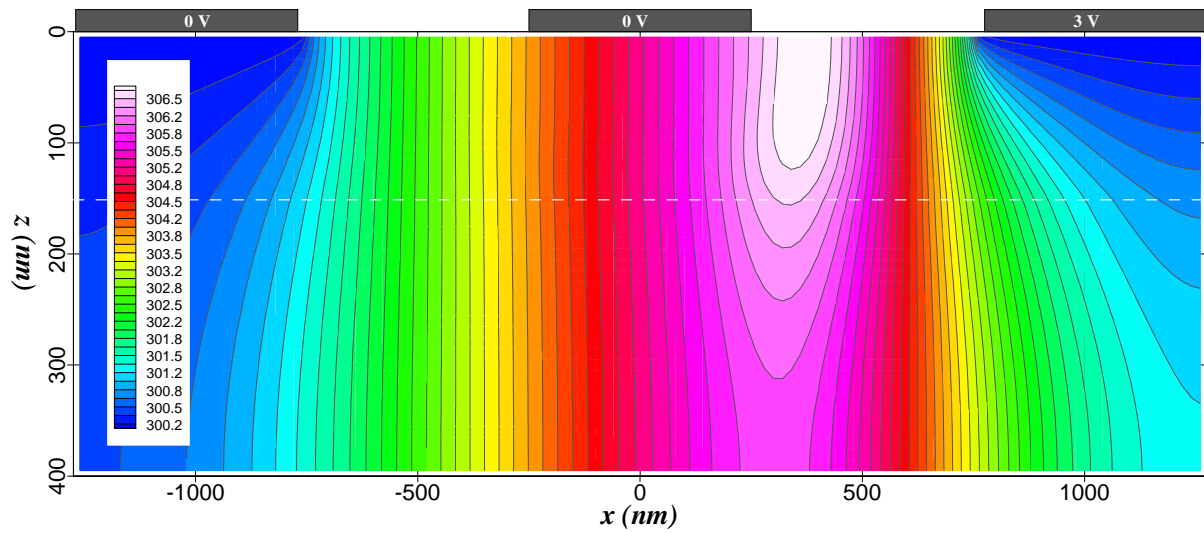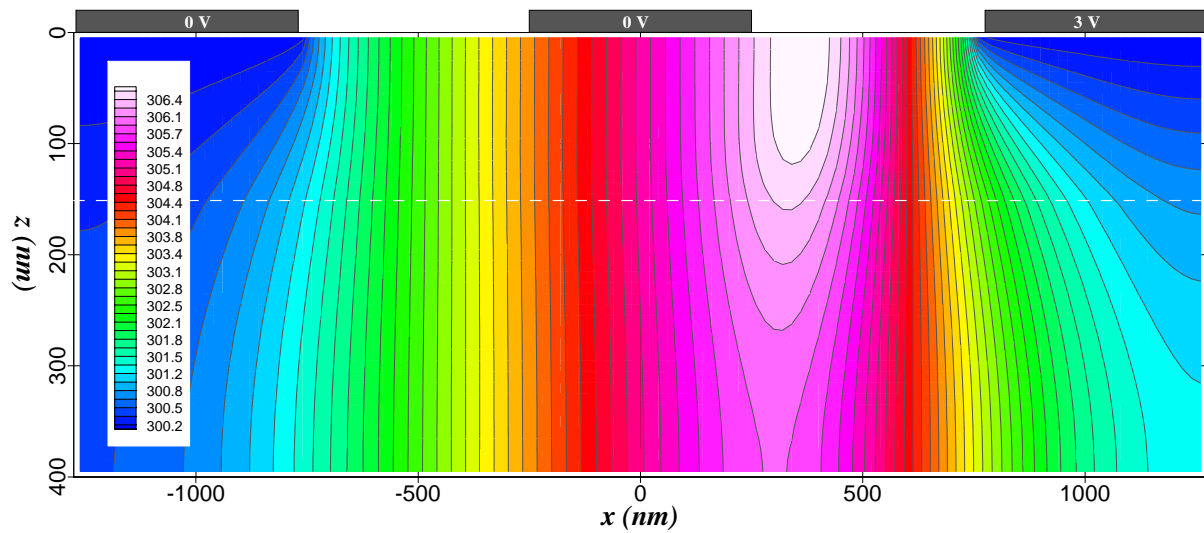
Figure 7.8   The optical (LO) phonon temperature and the acoustic (A) phonon temperature inside the MESFET after 40 ns are depicted.
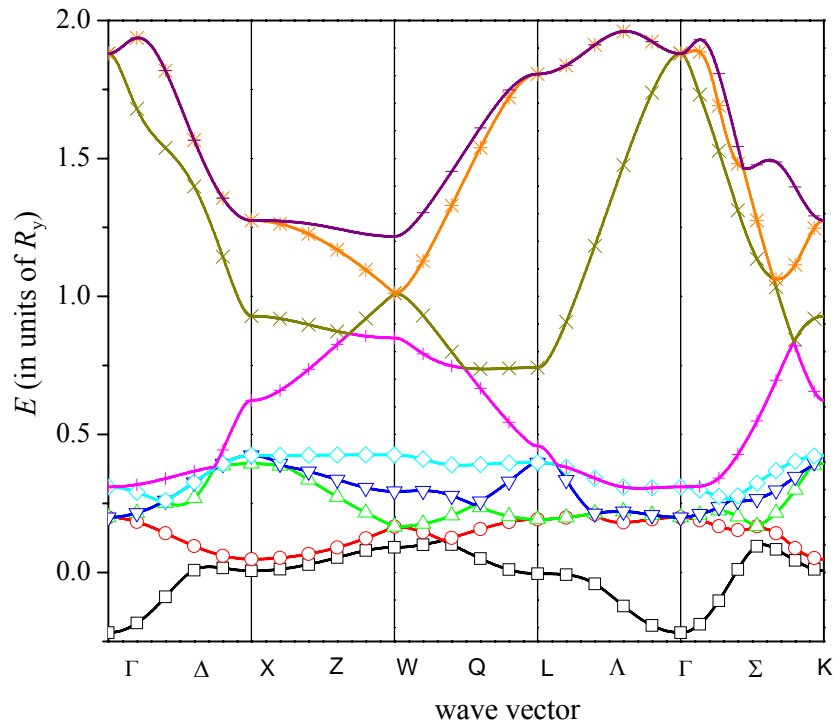
Figure 7.9 The electronic band structure of gold is shown in this figure. Notice the peculiar overlapping between different bands. Such behavior enhances the difficulty in deriving the scattering rates and hence the relaxation rates. Source data is obtained from the address, http://manybody.nrl.navy.mil/esdata/database.html.
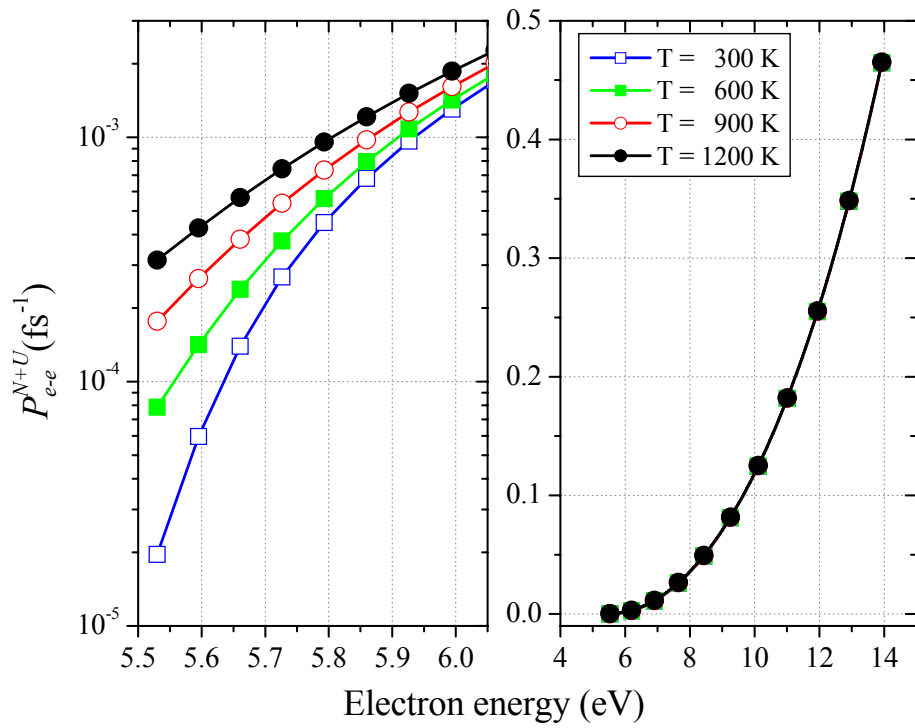
Figure 7.10 The electron-electron (e-e) scattering rate as a function temperature for gold as computed using Eqs. (7.26) and (7.27).
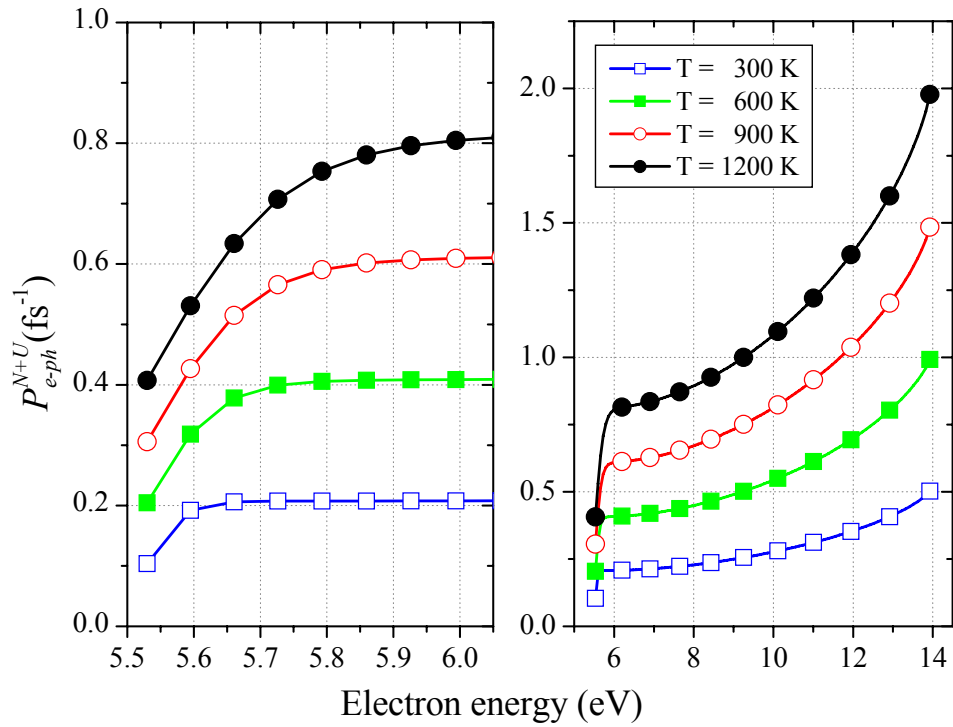
Figure 7.11 The electron-phonon scattering rate as a function temperature for gold as computed using Eqs. (7.26) and (7.27).
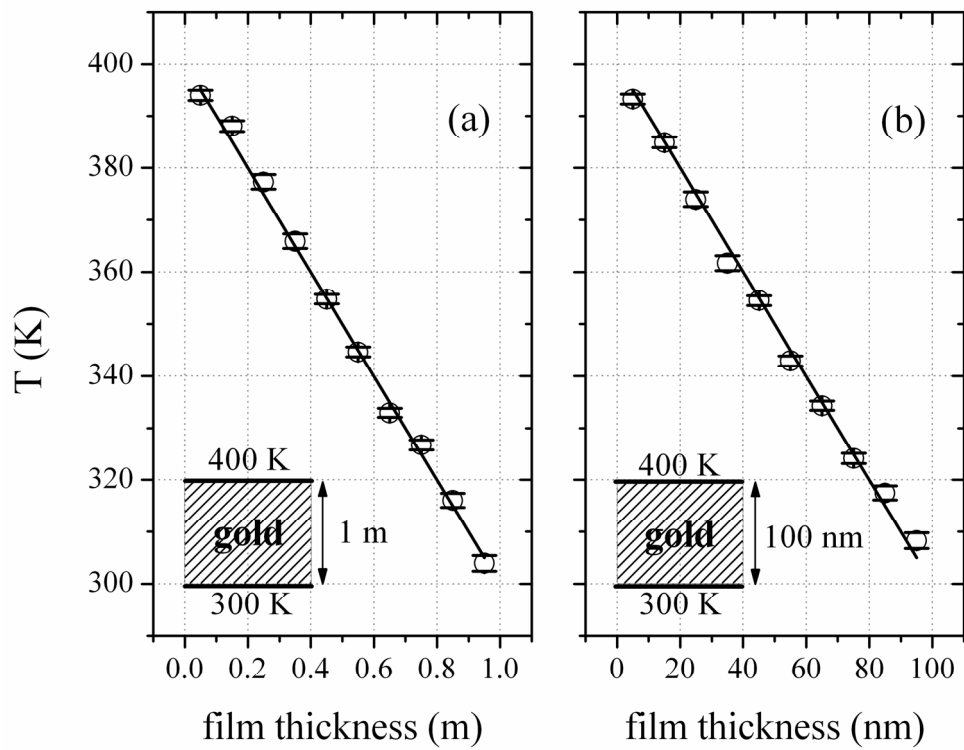
Figure 7.12 Temperature profiles for a film thickness of (a) 1 m, and (b) 100 nm demonstrating diffusion-like behavior and obeying the Fourier law of conduction (given as straight lines)
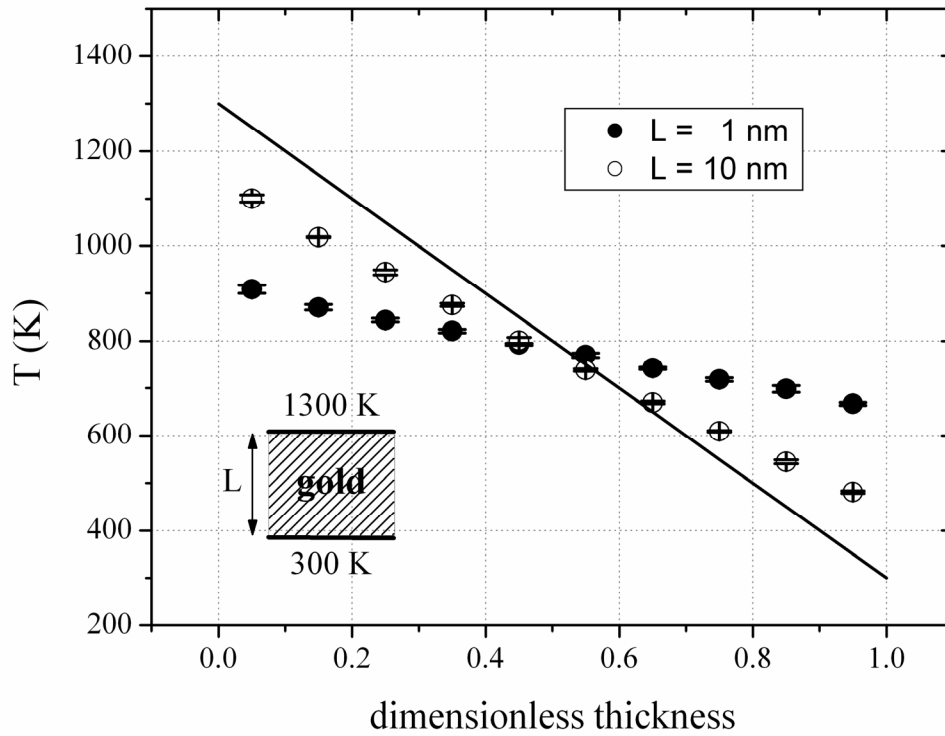
Figure 7.13 Temperature profiles for a film thickness of (a) 5 nm, and (b) 10 nm demonstrating semi-ballistic-like behavior at which the linearity of the Fourier law breaks down

CHAPTER 8
CONCLUSIONS

This dissertation emerges as a result of motivation in modeling the nano-machining process using the electron field emission from a nano-probe. Various theoretical models ranging from macro- to micro-thermal heat transport in solids are studied and derived thoroughly from the Boltzmann Transport Equation (BTE) in the dissertation. Also, the Monte Carlo methods for various transport phenomena are completely outlined, which mostly dealt with the energy-beam propagation. All these theoretical models then served as "tools" to predict the heating phenomena inside a workpiece when exposed to an energetic electron-beam.

The physical problem considered in this dissertation a workpiece exposed to an electron-beam. The electron-beam helps increasing the internal energy on a nano-scale area of the workpiece and subsequently induces melting and evaporation, or sublimation alone to deliver nano-indentation. Modeling such a problem is quite challenging due to the fact that complicated governing equations are involved. The basic idea in tackling this problem is to first predict the electron-energy deposition profile using a Monte Carlo simulation for the electron-beam propagation inside the workpiece. This profile is then treated as the energy source for the thermal heat conduction equation. The main assumption is that the electron-beam propagation inside the material reaches a steady-state in a time duration that is much shorter than the response time of the material. This is generally true since the energy transfer between the incoming electrons and the material itself occurs within femto-seconds, while it takes pico- to nano-seconds for the material to conduct the heat away.

In this dissertation, two different Monte Carlo simulations in predicting the electron-beam propagation inside a solid have been developed. One is based on the Continuous Slow-Down Approach (CSDA) while the other is based on the Discrete Inelastic Scattering approach (DIS). Both are discussed in detail within the dissertation. Using these methods, the electron-energy deposition profiles for various initial electron-beam energies, ranging from kilo-electronvolts down to hundreds of electronvolts were able to be predicted. These profiles were then coupled separately with the Fourier's law and the Two-Temperature Model (TTM), to determine the tem-

perature within the workpiece as a result of exposing it to an electron-beam. The results showed that nano-machining is possible in the range of nano-seconds if the electron-beam has an incident power of 0.1-0.5 watt with an incident Gaussian area of hundreds of nano-meters in diameter. Details of the specifications of the beam and of the geometrical configuration are all given in the dissertation. The concept and the possibility of sequential nano-patterning using these numerical approaches were also demonstrated.

In the final chapter, the electron-phonon hydrodynamical model for a MESFET was discussed as well as the Monte Carlo simulation of temperature profile inside the material due to semi-ballistic transport of electrons. The purpose for studying these models was to build a foundation for future works regarding the couplings between the models and the electron-energy deposition profiles. This will enable the consideration of the electrical and thermal response of the target workpiece simultaneously.

Another possible improvement to the simulation model in this dissertation will be to couple the electron-beam Monte Carlo method with the Monte Carlo method in electronic thermal conduction and phonon conduction. The use of the traditional heat equation is eliminated since the Monte Carlo method is utilized to predict the thermal response of the material. In this case, there will be three Monte Carlo simulations involved, and they are to be executed simultaneously. They need to be coupled correctly with the appropriate scattering cross-sections for electrons and phonons. Finally, the phonon energy equation in either the TTM or the hydrodynamical model is assumed to be diffusive in conducting the heat. The accuracy of the model can be further improved by replacing the equation with the molecular dynamic simulation.

In this appendix, the derivation of the matrix elements for the system of equations discussed in Section 5.2.8 is continued. Recall that:

$$N_{\mathrm{w}} = N_{z1} + N_{z2} - 1, \tag{A.1}$$

$$N_{\mathrm{uni}} = N_{r1} + N_{r2} - 1, \tag{A.2}$$

$$N_r = N_{r1} + N_{r2} + N_{r3} - 1, \tag{A.3}$$

$$N_z = N_{z1} + N_{z2} + N_{z3} - 1, \tag{A.4}$$

and the numerical boundary conditions are given as:

$$
\begin{aligned}
T_{-1,n}^{P+1} &= T_{0,n}^{P+1} & \forall \; n = 0,\, 1, \ldots, N_z - 1,\\
T_{m,-1}^{P+1} &= T_{m,0}^{P+1} & \forall \; m = 0,\, 1, \ldots, N_r - 1,\\
T_{m,N_z-1}^{P+1} &= T_{m,N_z-1}^{P+1} & \forall \; m = 0,\, 1, \ldots, N_r - 1,\\
T_{N_r,n}^{P+1} &= 2T_0 - T_{N_r-1,n}^{P+1} & \forall \; n = 0,\, 1, \ldots, N_z - 1.
\end{aligned}
\tag{A.5}
$$

In order to avoid carrying lengthy terms in the derivations, the following notations are assumed:

$$a_{\mathrm{w}} = 1 + A_{1\mathrm{w}}^{m-1 \to m} + A_{2\mathrm{w}}^{m+1 \to m} + A_{3\mathrm{w}}^{n-1 \to n} + A_{4\mathrm{w}}^{n+1 \to n}, \tag{A.6}$$

$$a_{\mathrm{s}} = 1 + A_{1\mathrm{s}}^{m-1 \to m} + A_{2\mathrm{s}}^{m+1 \to m} + A_{3\mathrm{s}}^{n-1 \to n} + A_{4\mathrm{s}}^{n+1 \to n}, \tag{A.7}$$

$$\widehat{a}_{4\mathrm{w,s}} = 1 + A_{1\mathrm{s}}^{m-1 \to m} + A_{2\mathrm{s}}^{m+1 \to m} + A_{3\mathrm{s}}^{n-1 \to n} + \widehat{A}_{4\mathrm{w,s}}^{n+1 \to n}, \tag{A.8}$$

$$\widehat{a}_{3\mathrm{w,s}} = 1 + A_{1\mathrm{s}}^{m-1 \to m} + A_{2\mathrm{s}}^{m+1 \to m} + \widehat{A}_{3\mathrm{w,s}}^{n-1 \to n} + A_{4\mathrm{w,s}}^{n+1 \to n}. \tag{A.9}$$

Referring to Figure 5.4, the energy balance equations for nodes within the workpiece are expressed as follows:

$$\left(a_{\mathrm{w}} - A_{1\mathrm{w}}^{m-1 \to m} - A_{3\mathrm{w}}^{n-1 \to n}\right)T_{0,0}^{P+1} - A_{2\mathrm{w}}^{m+1 \to m}T_{1,0}^{P+1} - A_{4\mathrm{w}}^{n+1 \to n}T_{0,1}^{P+1} = T_{0,0}^{P} + A_{5\mathrm{w}}\dot{g}_{0,0}, \tag{A.10}$$

$$-A_{1\mathrm{w}}^{m-1 \to m}T_{m-1,0}^{P+1} + \left(a_{\mathrm{w}} - A_{3\mathrm{w}}^{n-1 \to n}\right)T_{m,0}^{P+1} - A_{2\mathrm{w}}^{m+1 \to m}T_{m+1,0}^{P+1} - A_{4\mathrm{w}}^{n+1 \to n}T_{m,1}^{P+1} = T_{m,0}^{P} + A_{5\mathrm{w}}\dot{g}_{m,0},$$
$$\forall \; m = 1,\, 2, \ldots, N_r - 2 \; ; \; n = 0, \tag{A.11}$$

$$-A_{1\mathrm{w}}^{m-1 \to m}T_{N_r-2,0}^{P+1} + \left(a_{\mathrm{w}} + A_{2\mathrm{w}}^{m+1 \to m} - A_{3\mathrm{w}}^{n-1 \to n}\right)T_{N_r-1,0}^{P+1} - A_{4\mathrm{w}}^{n+1 \to n}T_{N_r-1,1}^{P+1} = T_{N_r-1,0}^{P}$$
$$+ A_{5\mathrm{w}}\dot{g}_{N_r-1,0} + 2A_{2\mathrm{w}}^{m+1 \to m}T_0 \tag{A.12}$$

$$-A_{3\mathrm{w}}^{n-1 \to n}T_{0,n-1}^{P+1} + \left(a_{\mathrm{w}} - A_{1\mathrm{w}}^{m-1 \to m}\right)T_{0,n}^{P+1} - A_{2\mathrm{w}}^{m+1 \to m}T_{1,n}^{P+1} - A_{4\mathrm{w}}^{n+1 \to n}T_{0,n+1}^{P+1} = T_{0,n}^{P} + A_{5\mathrm{w}}\dot{g}_{0,n},$$
$$\forall \; m = 0 \; ; \; n = 1,\, 2, \ldots, N_{\mathrm{w}} - 2, \tag{A.13}$$

$$-A_{3\mathrm{w}}^{n-1 \to n}T_{m,n-1}^{P+1} - A_{1\mathrm{w}}^{m-1 \to m}T_{m-1,n}^{P+1} + a_{\mathrm{w}}T_{m,n}^{P+1} - A_{2\mathrm{w}}^{m+1 \to m}T_{m+1,n}^{P+1} - A_{4\mathrm{w}}^{n+1 \to n}T_{m,n+1}^{P+1} = T_{m,n}^{P} + A_{5\mathrm{w}}\dot{g}_{m,n},$$
$$\forall \; m = 1,\, 2, \ldots, N_r - 2 \; ; \; n = 1,\, 2, \ldots, N_{\mathrm{w}} - 2, \tag{A.14}$$

$$-A_{3w}^{n-1\to n}T_{N_r-1,n-1}^{P+1} - A_{1w}^{m-1\to m}T_{N_r-2,n}^{P+1} + \left(a_w + A_{2w}^{m+1\to m}\right)T_{N_r-1,n}^{P+1} - A_{4w}^{n+1\to n}T_{N_r-1,n+1}^{P+1} = T_{N_r-1,n}^{P} + A_{5w}\dot{g}_{N_r-1,n}$$
$$+2A_{2w}^{m+1\to m}T_0, \forall \quad m = N_r-1 \; ; \; n = 1, 2, ..., N_w-2, \quad (A.15)$$

$$-A_{3w}^{n-1\to n}T_{0,N_w-2}^{P+1} + \left(\hat{a}_{4w,s} - A_{1w}^{m-1\to m}\right)T_{0,N_w-1}^{P+1} - A_{2w}^{m+1\to m}T_{1,N_w-1}^{P+1} - \hat{A}_{4w,s}^{n+1\to n}T_{0,N_w}^{P+1} = T_{0,N_w-1}^{P} + A_{5w}\dot{g}_{0,N_w-1},$$
$$\forall \quad m = 0 \; ; \; n = N_w-1, \quad (A.16)$$

$$-A_{3w}^{n-1\to n}T_{m,N_w-2}^{P+1} - A_{1w}^{m-1\to m}T_{m-1,N_w-1}^{P+1} + \hat{a}_{4w,s}T_{m,N_w-1}^{P+1} - A_{2w}^{m+1\to m}T_{m+1,N_w-1}^{P+1} - \hat{A}_{4w,s}^{n+1\to n}T_{m,N_w}^{P+1} = T_{m,N_w-1}^{P} + A_{5w}\dot{g}_{m,N_w-1}$$
,
$$\forall \quad m = 1, 2, ..., N_r-2 \; ; \; n = N_w-1, \quad (A.17)$$

$$-A_{3w}^{n-1\to n}T_{N_r-1,N_w-2}^{P+1} - A_{1w}^{m-1\to m}T_{N_r-2,N_w-1}^{P+1} + \left(\hat{a}_{4w,s} + A_{2w}^{m+1\to m}\right)T_{N_r-1,N_w-1}^{P+1} - \hat{A}_{4w,s}^{n+1\to n}T_{N_r-1,N_w}^{P+1} = T_{N_r-1,N_w-1}^{P}$$
$$+A_{5w}\dot{g}_{N_r-1,N_w-1} + 2A_{2w}^{m+1\to m}T_0, \forall \quad m = N_r-1 \; ; \; n = N_w-1, (A.18)$$

Similarly, the system of equations for the substrate is given as follows:

$$-\hat{A}_{3w,s}^{n-1\to n}T_{0,N_w-1}^{P+1} + \left(\hat{a}_{3w,s} - A_{1s}^{m-1\to m}\right)T_{0,N_w}^{P+1} - A_{2s}^{m+1\to m}T_{1,N_w}^{P+1} - A_{4s}^{n+1\to n}T_{0,N_w+1}^{P+1} = T_{0,N_w}^{P} + A_{5s}\dot{g}_{0,N_w},$$
$$\forall \quad m = 0 \; ; \; n = N_w, \quad (A.19)$$

$$-\hat{A}_{3w,s}^{n-1\to n}T_{m,N_w-1}^{P+1} - A_{1s}^{m-1\to m}T_{m-1,N_w}^{P+1} + \hat{a}_{3w,s}T_{m,N_w}^{P+1} - A_{2s}^{m+1\to m}T_{m+1,N_w}^{P+1} - A_{4s}^{n+1\to n}T_{m,N_w+1}^{P+1} = T_{m,N_w}^{P} + A_{5s}\dot{g}_{m,N_w},$$
$$\forall \quad m = 1, 2, ..., N_r-2 \; ; \; n = N_w, \quad (A.20)$$

$$-\hat{A}_{3w,s}^{n-1\to n}T_{N_r-1,N_w-1}^{P+1} - A_{1s}^{m-1\to m}T_{N_r-2,N_w}^{P+1} + \left(\hat{a}_{3w,s} + A_{2s}^{m+1\to m}\right)T_{N_r-1,N_w}^{P+1} - A_{4s}^{n+1\to n}T_{N_r-1,N_w+1}^{P+1} = T_{N_r-1,N_w}^{P}$$
$$+A_{5s}\dot{g}_{N_r-1,N_w} + 2A_{2s}^{m+1\to m}T_0, \forall \quad m = N_r-1 \; ; \; n = N_w, \quad (A.21)$$

$$-A_{3s}^{n-1\to n}T_{0,n-1}^{P+1} + \left(a_s - A_{1s}^{m-1\to m}\right)T_{0,n}^{P+1} - A_{2s}^{m+1\to m}T_{1,n}^{P+1} - A_{4s}^{n+1\to n}T_{0,n+1}^{P+1} = T_{0,n}^{P} + A_{5s}\dot{g}_{0,n},$$
$$\forall \quad m = 0 \; ; \; n = N_w+1, ..., N_z-2, \quad (A.22)$$

$$-A_{3s}^{n-1\to n}T_{m,n-1}^{P+1} - A_{1s}^{m-1\to m}T_{m-1,n}^{P+1} + a_s T_{m,n}^{P+1} - A_{2s}^{m-1\to m}T_{m+1,n}^{P+1} - A_{4s}^{n+1\to n}T_{m,n+1}^{P+1} = T_{m,n}^{P} + A_{5s}\dot{g}_{m,n},$$
$$\forall \quad m = 1, 2, ..., N_r-2 \; ; \; n = N_w+1, ..., N_z-2, \quad (A.23)$$

$$-A_{3s}^{n-1\to n}T_{N_r-1,n-1}^{P+1} - A_{1s}^{m-1\to m}T_{N_r-2,n}^{P+1} + \left(a_s + A_{2s}^{m+1\to m}\right)T_{N_r-1,n}^{P+1} - A_{4s}^{n+1\to n}T_{N_r-1,n+1}^{P+1} = T_{N_r-1,n}^{P} + A_{5s}\dot{g}_{N_r-1,n} + 2A_{2s}^{m+1\to m}T_0$$
,
$$\forall \quad m = N_r-1 \; ; \; n = N_w+1, ..., N_z-2, \quad (A.24)$$

$$-A_{3s}^{n-1\to n}T_{0,N_z-2}^{P+1} + \left(a_s - A_{1s}^{m-1\to m} - A_{4s}^{n+1\to n}\right)T_{0,N_z-1}^{P+1} - A_{2s}^{m+1\to m}T_{1,N_z-1}^{P+1} = T_{0,N_z-1}^{P} + A_{5s}\dot{g}_{0,N_z-1},$$
$$\forall \quad m = 0 \; ; \; n = N_z-1, \quad (A.25)$$

$$-A_{3s}^{n-1\to n}T_{m,N_z-2}^{P+1} - A_{1s}^{m-1\to m}T_{m-1,N_z-1}^{P+1} + \left(a_s - A_{4s}^{n+1\to n}\right)T_{m,N_z-1}^{P+1} - A_{2s}^{m+1\to m}T_{m+1,N_z-1}^{P+1} = T_{m,N_z-1}^{P} + A_{5s}\dot{g}_{m,N_z-1},$$
$$\forall \quad m = 1, 2, ..., N_r-2 \; ; \; n = N_z-1, \quad (A.26)$$

$$-A_{3s}^{n-1\to n}T_{N_r-1,N_z-2}^{P+1} - A_{1s}^{m-1\to m}T_{N_r-2,N_z-1}^{P+1} + \left(a_s + A_{2s}^{m+1\to m} - A_{4s}^{n+1\to n}\right)T_{N_r-1,N_z-1}^{P+1} = T_{N_r-1,N_z-1}^{P} + A_{5s}\dot{g}_{N_r-1,N_z-1}$$
$$+2A_{2s}^{m+1\to m}T_0, \forall \quad m = N_r-1 \; ; \; n = N_z-1, \quad (A.27)$$

Next, gather all the differenced equations and express them in terms of the matrix form,

$A\vec{T} = \vec{B}$, where A is a $(N_r{\times}N_z){\times}(N_r{\times}N_z)$ matrix. Note that A is a sparse, five-band matrix and it is given as:

$$A = \begin{bmatrix} & & & & & \\ & & & & & \\ & & & & & \\ & & & & & \\ & & & & & \\ & & & & & \end{bmatrix} \tag{A.28}$$

The solid lines in the matrix mean that the elements are non-zeros while the circles refer to zeros. For the sake of simplicity, each non-zero band is labeled from number 1 to 5. The matrix A shall be expressed in the following compact format:

$$
\begin{array}{r}
1 \to \\
2 \to \\
\vdots \\
\cdot \\
N_r \to \\
\cdot \\
\cdot \\
\vdots \\
\cdot \\
\vdots \\
\cdot \\
\vdots \\
\cdot \\
\cdot \\
\cdot \\
\vdots \\
N_r N_w \to \\
N_r N_w + 1 \to \\
N_r N_w + 2 \to \\
\vdots \\
\cdot \\
\cdot \\
\cdot \\
\vdots \\
\cdot \\
\vdots \\
\cdot \\
\vdots \\
\cdot \\
\cdot \\
\cdot \\
\vdots \\
\cdot \\
N_r N_z \to
\end{array}
\left[
\begin{array}{ccccc}
0 & 0 & a_w - A_{1w}^{m-1\to m} - A_{3w}^{n-1\to n} & -A_{2w}^{m+1\to m} & -A_{4w}^{n+1\to n} \\
0 & -A_{1w}^{m-1\to m} & a_w - A_{3w}^{n-1\to n} & -A_{2w}^{m+1\to m} & -A_{4w}^{n+1\to n} \\
\vdots & \vdots & \vdots & \vdots & \vdots \\
0 & -A_{1w}^{m-1\to m} & a_w - A_{3w}^{n-1\to n} & -A_{2w}^{m+1\to m} & -A_{4w}^{n+1\to n} \\
0 & -A_{1w}^{m-1\to m} & a_w + A_{2w}^{m+1\to m} - A_{3w}^{n-1\to n} & 0 & -A_{4w}^{n+1\to n} \\
-A_{3w}^{n-1\to n} & 0 & a_w - A_{1w}^{m-1\to m} & -A_{2w}^{m+1\to m} & -A_{4w}^{n+1\to n} \\
-A_{3w}^{n-1\to n} & -A_{1w}^{m-1\to m} & a_w & -A_{2w}^{m+1\to m} & -A_{4w}^{n+1\to n} \\
\vdots & \vdots & \vdots & \vdots & \vdots \\
-A_{3w}^{n-1\to n} & -A_{1w}^{m-1\to m} & a_w + A_{2w}^{m+1\to m} & 0 & -A_{4w}^{n+1\to n} \\
\vdots & \vdots & \vdots & \vdots & \vdots \\
-A_{3w}^{n-1\to n} & 0 & a_w - A_{1w}^{m-1\to m} & -A_{2w}^{m+1\to m} & -A_{4w}^{n+1\to n} \\
\vdots & \vdots & \vdots & \vdots & \vdots \\
-A_{3w}^{n-1\to n} & -A_{1w}^{m-1\to m} & a_w + A_{2w}^{m+1\to m} & 0 & -A_{4w}^{n+1\to n} \\
-A_{3w}^{n-1\to n} & 0 & \hat{a}_{4w,s} - A_{1w}^{m-1\to m} & -A_{2w}^{m+1\to m} & -\widehat{A}_{4w,s}^{n+1\to n} \\
-A_{3w}^{n-1\to n} & -A_{1w}^{m-1\to m} & \hat{a}_{4w,s} & -A_{2w}^{m+1\to m} & -\widehat{A}_{4w,s}^{n+1\to n} \\
\vdots & \vdots & \vdots & \vdots & \vdots \\
-A_{3w}^{n-1\to n} & -A_{1w}^{m-1\to m} & \hat{a}_{4w,s} + A_{2w}^{m+1\to m} & 0 & -\widehat{A}_{4w,s}^{n+1\to n} \\
-\widehat{A}_{3w,s}^{n-1\to n} & 0 & \hat{a}_{3w,s} - A_{1s}^{m-1\to m} & -A_{2s}^{m+1\to m} & -A_{4s}^{n+1\to n} \\
-\widehat{A}_{3w,s}^{n-1\to n} & -A_{1s}^{m-1\to m} & \hat{a}_{3w,s} & -A_{2s}^{m+1\to m} & -A_{4s}^{n+1\to n} \\
\vdots & \vdots & \vdots & \vdots & \vdots \\
-\widehat{A}_{3w,s}^{n-1\to n} & -A_{1s}^{m-1\to m} & \hat{a}_{3w,s} + A_{2s}^{m+1\to m} & 0 & -A_{4s}^{n+1\to n} \\
-A_{3s}^{n-1\to n} & 0 & a_s - A_{1s}^{m-1\to m} & -A_{2s}^{m+1\to m} & -A_{4s}^{n+1\to n} \\
-A_{3s}^{n-1\to n} & -A_{1s}^{m-1\to m} & a_s & -A_{2s}^{m+1\to m} & -A_{4s}^{n+1\to n} \\
\vdots & \vdots & \vdots & \vdots & \vdots \\
-A_{3s}^{n-1\to n} & -A_{1s}^{m-1\to m} & a_s + A_{2s}^{m+1\to m} & 0 & -A_{4s}^{n+1\to n} \\
\vdots & \vdots & \vdots & \vdots & \vdots \\
-A_{3s}^{n-1\to n} & 0 & a_s - A_{1s}^{m-1\to m} & -A_{2s}^{m+1\to m} & -A_{4s}^{n+1\to n} \\
\vdots & \vdots & \vdots & \vdots & \vdots \\
-A_{3s}^{n-1\to n} & -A_{1s}^{m-1\to m} & a_s + A_{2s}^{m+1\to m} & 0 & -A_{4s}^{n+1\to n} \\
-A_{3s}^{n-1\to n} & 0 & a_s - A_{1s}^{m-1\to m} - A_{4s}^{n+1\to n} & -A_{2s}^{m+1\to m} & 0 \\
-A_{3s}^{n-1\to n} & -A_{1s}^{m-1\to m} & a_s - A_{4s}^{n+1\to n} & -A_{2s}^{m+1\to m} & 0 \\
\vdots & \vdots & \vdots & \vdots & \vdots \\
-A_{3s}^{n-1\to n} & -A_{1s}^{m-1\to m} & a_s - A_{4s}^{n+1\to n} & -A_{2s}^{m+1\to m} & 0 \\
-A_{3s}^{n-1\to n} & -A_{1s}^{m-1\to m} & a_s + A_{2s}^{m+1\to m} - A_{4s}^{n+1\to n} & 0 & 0
\end{array}
\right]
\begin{array}{l}
\leftarrow (0,0) \\
\leftarrow (1,0) \\
\vdots \\
\leftarrow (N_r-2,0) \\
\leftarrow (N_r-1,0) \\
\leftarrow (0,1) \\
\leftarrow (1,1) \\
\vdots \\
\leftarrow (N_r-1,1) \\
\vdots \\
\leftarrow (0,N_w-2) \\
\vdots \\
\leftarrow (N_r-1,N_w-2) \\
\leftarrow (0,N_w-1) \\
\leftarrow (1,N_w-1) \\
\vdots \\
\leftarrow (N_r-1,N_w-1) \\
\leftarrow (0,N_w) \\
\leftarrow (1,N_w) \\
\vdots \\
\leftarrow (N_r-1,N_w) \\
\leftarrow (0,N_w+1) \\
\leftarrow (1,N_w+1) \\
\vdots \\
\leftarrow (N_r-1,N_w+1) \\
\vdots \\
\leftarrow (0,N_z-2) \\
\vdots \\
\leftarrow (N_r-1,N_z-2) \\
\leftarrow (0,N_z-1) \\
\leftarrow (1,N_z-1) \\
\vdots \\
\leftarrow (N_r-2,N_z-1) \\
\leftarrow (N_r-1,N_z-1)
\end{array}
$$

Workpiece (rows from $(0,0)$ to (N_r-1, N_w-1))

Substrate (rows from $(0, N_w)$ to (N_r-1, N_z-1))

Count   Band 1   Band 2   Band 3   Band 4   Band 5   Nodal points

$$
\bar{T} \equiv
\begin{array}{r}
1 \rightarrow \\
2 \rightarrow \\
\vdots \\
\\
N_r \rightarrow \\
\\
\\
\\
\\
\\
\\
\\
\\
\\
\\
N_r N_w \rightarrow \\
N_r N_w + 1 \rightarrow \\
N_r N_w + 2 \rightarrow \\
\vdots \\
\\
\\
\\
\\
\\
\\
\\
\\
\\
\\
\\
\\
\\
N_r N_z \rightarrow \\
\\
\end{array}
\begin{bmatrix}
T_{0,0}^{P+1} \\
T_{1,0}^{P+1} \\
\vdots \\
T_{N_r-2,0}^{P+1} \\
T_{N_r-1,0}^{P+1} \\
T_{0,1}^{P+1} \\
T_{1,1}^{P+1} \\
\vdots \\
T_{N_r-1,1}^{P+1} \\
\vdots \\
T_{0,N_w-2}^{P+1} \\
\vdots \\
T_{N_r-1,N_w-2}^{P+1} \\
T_{0,N_w-1}^{P+1} \\
T_{1,N_w-1}^{P+1} \\
\vdots \\
T_{N_r-1,N_w-1}^{P+1} \\
T_{0,N_w}^{P+1} \\
T_{1,N_w}^{P+1} \\
\vdots \\
T_{N_r-1,N_w}^{P+1} \\
T_{0,N_w+1}^{P+1} \\
T_{1,N_w+1}^{P+1} \\
\vdots \\
T_{N_r-1,N_w+1}^{P+1} \\
\vdots \\
T_{0,N_z-2}^{P+1} \\
\vdots \\
T_{N_r-1,N_z-2}^{P+1} \\
T_{0,N_z-1}^{P+1} \\
T_{1,N_z-1}^{P+1} \\
\vdots \\
T_{N_r-2,N_z-1}^{P+1} \\
T_{N_r-1,N_z-1}^{P+1}
\end{bmatrix}
$$

$$
\vec{B} \equiv
\begin{array}{r}
1 \rightarrow \\
2 \rightarrow \\
\vdots \\
\\
N_r \rightarrow \\
\\
\\
\\
\\
\\
\\
N_r N_w \rightarrow \\
N_r N_w + 1 \rightarrow \\
N_r N_w + 2 \rightarrow \\
\vdots \\
\\
\\
\\
\\
\\
\\
\\
N_r N_z \rightarrow \\
\end{array}
\begin{bmatrix}
T_{0,0}^{P} + A_{5w}\dot{g}_{0,0}^{\mathrm{gen}} \\
T_{1,0}^{P} + A_{5w}\dot{g}_{1,0}^{\mathrm{gen}} \\
\vdots \\
T_{N_r-2,0}^{P} + A_{5w}\dot{g}_{N_r-2,0}^{\mathrm{gen}} \\
T_{N_r-1,0}^{P} + A_{5w}\dot{g}_{N_r-1,0}^{\mathrm{gen}} + 2A_{2w}^{m+1\rightarrow m}T_0 \\
T_{0,1}^{P} + A_{5w}\dot{g}_{0,1}^{\mathrm{gen}} \\
T_{1,1}^{P} + A_{5w}\dot{g}_{1,1}^{\mathrm{gen}} \\
\vdots \\
T_{N_r-1,1}^{P} + A_{5w}\dot{g}_{N_r-1,1}^{\mathrm{gen}} + 2A_{2w}^{m+1\rightarrow m}T_0 \\
\vdots \\
T_{0,N_w-2}^{P} + A_{5w}\dot{g}_{0,N_w-2}^{\mathrm{gen}} \\
\vdots \\
T_{N_r-1,N_w-2}^{P} + A_{5w}\dot{g}_{N_r-1,N_w-2}^{\mathrm{gen}} + 2A_{2w}^{m+1\rightarrow m}T_0 \\
T_{0,N_w-1}^{P} + A_{5w}\dot{g}_{0,N_w-1}^{\mathrm{gen}} \\
T_{1,N_w-1}^{P} + A_{5w}\dot{g}_{1,N_w-1}^{\mathrm{gen}} \\
\vdots \\
T_{N_r-1,N_w-1}^{P} + A_{5w}\dot{g}_{N_r-1,N_w-1}^{\mathrm{gen}} + 2A_{2w}^{m+1\rightarrow m}T_0 \\
T_{0,N_w}^{P} + A_{5s}\dot{g}_{0,N_w}^{\mathrm{gen}} \\
T_{1,N_w}^{P} + A_{5s}\dot{g}_{1,N_w}^{\mathrm{gen}} \\
\vdots \\
T_{N_r-1,N_w}^{P} + A_{5s}\dot{g}_{N_r-1,N_w}^{\mathrm{gen}} + 2A_{2s}^{m+1\rightarrow m}T_0 \\
T_{0,N_w+1}^{P} + A_{5s}\dot{g}_{0,N_w+1}^{\mathrm{gen}} \\
T_{1,N_w+1}^{P} + A_{5s}\dot{g}_{1,N_w+1}^{\mathrm{gen}} \\
\vdots \\
T_{N_r-1,N_w+1}^{P} + A_{5s}\dot{g}_{N_r-1,N_w+1}^{\mathrm{gen}} + 2A_{2s}^{m+1\rightarrow m}T_0 \\
\vdots \\
T_{0,N_z-2}^{P} + A_{5s}\dot{g}_{0,N_z-2}^{\mathrm{gen}} \\
\vdots \\
T_{N_r-1,N_z-2}^{P} + A_{5s}\dot{g}_{N_r-1,N_z-2}^{\mathrm{gen}} + 2A_{2s}^{m+1\rightarrow m}T_0 \\
T_{0,N_z-1}^{P} + A_{5s}\dot{g}_{0,N_z-1}^{\mathrm{gen}} \\
T_{1,N_z-1}^{P} + A_{5s}\dot{g}_{1,N_z-1}^{\mathrm{gen}} \\
\vdots \\
T_{N_r-2,N_z-1}^{P} + A_{5s}\dot{g}_{N_r-2,N_z-1}^{\mathrm{gen}} \\
T_{N_r-1,N_z-1}^{P} + A_{5s}\dot{g}_{N_r-1,N_z-1}^{\mathrm{gen}} + 2A_{2s}^{m+1\rightarrow m}T_0
\end{bmatrix}
\begin{array}{l}
\leftarrow (0\,,\,0) \\
\leftarrow (1\,,\,0) \\
\vdots \\
\leftarrow (N_r-2\,,\,0) \\
\leftarrow (N_r-1\,,\,0) \\
\leftarrow (0\,,\,1) \\
\leftarrow (1\,,\,1) \\
\vdots \\
\leftarrow (N_r-1\,,\,1) \\
\vdots \\
\leftarrow (0\,,\,N_w-2) \\
\vdots \\
\leftarrow (N_r-1\,,\,N_w-2) \\
\leftarrow (0\,,\,N_w-1) \\
\leftarrow (1\,,\,N_w-1) \\
\vdots \\
\leftarrow (N_r-1\,,\,N_w-1) \\
\leftarrow (0\,,\,N_w) \\
\leftarrow (1\,,\,N_w) \\
\vdots \\
\leftarrow (N_r-1\,,\,N_w) \\
\leftarrow (0\,,\,N_w+1) \\
\leftarrow (1\,,\,N_w+1) \\
\vdots \\
\leftarrow (N_r-1\,,\,N_w+1) \\
\vdots \\
\leftarrow (0\,,\,N_z-2) \\
\vdots \\
\leftarrow (N_r-1\,,\,N_z-2) \\
\leftarrow (0\,,\,N_z-1) \\
\leftarrow (1\,,\,N_z-1) \\
\vdots \\
\leftarrow (N_r-2\,,\,N_z-1) \\
\leftarrow (N_r-1\,,\,N_z-1)
\end{array}
\left.\begin{array}{c} \\ \\ \\ \\ \\ \\ \\ \\ \\ \\ \\ \end{array}\right\} \text{Workpiece}
\left.\begin{array}{c} \\ \\ \\ \\ \\ \\ \\ \\ \\ \\ \\ \end{array}\right\} \text{Substrate}
$$

APPENDIX B
SIMPLIFIED ELECTRON-PHONON HYDRODYNAMIC EQUATIONS

In this appendix, the electron-phonon hydrodynamic equations given in Section 2.7.3 are further simplified. The equations will be cast in terms of five independent variables. They are electron density n_e, electron velocity vector $\vec{v}_e$, electron temperature T_e, optical phonon temperature T_{LO}, and acoustic phonon temperature T_A. Recall that the electron-phonon hydrodynamic equations in terms of electron density n_e, electron momentum $\vec{P}_{d,e}$, electron energy W_e, optical phonon temperature T_{LO}, and acoustic phonon temperature T_A are expressed as:

$$(\textit{e-Continuity}) \qquad \frac{\partial n_e}{\partial t} + \nabla_{\vec{r}} \cdot \left(\vec{v}_{d,e} n_e \right) = \left(\frac{\partial n_e}{\partial t} \right)_c, \qquad (\text{B.1})$$

$$(\textit{e-Momentum}) \qquad \frac{\partial \vec{P}_{d,e}}{\partial t} + \nabla_{\vec{r}} \cdot \left(\vec{v}_{d,e} \vec{P}_{d,e} \right) = -e n_e \vec{E} - \nabla_{\vec{r}} \left(n_e k_B T_e \right) + \left(\frac{\partial \vec{P}_{d,e}}{\partial t} \right)_c, \qquad (\text{B.2})$$

$$\frac{\partial W_e}{\partial t} + \nabla_{\vec{r}} \cdot \left(\vec{v}_{d,e} W_e \right) = -e n_e \vec{v}_{d,e} \cdot \vec{E} - \nabla_{\vec{r}} \cdot \left(\vec{v}_{d,e} n_e k_B T_e \right)$$

$$(\textit{e-Energy}) \qquad \qquad\qquad\qquad + \nabla_{\vec{r}} \cdot \left(k_e \nabla_{\vec{r}} T_e \right) + \left(\frac{\partial W_e}{\partial t} \right)_c + \dot{W}_{e,gen} \qquad (\text{B.3})$$

$$(\textit{Optical Phonon Energy}) \qquad C_{LO} \frac{\partial T_{LO}}{\partial t} = \left(\frac{\partial W_{LO}}{\partial t} \right)_{col}, \qquad (\text{B.4})$$

$$(\textit{Acoustic Phonon Energy}) \qquad C_A \frac{\partial T_A}{\partial t} = \nabla_{\vec{r}} \cdot \left(k_A \nabla_{\vec{r}} T_A \right) + \left(\frac{\partial W_A}{\partial t} \right)_{col}, \qquad (\text{B.5})$$

while the various collision terms are given as:

$$\left(\frac{\partial n_e}{\partial t} \right)_c = \dot{n}_{e,gen}, \qquad (\text{B.6})$$

$$\left(\frac{\partial \vec{P}_{d,e}}{\partial t} \right)_c = -\frac{m_e n_e \vec{v}_{d,e}}{\tau_m}, \qquad (\text{B.7})$$

$$\left(\frac{\partial W_e}{\partial t} \right)_c = -\frac{n_e \left(3 k_B T_e / 2 + m_e v_{d,e}^2 / 2 - 3 k_B T_{LO} / 2 \right)}{\tau_{e-LO}}$$

$$\qquad\qquad - \frac{n_e \left(3 k_B T_e / 2 + m_e v_{d,e}^2 / 2 - 3 k_B T_A / 2 \right)}{\tau_{e-A}}, \qquad (\text{B.8})$$

$$\left(\frac{\partial W_{LO}}{\partial t}\right)_{col} = \frac{n_e\left(3k_B T_e / 2 + m_e v_{d,e}^2 / 2 - 3k_B T_{LO} / 2\right)}{\tau_{e-LO}} - \frac{C_{LO}\left(T_{LO} - T_A\right)}{\tau_{LO-A}}, \tag{B.9}$$

$$\left(\frac{\partial W_A}{\partial t}\right)_{col} = \frac{n_e\left(3k_B T_e / 2 + m_e v_{d,e}^2 / 2 - 3k_B T_A / 2\right)}{\tau_{e-A}} + \frac{C_{LO}\left(T_{LO} - T_A\right)}{\tau_{LO-A}}. \tag{B.10}$$

Assume spherical parabolic electronic band structure. The electron momentum, $\bar{P}_{d,e}$, and the average electron energy, W_e, are then given as:

$$\bar{P}_{d,e} = m_e n_e \bar{v}_{d,e}, \tag{B.11}$$

$$W_e = \frac{3}{2} n_e k_B T_e + \frac{1}{2} n_e m_e v_{d,e}^2. \tag{B.12}$$

Next, each conservation equation shall be examined independently.

Electron Continuity

By substituting the collision term for the continuity equation for electrons, it reads:

$$\frac{\partial n_e}{\partial t} + \nabla_{\bar{r}} \cdot \left(\bar{v}_{d,e} n_e\right) = \dot{n}_{e,gen}. \tag{B.13}$$

Electron Momentum Conservation

Expanding the inertia term in the electron momentum equation yields:

$$\frac{\partial \bar{P}_{d,e}}{\partial t} + \bar{v}_{d,e} \cdot \nabla_{\bar{r}} \bar{P}_{d,e} + \bar{P}_{d,e} \nabla_{\bar{r}} \cdot \bar{v}_{d,e} = -e n_e \bar{E} - k_B \nabla_{\bar{r}}\left(n_e T_e\right) + \left(\frac{\partial \bar{P}_{d,e}}{\partial t}\right)_c, \tag{B.14}$$

The left-hand side (LHS) of the equation can be re-expressed as:

$$\frac{\partial\left(m_e n_e \bar{v}_{d,e}\right)}{\partial t} + \bar{v}_{d,e} \cdot \nabla_{\bar{r}}\left(m_e n_e \bar{v}_{d,e}\right) + \left(m_e n_e \bar{v}_{d,e}\right)\nabla_{\bar{r}} \cdot \bar{v}_{d,e}. \tag{B.15}$$

Expanding the various terms produces:

$$m_e \bar{v}_{d,e} \frac{\partial n_e}{\partial t} + m_e n_e \frac{\partial \bar{v}_{d,e}}{\partial t} + m_e\left[n_e\left(\bar{v}_{d,e} \cdot \nabla_{\bar{r}} \bar{v}_{d,e}\right) + \bar{v}_{d,e}\left(\bar{v}_{d,e} \cdot \nabla_{\bar{r}} n_e\right)\right] + \left(m_e n_e \bar{v}_{d,e}\right)\nabla_{\bar{r}} \cdot \bar{v}_{d,e}, \tag{B.16}$$

where it is assumed that the effective mass of the electron, m_e, is constant. Using the continuity equation the LHS of the momentum equation becomes:

$$m_e n_e \frac{\partial \vec{v}_{d,e}}{\partial t} + m_e n_e \left(\vec{v}_{d,e} \cdot \nabla_{\bar{r}} \vec{v}_{d,e} \right) + m_e \vec{v}_{d,e} \left(\frac{\partial n_e}{\partial t} \right)_c . \tag{B.17}$$

After equating this newly-derived LHS to the original RHS and dividing by $(m_e n_e)$, the electron momentum equation reads:

$$\frac{\partial \vec{v}_{d,e}}{\partial t} + \vec{v}_{d,e} \cdot \nabla_{\bar{r}} \vec{v}_{d,e} = -\frac{e}{m_e} \bar{E} - \frac{k_B}{m_e n_e} \nabla_{\bar{r}} \left(n_e T_e \right) + \frac{1}{m_e n_e} \left(\frac{\partial \bar{P}_{d,e}}{\partial t} \right)_c - \frac{\vec{v}_{d,e}}{n_e} \left(\frac{\partial n_e}{\partial t} \right)_c . \tag{B.18}$$

Now substituting the collision terms, the following equation is obtained:

$$\frac{\partial \vec{v}_{d,e}}{\partial t} + \vec{v}_{d,e} \cdot \nabla_{\bar{r}} \vec{v}_{d,e} = -\frac{e}{m_e} \bar{E} - \frac{k_B}{m_e n_e} \nabla_{\bar{r}} \left(n_e T_e \right) - \left(\frac{1}{\tau_m} + \frac{\dot{n}_{e,gen}}{n_e} \right) \vec{v}_{d,e} . \tag{B.19}$$

Electron Energy Conservation

Expanding the electron energy advection term and the work done by the electron pressure and shuffling the terms give the electron energy equation in the following form:

$$\frac{\partial W_e}{\partial t} + \vec{v}_{d,e} \cdot \nabla_{\bar{r}} W_e + \left(W_e + k_B n_e T_e \right) \nabla_{\bar{r}} \cdot \vec{v}_{d,e} = -e n_e \vec{v}_{d,e} \cdot \bar{E} - k_B \vec{v}_{d,e} \cdot \nabla_{\bar{r}} \left(n_e T_e \right)$$
$$+ \nabla_{\bar{r}} \cdot \left(k_e \nabla_{\bar{r}} T_e \right) + \left(\frac{\partial W_e}{\partial t} \right)_c + \dot{W}_{e,gen} . \tag{B.20}$$

The LHS of the equation is expanded accordingly as:

$$\frac{\partial}{\partial t} \left[\frac{3}{2} n_e k_B T_e + \frac{1}{2} n_e m_e \left(\vec{v}_{d,e} \cdot \vec{v}_{d,e} \right) \right] + \vec{v}_{d,e} \cdot \nabla_{\bar{r}} \left[\frac{3}{2} n_e k_B T_e + \frac{1}{2} n_e m_e \left(\vec{v}_{d,e} \cdot \vec{v}_{d,e} \right) \right]$$
$$+ \left[\frac{5}{2} n_e k_B T_e + \frac{1}{2} n_e m_e \left(\vec{v}_{d,e} \cdot \vec{v}_{d,e} \right) \right] \nabla_{\bar{r}} \cdot \vec{v}_{d,e} . \tag{B.21}$$

The LHS shall be simplified term by term by starting from the first left. Expanding the derivative in time, it reads:

$$\frac{3}{2} n_e k_B \frac{\partial T_e}{\partial t} + \left[\frac{3}{2} k_B T_e + \frac{1}{2} m_e \left(\vec{v}_{d,e} \cdot \vec{v}_{d,e} \right) \right] \frac{\partial n_e}{\partial t} + \frac{1}{2} m_e n_e \frac{\partial}{\partial t} \left(\vec{v}_{d,e} \cdot \vec{v}_{d,e} \right) . \tag{B.22}$$

Again, after substituting the continuity equation, the equation becomes:

$$\frac{3}{2}n_e k_B \frac{\partial T_e}{\partial t} + \left[\frac{3}{2}k_B T_e + \frac{1}{2}m_e\left(\vec{v}_{d,e}\cdot\vec{v}_{d,e}\right)\right]\left[-\vec{v}_{d,e}\cdot\nabla_{\bar{r}} n_e - n_e \nabla_{\bar{r}}\cdot\vec{v}_{d,e} + \left(\frac{\partial n_e}{\partial t}\right)_c\right]$$
$$+\frac{1}{2}m_e n_e \frac{\partial}{\partial t}\left(\vec{v}_{d,e}\cdot\vec{v}_{d,e}\right)$$
(B.23)

Next, consider the second term in the LHS of the energy conservation equation as:

$$\frac{3}{2}k_B n_e\left(\vec{v}_{d,e}\cdot\nabla_{\bar{r}} T_e\right) + \left[\frac{3}{2}k_B T_e + \frac{1}{2}m_e\left(\vec{v}_{d,e}\cdot\vec{v}_{d,e}\right)\right]\left(\vec{v}_{d,e}\cdot\nabla_{\bar{r}} n_e\right) + \frac{1}{2}m_e n_e\left[\vec{v}_{d,e}\cdot\nabla_{\bar{r}}\left(\vec{v}_{d,e}\cdot\vec{v}_{d,e}\right)\right].$$ (B.24)

while the third term in the LHS remains as is. Combining all these expanded terms the entire LHS of the equation under consideration is given as:

$$\frac{3}{2}n_e k_B \frac{\partial T_e}{\partial t} + \frac{3}{2}k_B n_e\left(\vec{v}_{d,e}\cdot\nabla_{\bar{r}} T_e\right) + n_e k_B T_e \nabla_{\bar{r}}\cdot\vec{v}_{d,e} + \left[\frac{3}{2}k_B T_e + \frac{1}{2}m_e\left(\vec{v}_{d,e}\cdot\vec{v}_{d,e}\right)\right]\left(\frac{\partial n_e}{\partial t}\right)_c$$
$$+\frac{1}{2}m_e n_e\left[\frac{\partial}{\partial t}\left(\vec{v}_{d,e}\cdot\vec{v}_{d,e}\right) + \vec{v}_{d,e}\cdot\nabla_{\bar{r}}\left(\vec{v}_{d,e}\cdot\vec{v}_{d,e}\right)\right]$$
(B.25)

Using the electron-momentum equation the LHS of the electron-energy conservation equation is simplified into the following form:

$$\frac{3}{2}n_e k_B \frac{\partial T_e}{\partial t} + \frac{3}{2}k_B n_e\left(\vec{v}_{d,e}\cdot\nabla_{\bar{r}} T_e\right) + n_e k_B T_e \nabla_{\bar{r}}\cdot\vec{v}_{d,e} + \left[\frac{3}{2}k_B T_e + \frac{1}{2}m_e\left(\vec{v}_{d,e}\cdot\vec{v}_{d,e}\right)\right]\left(\frac{\partial n_e}{\partial t}\right)_c$$
$$-en_e\vec{v}_{d,e}\cdot\vec{E} - k_B\vec{v}_{d,e}\cdot\nabla_{\bar{r}}\left(n_e T_e\right) + \vec{v}_{d,e}\cdot\left(\frac{\partial\vec{P}_{d,e}}{\partial t}\right)_c - m_e\left(\vec{v}_{d,e}\cdot\vec{v}_{d,e}\right)\left(\frac{\partial n_e}{\partial t}\right)_c$$
(B.26)

Equating the newly-derived LHS to the RHS of the equation and dividing the equation by $(3/2n_e k_B)$, the entire electron-energy conservation has the following form:

$$\frac{\partial T_e}{\partial t} + \left(\vec{v}_{d,e}\cdot\nabla_{\bar{r}} T_e\right) = -\frac{2}{3}T_e\nabla_{\bar{r}}\cdot\vec{v}_{d,e} + \frac{2}{3n_e k_B}\nabla_{\bar{r}}\cdot\left(k_e\nabla_{\bar{r}} T_e\right) + \frac{2}{3n_e k_B}\left(\frac{\partial W_e}{\partial t}\right)_c$$
$$-\frac{2}{3n_e k_B}\vec{v}_{d,e}\cdot\left(\frac{\partial\vec{P}_{d,e}}{\partial t}\right)_c - \left[\frac{T_e}{n_e} - \frac{1}{3n_e k_B}m_e\left(\vec{v}_{d,e}\cdot\vec{v}_{d,e}\right)\right]\left(\frac{\partial n_e}{\partial t}\right)_c.$$ (B.27)
$$+\frac{2}{3n_e k_B}\dot{W}_{e,gen}$$

Substituting the collision terms into the equation yields:

$$\frac{\partial T_e}{\partial t}+\left(\vec{v}_{d,e}\cdot\nabla_{\vec{r}}T_e\right)=-\frac{2}{3}T_e\nabla_{\vec{r}}\cdot\vec{v}_{d,e}+\frac{2}{3n_ek_B}\nabla_{\vec{r}}\cdot\left(k_e\nabla_{\vec{r}}T_e\right)-\frac{T_e-T_{LO}}{\tau_{e-LO}}-\frac{T_e-T_A}{\tau_{e-A}}$$
$$+\left(\frac{2}{\tau_m}-\frac{1}{\tau_{e-LO}}-\frac{1}{\tau_{e-A}}+\frac{\dot{n}_{e,gen}}{n_e}\right)\frac{m_ev_{d,e}^2}{3k_B}-\left(\frac{\dot{n}_{e,gen}}{n_e}\right)T_e+\left(\frac{2}{3n_ek_B}\right)\dot{W}_{e,gen} \qquad \text{(B.28)}$$

Phonon Energy Conservations

There are no additional simplifications that can be applied for the two phonon energy equations, except substituting the collision terms into them. By doing so, one obtains:

$$C_{LO}\frac{\partial T_{LO}}{\partial t}=\frac{n_e\left(3k_BT_e/2+m_ev_{d,e}^2/2-3k_BT_{LO}/2\right)}{\tau_{e-LO}}-\frac{C_{LO}\left(T_{LO}-T_A\right)}{\tau_{LO-A}}, \qquad \text{(B.29)}$$

$$C_A\frac{\partial T_A}{\partial t}=\nabla_{\vec{r}}\cdot\left(k_A\nabla_{\vec{r}}T_A\right)+\frac{n_e\left(3k_BT_e/2+m_ev_{d,e}^2/2-3k_BT_A/2\right)}{\tau_{e-A}}+\frac{C_{LO}\left(T_{LO}-T_A\right)}{\tau_{LO-A}}, \qquad \text{(B.30)}$$

After dividing the equations by the corresponding specific heats and rearranging them, the following equations are obtained:

$$\frac{\partial T_{LO}}{\partial t}=\frac{n_em_ev_{d,e}^2}{2C_{LO}\tau_{e-LO}}-\frac{3n_ek_B\left(T_{LO}-T_e\right)}{2C_{LO}\tau_{e-LO}}-\frac{T_{LO}-T_A}{\tau_{LO-A}}, \qquad \text{(B.31)}$$

$$\frac{\partial T_A}{\partial t}=\frac{1}{C_A}\nabla_{\vec{r}}\cdot\left(k_A\nabla_{\vec{r}}T_A\right)+\frac{n_em_ev_{d,e}^2}{2C_A\tau_{e-A}}-\frac{3n_ek_B\left(T_A-T_e\right)}{2C_A\tau_{e-A}}-\frac{C_{LO}\left(T_A-T_{LO}\right)}{C_A\tau_{LO-A}}, \qquad \text{(B.32)}$$

Electron-Phonon Hydrodynamic Equations

Now all the conservation equations are collected and the conclusion of the electron-phonon hydrodynamic equations consist of:

(*e-Continuity*)
$$\frac{\partial n_e}{\partial t}+\nabla_{\vec{r}}\cdot\left(\vec{v}_{d,e}n_e\right)=\dot{n}_{e,gen}, \qquad \text{(B.33)}$$

(*e-Momentum*)
$$\frac{\partial\vec{v}_{d,e}}{\partial t}+\vec{v}_{d,e}\cdot\nabla_{\vec{r}}\vec{v}_{d,e}=-\frac{e}{m_e}\vec{E}-\frac{k_B}{m_en_e}\nabla_{\vec{r}}\left(n_eT_e\right)-\left(\frac{1}{\tau_m}+\frac{\dot{n}_{e,gen}}{n_e}\right)\vec{v}_{d,e}, \qquad \text{(B.34)}$$

$$\frac{\partial T_e}{\partial t} + \left(\vec{v}_{d,e} \cdot \nabla_{\vec{r}} T_e \right) = -\frac{2}{3} T_e \nabla_{\vec{r}} \cdot \vec{v}_{d,e} + \frac{2}{3 n_e k_B} \nabla_{\vec{r}} \cdot \left(k_e \nabla_{\vec{r}} T_e \right) - \frac{T_e - T_{LO}}{\tau_{e-LO}}$$

(*e-Energy*)
$$-\frac{T_e - T_A}{\tau_{e-A}} + \left(\frac{2}{\tau_m} - \frac{1}{\tau_{e-LO}} - \frac{1}{\tau_{e-A}} + \frac{\dot{n}_{e,gen}}{n_e} \right) \frac{m_e v_{d,e}^2}{3 k_B} \quad , \tag{B.35}$$

$$-\left(\frac{\dot{n}_{e,gen}}{n_e} \right) T_e + \left(\frac{2}{3 n_e k_B} \right) \dot{W}_{e,gen}$$

(*Optical Phonon Energy*)
$$\frac{\partial T_{LO}}{\partial t} = \frac{n_e m_e v_{d,e}^2}{2 C_{LO} \tau_{e-LO}} - \frac{3 n_e k_B \left(T_{LO} - T_e \right)}{2 C_{LO} \tau_{e-LO}} - \frac{T_{LO} - T_A}{\tau_{LO-A}} \quad , \tag{B.36}$$

$$\frac{\partial T_A}{\partial t} = \frac{1}{C_A} \nabla_{\vec{r}} \cdot \left(k_A \nabla_{\vec{r}} T_A \right) + \frac{n_e m_e v_{d,e}^2}{2 C_A \tau_{e-A}}$$

(*Acoustic Phonon Energy*)
$$-\frac{3 n_e k_B \left(T_A - T_e \right)}{2 C_A \tau_{e-A}} - \frac{C_{LO} \left(T_A - T_{LO} \right)}{C_A \tau_{LO-A}} \quad , \tag{B.37}$$

These five transport equations are to be solved simultaneously in order to predict the transport phenomena inside an electron-phonon system.

APPENDIX C
DERIVATION OF HDM FOR SEMICONDUCTORS

The derivation of the HDM for semiconductors is similar to that of metals except that the governing equation for phonons is split into two, since there are two types of phonons existed in semiconductors (i.e., optical phonons and acoustic phonons). Therefore:

(*e-Continuity*)
$$\frac{\partial n_e}{\partial t} + \nabla \cdot (\vec{v}_e n_e) = \left(\frac{\partial n_e}{\partial t}\right)_c,$$
(C.1)

(*e-Momentum*)
$$\frac{\partial \vec{p}_e}{\partial t} + \nabla \cdot (\vec{v}_e \vec{p}_e) = -e n_e \vec{E} - \nabla(n_e k_B T_e) + \left(\frac{\partial \vec{p}_e}{\partial t}\right)_c,$$
(C.2)

(*e-Energy*)
$$\frac{\partial W_e}{\partial t} + \nabla \cdot (\vec{v}_e W_e) = -e n_e \vec{v}_e \cdot \vec{E} - \nabla \cdot (\vec{v}_e n_e k_B T_e) - \nabla \cdot \vec{q}_e + \left(\frac{\partial W_e}{\partial t}\right)_c + \dot{W}_{e,gen},$$
(C.3)

(LO-*Phonons*)
$$\frac{\partial W_{LO}}{\partial t} = -\left(\frac{\partial W_e}{\partial t}\right)_c + \left(\frac{\partial W_{LO}}{\partial t}\right)_c.$$
(C.4)

(*Acoustic Phonons*)
$$\frac{\partial W_A}{\partial t} = -\nabla \cdot \vec{q}_A - \left(\frac{\partial W_{LO}}{\partial t}\right)_c.$$
(C.5)

The transformations of the electron continuity, momentum, and energy equations follow those given for metals, and they are expressed as:

(*e-Continuity*)
$$\frac{\partial n_e}{\partial t} + \vec{v}_e \cdot \nabla n_e = -n_e \nabla \cdot \vec{v}_e + \left(\frac{\partial n_e}{\partial t}\right)_c,$$
(C.6)

(*e-Momentum*)
$$\frac{\partial \vec{v}_e}{\partial t} + \vec{v}_e \cdot \nabla \vec{v}_e = -\frac{e}{m_e}\vec{E} - \frac{k_B}{m_e n_e}\nabla(n_e T_e) + \frac{1}{m_e n_e}\left(\frac{\partial \vec{p}_e}{\partial t}\right)_c - \frac{\vec{v}_e}{n_e}\left(\frac{\partial n_e}{\partial t}\right)_c,$$
(C.7)

(*e-Energy*)
$$\frac{\partial T_e}{\partial t} + (\vec{v}_e \cdot \nabla T_e) = -\frac{2}{3}T_e \nabla \cdot \vec{v}_e + \frac{2}{3 n_e k_B}\nabla \cdot (k_e \nabla T_e) + \frac{2}{3 n_e k_B}\left(\frac{\partial W_e}{\partial t}\right)_c$$
$$-\frac{2}{3 n_e k_B}\vec{v}_e \cdot \left(\frac{\partial \vec{p}_e}{\partial t}\right)_c - \left[\frac{T_e}{n_e} - \frac{1}{3 n_e k_B}m_e(\vec{v}_e \cdot \vec{v}_e)\right]\left(\frac{\partial n_e}{\partial t}\right)_c,$$
(C.8)
$$+\frac{2}{3 n_e k_B}\dot{W}_{e,gen}$$

Using the relaxation approximation, we shall express the various collision terms shall be expressed as:

$$\left(\frac{\partial n_e}{\partial t}\right)_c = \dot{n}_{e,gen},$$
(C.9)

225

$$\left(\frac{\partial \bar{p}_e}{\partial t}\right)_c = -\frac{m_e n_e \bar{v}_e}{\tau_m}, \tag{C.10}$$

$$\left(\frac{\partial W_e}{\partial t}\right)_c = -\frac{n_e\left(3k_B T_e/2 + m_e v_e^2/2 - 3k_B T_{LO}/2\right)}{\tau_{e-LO}}. \tag{C.11}$$

$$\left(\frac{\partial W_{LO}}{\partial t}\right)_c = -C_{LO}\frac{\left(T_{LO}-T_A\right)}{\tau_{LO-A}}. \tag{C.12}$$

Note that these collision terms are identical to those of metals, however electrons are expected to transfer energy first to optical phonons instead of the acoustic phonons. Substituting these collision terms into the all transport equations yields:

(*Poisson's Equation*)
$$\nabla^2 V = \frac{e}{\varepsilon_e}\left(n_e - n_+\right);\ \bar{E} = -\nabla V, \tag{C.13}$$

(*e-Continuity*)
$$\frac{\partial n_e}{\partial t} + \bar{v}_e\cdot\nabla n_e = -n_e\nabla\cdot\bar{v}_e + \dot{n}_{e,gen}, \tag{C.14}$$

(*e-Momentum*)
$$\frac{\partial \bar{v}_e}{\partial t} + \bar{v}_e\cdot\nabla\bar{v}_e = -\frac{e}{m_e}\bar{E} - \frac{k_B}{m_e n_e}\nabla\left(n_e T_e\right) - \left(\frac{1}{\tau_m} + \frac{\dot{n}_{e,gen}}{n_e}\right)\bar{v}_e, \tag{C.15}$$

(*e-Energy*)
$$\begin{aligned}\frac{\partial T_e}{\partial t} + \left(\bar{v}_e\cdot\nabla T_e\right) &= -\frac{2}{3}T_e\nabla\cdot\bar{v}_e + \frac{2}{3n_e k_B}\nabla\cdot\left(k_e\nabla T_e\right) - \frac{T_e - T_{ph}}{\tau_{e-ph}}\\ &\quad + \left(\frac{2}{\tau_{e-e}} - \frac{1}{\tau_{e-LO}}\right)\frac{m_e v_e^2}{3k_B} - \left[\frac{T_e}{n_e} - \frac{m_e v_e^2}{3n_e k_B}\right]\dot{n}_{e,gen} + \frac{2}{3n_e k_B}\dot{W}_{e,gen}\end{aligned} \tag{C.16}$$

(LO-*Phonons*)
$$C_{LO}\frac{\partial T_{LO}}{\partial t} = \frac{3}{2}n_e k_B\frac{\left(T_e - T_{LO}\right)}{\tau_{e-LO}} + \frac{n_e m_e v_e^2}{2\tau_{e-LO}} - C_{LO}\frac{\left(T_{LO}-T_A\right)}{\tau_{LO-A}}, \tag{C.17}$$

(*Acoustic Phonons*)
$$C_A\frac{\partial T_A}{\partial t} = \nabla\cdot\left(k_A\nabla T_A\right) + C_{LO}\frac{\left(T_{LO}-T_A\right)}{\tau_{LO-A}}, \tag{C.18}$$

including the Poisson equation for determining the electric field acting on the system.

APPENDIX D
NUMERICAL DISCRETIZATION OF HDM FOR SEMICONDUCTORS

In this appendix, the numerical discretizations of the hydrodynamic equations are shown. Accordingly, the hydrodynamic equations for semiconductors, particularly gallium arsenide, are expressed as:

(*Poisson's Equation*)
$$\nabla^2 V = -\frac{e}{\varepsilon_s}\left(N_D - n_e\right); \; \vec{E} = -\nabla V \, , \tag{D.1}$$

(*e-Continuity*)
$$\frac{\partial n_e}{\partial t} - \frac{e}{m_e^*}\nabla\cdot\left(\tau_m n_e \vec{E}\right) - \frac{k_B}{m_e^*}\nabla\cdot\left(\tau_m \nabla\left(n_e T_e\right)\right) = 0 \, , \tag{D.2}$$

(*e-Momentum*)
$$\vec{v}_e = -\frac{e\tau_m}{m_e^*}\vec{E} - \frac{k_B \tau_m}{m_e^* n_e}\nabla\left(n_e T_e\right) \, , \tag{D.3}$$

(*e-Energy*) $\dfrac{\partial T_e}{\partial t} + \nabla\cdot\left(\vec{v}_e T_e\right) = \dfrac{1}{3}T_e\nabla\cdot\vec{v}_e + \dfrac{2}{3n_e k_B}\nabla\cdot\left(k_e\nabla T_e\right) + \left(\dfrac{2}{\tau_m} - \dfrac{1}{\tau_{e-LO}}\right)\dfrac{m_e^*\left|\vec{v}_e\right|^2}{3k_B} - \dfrac{T_e - T_{LO}}{\tau_{e-LO}}$,(D.4)

(*LO-Phonons*)
$$C_{LO}\frac{\partial T_{LO}}{\partial t} = \frac{3}{2}n_e k_B \frac{\left(T_e - T_{LO}\right)}{\tau_{e-LO}} + \frac{n_e m_e^*\left|\vec{v}_e\right|^2}{2\tau_{e-LO}} - C_{LO}\frac{T_{LO} - T_A}{\tau_{LO-A}} \, . \tag{D.5}$$

(*Acoustic Phonons*)
$$C_A\frac{\partial T_A}{\partial t} = \nabla\cdot\left(k_A\nabla T_A\right) + C_{LO}\frac{T_{LO} - T_A}{\tau_{LO-A}} \, . \tag{D.6}$$

Poisson's Equation

In the following discretization, one assumes that the electrical permitivity is constant throughout the entire computational domain, therefore the Poisson equation becomes:

$$\frac{\partial^2 V}{\partial x^2} + \frac{\partial^2 V}{\partial y^2} + \frac{\partial^2 V}{\partial z^2} = -\frac{e}{\varepsilon_s}\left(N_D - n_e\right) \, , \tag{D.7}$$

and the differenced equation is given as:

$$\left[\frac{V_{i+1,j,k}^{P+1} - V_{i,j,k}^{P+1}}{\frac{\Delta x_i}{2}\left(\Delta x_{i+1} + \Delta x_i\right)} + \frac{V_{i-1,j,k}^{P+1} - V_{i,j,k}^{P+1}}{\frac{\Delta x_i}{2}\left(\Delta x_{i-1} + \Delta x_i\right)}\right] + \left[\frac{V_{i,j+1,k}^{P+1} - V_{i,j,k}^{P+1}}{\frac{\Delta y_j}{2}\left(\Delta y_{j+1} + \Delta y_j\right)} + \frac{V_{i,j-1,k}^{P+1} - V_{i,j,k}^{P+1}}{\frac{\Delta y_j}{2}\left(\Delta y_{j-1} + \Delta y_j\right)}\right]$$
$$+ \left[\frac{V_{i,j,k+1}^{P+1} - V_{i,j,k}^{P+1}}{\frac{\Delta z_k}{2}\left(\Delta z_{k+1} + \Delta z_k\right)} + \frac{V_{i,j,k-1}^{P+1} - V_{i,j,k}^{P+1}}{\frac{\Delta z_k}{2}\left(\Delta z_{k-1} + \Delta z_k\right)}\right] = -\frac{e}{\varepsilon_s}\left(N_D - \left(n_e\right)_{i,j,k}^{P+1}\right) \tag{D.8}$$

Continuity Equation
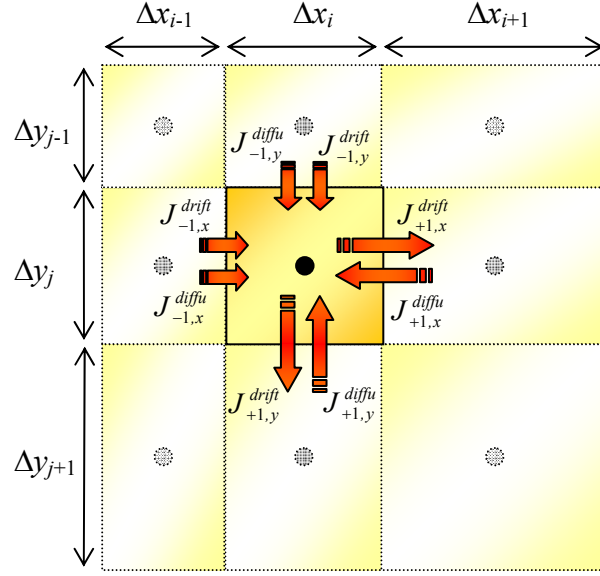
The diffusion components of the continuity equation are given as:

$$\Delta y_j \Delta z_k J_{-1,x}^{diffu} = \Delta y_j \Delta z_k \frac{k_B}{m_e^*} \frac{\left(n_e T_e\right)_{i-1,j,k}^{P+1} - \left(n_e T_e\right)_{i,j,k}^{P+1}}{\frac{1}{2}\left(\frac{\Delta x_{i-1}}{\left(\tau_m\right)_{i-1,j,k}^{P+1}} + \frac{\Delta x_i}{\left(\tau_m\right)_{i,j,k}^{P+1}}\right)}, \tag{D.9}$$

$$\Delta y_j \Delta z_k J_{+1,x}^{diffu} = \Delta y_j \Delta z_k \frac{k_B}{m_e^*} \frac{\left(n_e T_e\right)_{i+1,j,k}^{P+1} - \left(n_e T_e\right)_{i,j,k}^{P+1}}{\frac{1}{2}\left(\frac{\Delta x_{i+1}}{\left(\tau_m\right)_{i+1,j,k}^{P+1}} + \frac{\Delta x_i}{\left(\tau_m\right)_{i,j,k}^{P+1}}\right)}, \tag{D.10}$$

$$\Delta x_i \Delta z_k J_{-1,y}^{diffu} = \Delta x_i \Delta z_k \frac{k_B}{m_e^*} \frac{\left(n_e T_e\right)_{i,j-1,k}^{P+1} - \left(n_e T_e\right)_{i,j,k}^{P+1}}{\frac{1}{2}\left(\frac{\Delta y_{j-1}}{\left(\tau_m\right)_{i,j-1,k}^{P+1}} + \frac{\Delta y_j}{\left(\tau_m\right)_{i,j,k}^{P+1}}\right)}, \tag{D.11}$$

$$\Delta x_i \Delta z_k J_{+1,y}^{diffu} = \Delta x_i \Delta z_k \frac{k_B}{m_e^*} \frac{\left(n_e T_e\right)_{i,j+1,k}^{P+1} - \left(n_e T_e\right)_{i,j,k}^{P+1}}{\frac{1}{2}\left(\frac{\Delta y_{j+1}}{\left(\tau_m\right)_{i,j+1,k}^{P+1}} + \frac{\Delta y_j}{\left(\tau_m\right)_{i,j,k}^{P+1}}\right)}, \tag{D.12}$$

228

$$\Delta x_i \Delta y_j J^{diffu}_{-1,z} = \Delta x_i \Delta y_j \frac{k_B}{m_e^*} \frac{\left(n_e T_e\right)^{P+1}_{i,j,k-1} - \left(n_e T_e\right)^{P+1}_{i,j,k}}{\frac{1}{2}\left(\frac{\Delta z_{k-1}}{\left(\tau_m\right)^{P+1}_{i,j,k-1}} + \frac{\Delta z_k}{\left(\tau_m\right)^{P+1}_{i,j,k}}\right)}, \tag{D.13}$$

$$\Delta x_i \Delta y_j J^{diffu}_{+1,z} = \Delta x_i \Delta y_j \frac{k_B}{m_e^*} \frac{\left(n_e T_e\right)^{P+1}_{i,j,k+1} - \left(n_e T_e\right)^{P+1}_{i,j,k}}{\frac{1}{2}\left(\frac{\Delta z_{k+1}}{\left(\tau_m\right)^{P+1}_{i,j,k+1}} + \frac{\Delta z_k}{\left(\tau_m\right)^{P+1}_{i,j,k}}\right)}. \tag{D.14}$$

For the drift components of the continuity equation, the upwind method will be utilized:

$$\Delta y_j \Delta z_k J^{drift}_{-1,x} = \Delta y_j \Delta z_k \frac{e}{m_e^*}\left(\tau_m\right)^{P+1}_{i-1,j,k}\left(n_e\right)^{P+1}_{i-1,j,k} E^{P+1}_{i-1/2,j,k}, \text{ if } E^{P+1}_{i-1/2,j,k} < 0 \tag{D.15}$$

$$\Delta y_j \Delta z_k J^{drift}_{-1,x} = \Delta y_j \Delta z_k \frac{e}{m_e^*}\left(\tau_m\right)^{P+1}_{i,j,k}\left(n_e\right)^{P+1}_{i,j,k} E^{P+1}_{i-1/2,j,k}, \text{ if } E^{P+1}_{i-1/2,j,k} > 0 \tag{D.16}$$

$$\Delta y_j \Delta z_k J^{drift}_{+1,x} = -\Delta y_j \Delta z_k \frac{e}{m_e^*}\left(\tau_m\right)^{P+1}_{i,j,k}\left(n_e\right)^{P+1}_{i,j,k} E^{P+1}_{i+1/2,j,k}, \text{ if } E^{P+1}_{i+1/2,j,k} < 0 \tag{D.17}$$

$$\Delta y_j \Delta z_k J^{drift}_{+1,x} = -\Delta y_j \Delta z_k \frac{e}{m_e^*}\left(\tau_m\right)^{P+1}_{i+1,j,k}\left(n_e\right)^{P+1}_{i+1,j,k} E^{P+1}_{i+1/2,j,k}, \text{ if } E^{P+1}_{i+1/2,j,k} > 0 \tag{D.18}$$

$$\Delta x_i \Delta z_k J^{drift}_{-1,y} = \Delta x_i \Delta z_k \frac{e}{m_e^*}\left(\tau_m\right)^{P+1}_{i,j-1,k}\left(n_e\right)^{P+1}_{i,j-1,k} E^{P+1}_{i,j-1/2,k}, \text{ if } E^{P+1}_{i,j-1/2,k} < 0 \tag{D.19}$$

$$\Delta x_i \Delta z_k J^{drift}_{-1,y} = \Delta x_i \Delta z_k \frac{e}{m_e^*}\left(\tau_m\right)^{P+1}_{i,j,k}\left(n_e\right)^{P+1}_{i,j,k} E^{P+1}_{i,j-1/2,k}, \text{ if } E^{P+1}_{i,j-1/2,k} > 0 \tag{D.20}$$

$$\Delta x_i \Delta z_k J^{drift}_{+1,y} = -\Delta x_i \Delta z_k \frac{e}{m_e^*}\left(\tau_m\right)^{P+1}_{i,j,k}\left(n_e\right)^{P+1}_{i,j,k} E^{P+1}_{i,j+1/2,k}, \text{ if } E^{P+1}_{i,j+1/2,k} < 0 \tag{D.21}$$

$$\Delta x_i \Delta z_k J^{drift}_{+1,y} = -\Delta x_i \Delta z_k \frac{e}{m_e^*}\left(\tau_m\right)^{P+1}_{i,j+1,k}\left(n_e\right)^{P+1}_{i,j+1,k} E^{P+1}_{i,j+1/2,k}, \text{ if } E^{P+1}_{i,j+1/2,k} > 0 \tag{D.22}$$

$$\Delta x_i \Delta y_j J^{drift}_{-1,z} = \Delta x_i \Delta y_j \frac{e}{m_e^*}\left(\tau_m\right)^{P+1}_{i,j,k-1}\left(n_e\right)^{P+1}_{i,j,k-1} E^{P+1}_{i,j,k-1/2}, \text{ if } E^{P+1}_{i,j,k-1/2} < 0 \tag{D.23}$$

$$\Delta x_i \Delta y_j J^{drift}_{-1,z} = \Delta x_i \Delta y_j \frac{e}{m_e^*}\left(\tau_m\right)^{P+1}_{i,j,k}\left(n_e\right)^{P+1}_{i,j,k} E^{P+1}_{i,j,k-1/2}, \text{ if } E^{P+1}_{i,j,k-1/2} > 0 \tag{D.24}$$

$$\Delta x_i \Delta y_j J^{drift}_{+1,z} = -\Delta x_i \Delta y_j \frac{e}{m_e^*}\left(\tau_m\right)^{P+1}_{i,j,k}\left(n_e\right)^{P+1}_{i,j,k} E^{P+1}_{i,j,k+1/2}, \text{ if } E^{P+1}_{i,j,k+1/2} < 0 \tag{D.25}$$

$$\Delta x_i \Delta y_j J^{drift}_{+1,z} = -\Delta x_i \Delta y_j \frac{e}{m_e^*}\left(\tau_m\right)^{P+1}_{i,j,k+1}\left(n_e\right)^{P+1}_{i,j,k+1} E^{P+1}_{i,j,k+1/2}, \text{ if } E^{P+1}_{i,j,k+1/2} > 0 \tag{D.26}$$

Collecting all the terms, the mass balance reads:

$$\frac{\left(n_e\right)^{P+1}_{i,j,k}-\left(n_e\right)^{P}_{i,j,k}}{\Delta t}=\frac{J^{drift}_{-1,x}+J^{drift}_{+1,x}+J^{diffu}_{-1,x}+J^{diffu}_{+1,x}}{\Delta x_i}+\frac{J^{drift}_{-1,y}+J^{drift}_{+1,y}+J^{diffu}_{-1,y}+J^{diffu}_{+1,y}}{\Delta y_j}$$
$$+\frac{J^{drift}_{-1,z}+J^{drift}_{+1,z}+J^{diffu}_{-1,z}+J^{diffu}_{+1,z}}{\Delta z_k}$$

(D.27)

Separating terms between the current time step and the previous time step yields:

$$\left(n_e\right)^{P+1}_{i,j,k}-\Delta t\left(\begin{array}{c}\dfrac{J^{drift}_{-1,x}+J^{drift}_{+1,x}+J^{diffu}_{-1,x}+J^{diffu}_{+1,x}}{\Delta x_i}+\dfrac{J^{drift}_{-1,y}+J^{drift}_{+1,y}+J^{diffu}_{-1,y}+J^{diffu}_{+1,y}}{\Delta y_j}\\+\dfrac{J^{drift}_{-1,z}+J^{drift}_{+1,z}+J^{diffu}_{-1,z}+J^{diffu}_{+1,z}}{\Delta z_k}\end{array}\right)=\left(n_e\right)^{P}_{i,j,k}.$$

(D.28)

Note that the electric field at the intermediate of two nodal points, for example, between nodes (i,j,k) and $(i-1,j,k)$, is given as:

$$E^{P+1}_{i-1/2,j,k}=\frac{V^{P+1}_{i,j,k}-V^{P+1}_{i-1,j,k}}{\frac{1}{2}\left(\Delta x_i+\Delta x_{i-1}\right)}.$$

(D.29)

Neumann boundary for both density and temperature at $i+1/2$ for diffusion component:

$$\left(n_e\right)^{P+1}_{i+1,j,k}=\left(n_e\right)^{P+1}_{i,j,k},$$

(D.30)

$$\left(T_e\right)^{P+1}_{i+1,j,k}=\left(T_e\right)^{P+1}_{i,j,k},$$

(D.31)

$$J^{diffu}_{+1}=0,$$

(D.32)

Dirichlet boundary for density and Neumann boundary for temperature at $i+1/2$ for diffusion component:

$$\left(n_e\right)^{P+1}_{i+1,j,k}=2N_D-\left(n_e\right)^{P+1}_{i,j,k},$$

(D.33)

$$\left(T_e\right)^{P+1}_{i+1,j,k}=\left(T_e\right)^{P+1}_{i,j,k},$$

(D.34)

$$\left(\tau_m\right)^{P+1}_{i+1,j,k}=\tau_m\left(N_D,\left(T_e\right)^{P+1}_{i,j,k}\right),$$

(D.35)

$$J^{diffu}_{+1}=\frac{k_B}{m^*_e}\tau_m\left(N_D,\left(T_e\right)^{P+1}_{i,j,k}\right)\frac{2N_D\left(T_e\right)^{P+1}_{i+1,j,k}-2\left(n_eT_e\right)^{P+1}_{i,j,k}}{\frac{\Delta x_i}{2}\left(\Delta x_{i+1}+\Delta x_i\right)},$$

(D.36)

Dirichlet boundary for both density and temperature at $i+1/2$ for diffusion component:

$$\left(n_e\right)^{P+1}_{i+1,j,k}=2N_D-\left(n_e\right)^{P+1}_{i,j,k},$$

(D.37)

$$\left(T_e\right)_{i+1,j,k}^{P+1} = 2T_L - \left(T_e\right)_{i,j,k}^{P+1}, \tag{D.38}$$

Since the momentum relaxation time is typically a function of density and temperature

$$\left(\tau_m\right)_{i+1,j,k}^{P+1} = \tau_m\left(N_D, T_L\right), \tag{D.39}$$

$$J_{+1}^{diffu} = \frac{k_B}{m_e^*}\tau_m\left(N_D, T_L\right)\frac{\left(2N_D - \left(n_e\right)_{i,j,k}^{P+1}\right)\left(2T_L - \left(T_e\right)_{i,j,k}^{P+1}\right) - \left(n_e T_e\right)_{i,j,k}^{P+1}}{\frac{\Delta x_i}{2}\left(\Delta x_{i+1} + \Delta x_i\right)}, \tag{D.40}$$

$$J_{+1}^{diffu} = \frac{k_B}{m_e^*}\tau_m\left(N_D, T_L\right)\frac{4N_D T_L - 2N_D\left(T_e\right)_{i,j,k}^{P+1} - 2T_L\left(n_e\right)_{i,j,k}^{P+1}}{\frac{\Delta x_i}{2}\left(\Delta x_{i+1} + \Delta x_i\right)}, \tag{D.41}$$

Neumann boundary for density at $i+1/2$ for drift component:

$$J_{+i}^{drift} = 0. \tag{D.42}$$

Dirichlet boundary for density at $i+1/2$ for drift component:

$$\left(n_e\right)_{i+1,j,k}^{P+1} = 2N_D - \left(n_e\right)_{i,j,k}^{P+1}, \tag{D.43}$$

$$J_{+1,x}^{drift} = -\frac{e}{m_e^*}\left(\tau_m\right)_{i+1,j,k}^{P}\left(n_e\right)_{i+1,j,k}^{P+1} E_{i+1/2,j,k}^{P+1}, \text{ if } E_{i+1/2,j,k}^{P+1} < 0. \tag{D.44}$$

Momentum Equation

The three velocity components can be evaluated as follows:

$$(-x\text{-comp.}) \qquad \left(v_{e,x}\right)_{i-1/2,j,k}^{P+1} = \frac{J_{-1,x}^{drift} + J_{-1,x}^{diffu}}{\left(n_e\right)_{i-1,j,k}^{P+1}}, \text{ if } \left(v_{e,x}\right)_{i-1/2,j,k}^{P+1} > 0 \tag{D.45}$$

$$\text{or} \qquad \left(v_{e,x}\right)_{i-1/2,j,k}^{P+1} = \frac{J_{-1,x}^{drift} + J_{-1,x}^{diffu}}{\left(n_e\right)_{i,j,k}^{P+1}}, \text{ if } \left(v_{e,x}\right)_{i-1/2,j,k}^{P+1} < 0 \tag{D.46}$$

$$(+x\text{-comp.}) \qquad \left(v_{e,x}\right)_{i+1/2,j,k}^{P+1} = \frac{J_{+1,x}^{drift} - J_{+1,x}^{diffu}}{\left(n_e\right)_{i,j,k}^{P+1}}, \text{ if } \left(v_{e,x}\right)_{i+1/2,j,k}^{P+1} > 0 \tag{D.47}$$

$$\text{or} \qquad \left(v_{e,x}\right)_{i+1/2,j,k}^{P+1} = \frac{J_{+1,x}^{drift} - J_{+1,x}^{diffu}}{\left(n_e\right)_{i+1,j,k}^{P+1}}, \text{ if } \left(v_{e,x}\right)_{i+1/2,j,k}^{P+1} < 0 \tag{D.48}$$

$$(-y\text{-comp.}) \qquad \left(v_{e,y}\right)_{i,j-1/2,k}^{P+1} = \frac{J_{-1,y}^{drift} + J_{-1,y}^{diffu}}{\left(n_e\right)_{i,j-1,k}^{P+1}}, \text{ if } \left(v_{e,y}\right)_{i,j-1/2,k}^{P+1} > 0 \tag{D.49}$$

$$\text{or} \qquad \left(v_{e,y}\right)^{P+1}_{i,j-1/2,k} = \frac{J^{drift}_{-1,y} + J^{diffu}_{-1,y}}{\left(n_e\right)^{P+1}_{i,j,k}}, \text{ if } \left(v_{e,y}\right)^{P+1}_{i,j-1/2,k} < 0 \qquad (D.50)$$

$$\text{(+y-comp.)} \qquad \left(v_{e,y}\right)^{P+1}_{i,j+1/2,k} = \frac{J^{drift}_{+1,y} - J^{diffu}_{+1,y}}{\left(n_e\right)^{P+1}_{i,j,k}}, \text{ if } \left(v_{e,y}\right)^{P+1}_{i,j+1/2,k} > 0 \qquad (D.51)$$

$$\text{or} \qquad \left(v_{e,y}\right)^{P+1}_{i,j+1/2,k} = \frac{J^{drift}_{+1,y} - J^{diffu}_{+1,y}}{\left(n_e\right)^{P+1}_{i,j+1,k}}, \text{ if } \left(v_{e,y}\right)^{P+1}_{i,j+1/2,k} < 0 \qquad (D.52)$$

$$\text{(−z-comp.)} \qquad \left(v_{e,z}\right)^{P+1}_{i,j,k-1/2} = \frac{J^{drift}_{-1,z} + J^{diffu}_{-1,z}}{\left(n_e\right)^{P+1}_{i,j,k-1}}, \text{ if } \left(v_{e,z}\right)^{P+1}_{i,j,k-1/2} > 0 \qquad (D.53)$$

$$\text{or} \qquad \left(v_{e,z}\right)^{P+1}_{i,j,k-1/2} = \frac{J^{drift}_{-1,z} + J^{diffu}_{-1,z}}{\left(n_e\right)^{P+1}_{i,j,k}}, \text{ if } \left(v_{e,z}\right)^{P+1}_{i,j,k-1/2} < 0 \qquad (D.54)$$

$$\text{(+z-comp.)} \qquad \left(v_{e,z}\right)^{P+1}_{i,j,k+1/2} = \frac{J^{drift}_{+1,z} - J^{diffu}_{+1,z}}{\left(n_e\right)^{P+1}_{i,j,k}}, \text{ if } \left(v_{e,z}\right)^{P+1}_{i,j,k+1/2} > 0 \qquad (D.55)$$

$$\text{or} \qquad \left(v_{e,z}\right)^{P+1}_{i,j,k+1/2} = \frac{J^{drift}_{+1,z} - J^{diffu}_{+1,z}}{\left(n_e\right)^{P+1}_{i,j,k+1}}, \text{ if } \left(v_{e,z}\right)^{P+1}_{i,j,k+1/2} < 0 \qquad (D.56)$$

In the following derivations, the upwind method is used to discretize the inertia terms in the momentum equations. Here the various velocity components are assumed to be positive.

$$\text{(x-Momentum)} \qquad \frac{\partial v_{e,x}}{\partial t} + \vec{v}_e \cdot \nabla v_{e,x} = -\frac{e}{m_e}E_x - \frac{k_B}{m_e n_e}\frac{\partial\left(n_e T_e\right)}{\partial x} - \left(\frac{1}{\tau_m} + \frac{\dot{n}_{e,gen}}{n_e}\right)v_{e,x}, \qquad (D.57)$$

$$\frac{\left(v_{e,x}\right)^{P+1}_{i+1/2,j,k} - \left(v_{e,x}\right)^{P}_{i+1/2,j,k}}{\Delta t} + \left(v_{e,x}\right)^{P}_{i+1/2,j,k}\left[\frac{\left(v_{e,x}\right)^{P+1}_{i+1/2,j,k} - \left(v_{e,x}\right)^{P+1}_{i-1/2,j,k}}{\Delta x_i}\right]$$

$$+2\left(v_{e,y}\right)^{P+1}_{i+1/2,j,k}\left[\frac{\left(v_{e,x}\right)^{P+1}_{i+1/2,j,k} - \left(v_{e,x}\right)^{P+1}_{i+1/2,j-1,k}}{\Delta y_{j-1} + \Delta y_j}\right]$$

$$+2\left(v_{e,z}\right)^{P+1}_{i+1/2,j,k}\left[\frac{\left(v_{e,x}\right)^{P+1}_{i+1/2,j,k} - \left(v_{e,x}\right)^{P+1}_{i+1/2,j,k-1}}{\Delta z_{k-1} + \Delta z_k}\right] \qquad , \qquad (D.58)$$

$$= \frac{2e}{m_e}\left(\frac{\phi^{P+1}_{i+1,j,k} - \phi^{P+1}_{i,j,k}}{\Delta x_i + \Delta x_{i+1}}\right) - \frac{2k_B}{m_e}\left[\frac{\left(T_e\right)^{P+1}_{i+1,j,k} - \left(T_e\right)^{P+1}_{i,j,k}}{\Delta x_i + \Delta x_{i+1}}\right]$$

$$-\frac{2k_B\left(T_e\right)^{P+1}_{i+1/2,j,k}}{m_e\left(n_e\right)^{P+1}_{i+1/2,j,k}}\left[\frac{\left(n_e\right)^{P+1}_{i+1,j,k} - \left(n_e\right)^{P+1}_{i,j,k}}{\Delta x_i + \Delta x_{i+1}}\right] - \left(\frac{1}{\tau_m} + \frac{\dot{n}_{e,gen}}{n_e}\right)^{P+1}_{i+1/2,j,k}\left(v_{e,x}\right)^{P+1}_{i+1/2,j,k}$$

with the following assumptions that:

$$\left(v_{e,z}\right)^{P+1}_{i+1/2,j,k} > 0 \,, \tag{D.59}$$

$$\left(v_{e,y}\right)^{P+1}_{i,j+1/2,k} > 0 \,, \tag{D.60}$$

$$\left(v_{e,z}\right)^{P+1}_{i,j,k+1/2} > 0 \,, \tag{D.61}$$

$$\left(v_{e,y}\right)^{P+1}_{i+1/2,j,k} = \frac{1}{4}\left[\left(v_{e,y}\right)^{P+1}_{i,j-1/2,k} + \left(v_{e,y}\right)^{P+1}_{i,j+1/2,k} + \left(v_{e,y}\right)^{P+1}_{i+1,j-1/2,k} + \left(v_{e,y}\right)^{P+1}_{i+1,j+1/2,k}\right], \tag{D.62}$$

$$\left(v_{e,z}\right)^{P+1}_{i+1/2,j,k} = \frac{1}{4}\left[\left(v_{e,y}\right)^{P+1}_{i,j,k-1/2} + \left(v_{e,y}\right)^{P+1}_{i,j,k+1/2} + \left(v_{e,y}\right)^{P+1}_{i+1,j,k-1/2} + \left(v_{e,y}\right)^{P+1}_{i+1,j,k+1/2}\right]. \tag{D.63}$$

(*y-Momentum*)
$$\frac{\partial v_{e,y}}{\partial t} + \vec{v}_e \cdot \nabla v_{e,y} = -\frac{e}{m_e}E_y - \frac{k_B}{m_e n_e}\frac{\partial(n_e T_e)}{\partial y} - \left(\frac{1}{\tau_m} + \frac{\dot{n}_{e,gen}}{n_e}\right)v_{e,y} \,, \tag{D.64}$$

$$\frac{\left(v_{e,y}\right)^{P+1}_{i,j+1/2,k} - \left(v_{e,y}\right)^{P}_{i,j+1/2,k}}{\Delta t} + 2\left(v_{e,x}\right)^{P+1}_{i,j+1/2,k}\left[\frac{\left(v_{e,y}\right)^{P+1}_{i,j+1/2,k} - \left(v_{e,y}\right)^{P+1}_{i-1,j+1/2,k}}{\Delta x_{i-1} + \Delta x_i}\right]$$

$$+\left(v_{e,y}\right)^{P+1}_{i,j+1/2,k}\left[\frac{\left(v_{e,y}\right)^{P+1}_{i,j+1/2,k} - \left(v_{e,y}\right)^{P+1}_{i,j-1/2,k}}{\Delta y_j}\right]$$

$$+2\left(v_{e,z}\right)^{P+1}_{i,j+1/2,k}\left[\frac{\left(v_{e,y}\right)^{P+1}_{i,j+1/2,k} - \left(v_{e,y}\right)^{P+1}_{i,j+1/2,k-1}}{\Delta z_{k-1} + \Delta z_k}\right] \qquad , \tag{D.65}$$

$$= \frac{2e}{m_e}\left(\frac{\phi^{P+1}_{i,j+1,k} - \phi^{P+1}_{i,j,k}}{\Delta y_j + \Delta y_{j+1}}\right) - \frac{2k_B}{m_e}\left[\frac{\left(T_e\right)^{P+1}_{i,j+1,k} - \left(T_e\right)^{P+1}_{i,j,k}}{\Delta y_j + \Delta y_{j+1}}\right]$$

$$-\frac{2k_B\left(T_e\right)^{P+1}_{i,j+1/2,k}}{m_e\left(n_e\right)^{P+1}_{i,j+1/2,k}}\left[\frac{\left(n_e\right)^{P+1}_{i,j+1,k} - \left(n_e\right)^{P+1}_{i,j,k}}{\Delta y_j + \Delta y_{j+1}}\right] - \left(\frac{1}{\tau_m} + \frac{\dot{n}_{e,gen}}{n_e}\right)^{P+1}_{i,j+1/2,k}\left(v_{e,y}\right)^{P+1}_{i,j+1/2,k}$$

with the following assumptions that:

$$\left(v_{e,z}\right)^{P+1}_{i+1/2,j,k} > 0 \,, \tag{D.66}$$

$$\left(v_{e,y}\right)^{P+1}_{i,j+1/2,k} > 0 \,, \tag{D.67}$$

$$\left(v_{e,z}\right)^{P+1}_{i,j,k+1/2} > 0 \,, \tag{D.68}$$

$$\left(v_{e,x}\right)^{P+1}_{i,j+1/2,k} = \frac{1}{4}\left[\left(v_{e,x}\right)^{P+1}_{i-1/2,j,k} + \left(v_{e,x}\right)^{P+1}_{i+1/2,j,k} + \left(v_{e,x}\right)^{P+1}_{i-1/2,j+1,k} + \left(v_{e,x}\right)^{P+1}_{i+1/2,j+1,k}\right], \tag{D.69}$$

$$\left(v_{e,z}\right)^{P+1}_{i,j+1/2,k} = \frac{1}{4}\left[\left(v_{e,z}\right)^{P+1}_{i,j,k-1/2} + \left(v_{e,z}\right)^{P+1}_{i,j,k+1/2} + \left(v_{e,z}\right)^{P+1}_{i,j+1,k-1/2} + \left(v_{e,z}\right)^{P+1}_{i,j+1,k+1/2}\right]. \tag{D.70}$$

$(z\text{-}Momentum)$
$$\frac{\partial v_{e,z}}{\partial t} + \vec{v}_e \cdot \nabla v_{e,z} = -\frac{e}{m_e}E_z - \frac{k_B}{m_e n_e}\frac{\partial(n_e T_e)}{\partial z} - \left(\frac{1}{\tau_m} + \frac{\dot{n}_{e,gen}}{n_e}\right)v_{e,z},\tag{D.71}$$

$$\frac{\left(v_{e,z}\right)^{P+1}_{i,j,k+1/2} - \left(v_{e,z}\right)^{P}_{i,j,k+1/2}}{\Delta t} + 2\left(v_{e,x}\right)^{P+1}_{i,j,k+1/2}\left[\frac{\left(v_{e,z}\right)^{P+1}_{i,j,k+1/2} - \left(v_{e,z}\right)^{P+1}_{i-1,j,k+1/2}}{\Delta x_{i-1} + \Delta x_i}\right]$$

$$+2\left(v_{e,y}\right)^{P+1}_{i,j,k+1/2}\left[\frac{\left(v_{e,z}\right)^{P+1}_{i,j,k+1/2} - \left(v_{e,z}\right)^{P+1}_{i,j-1,k-1/2}}{\Delta y_{j-1} + \Delta y_j}\right]$$

$$+\left(v_{e,z}\right)^{P+1}_{i,j,k+1/2}\left[\frac{\left(v_{e,z}\right)^{P+1}_{i,j,k+1/2} - \left(v_{e,z}\right)^{P+1}_{i,j,k-1/2}}{\Delta z_k}\right] \tag{D.72}$$

$$=\frac{2e}{m_e}\left(\frac{\phi^{P+1}_{i,j,k+1} - \phi^{P+1}_{i,j,k}}{\Delta z_k + \Delta z_{k+1}}\right) - \frac{2k_B}{m_e}\left[\frac{\left(T_e\right)^{P+1}_{i,j,k+1} - \left(T_e\right)^{P+1}_{i,j,k}}{\Delta z_k + \Delta z_{k+1}}\right]$$

$$-\frac{2k_B\left(T_e\right)^{P+1}_{i,j,k+1/2}}{m_e\left(n_e\right)^{P+1}_{i,j,k+1/2}}\left[\frac{\left(n_e\right)^{P+1}_{i,j,k+1} - \left(n_e\right)^{P+1}_{i,j,k}}{\Delta z_k + \Delta z_{k+1}}\right] - \left(\frac{1}{\tau_m} + \frac{\dot{n}_{e,gen}}{n_e}\right)^{P+1}_{i,j,k+1/2}\left(v_{e,z}\right)^{P+1}_{i,j,k+1/2}$$

with the following assumptions that:

$$\left(v_{e,z}\right)^{P+1}_{i+1/2,j,k} > 0,\tag{D.73}$$

$$\left(v_{e,y}\right)^{P+1}_{i,j+1/2,k} > 0,\tag{D.74}$$

$$\left(v_{e,z}\right)^{P+1}_{i,j,k+1/2} > 0,\tag{D.75}$$

$$\left(v_{e,x}\right)^{P+1}_{i,j,k+1/2} = \frac{1}{4}\left[\left(v_{e,x}\right)^{P+1}_{i-1/2,j,k} + \left(v_{e,x}\right)^{P+1}_{i+1/2,j,k} + \left(v_{e,x}\right)^{P+1}_{i-1/2,j,k+1} + \left(v_{e,x}\right)^{P+1}_{i+1/2,j,k+1}\right],\tag{D.76}$$

$$\left(v_{e,y}\right)^{P+1}_{i,j,k+1/2} = \frac{1}{4}\left[\left(v_{e,y}\right)^{P+1}_{i,j-1/2,k} + \left(v_{e,y}\right)^{P+1}_{i,j+1/2,k} + \left(v_{e,y}\right)^{P+1}_{i,j-1/2,k+1} + \left(v_{e,y}\right)^{P+1}_{i,j+1/2,k+1}\right].\tag{D.77}$$

Electron-Energy Equation

Rearranging the electron-energy equation gives:

$$\frac{\partial T_e}{\partial t} + \nabla\cdot\left(\vec{v}_e T_e\right) - \frac{2}{3n_e k_B}\nabla\cdot\left(k_e \nabla T_e\right) + \left(\frac{1}{\tau_{e-LO}} - \frac{1}{3}\nabla\cdot\vec{v}\right)T_e = \frac{T_{LO}}{\tau_{e-LO}} + \left(\frac{2}{\tau_m} - \frac{1}{\tau_{e-LO}}\right)\frac{m_e^*|\vec{v}_e|^2}{3k_B}.\tag{D.78}$$

Discretizing the equation using the first-order forward-differencing in time, the second-order centered-differencing in space for the diffusion term, and the first-upwind method for the advec-

tion term, the following implicit-differenced equation is obtained:

$$
\frac{\left(T_e\right)_{i,j,k}^{P+1} - \left(T_e\right)_{i,j,k}^{P}}{\Delta t} + \frac{\left(J_e^{Th}\right)_{i+1/2,j,k}^{P+1} - \left(J_e^{Th}\right)_{i-1/2,j,k}^{P+1}}{\Delta x_i} + \frac{\left(J_e^{Th}\right)_{i,j+1/2,k}^{P+1} - \left(J_e^{Th}\right)_{i,j-1/2,k}^{P+1}}{\Delta y_j} +
$$

$$
+ \frac{\left(J_e^{Th}\right)_{i,j,k+1/2}^{P+1} - \left(J_e^{Th}\right)_{i,j,k-1/2}^{P+1}}{\Delta z_k} - \frac{2}{3k_B\left(n_e\right)_{i,j,k}^{P+1}} \frac{\left(T_e\right)_{i+1,j,k}^{P+1} - \left(T_e\right)_{i,j,k}^{P+1}}{\dfrac{\Delta x_i}{2}\left(\dfrac{\Delta x_i}{\left(k_e\right)_{i,j,k}^{P+1}} + \dfrac{\Delta x_{i+1}}{\left(k_e\right)_{i+1,j,k}^{P+1}}\right)} -
$$

$$
- \frac{2}{3k_B\left(n_e\right)_{i,j,k}^{P+1}} \frac{\left(T_e\right)_{i-1,j,k}^{P+1} - \left(T_e\right)_{i,j,k}^{P+1}}{\dfrac{\Delta x_i}{2}\left(\dfrac{\Delta x_i}{\left(k_e\right)_{i,j,k}^{P+1}} + \dfrac{\Delta x_{i-1}}{\left(k_e\right)_{i-1,j,k}^{P+1}}\right)} - \frac{2}{3k_B\left(n_e\right)_{i,j,k}^{P+1}} \frac{\left(T_e\right)_{i,j+1,k}^{P+1} - \left(T_e\right)_{i,j,k}^{P+1}}{\dfrac{\Delta y_j}{2}\left(\dfrac{\Delta y_j}{\left(k_e\right)_{i,j,k}^{P+1}} + \dfrac{\Delta y_{j+1}}{\left(k_e\right)_{i,j+1,k}^{P+1}}\right)} -
$$

$$
- \frac{2}{3k_B\left(n_e\right)_{i,j,k}^{P+1}} \frac{\left(T_e\right)_{i,j-1,k}^{P+1} - \left(T_e\right)_{i,j,k}^{P+1}}{\dfrac{\Delta y_j}{2}\left(\dfrac{\Delta y_j}{\left(k_e\right)_{i,j,k}^{P+1}} + \dfrac{\Delta y_{j-1}}{\left(k_e\right)_{i,j-1,k}^{P+1}}\right)} - \frac{2}{3k_B\left(n_e\right)_{i,j,k}^{P+1}} \frac{\left(T_e\right)_{i,j,k+1}^{P+1} - \left(T_e\right)_{i,j,k}^{P+1}}{\dfrac{\Delta z_k}{2}\left(\dfrac{\Delta z_k}{\left(k_e\right)_{i,j,k}^{P+1}} + \dfrac{\Delta z_{k+1}}{\left(k_e\right)_{i,j,k+1}^{P+1}}\right)} -
$$

$$
- \frac{2}{3k_B\left(n_e\right)_{i,j,k}^{P+1}} \frac{\left(T_e\right)_{i,j,k-1}^{P+1} - \left(T_e\right)_{i,j,k}^{P+1}}{\dfrac{\Delta z_k}{2}\left(\dfrac{\Delta z_k}{\left(k_e\right)_{i,j,k}^{P+1}} + \dfrac{\Delta z_{k-1}}{\left(k_e\right)_{i,j,k-1}^{P+1}}\right)} + \frac{1}{\tau_{e-LO}}\left(T_e\right)_{i,j,k}^{P+1} -
$$

$$
-\frac{1}{3}\left(\frac{\dfrac{\left(v_{e,x}\right)_{i+1/2,j,k}^{P+1} - \left(v_{e,x}\right)_{i-1/2,j,k}^{P+1}}{\Delta x_i} + \dfrac{\left(v_{e,x}\right)_{i,j+1/2,k}^{P+1} - \left(v_{e,x}\right)_{i,j-1/2,k}^{P+1}}{\Delta y_j}}{+\dfrac{\left(v_{e,x}\right)_{i,j,k+1/2}^{P+1} - \left(v_{e,x}\right)_{i,j,k-1/2}^{P+1}}{\Delta z_k}}\right)\left(T_e\right)_{i,j,k}^{P+1}
$$

$$
= \frac{\left(T_{LO}\right)_{i,j,k}^{P+1}}{\tau_{e-LO}} + \left(\frac{2}{\left(\tau_m\right)_{i,j,k}^{P+1}} - \frac{1}{\tau_{e-LO}}\right)\frac{m_e^*\left|\left(\bar{v}_e\right)_{i,j,k}^{P+1}\right|^2}{3k_B}. \qquad (D.79)
$$

The convective thermal currents (i.e., J_e^{Th}'s) in the above expression are approximated using the first-upwind method, for example, along the x-direction:

$$
\left(J_e^{Th}\right)_{i+1/2,j,k}^{P+1} = \left(v_{e,x}\right)_{i+1/2,j,k}^{P+1}\left(T_e\right)_{i,j,k}^{P+1}, \text{ if } \left(v_{e,x}\right)_{i+1/2,j,k}^{P+1} > 0, \qquad (D.80)
$$

or
$$
\left(J_e^{Th}\right)_{i+1/2,j,k}^{P+1} = \left(v_{e,x}\right)_{i+1/2,j,k}^{P+1}\left(T_e\right)_{i+1,j,k}^{P+1}, \text{ if } \left(v_{e,x}\right)_{i+1/2,j,k}^{P+1} < 0, \qquad (D.81)
$$

$$
\left(J_e^{Th}\right)_{i-1/2,j,k}^{P+1} = \left(v_{e,x}\right)_{i-1/2,j,k}^{P+1}\left(T_e\right)_{i-1,j,k}^{P+1}, \text{ if } \left(v_{e,x}\right)_{i-1/2,j,k}^{P+1} > 0, \qquad (D.82)
$$

or
$$\left(J_e^{Th}\right)_{i-1/2,j,k}^{P+1} = \left(v_{e,x}\right)_{i-1/2,j,k}^{P+1}\left(T_e\right)_{i,j,k}^{P+1}, \text{ if } \left(v_{e,x}\right)_{i-1/2,j,k}^{P+1} < 0. \tag{D.83}$$

The same discretization applies for the convective thermal currents along the y- and z-directions.

LO-Phonon Energy Equation

Reconfiguring the optical phonon energy conservation equation gives:

$$\frac{\partial T_{LO}}{\partial t} + \left(\frac{3}{2}\frac{n_e k_B}{C_{LO}\tau_{e-LO}} + \frac{1}{\tau_{LO-A}}\right)T_{LO} = \frac{3}{2}\frac{n_e k_B}{C_{LO}\tau_{e-LO}}T_e + \frac{n_e m_e^* |\bar{v}_e|^2}{2C_{LO}\tau_{e-LO}} + \frac{1}{\tau_{LO-A}}T_A. \tag{D.84}$$

Note that for a first-order linear differential equation given as:

$$\frac{dT}{dt} + AT = B, \tag{D.85}$$

where A and B are constants, its solution is expressed as:

$$T(t) = \frac{B}{A} + \left(T_0 - \frac{B}{A}\right)\exp\left[A(t_0 - t)\right], \tag{D.86}$$

assuming that the initial condition is T_0 at t_0. Applying the solution to the optical phonon equation yields the following equalities:

$$A = \frac{3}{2}\frac{n_e k_B}{C_{LO}\tau_{e-LO}} + \frac{1}{\tau_{LO-A}}, \tag{D.87}$$

$$B = \frac{3}{2}\frac{n_e k_B}{C_{LO}\tau_{e-LO}}T_e + \frac{n_e m_e^* |\bar{v}_e|^2}{2C_{LO}\tau_{e-LO}} + \frac{1}{\tau_{LO-A}}T_A. \tag{D.88}$$

In practice, A and B depend on T; therefore, the solution given above is invalid for such a case. However, the correct solution can be obtained numerically by iterating the solution (i.e., for the case where A and B are constants) while changing A and B according to the solution at the previous iteration until it converges. Alternatively, if A and B are known explicitly as a function of T, then the correct solution can be evaluated as:

$$T(t) = \exp\left[-\int_t A(t')dt'\right]\left\{\int_t \exp\left[\int_{t'} A(t'')dt''\right]B(t')dt' + C\right\}, \tag{D.89}$$

where C, a constant, is to be determined from the given initial condition.

Similarly, the discretization of the phonon energy equation leads to the following differenced equation:

$$
\frac{(T_{LO})_{i,j,k}^{P+1} - (T_{LO})_{i,j,k}^{P}}{\Delta t} + \left(\frac{3k_B}{2} \frac{(n_e)_{i,j,k}^{P+1}}{(C_{LO})_{i,j,k}^{P+1} \tau_{e-LO}} + \frac{1}{\tau_{LO-A}} \right)(T_{LO})_{i,j,k}^{P+1}
$$
$$
= \frac{3k_B}{2} \frac{(n_e)_{i,j,k}^{P+1}}{(C_{LO})_{i,j,k}^{P+1} \tau_{e-LO}}(T_e)_{i,j,k}^{P+1} + \frac{(n_e)_{i,j,k}^{P+1} m_e^* \left| (\vec{v}_e)_{i,j,k}^{P+1} \right|^2}{2(C_{LO})_{i,j,k}^{P+1} \tau_{e-LO}} + \frac{1}{\tau_{e-LO}}(T_A)_{i,j,k}^{P+1}
$$
. (D.90)

Acoustic Phonon Energy Equation

Reconfiguring the phonon energy conservation equation gives:

$$
\frac{\partial T_A}{\partial t} - \frac{1}{C_A}\nabla \cdot (k_A \nabla T_A) + \frac{C_{LO}}{C_A \tau_{LO-A}}T_A = \frac{C_{LO}}{C_A \tau_{LO-A}}T_{LO} .
$$
(D.91)

Similarly, the discretization of the phonon energy equation leads to the following differenced equation:

$$
\frac{(T_A)_{i,j,k}^{P+1} - (T_A)_{i,j,k}^{P}}{\Delta t} - \frac{1}{(C_A)_{i,j,k}^{P+1}} \frac{(T_A)_{i+1,j,k}^{P+1} - (T_A)_{i,j,k}^{P+1}}{\frac{\Delta x_i}{2}\left(\frac{\Delta x_i}{(k_A)_{i,j,k}^{P+1}} + \frac{\Delta x_{i+1}}{(k_A)_{i+1,j,k}^{P+1}} \right)} -
$$
$$
- \frac{1}{(C_A)_{i,j,k}^{P+1}} \frac{(T_A)_{i-1,j,k}^{P+1} - (T_A)_{i,j,k}^{P+1}}{\frac{\Delta x_i}{2}\left(\frac{\Delta x_i}{(k_A)_{i,j,k}^{P+1}} + \frac{\Delta x_{i-1}}{(k_A)_{i-1,j,k}^{P+1}} \right)} - \frac{1}{(C_A)_{i,j,k}^{P+1}} \frac{(T_A)_{i,j+1,k}^{P+1} - (T_A)_{i,j,k}^{P+1}}{\frac{\Delta y_j}{2}\left(\frac{\Delta y_j}{(k_A)_{i,j,k}^{P+1}} + \frac{\Delta y_{j+1}}{(k_A)_{i,j+1,k}^{P+1}} \right)} -
$$
$$
- \frac{1}{(C_A)_{i,j,k}^{P+1}} \frac{(T_A)_{i,j-1,k}^{P+1} - (T_A)_{i,j,k}^{P+1}}{\frac{\Delta y_j}{2}\left(\frac{\Delta y_j}{(k_A)_{i,j,k}^{P+1}} + \frac{\Delta y_{j-1}}{(k_A)_{i,j-1,k}^{P+1}} \right)} - \frac{1}{(C_A)_{i,j,k}^{P+1}} \frac{(T_A)_{i,j,k+1}^{P+1} - (T_A)_{i,j,k}^{P+1}}{\frac{\Delta z_k}{2}\left(\frac{\Delta z_k}{(k_A)_{i,j,k}^{P+1}} + \frac{\Delta z_{k+1}}{(k_A)_{i,j,k+1}^{P+1}} \right)} -
$$
$$
- \frac{1}{(C_A)_{i,j,k}^{P+1}} \frac{(T_A)_{i,j,k-1}^{P+1} - (T_A)_{i,j,k}^{P+1}}{\frac{\Delta z_k}{2}\left(\frac{\Delta z_k}{(k_A)_{i,j,k}^{P+1}} + \frac{\Delta z_{k-1}}{(k_A)_{i,j,k-1}^{P+1}} \right)} + \frac{(C_{LO})_{i,j,k}^{P+1}}{(C_A)_{i,j,k}^{P+1} \tau_{LO-A}}(T_A)_{i,j,k}^{P+1} = \frac{(C_{LO})_{i,j,k}^{P+1}}{(C_A)_{i,j,k}^{P+1} \tau_{LO-A}}(T_{LO})_{i,j,k}^{P+1}
$$
. (D.92)

In this appendix, the numerical discretization of the Two-Temperature Model (TTM) and the proposed algorithm are shown. According to Section 2.7.1, the governing equations for the TTM for metals are expressed as:

$$C_e \frac{\partial T_e}{\partial t} = \nabla \cdot (k_e \nabla T_e) - G(T_e - T_l) + S(x, y, z), \tag{E.1}$$

$$C_l \frac{\partial T_l}{\partial t} = \nabla \cdot (k_l \nabla T_l) - G(T_l - T_e). \tag{E.2}$$

Discretizing both equations using the centered-difference approximation in space and the forward Euler approximation in time leads to the following differenced equations:

$$C_e \frac{(T_e)_{m,n,o}^{P+1} - (T_e)_{m,n,o}^{P}}{\Delta t} = k_e \frac{(T_e)_{m+1,n,o}^{P+1} - 2(T_e)_{m,n,o}^{P+1} + (T_e)_{m-1,n,o}^{P+1}}{(\Delta x)^2}$$

$$+ k_e \frac{(T_e)_{m,n+1,o}^{P+1} - 2(T_e)_{m,n,o}^{P+1} + (T_e)_{m,n-1,o}^{P+1}}{(\Delta y)^2} \tag{E.3}$$

$$+ k_e \frac{(T_e)_{m,n,o+1}^{P+1} - 2(T_e)_{m,n,o}^{P+1} + (T_e)_{m,n,o-1}^{P+1}}{(\Delta z)^2} - G\left((T_e)_{m,n,o}^{P+1} - (T_l)_{m,n,o}^{P}\right) + S_{m,n,o}^{P+1}$$

$$C_l \frac{(T_l)_{m,n,o}^{P+1} - (T_l)_{m,n,o}^{P}}{\Delta t} = k_l \frac{(T_l)_{m+1,n,o}^{P+1} - 2(T_l)_{m,n,o}^{P+1} + (T_l)_{m-1,n,o}^{P+1}}{(\Delta x)^2}$$

$$+ k_l \frac{(T_l)_{m,n+1,o}^{P+1} - 2(T_l)_{m,n,o}^{P+1} + (T_l)_{m,n-1,o}^{P+1}}{(\Delta y)^2} \tag{E.4}$$

$$+ k_l \frac{(T_l)_{m,n,o+1}^{P+1} - 2(T_l)_{m,n,o}^{P+1} + (T_l)_{m,n,o-1}^{P+1}}{(\Delta z)^2} - G\left((T_l)_{m,n,o}^{P+1} - (T_e)_{m,n,o}^{P+1}\right)$$

Rearranging the second equation yields:

$$\left(T_l\right)^P_{m,n,o} = \left(T_l\right)^{P+1}_{m,n,o} - \frac{\Delta t}{C_l}\left[k_l \frac{\left(T_l\right)^{P+1}_{m+1,n,o} - 2\left(T_l\right)^{P+1}_{m,n,o} + \left(T_l\right)^{P+1}_{m-1,n,o}}{\left(\Delta x\right)^2}\right.$$

$$+ k_l \frac{\left(T_l\right)^{P+1}_{m,n+1,o} - 2\left(T_l\right)^{P+1}_{m,n,o} + \left(T_l\right)^{P+1}_{m,n-1,o}}{\left(\Delta y\right)^2} + k_l \frac{\left(T_l\right)^{P+1}_{m,n,o+1} - 2\left(T_l\right)^{P+1}_{m,n,o} + \left(T_l\right)^{P+1}_{m,n,o-1}}{\left(\Delta z\right)^2}$$

$$\left. - G\left(\left(T_l\right)^{P+1}_{m,n,o} - \left(T_e\right)^{P+1}_{m,n,o}\right)\right] . \tag{E.5}$$

Now substituting it into the first equation leads to:

$$C_e \frac{\left(T_e\right)^{P+1}_{m,n,o} - \left(T_e\right)^P_{m,n,o}}{\Delta t} = k_e \left\{ \begin{array}{l} \dfrac{\left(T_e\right)^{P+1}_{m+1,n,o} - 2\left(T_e\right)^{P+1}_{m,n,o} + \left(T_e\right)^{P+1}_{m-1,n,o}}{\left(\Delta x\right)^2} \\[2ex] + \dfrac{\left(T_e\right)^{P+1}_{m,n+1,o} - 2\left(T_e\right)^{P+1}_{m,n,o} + \left(T_e\right)^{P+1}_{m,n-1,o}}{\left(\Delta y\right)^2} \\[2ex] + \dfrac{\left(T_e\right)^{P+1}_{m,n,o+1} - 2\left(T_e\right)^{P+1}_{m,n,o} + \left(T_e\right)^{P+1}_{m,n,o-1}}{\left(\Delta z\right)^2} \end{array} \right\} - G\left(\left(T_e\right)^{P+1}_{m,n,o} - \left(T_l\right)^{P+1}_{m,n,o}\right)$$

$$+ S^{P+1}_{m,n,o} - \frac{k_l G \Delta t}{C_l} \left\{ \begin{array}{l} \dfrac{\left(T_l\right)^{P+1}_{m+1,n,o} - 2\left(T_l\right)^{P+1}_{m,n,o} + \left(T_l\right)^{P+1}_{m-1,n,o}}{\left(\Delta x\right)^2} \\[2ex] + \dfrac{\left(T_l\right)^{P+1}_{m,n+1,o} - 2\left(T_l\right)^{P+1}_{m,n,o} + \left(T_l\right)^{P+1}_{m,n-1,o}}{\left(\Delta y\right)^2} \\[2ex] + \dfrac{\left(T_l\right)^{P+1}_{m,n,o+1} - 2\left(T_l\right)^{P+1}_{m,n,o} + \left(T_l\right)^{P+1}_{m,n,o-1}}{\left(\Delta z\right)^2} \end{array} \right\} , \tag{E.6}$$

$$- \frac{G^2 \Delta t}{C_l}\left(\left(T_e\right)^{P+1}_{m,n,o} - \left(T_l\right)^{P+1}_{m,n,o}\right)$$

Notice that the first three terms on the right hand side of the equation represent the discretization of the equation if the implicit scheme were employed. Therefore, the last two terms are the additional errors introduced into the differenced equation when the phonon temperature at a previous time step is used in the electron energy conservation equation. Hence, they need to be minimized in order to reduce these errors.

Pulsed Laser Source Term

Here, a pulsed laser is considered. The pulse width of the laser is assumed to be a Gaussian pro-

file. Without scattering, the source term for a laser pulse with Gaussian distributed temporally and spatially in xy-plane, and with energy exponentially decaying (i.e., absorbed by the medium) along the z-axis, can be written as:

$$S(x,y,z,t) = \dot{q}_m \, exp\left\{-\kappa z - 4\ln 2\left[\left(\frac{t-4t_p}{t_p}\right)^2 + \left(\frac{x^2+y^2}{r_p^2}\right)\right]\right\}, \tag{E.7}$$

where $\dot{q}_m$ is the maximum volumetric heat generation, t_p the pulse duration of the full width at half maximum (FWHM), r_p the spatial width at FWHM, and κ the absorption coefficient of the medium. In this case, the maximum power delivered by the pulse occurs at $t = 2t_p$ and centers at the xy-plane. To determine the maximum power delivered by the pulse in terms of the total energy E_{pulse} of the pulse, Eq. (E.7) needs to be integrated over space and time (i.e., x, y, z, and t), to obtain E_{pulse}, leading to the following expression:

$$E_{pulse} = \dot{q}_m \int_0^\infty \int_0^\infty \int_0^{2\pi} \int_0^\infty exp\left\{-\kappa z - 4\ln 2\left[\left(\frac{t-4t_p}{t_p}\right)^2 + \left(\frac{r^2}{r_p^2}\right)\right]\right\} r\,dr\,d\theta\,dz\,dt$$

$$= \left(\sqrt{\frac{\pi}{4\ln 2}}\, t_p\right)\left(\frac{1}{\kappa}\right)\left(\frac{r_p^2}{8\ln 2}\right)2\pi\dot{q}_m \tag{E.8}$$

Therefore, the $\dot{q}_m$ can be determined in terms of the pulse energy and properties of the Gaussian distribution:

$$\dot{q}_m = 8\left(\frac{\ln 2}{\pi}\right)^{1.5}\frac{\kappa}{t_p\, r_p^2}E_{pulse}. \tag{E.9}$$

Hence, the source term for the laser pulse is given as:

$$S(x,y,z,t) = 8\left(\frac{\ln 2}{\pi}\right)^{1.5}\frac{\kappa E_{pulse}}{t_p\, r_p^2}exp\left\{-\kappa z - 4\ln 2\left[\left(\frac{t-4t_p}{t_p}\right)^2 + \left(\frac{x^2+y^2}{r_p^2}\right)\right]\right\}. \tag{E.10}$$

For a mismatched interface at which the laser is incident on, a factor of $(1-R)$ needs to be included in the source term since R fraction of the incident energy is reflected.

$$S(x,y,z,t) = 8\left(\frac{\ln 2}{\pi}\right)^{1.5}\frac{\kappa E_{pulse}(1-R)}{t_p\, r_p^2}exp\left\{-\kappa z - 4\ln 2\left[\left(\frac{t-4t_p}{t_p}\right)^2 + \left(\frac{x^2+y^2}{r_p^2}\right)\right]\right\}. \tag{E.11}$$

APPENDIX F
BUILDING A CPDF TABLE FOR A MCM

Often, it is difficult to have an explicit equation for determining the scattering direction for particles. Therefore, a table containing all the scattering data including the CPDF should be established for determining the scattering angle for a given random number. This method can be used for obtaining the argument of a CPDF where it is difficult to invert analytically. For a given distribution $Z(\xi)$ ranging from ξ_a to ξ_b, its CPDF can be expressed as:

$$R(\xi) = \int_{\xi_a}^{\xi} Z(\xi')d\xi' \bigg/ \int_{\xi_a}^{\xi_b} Z(\xi')d\xi' .$$
(F.1)

For the sake simplicity, we define the followings:

$$\gamma = \int_{\xi_a}^{\xi} Z(\xi')d\xi' ,$$
(F.2)

and

$$\eta = \int_{\xi_a}^{\xi_b} Z(\xi')d\xi' .$$
(F.3)

The goal here is to evaluate $R(\xi)$ as a function ξ and store them. Any numerical integration technique can be employed to solve γ and η. For example, to evaluate η using the Composite Simpson rule, $[\xi_a, \xi_b]$ is subdivided into 2M subintervals of equal width:

$$h = \frac{\xi_b - \xi_a}{2M} .$$
(F.4)

By using $\xi_k = \xi_a + kh$ for k=0, 1,…, 2M, η is approximated as:

$$\eta \approx \frac{h}{3} \sum_{k=1}^{M} \left(Z(\xi_{2k-2}) + 4Z(\xi_{2k-1}) + Z(\xi_{2k}) \right) .$$
(F.5)

After evaluating and storing both $R(\xi)$'s and ξ's in a table, it is ready to be used for interpolations. For a given random number Ran_ξ, we compare it with $R(\xi)$'s in the table and search for the case where $Ran_\xi = R(\xi)$ by using the *bisectional method* instead of the sequential search. A final linear interpolation is required if Ran_ξ is in between two $R(\xi)$'s.

REFERENCES

Ambirajan, A. and D. C. Look (1997). "A Backward Monte Carlo Study of the Multiple Scattering of a Polarized Laser Beam." Journal of Quantitative Spectroscopy and Radiative Transfer **58**(2): 171-192.

Archard, G. D. (1961). "Back Scattering of Electrons." Journal of Applied Physics **32**(8): 1505-1509.

Ashcroft, N. W. and N. D. Mermin (1976). Solid State Physics. Philadelphia, Saunders Company.

Attard, C. and J. P. Ganachaud (1997). "Study of the Space Charge Indeuced by an Electron Beam in an Insulating Target - II. Presentation of the Results." Physica Status Solidi (b) **199**(2): 455-465.

Barkstorm, B. R. (1995). "An Efficient Algorithm for Choosing Scattering Directions in Monte Carlo Work with Arbitrary Phase Functions." Journal of Quantitative Spectroscopy and Radiative Transfer **53**(1): 23-38.

Berman, R. (1976). Thermal Conduction in Solids. Oxford, Oxford University Press.

Bethe, H. A. (1930). Annalen der Physik **5**: 325.

Bethune, D. S., K. C. H., et al. (1993). "Cobalt-Catalized Growth of Carbon Nanotubes With Single-Atomic-Layerwalls." Nature **363**: 605-607.

Blotekjaer, K. (1970). "Transport Equations for Electrons in Two-Valley Semiconductors." IEEE Transactions on Electron Devices **ED-17**(1): 38-47.

Bohren, C. F. and D. R. Huffman (1983). Absorption and Scattering of Light by Small Particles.

New York, John Wiley & Sons, Inc.

Bonard, J. M., F. Maier, et al. (1998). "Field Emission Properties of Multiwalled Carbon Nanotubes." <u>Ultramicroscopy</u> **73**: 7-15.

Bonard, J. M., J. P. Salvetat, et al. (1999). "Field Emission from Carbon Nanotubes: Perspectives for Applications and Clues to the Emission Mechanism." <u>Applied Physics A: Material Science & Processing</u> **69**(3): 245-254.

Bongeler, R., U. Golla, et al. (1993). "Electron-Specimen Interactions in Low Voltage Scanning Electron Microscopy." <u>Scanning</u> **15**(1): 1-18.

Brewster, M. Q. (1992). <u>Thermal Radiative Transfer and Properties</u>. New York, Wiley-Interscience.

Browning, R., T. Z. Li, et al. (1994). "Empirical Forms for the Electron/Atom Elastic Scattering Cross Sections from 0.1 to 30 keV." <u>Journal of Applied Physics</u> **76**(4): 2016-2022.

Bube, R. H. (1992). <u>Electrons in Solids</u>. San Diego, CA, Academic Press, INC.

Burchell, T. D., Ed. (1999). <u>Carbon Materials for Advanced Technologies</u>. New York, Eisevier Science Ltd.

Cahill, D. G., W. K. Ford, et al. (2003). "Nanoscale Thermal Transport." <u>Applied Physics Reviews</u> **93**(2): 793-818.

Cercignani, C. (1988). <u>The Boltzmann Equation and Its Applications</u>. New York, Springer-Verlag New York, Inc.

Cohen-Tannoudji, C., B. Diu, et al. (1977). <u>Quantum Mechanics</u>. Paris, Hermann.

Czyzewski, Z., D. O. N. MacCalium, et al. (1990). "Calculations of Mott Scattering Cross Section." <u>Journal of Applied Physics</u> **68**(7): 3066-3072.

Dapor, M. (2003). <u>Electron-Beam Interactions with Solids</u>. Berlin, Springer-Verlag Berlin Heidelberg.

De Crescenzi, M. and M. N. Piancastelli (1996). <u>Electron Scattering and Related Spectroscopies</u>. Singapore, World Scientific Publishing Co. Pte. Ltd.

Ding, Z. J. and R. Shimizu (1996). "A Monte Carlo Modeling of Electron Interaction with Solids Including Cascade Secondary Electron Production." <u>Scanning</u> **18**: 92-113.

Ebbesen, T. W. (1994). "Carbon Nanotubes." <u>Annual Review of Materials Science</u> **24**: 235-264.

Egerton, R. F. (1996). <u>Electron Energy Loss Spectrometry in the Electron Microscope</u>. New York, Plenum Press.

Ferry, D. K. and S. M. Goodnick (1997). <u>Transport in Nanostructures</u>. New York, Cambridge University Press.

Filip, V., D. Nicolaescu, et al. (2001). "Modeling of the Electron Field Emission from Carbon Nanotubes." <u>Journal of Vacuum Science Technology B</u> **19**(3): 1016-1022.

Fischetti, M. V. and S. E. Laux (1988). "Monte Carlo Analysis of Electron Transport in Small Semiconductor Devices including Band-Structure and Space-Charge Effects." <u>Physical Review B</u> **38**(14): 9721-9745.

Flock, S. T., M. S. Patterson, et al. (1989). "Monte Carlo Modeling of Light Propagation in Highly Scattering Tissues - I: Model Predictions and Comparison with Diffusion Theory." <u>IEEE Trans. Med. Eng.</u> **36**: 1162-1168.

Fowler, A. and M. P. Mengüç (2000). "Propagation of Focused and Multibeam Laser Energy in Biologi-cal Tissues." ASME Journal of Biomechanical Engineering **122**: 534-540.

Fransen, M. J., T. L. van Rooy, et al. (1999). "Field Emission Energy Distributions from Individual Multiwalled Carbon Nanotubes." Applied Surface Science **146**: 312-327.

Fushinobu, K., A. Majumdar, et al. (1995). "Heat Generation and Transport in Submicron Semi-conductor Devices." Journal of Heat Transfer **117**: 25-31.

Ganachaud, J. P., C. Attard, et al. (1997). "Study of the Space Charge Induced by an Electron Beam in an Insulating Target I. Monte Carlo Simulation Model." Physica Status Solidi (b) **199**: 175-184.

Gibson, L. S. and M. F. Ashby (1997). Cellular Solids, Cambridge.

Giovanelli, R. G. (1955). "Reflection by Semi-Infinite Diffusers." Opt. Acta 2: 153-162.

Grosso, G. and G. P. Parravicini (2000). Solid State Physics. San Diego, Academic Press.

Hecht, E. (1998). Optics, Addison Wesley Longman, Inc.

Hii, K.-F. (2006/2007). Doctoral Dissertation. Mechanical Engineering. Lexington, University of Kentucky (in progress).

Hochstrasser, R. M. (1964). Behavior of Electrons in Atoms. New York, W. A. Benjamin, Inc.

Hohlfeld, J., S.-S. Wellershoff, et al. (2000). "Electron and Lattice Dynamics Following Optical Excitation of Metals." Chemical Physics **251**: 237-258.

Howell, J. R. (1968). Application of Monte Carlo to Heat Transfer Problems. Advances in Heat Transfer. J. P. Hartnett and T. F. Irvine. New York, Academic Press. **5**.

Ibach, H. and D. L. Mills (1982). <u>Electron Energy Loss Spectroscopy and Surface Vibrations</u>. New York, Academic Press, Inc.

Iijima, S. and T. Ichihashi (1993). "Single-shell Carbon Nanotubes of 1-nm Diameter." <u>Nature</u> **363**: 603-605.

Incropera, F. P. and D. P. DeWitt (1996). <u>Fundamentals of Heat and Mass Transfer</u>. New York, John Wiley & Sons.

Ivanov, D. S. and L. V. Zhigilei (2003). "Combined Atomistic-Continuum Modeling of Short-Pulse Laser Melting and Disintegration of Metal Films." <u>Physical Review B</u> **68**: 064114.

Jacoboni, C. and L. Reggiani (1983). "The Monte Carlo Method for the Solution of Charge Transport in Semiconductors with Applications to Covalent Materials." <u>Reviews of Modern Physics</u> **55**(3): 645-705.

Jacques, S. L. and L. Wang (1995). Monte Carlo Modeling of Light Transport in Tissues. <u>Optical-Thermal Response of Laser-Irradiated Tissue</u>. A. J. Welch and M. J. C. Van Gemert. New York, Plenum Press**:** 73-100.

Joy, D. C. (1995). <u>Monte Carlo Modeling for Electron Microscopy and Microanalysis</u>. New York, Oxford University Press.

Joy, D. C. (2001). "A Database of Electron-Solid Interactions." http://web.utk.edu/~srcutk/htm/interact.htm

Joy, D. C. and S. Luo (1989). <u>Scanning</u> **11**: 176.

Kanaya, K. and S. Okayama (1972). "Penetration and Energy-Loss Theory of Electrons in Solid Targets." <u>Journal of Physics D: Applied Physics</u> **5**: 43-58.

Kessler, J. (1976). <u>Polarized Electrons</u>. New York, Springer Verlag.

Kim, S. H., Y. M. Ham, et al. (1998). "New Approach of Monte Carlo Simulation for Low Energy Electron Lithography." <u>Microelectronic Engineering</u> **41/42**: 179-182.

Kotera, M. (1989). "A Monte Carlo Simulation of Primary and Secondary Electron Trajectories in a Specimen." <u>Journal of Applied Physics</u> **65**(10): 3991-3998.

Kumar, S. and K. Mitra (1999). "Microscale Aspects of Thermal Radiation Transport and Laser Applications." <u>Advances in Heat Transfer</u> **33**: 187-294.

Lockwood, C. E., P. M. Bummer, et al. (1997). "Purification of Proteins Using Foam Fractionation." <u>Pharm. Res.</u> **14**: 1511-1515.

Longtin, J. P. and C. L. Tien (1996). "Saturable Absorption during High-Intensity Laser Heating of Liquids." <u>Journal of Heat Transfer</u> **118**: 924-930.

Lugovskoy, A. V. and B. I. (2001). "Electron-Electron Scattering Rate in Thin Metal Films." <u>Physical Review B</u> **65**: 045405-1.

Luo, S. C., X. Zhang, et al. (1991). "Experimental Determinations of Electron Stopping Power at Low Energies." <u>Radiation Effects and Defects in Solids</u> **117**: 235-242.

Majumdar, A., K. Fushinobu, et al. (1995). "Effect of Gate Voltage on Hot-Electron and Hot-Phonon Interaction and Transport in a Submicrometer Transistor." <u>Journal of Applied Physics</u> **77**(12): 6686-6694.

Majumdar, A. (1998). Microscale Energy Transport in Solids. <u>Microscale Energy Transport</u>. C. L. Tien. New York, Begell House**:** 1-93.

Martinez, J. D., R. Mayol, et al. (1990). "Monte Carlo Simulation of Kilovolt Electron Transport in Solids." Journal of Applied Physics **67**(6): 2955-2964.

Matthews, J. H. and K. D. Fink (1999). Numerical Methods Using Matlab. New Jersey, Prentice Hall, Inc.

Mazumder, S. and A. Majumdar (2001). "Monte Carlo Study of Phonon Transport in Solid Thin Films Including Dispersion and Polarization." Journal of Heat Transfer **123**: 749-759.

Mitin, V. V., V. A. Kochelap, et al. (1999). Quantum Heterostructures - Microelectronics and Optoelectronics. New York, Cambridge University Press.

Modest, M. F. (1993). Radiative Heat Transfer, McGraw-Hill, Inc.

Møller, C. (1931). Zeitschrift für Physik **70**: 786.

Mott, N. (1986). Conduction in Non-Crystaline Materials. New York, Oxford University Press.

Mott, N. F. (1979). Electronic Processes in Non-Crystaline Materials. New York, Oxford University Press.

Mott, N. F. and H. S. W. Massey (1965). The Theory of Atomic Collisions. Oxford, Clarendon Press.

Murata, K., T. Matsukawa, et al. (1971). "Monte Carlo Calculations on Electron Scattering in a Solid Target." Japanese Journal of Applied Physics **10**(6): 678-686.

Newbury, D. E. and R. L. Myklebust (1981). Analytical Electron Microscopy. R. H. Geiss. San Francisco, San Francisco Press**:** 91.

Palik, E. D. (1985). Handbook of Optical Constants of Solids. New York, Academic Press.

Pines, D. and P. Nozières (1966). The Theory of Quantum Liquids. New York, Benjamin.

Qui, T. G. and C. L. Tien (1992). "Short Pulse Laser Heating in Metals." International Journal of Heat and Mass Transfer **35**: 719-726.

Quinn, J. J. (1962). "Range of excited Electrons in Metals." Physical Review **126**(4): 1453-1457.

Ralston, J., D. Fornasiero, et al. (1999). "Bubble-Particle Attachment and Detachment in Floatation." Int. J. Mineral Processing **56**: 133-164.

Renoud, R., F. Mady, et al. (2002). "Monte Carlo Simulation of the Charge Distribution Induced by a High-Energy Electron Beam in an Insulating Target." Journal of Physics: Condensed Matter **14**: 231-247.

Saito, Y., K. Hamaguchi, et al. (1998). "Field Emission from Carbon Nanotubes Purified Single-Walled and Multi-Walled Tubes." Ultramicroscopy **73**: 1-6.

Saito, Y., K. Hamaguchi, et al. (1998). "Field Emission from Multi-Walled Carbon Nanotubes and Its Application to Electron Tubes." Applied Physics A, Materials Science & Processing **67**(1): 95-100.

Salvat, F., J. D. Martinez, et al. (1985). "A Simple Model for Electron Scattering: Inelastic Collisions." Journal of Physics D: Applied Physics **18**: 299-315.

Shimizu, R., T. Ikuta, et al. (1972). "The Monte Carlo Technique as Applied to the Fundamentals of EPMA and SEM." Journal of Applied Physics **43**: 4233-4249.

Siegel, R. and J. R. Howell (2002). Thermal Radiation Heat Transfer. New York, Taylor & Francis.

Singh, N. and S. Prakash (1973). "Phonon Frequencies and Cohesive Energies of Copper, Silver, and Gold." Physical Review B **8**(12): 5532-5544.

Slater, J. C. (1965). Quantum Theory of Molecules and Solids. New York, McGraw-Hill Book Company.

Taniguchi, N., M. Ikeda, et al. (1989). Energy-Beam Processing of Materials: Advanced Manufacturing Using Various Energy Sources. New York, Oxford University Press.

Tien, C.-L., A. Majumdar, et al., Eds. (1998). Microscale Energy Transport. Series in Chemical and Mechanical Engineering. Washington, DC, Taylor & Francis.

Tomizawa, K. (1993). Numerical Simulation of Submicron Semiconductor Devices. Norwood, Artech House, Inc.

Trinkle, C. A. (2003). Fabrication of Nanotube-Tipped Tools and Flexural Bearing Displacement System for Field-Emission Nanomachining. M.S. Thesis. Mechanical Engineering. Lexington, University of Kentucky.

Tung, C. J., J. C. Ashley, et al. (1979). "Electron Inelastic Mean Free Paths and Energy Losses in solids II - Electron Gas Statistical Model." Surface Science **81**(2): 427-439.

Tzou, D. Y. (1997). Macro- to Microscale Heat Transfer. Washington, DC, Taylor & Francis.

Van de Hulst, H. C. (1957). Light Scattering by Small Particles. New York, John Wiley & Sons, Inc.

Van de Hulst, H. C. (1980). Multiple Light Scattering. New York, Academic Press.

Vriens, L. (1966). "Electron Exchange in Binary Encounter Collision Theory." Proceedings of the Physical Society **89**(1): 13-21.

Wagner, D. K. and R. Bowers (1978). "The Radio-Frequency Size Effect: A Tool for the Investigation of Conduction Electron Scattering in Metals." <u>Advances in Physics</u> **27**(5): 651-746.

Wang, L. and S. L. Jacques (1995). "Use of a Laser Beam with an Oblique Angle of Incidence to Measure the Reduced Scattering Coefficient of a Turbid Medium." <u>Applied Optics</u> **34**(13): 2362-2366.

Wang, L., S. L. Jacques, et al. (1995). "MCML-Monte Carlo Modeling of Light Transport in Multi-Layered Tissues." <u>Computer Method and Programs in Biomedicine</u> **47**: 131-146.

Whiddington, R. (1912). "The Transmission of Cathode Rays through Matter." <u>Proceedings of the Royal Society of London. Series A, Containing Papers of a Mathematical and Physical Character</u> **86**(588): 360-370.

Whitesides, G. M. and J. C. Love (2001). <u>The Art of Building Small</u>. Scientific American**:** 39-47.

Wong, B. T. (2001). Monte Carlo Techniques for the Solution of the Transient and Steady Radiative Transfer Equation. M.S. Thesis. <u>Mechanical Engineering</u>. Lexington, University of Kentucky.

Wong, B. T. and M. P. Mengüç (2002). "Comparison of Monte Carlo Techniques to Predict the Propagation of a Collimated Beam in Participating Media." <u>Numerical Heat Transfer, Part B</u> **42**: 119-140.

Wong, B. T. and M. P. Mengüç (2002). "Depolarization of Radiation by Non-Absorbing Foams." <u>Journal of Quantitative Spectroscopy and Radiative Transfer</u> **73**(2): 273-284.

Wong, B. T. and M. P. Mengüç (2003). <u>Electronic Thermal Conduction in Thin Gold Films</u>. ASME Summer Heat Transfer Conference, Las Vegas, Nevada.

Wong, B. T. and M. P. Mengüç (2004). "Monte Carlo Methods in Radiative Transfer and Electron-Beam Processing." <u>Journal of Quantitative Spectroscopy and Radiative Transfer</u> **84**: 437-450.

Wong, B. T., M. P. Mengüç, et al. (2002). <u>Modeling of Energy Transfer in Field Emission of Carbon Nanotubes</u>. 8th AIAA/ASME Joint Thermophysics and Heat Transfer Conference, St. Louis, Missouri.

Yasuda, M., H. Kawata, et al. (1995). "Study of the Spatial Distribution of Backscattered Electrons from a Gold Target with a New Monte Carlo Simulation." <u>Journal of Applied Physics</u> **77**(9): 4706-4713.

Yasuda, M., K. Tamura, et al. (2001). "A Monte Carlo Study of Spin-polarized Electron Backscattering from Gold Thin Films." <u>Nuclear Instruments and Methods in Physics Research B</u> **183**: 196-202.

Yoganathan, S. and S. K. Banerjee (1992). "A New Decoupled Algorithm for Nonstationary, Transient Simulations of GaAs MESFET's." <u>IEEE Transactions on Electron Devices</u> **39**(7): 1578-1587.

Ziman, J. M. (1960). <u>Electrons and Phonons</u>. London, Oxford University Press.

Ziman, J. M. (1964). <u>Principles of the Theory of Solids</u>. Cambridge, Cambridge University Press.

Personal Data

- Year of Birth: 1977.
- Place of Birth: Sarawak, Malaysia.

Education

- May 1999-May 2001 M. S. in Mechanical Engineering, University of Kentucky, Lexington, Kentucky, Cum GPA: 4.00/4.00.
- Jan. 1997-May 1999 B. S. in Mechanical Engineering, University of Kentucky, Lexington, Kentucky, Cum GPA: 3.81/4.00. Magna Cum Laude.
- Apr. 1995-Dec.1996 American University Program in Engineering, Inti College Sarawak, Sarawak, Malaysia, Cum GPA: 3.80/4.00.

Scholastic Honors and Awards

- University Scholar Program – The University Scholars Program is designed for particularly gifted and highly motivated students. Because of the savings in credit hours offered to these students, they may finish the baccalaureate and masters program in five years.
- National Science Foundation (NSF) Travel Grant – A National Science Foundation (NSF) grant for traveling to Third International Symposium on Radiative transfer, in Antalya, Turkey, June 17-22, 2001.
- Tennessee Valley Authority (TVA) Fellowship – A fellowship grant from the Tennessee Valley Authority (TVA) for financial support in 2002-2003.
- Dissertation Year Fellowship – Funding to support Dissertation Year Fellowships for the 2003-2004 Academic Year provided by the President's Office in order to enhance the research dimension of graduate education.

Research Projects

Doctoral Dissertation, University of Kentucky (2001-2006)

- Studying electron microscopy inside solids using the Monte Carlo simulation of electron trajectories.

- Modeling heat transfer phenomena in the field of electron emission from the carbon nanotubes coupled with the radiation heating and/or joule heating at nano-scales.

- Developing computational heat conduction models using (macro-/micro-/nanoscopic) approaches such as the Fourier heat conduction model, the two-temperature model, and/or the hydrodynamic model, involving coupled electron-phonon transport.

- Investigating the nano-scale transport phenomena/heat transfer based on the Boltzmann Transport Equation (BTE). Particularly, the Monte Carlo (MC) models are developed for the electron, phonon, and photon transport. Coupling these three transport models gives insight to the heat transfer at nano-scale levels, which is becoming more common in today's high-technology applications due to the fast development of nanotechnology.

Master's Thesis, University of Kentucky (1999-2001)

- Developed FORTRAN codes for simulating the propagating of collimated light in a participating medium using the Monte Carlo Method.

- Simulated light propagation in foams using a Monte Carlo Method combined with the ray-tracing technique and the Fresnel relations.

Additional Research, University of Kentucky (2000-2006)

- Modeling polarization of light as scattered multiply by moving air bubbles inside absorbing/non-absorbing liquid solution. Characterization of air bubble size can be achieved by detecting polarization change of the incident light.

- Studying polarization change of light after multiple scattering by participating medium.

Journal Publications

- Basil T. Wong, M. Pınar Mengüç, and R. Ryan Vallance, "Sequential Nano-Patterning Using Electron and Laser Beams: A Numerical Methodology," *Journal of Computational and Theoretical Nanoscience*, Vol. 3, No. 2, 2006, pp. 1-12.

- Basil T. Wong, M. Pınar Mengüç, and R. Ryan Vallance, "Nano-Scale Machining Via Electron Beam and Laser Processing," *ASME Journal of Heat Transfer*, Vol. 126, No. 4, 2004, pp. 566-576.

- Basil T. Wong and M. Pınar Mengüç, "Monte Carlo Methods in Radiative Transfer and

Electron-Beam Processing," *Journal of Quantitative Spectroscopy and Radiative Transfer*, Vol. 84, 2004, pp. 437-450.

- Rodolphe Vaillon, Basil T. Wong, and M. Pınar. Mengüç, "Polarized Radiative Transfer in a Particle-Laden Semi-Transparent Medium via a Vector Monte Carlo Method," *Journal of Quantitative Spectroscopy and Radiative Transfer*, Vol. 84, 2004, pp. 383-394.

- Christy A. Trinkle, P. Kichambare, R. Ryan Vallance, Basil T. Wong, M. Pınar Mengüç, B. Sadanadan, A. M. Rao, A. Bah and K. Javed, "Thermal Transport During Nanoscale Machining by Field Emission of Electrons from Carbon Nanotubes," *ASME Journal of Heat Transfer*, Vol. 125, No. 4, 2003, pp. 546.

- Basil T. Wong and M. Pınar Mengüç, "Comparison of Monte Carlo Techniques to Predict the Propagation of a Collimated Beam in Participating Media," *Numerical Heat Transfer: Part B Fundamentals*, Vol. 42, 2002, pp. 1-22.

- Basil T. Wong and M. Pınar Mengüç, "Depolarization of Radiation by Non-Absorbing Foams," *Journal of Quantitative Spectroscopy and Radiative Transfer* Vol. 73 Issue 2, No. 5, 2002, pp. 273-284.

Conference Publications

- Basil T. Wong, M. Pınar Mengüç, and R. Ryan Vallance, "Thermal Heating Induced by Electron-Beam: The Coupling of Monte Carlo Simulation in e-Beam and Electron-Phonon Equations," (*In preparation*)

- Basil T. Wong, M. Pınar Mengüç, and R. Ryan Vallance, "Sequential Nano-Patterning Using Electron and Laser Beams: A Numerical Methodology," *4th International Symposium on Radiation*, Istanbul, Turkey, June 21-25, 2004.

- Basil T. Wong, Rodolphe Vaillon, and M. Pınar Mengüç, "Propagation of Polarized Light in Foamy Materials: A Vector Monte Carlo Approach via Stokes Parameters," *ASME International Mechanical Engineering Congress and Exposition*, Washington, D.C., November 15-21, 2003. Paper# IMECE 2003-42018.

- Basil T. Wong and M. Pınar Mengüç, "Electronic Thermal Conduction in Thin Gold Films," *ASME Summer Heat Transfer Conference*, July 21-23, 2003. Paper# HT 2003-47172.

- Basil T. Wong and M. Pınar Mengüç, "Monte Carlo Methods in Radiative Transfer and

Electron-Beam Processing," *Proceedings of Eurotherm 73 on Computational Thermal Radiation in Participating Media*, Mons, Belgium, April 15-17, 2003.

- Rodolphe Vaillon, Basil T. Wong, and M. Pınar. Mengüç, "Polarized Radiative Transfer in a Particle-Laden Semi-Transparent Medium via a Vector Monte Carlo Method," *Proceedings of Eurotherm 73 on Computational Thermal Radiation in Participating Media*, Mons, Belgium April 15-17, 2003.

- Christy A. Trinkle, Philip Smith, R. Ryan Vallance, Basil T. Wong, and M. Pınar Mengüç, "Thermal Finite Difference Analysis of Threshold Heating for Nanoscale Machining," presented at the *ASME International Mechanical Engineering Congress and Exposition*, New Orleans, Louisiana, November 17-22, 2002.

- Basil T. Wong, M. Pınar Mengüç, R. Ryan Vallance, and Christy A. Tinkle, "Modeling of Energy Transfer in Field Emission of Carbon Nanotubes," presented at the *8th AIAA/ASME Joint Thermophysics and Heat Transfer Conference*, St. Louis, Missouri, June, 2002.

- Basil T. Wong and M. Pınar Mengüç, "Depolarization of Radiation by Non-Absorbing Foams," presented at *3rd International Symposium on Radiative Transfer*, Antalya, Turkey, 2001.

- Basil T. Wong and M. Pınar Mengüç, "Comparison of Monte Carlo Techniques to Predict the Propagation of a Collimated Beam in Participating Media," paper #1-22-24, presented at *35th National Heat Transfer Conference* (NHTC), California, 2001.

Posters

- Basil T. Wong, R. Ryan Vallance, and M. Pınar Mengüç, "Modeling of Thermal Transport During Nanoscale Machining by Field Emission of Electrons," presented at the *International Forum on Heat Transfer* (IFHT), Kyoto, Japan, November 24-26, 2004.

- Basil T. Wong, R. Ryan Vallance, and M. Pınar Mengüç, "Modeling of Thermal Transport During Nanoscale Machining by Field Emission of Electrons," presented at the KY-NANOMAT, Louisville, Kentucky, November 17-22, 2002.

- Christy A. Trinkle, P. Kichambare, R. Ryan Vallance, Basil T. Wong, M. Pınar Mengüç, B. Sadanadan, A. M. Rao, A. Bah and K. Javed, "Thermal Transport During Nanoscale Machining by Field Emission of Electrons from Carbon Nanotubes," presented at the

ASME International Mechanical Engineering Congress and Exposition, New Orleans, Louisiana, November 17-22, 2002.

- M. Pınar Mengüç, M. Kozan, Basil T. Wong, S. Manickavasagam, and C. Saltiel, "A Compact System for Characterization of Size and Shape of Nano-Particles and Agglomerates," presented at *3rd International Symposium on Radiative Transfer*, Antalya, Turkey, 2001.

Work Experiences

- Jul. 2004-May 2006   Research Assistant. Conduct research on nano-scale heat transfer.
- Jul. 2004-Dec. 2004   Teaching/Research Assistant. Partially taught/responsible for ME599 – Nano-scale Thermal Science, and conduct research.
- Jul. 2003-Jun. 2004   Fellow. Funded by the Dissertation Year fellowship.
- Jul. 2002-Jun. 2003   Fellow. Funded by the TVA fellowship.
- Jan. -Jun. 2002 Research Assistant. Conducted experiments, writing technical publications.
- May 1999-Dec. 2001 Teaching Assistant. Assisted the lecturer, gave tutorials and supervised students, graded homework and examination papers for the following courses: Engineering Dynamics, Fluid Mechanics, and Engineering Thermodynamics.
- May-Aug. 2000 Research Assistant. Conducted experiments for the particles characterization research, particularly, soot and nanoparticles.